UNCLASSIFIED

AD NUMBER
AD864446
LIMITATION CHANGES

TO:

Approved for public release; distribution is unlimited.

FROM:

Distribution authorized to U.S. Gov't. agencies and their contractors; Administrative/Operational Use; SEP 1969. Other requests shall be referred to Army Aviation Materiel Labs., Fort Eustis, VA.

AUTHORITY

AMRDL ltr 23 Jun 1971

THIS PAGE IS UNCLASSIFIED

AD

USAAVLABS TECHNICAL REPORT 69-59

DETAILED DESIGN OF A 2000-SHP ADVANCED TECHNOLOGY V/STOL PROPELLER SYSTEM

By

D. P. Currie

D D C

FEB 4 1978

B

September 1969

U. S. ARMY AVIATION MATERIEL LABORATORIES
FORT EUSTIS, VIRGINIA

CONTRACT DAAJ02-68-C-0079
HAMILTON STANDARD
DIVISION OF UNITED AIRCRAFT CORPORATION
WINDSOR LOCKS, CONNECTICUT

247

DEPARTMENT OF THE ARMY
U. S. ARMY AVIATION MATERIEL LABORATORIES
FORT EUSTIS. VIRGINIA 23604

This report was prepared by the Hamilton Standard Division
of United Aircraft Corporation under the terms of Contract
DAAJ02-68-C-0079. It consists of a composite material blade
retention feasibility investigation, a titanium barrel and
main propeller bearing design and analysis, and a titanium
gear coating process investigation and laboratory testing.

The object of this contractual effort was to conduct detailed
design and to perform limited laboratory testing of the most
critical components of an advanced technology V/STOL propeller
system for the 1975 time period. Two scaled boron-aluminum
retention specimens were fabricated and tensile tested, and
several titanium gear coating processes were investigated
through limited gear testing.

DETAILED DESIGN OF A 2000-SHP ADVANCED TECHNOLOGY V/STOL PROPELLER SYSTEM

Final Report

By

D. P. Currie

Prepared by

Hamilton Standard
Division of United Aircraft Corporation
Windsor Locks, Connecticut

for

U.S. ARMY AVIATION MATERIEL LABORATORIES
FORT EUSTIS, VIRGINIA

SUMMARY

The purpose of this program was to establish a sound technical foundation for the inclusion of lightweight titanium barrels, titanium power gearing, and composite boron-aluminum spar blades in an advanced (1970-1975) V/STOL propeller system.

Several new titanium barrel concepts were designed and analyzed. This study has led to the recommendation of a titanium barrel with a spherical hub structure for subsequent fabrication and development testing.

Endurance testing of titanium gears indicated that improved wear coatings would be required in order to demonstrate a significant weight-saving potential over 1975 steel gearing. However, the diffused nickel coating would permit significant weight reductions over current steel power gearing.

Titanium gears were also coated and evaluated under this program using an ion-sputtering coating technique. Limited testing of such gears resulted in early scuffing and wear of the coating; however, the basic coating concept is sound and processing refinements have been defined that indicate potential for sputtered-coated titanium gears.

The fabrication and testing of boron-aluminum composite blade retention specimens proved to be successful and have provided a sound basis for the fabrication and development testing of full-scale propeller blades.

FOREWORD

The preparation of this final report concluded a 9-month exploratory program conducted by Hamilton Standard under U.S. Army Aviation Materiel Laboratories (USAAVLABS) Contract DAAJ02-68-C-0079, Task 1G162203D14415. This program was an outgrowth of a previous contract with USAAVLABS (Contract DAAJ02-67-C-0073) which involved a feasibility study of "Advanced V/STOL Propeller Technology" for the 1970-1975 time period.

The work associated with this program served to strengthen the technological background for specific components that had been recommended for inclusion in an advanced V/STOL propeller system as a result of the initial feasibility study.

The program was directed by Mr. D. P. Currie, Program Manager, under the supervision of Mr. A. D. Croxall, Chief Project Engineer. Significant contributions in each specific area of the program were made by the following Hamilton Standard technical personnel:

Design Studies: Mr. R. Gustafson, Design Engineer

Titanium Gear Coating
Investigation: Mr. E. Fahy, Senior Experimental Engineer

Borsic®Aluminum Blade
Retention Investigation: Mr. G. Kutner, Assistant Project Engineer

v

TABLE OF CONTENTS

TABLE OF CONTENTS (CONT)

LIST OF ILLUSTRATIONS

LIST OF ILLUSTRATIONS (CONT)

LIST OF ILLUSTRATIONS (CONT)

LIST OF ILLUSTRATIONS (CONT)

LIST OF ILLUSTRATIONS (CONT)

LIST OF ILLUSTRATIONS (CONT)

LIST OF TABLES

LIST OF TABLES (CONT)

LIST OF SYMBOLS

A	area, in.^{2}
AF	blade activity factor
asf	current density, amp/ft^2
B	beam
b	thickness, in.
CB	bearing dynamic load capacity, 'b
CF	centrifugal load, lb
C_L	lift coefficient
C_{L_i}	integrated lift coefficient
D	disc
d	diameter, in.
dm	pitch diameter, in.
E	modulus of elasticity, psi
EF	excitation factor
e	elongation, in.
F	force, lb
Fa	allowable stress, psi
FT	frictional torque, in.-os
f	calculated stress, psi
G	shear modulus, psi
GW	gross weight, lb

LIST OF SYMBOLS (CONT)

h   distance from neutral axis to centroidal axis, in.

I   moment of inertia, $in.^4$

I(NA)   moment of inertia about neutral axis, $in.^4$

J   polar moment of inertia, $in.^4$

K   constant

K_t stress concentration factor

L   length, in.

Le   effective length, in.

Li   life, hr

L_r radial length, in.

M   moment, in.-lb

M_{ME} mean effective moment, in.-lb

MS   margin of safety

N   number of elements

N_z load factor

P   load, lb

P_a axial load, lb

P_e equivalent radial load, lb

P_r radial load, lb

prpm   propeller speed, rpm

Q   thrust, lb

Q_e	effective thrust, lb
Q_{ME}	mean effective thrust, lb
q	airstream dynamic pressure, lb/ft^2
R	radius, in.
r	pitch radius, in.
SBM	steady bending moment, in.-lb
SF	stress factor
SR	spring rate, lb/in.
SPHI/BOT	meridional normal stress on bottom fiber, psi
SPHI/TOP	meridional normal stress on top fiber, psi
STHET/BOT	circumferential normal stress on bottom fiber, psi
STHET/TOP	circumferential normal stress on top fiber, psi
SFITH/BOT	in-plane shear stress on bottom fiber, psi
SFITH/TOP	in-plane shear stress on top fiber, psi
T	torque, lb-in.
T_1	total coating thickness in one revolution, in.
T_N	total coating thickness after N revolutions, in.
t	time, sec
t_T	total time, sec
V	bearing rotational factor
Ve	equivalent airspeed, kn

LIST OF SYMBOLS (CONT)

VBM	vibratory bending moment, in.-lb
X	bearing load factor
Y	bearing load factor
y	distance to neutral axis, in.
z	number of rollers
α	angle of attack, deg
ψ	angle of thrust axis to airstream at the propeller disc, deg
θ	angle, deg
δ	deflection, in.
π	Pi, 3.1416
θ_T	total angle of rotation, rad
ω	angular velocity, rad/sec

INTRODUCTION

Under U.S. Army Aviation Materiel Laboratories (USAAVLABS) Contract DAAJ02-67-C-0073, a feasibility study of an advanced V/STOL propeller system was conducted. The primary focus of this study was to ascertain what weight reductions could be achieved for the 1970-1975 time period in comparison to present-day V/STOL systems. To accomplish this weight reduction, new concepts and materials were used in preliminary designs of three specific propeller systems.

Under the present contract, four specific areas related to this advanced V/STOL propeller system were investigated. The undertaking of these tasks (listed below) provided a logical follow-on program to the initial feasibility study.

A New Barrel Concept Design and Analysis Study Program

A Main Bearing Design and Analysis Program

A Titanium Gear Coating Optimization Program

A Boron Spar Blade Retention Design and Test Program

1

TITANIUM BARREL DESIGN STUDIES

INTRODUCTION

Under this portion of the contract, detailed designs were conducted on two components of the propeller system. These were the propeller barrel and the main propeller mount bearing. For a concrete forecast of barrel weight reduction, detailed designs of several different barrel concepts were constructed. Both 3-blade and 4-blade barrels were investigated for each concept. The analysis and comparison of these barrels comprise the following section. The subsequent section contains the main propeller mount bearing loads and analysis to verify the capacity required to produce a 3000-hour bearing design. As part of the bearing design, it was necessary to analyze the front housing to ensure compatibility between the housing and the main bearing.

BARREL DESCRIPTIONS

A basic description of the various barrel concepts analyzed under this program is given below.

Spherical Barrel

The spherical barrel construction (see Figure 1) is essentially made up of two components:

1. A spherical centerbody.
2. Intersecting cylindrical barrel arms.

Because the centerbody is spherical and the barrel arms are cylindrical, the line of intersection is a circle. About this circle a blend fillet is made to smooth the transition from the arm to the centerbody. That portion of the centerbody inside the barrel arm is removed. At the end of each barrel arm are the blade retention areas. The front and rear rings both intersect the centerbody in a circle making the fillet blend constant. The tailshaft is of a larger radius than that of the front and rear rings, thereby intersecting both the centerbody and the barrel arm cylinders. Drawings of the 3-blade and 4-blade spherical barrels are shown in Figures 2 and 3.

3

SPHERICAL CENTERBODY

CYLINDRICAL BARREL ARM

CIRCULAR LINE OF INTERSECTION

MODEL CROSS SECTION

REMOVE
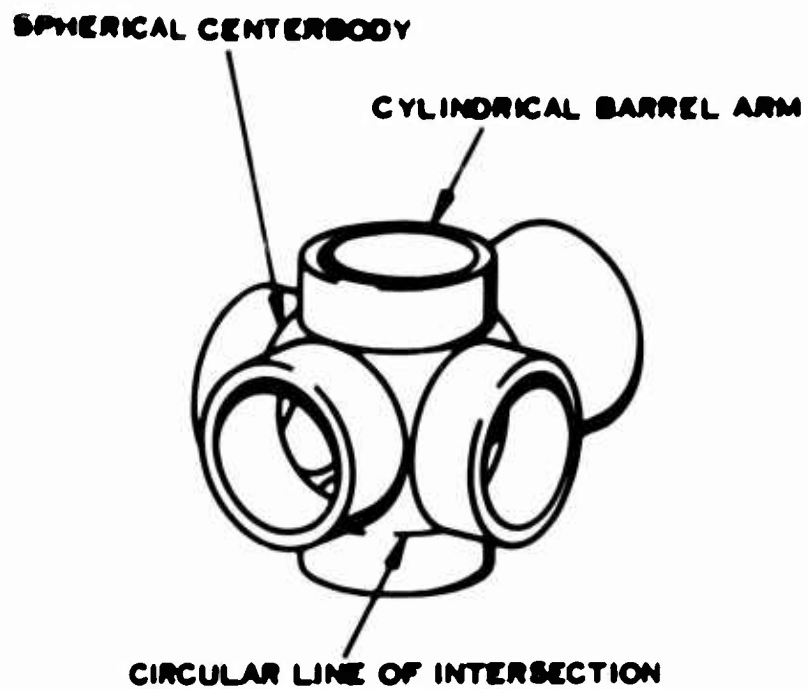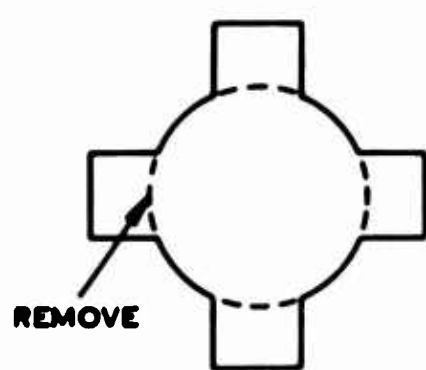
Figure 1. Spherical Barrel Construction.
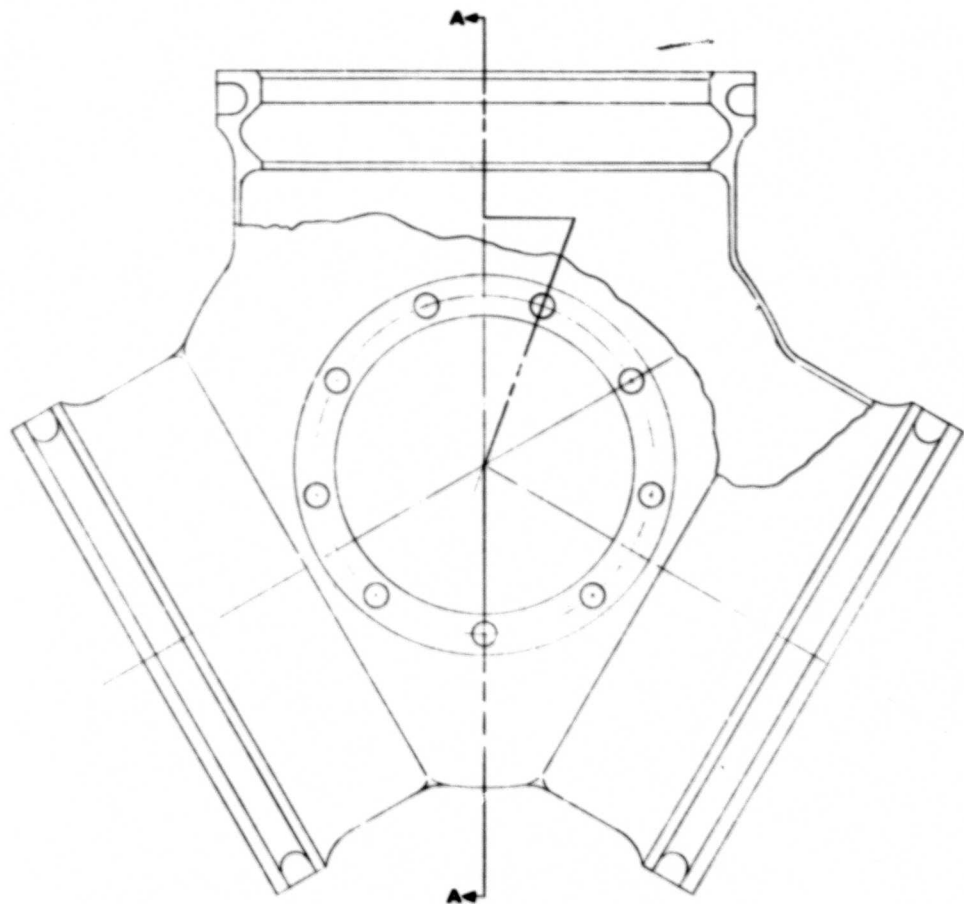
Figure 2. 3-Blade Spherical Barrel.

.125 THK

.500-20 UNF-2B
9 PLACES
EQUALLY SPACED

.125
THK
TYP

SPUR SPLINE

LOCAL
OPENING
3 PLACES

.125 THK

SECTION A-A

8-DESTRUCTIVE INSPECTION REQUIRED FOR FIRST DEVELOPMENT LOT ANY
CHANGES TO PROCESSING OR TOOLING OR THE VENDOR REQ.
REQUALIFYING TO THIS SPEC.
7-STRESS RELIEVE AT 750°F IN AIR FOR 1 HOUR, STOCK REMOVAL NOT
TO EXCEED .020 ON DIA AFTER STRESS RELIEF, EXCEPT THD
(MACH. PART ONLY)
6-MIL-I-6866 TYPE I PER HS447 & TEST PER HS 1556 CL C
BOTH ALL AREAS
5-V-NOTCHED CHARPY IMPACT TEST SPECIMEN-IMPACT TEST PER
MIL-T-9047
4-NOTCHED BAR STRESS RUPTURE TEST SPECIMEN PER HS463
3-SMOOTH BAR TENSILE SPECIMEN PER FED-STD-151 TY R3
(SELECTION OF TEST BAR LOCATION SHOWN ON F734507
AND F704502)
2-MAT'L: HS463 TYPE I WITH ADDED REQUIREMENTS AS FOLLOWS:
COMPLETELY DESCALED MECHANICAL PROPERTIES SHALL
CONFORM TO REQUIREMENTS OF HS 463 TYPE I EXCEPT
TENSILE PROPERTY REQUIREMENTS
TENSILE STRENGTH - - - - - PSI MIN - - - - - 140,000
YIELD STRENGTH AT 0.2% ELONG - - - - - - PSI MIN - - -130,000
ELONGATION PERCENT IN 2 INCHES - - - - MIN - - - -10
REDUCTION OF AREA PERCENT - - - - - MIN - - - -25
1-HEAT TREAT PER MIL-H-81200 IN FORGED COND 30-39 Rc

Figure 3. 4-Blade Spherical Barrel.

.500-20 LNF-2B
9 PLACES
EQUALLY SPACED

SPUR SPLINE

.25 THK
TYP

LOCAL OPENINGS
4 PLACES

.43 WALL

SECTION BB
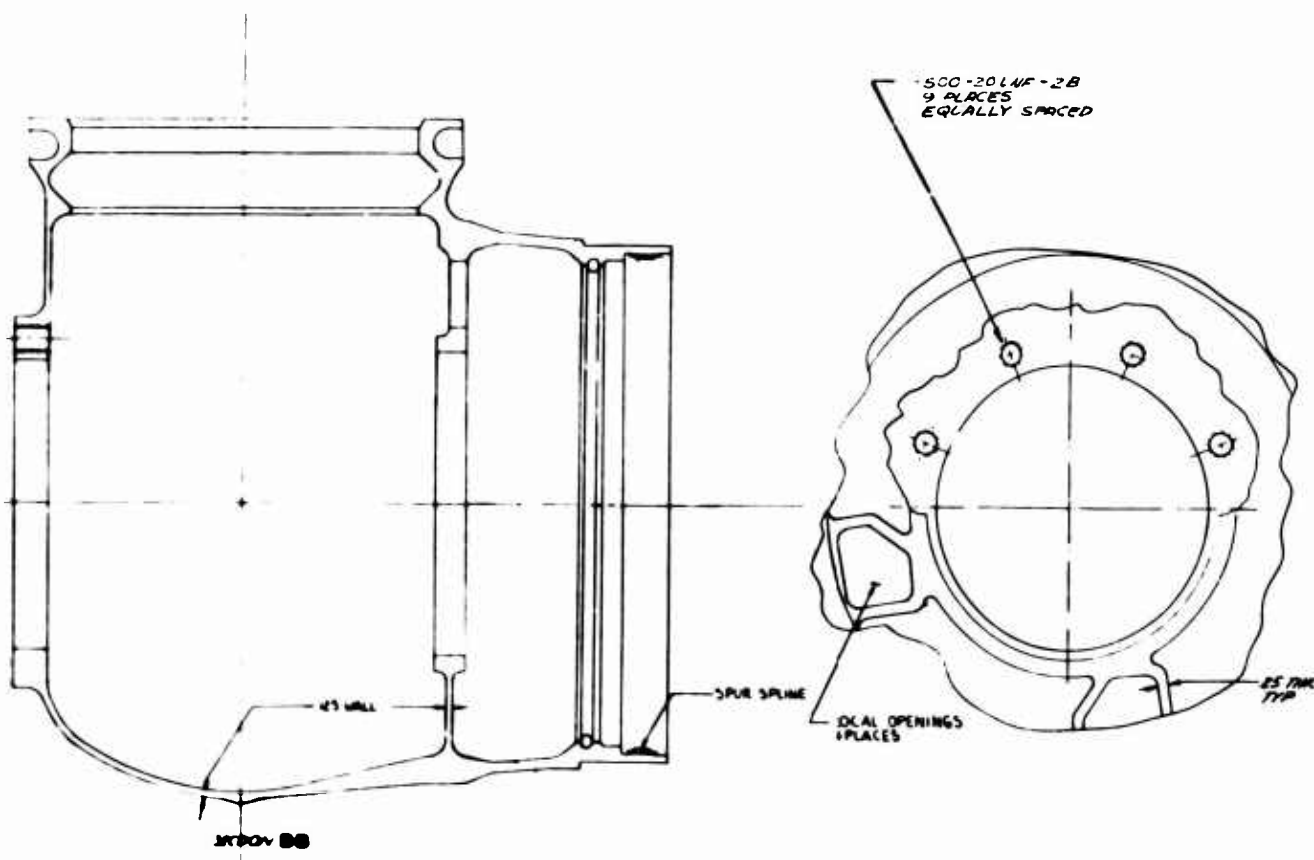
Shell Barrel

The shell barrel construction (see Figure 4) consists of a curved surface projected from one retention ring area to another, making a line drawn from a point on one ring to an identical point on the other ring a straight line. In the area of the front and rear rings, these surfaces extend from between arms and begin a transition from a curved surface to a flat surface. The front and rear rings are mounted mostly on this flat surface, with small portions intersecting the curve. The tail-shaft is larger in diameter than either the front or the rear ring, and its intersection with the barrel occurs almost exclusively in the curved surface area. Drawings of the 3-blade and 4-blade shell barrels are shown in Figures 5 and 6.

Figure 4. Shell Barrel Construction.

9

Figure 5. 3-Blade Shell Barrel.

8-DESTRUCTIVE INSPECTION REQUIRED FOR FIRST DEVELOPMENT LOT, ANY
CHANGES TO PROCESSING OR TOOLING OR THE VENDOR REQ.
REQUALIFYING TO THIS SPEC.

7-STRESS RELIEVE AT 750° F IN AIR FOR 1 HOUR, STOCK REMOVAL NOT
TO EXCEED .020 ON DIA AFTER STRESS RELIEF, EXCEPT THD
(MACH. PART ONLY)

6-MIL-I-6866 TYPE I PER HS 447 & TEST PER HS 1556 CL C
BOTH ALL AREAS

5-V-NOTCHED CHARPY IMPACT TEST SPECIMEN-IMPACT TEST PER
MIL-T-9047

4-NOTCHED BAR STRESS RUPTURE TEST SPECIMEN PER HS 463

3-SMOOTH BAR TENSILE SPECIMEN PER FED-STD-151 TY RS
(SELECTION OF TEST BAR LOCATION SHOWN ON F734507
AND F704502)

2-MATL: HS 463 TYPE I WITH ADDED REQUIREMENTS AS FOLLOWS:
COMPLETELY DESCALED MECHANICAL PROPERTIES SHALL
CONFORM TO REQUIREMENTS OF HS 463 TYPE I EXCEPT
TENSILE PROPERTY REQUIREMENTS
TENSILE STRENGTH - - - - - PSI MIN - - - - - 140,000
YIELD STRENGTH AT 0.2% ELONG - - - - - - PSI MIN - - - 130,000
ELONGATION PERCENT IN 2 INCHES - - - MIN - - - - 10
REDUCTION OF AREA PERCENT - - - - - MIN - - - - 25

1-HEAT TREAT PER MIL-H-81200 IN FORGED COND 30-39 Rc

.125 THK

.125 THK

SECTION A-A

SPUR SPLINE

.500-20 UNF-2B
9 PLACES
EQUALLY
SPACED

LOCAL
OPENING
3 PLACES

.25
THK
TYP

Figure 6.   4-Blade Shell Barrel.

13

.25 THK TYP

SPUR SPLINE

LOCAL
OPENINGS
4 PLACES

.25 WALL

SECTION BB

.200-30UNF-2B
8 PLACES
EQUALLY
SPACED

Crossed Tube Barrel

Geometrically, the 4-blade crossed tube barrel (Figure 7) can be visualized as two cylinders passed through each other at right angles with all the cylinder walls undistrubed. On the end of each barrel arm are the blade retention areas. The front ring structure, which provides a mount for the actuator dome assembly, interrupts the cylinders in their intersection area. This also occurs at the rear ring which provides support for the translating actuator assembly. The tailshaft can be thought of as a third cylinder intersecting the other two at right angles (i.e., the tailshaft is symmetrical about a third axis of "Z" axis which is normal to the "X" and "Y" axes). Drawings of the 3-blade and 4-blade crossed tube barrels are shown in Figures 8 and 9.

FABRICATION CONSIDERATIONS

Forging

The strength obtainable from a titanium forging is related to the wall thickness. Since the forging strength is directly related to the amount of working during forging, the thinner the wall the greater the strength. A 4-blade barrel permits piercing of the arms without requiring expensive blocker dies. The shell and spherical barrels with their open centerbody construction permit the piercing tool to pass completely through the arm into the centerbody area, producing relatively thin sections. The 4-blade crossed tube with its closed centerbody prevents piercing of the arms. The front ring and tailshaft-rear ring area can be worked, but the wall thickness is greater for the crossed tube than for the shell or spherical barrel. In titanium, better forging properties can be obtained for a shell or spherical barrel than for a crossed tube barrel. A 3-blade barrel requires the use of expensive blocker dies to support and position the forging while one arm is being pierced.

Machining

Two general methods of machining the barrels will be considered: the traditional method using cutting tools and electro chemical milling (ECM).

The first method to be considered is the traditional method. The outer surface of the barrel centerbodies is machined on a milling machine with a tracer attachment. The final operation is hand grinding to change the rough milling surface into a smooth surface. The barrel tailshaft outside and inside surfaces and the inside diameters of the front and rear rings are turned about the barrel centerline. The aft surface of the rear ring is contour-milled to produce the reinforcing ribs around the holes that the links pass through. The above discussion applies to all

15

CONTINUOUS
WALLS

CUTTING
LINE
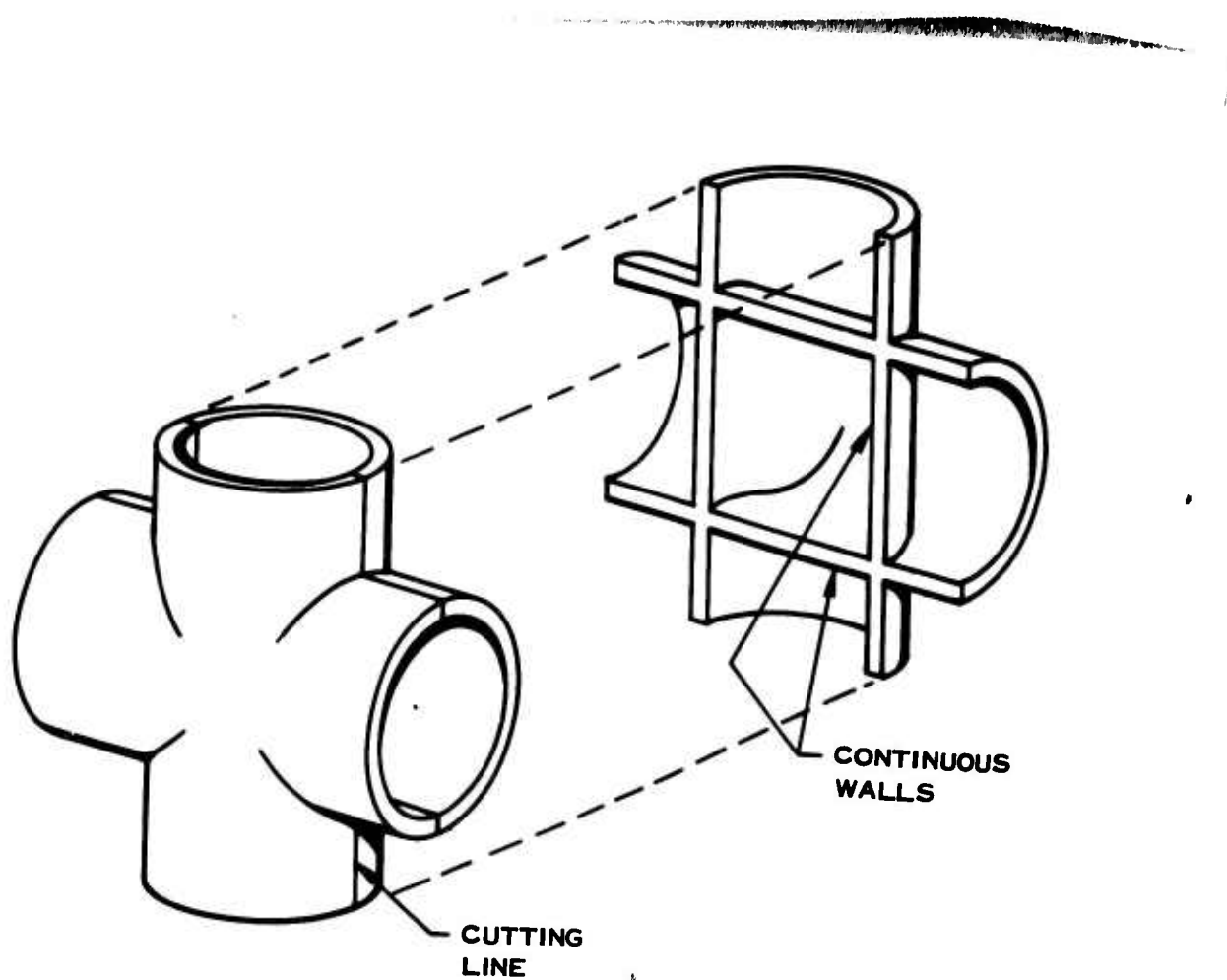
TWO CYLINDERS INTERSECTING AT
RIGHT ANGLES

FRONT AND REAR
HOLES

FILLETED
AREA

BARREL ARM
CYLINDER

RETENTION
RACES
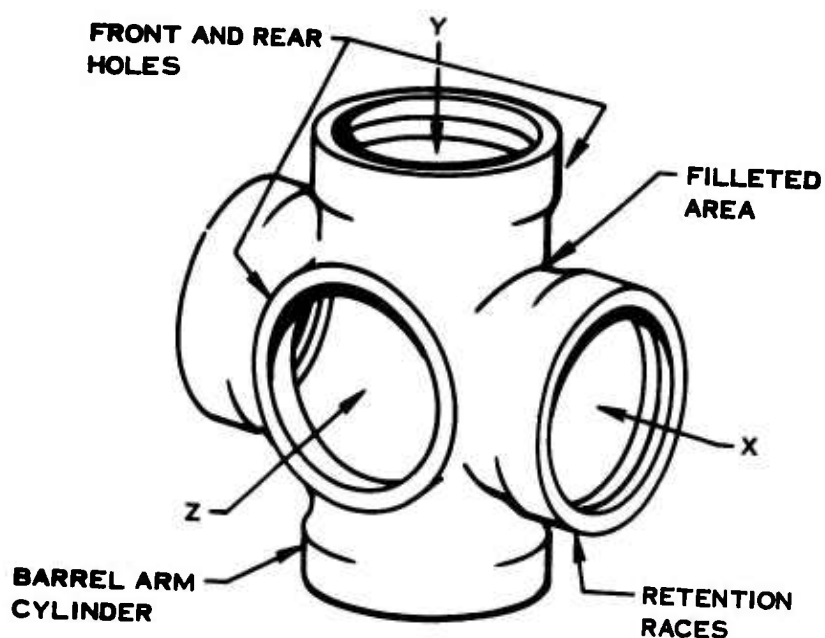
Figure 7. Crossed Tube Barrel Construction.

16

SECTION A-A
SCALE: FULL
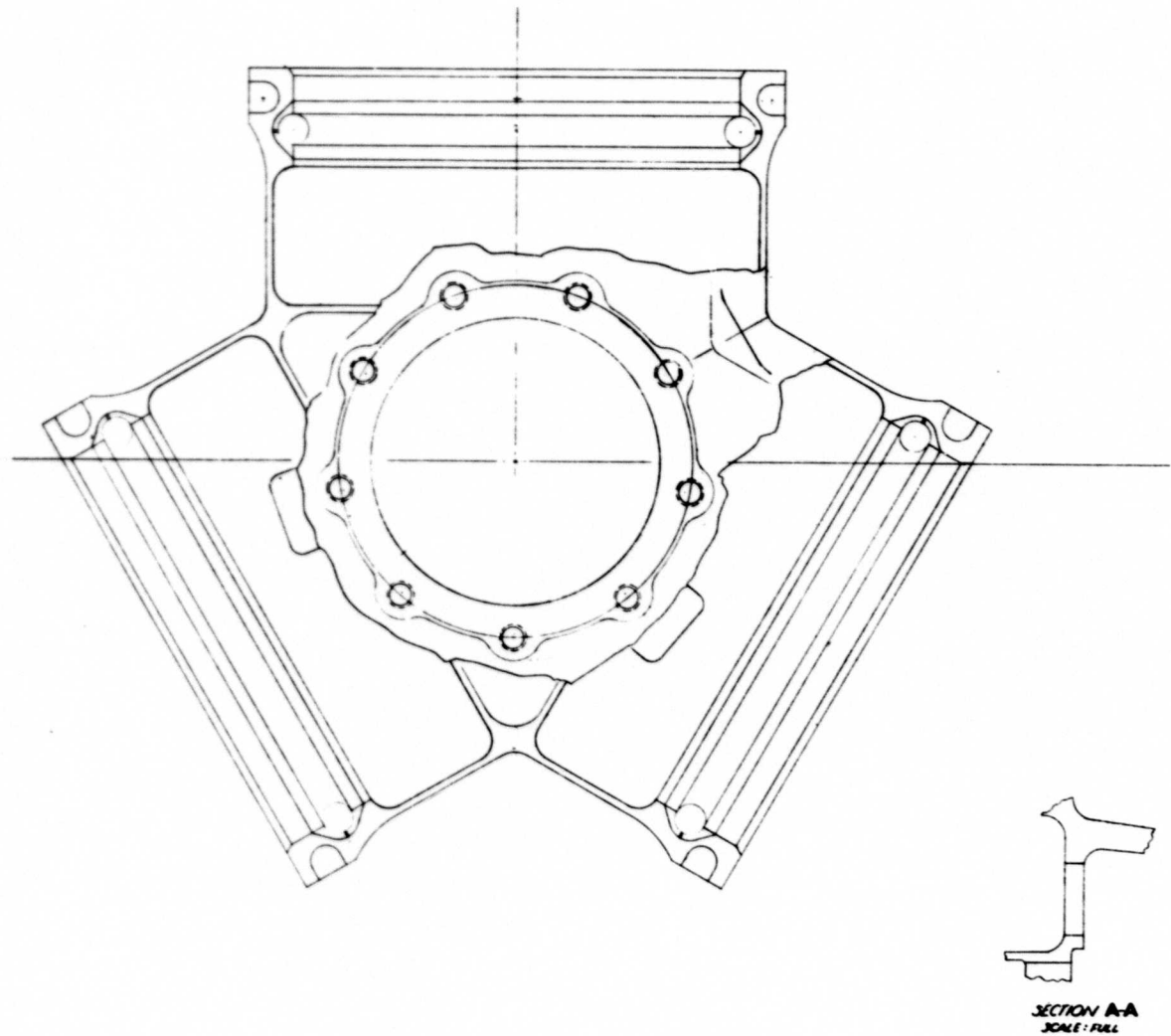
Figure 8. 3-Blade Crossed Tube Barrel.

17

8. DESTRUCTIVE INSPECTION REQUIRED FOR FIRST DEVELOPMENT LOT. ANY
   CHANGES TO PROCESSING OR TOOLING OR THE VENDOR REQ.
   REQUALIFYING TO THIS SPEC.
7. STRESS RELIEVE AT 750°F IN AIR FOR 1 HOUR, STOCK REMOVAL NOT
   TO EXCEED .020 ON DIA AFTER STRESS RELIEF, EXCEPT THD
   (MACH. PART ONLY)
6. MIL-I-6866 TYPE I PER HS447 & TEST PER HS 556 CL C
   BOTH ALL AREAS
5. V-NOTCHED CHARPY IMPACT TEST SPECIMEN-IMPACT TEST PER
   MIL-T-9047
4. NOTCHED BAR STRESS RUPTURE TEST SPECIMEN PER HS463
3. SMOOTH BAR TENSILE SPECIMEN PER FED-STD-151 TY R3
   (SELECTION OF TEST BAR LOCATION SHOWN ON F734307
   AND F734302)
2. MATL: HS463 TYPE I WITH ADDED REQUIREMENTS AS FOLLOWS:
   COMPLETELY DESCALED MECHANICAL PROPER TIES SHALL
   CONFORM TO REQUIREMENTS OF HS 463 TYPE I EXCEPT
   TENSILE PROPERTY REQUIREMENTS
   TENSILE STRENGTH - - - - - PSI MIN - - - - - - 140,000
   YIELD STRENGTH AT 0.2% ELONG - - - - - PSI MIN - - - - 130,000
   ELONGATION PERCENT IN 2 INCHES - - - - MIN - - - - 10
   REDUCTION OF AREA PERCENT - - - - - MIN - - - - - 25
1. HEAT TREAT PER MIL-H-81200 IN FORGED COND 30-39 Rc

Figure 9. 4-Blade Crossed Tube Barrel.

19

SECTION A-A

SECTION B-B

.10
4 PLACES

.0875
4 PLACES

.09 TO FULL R

.75
MIN
THD

.75
TYP

SPUR
SPLINE

B

NONDESTRUCTIVE INSPECTION REQUIRED FOR FIRST DEVELOPMENT LOT ANY
CHANGES TO TOOLING OR TOOLING ON THE VENDOR SHALL
REQUALIFYING TO THIS SPEC.

STRESS RELIEVE AT 1200°F MIN PER 1 HOUR, BULK REMOVAL NOT
TO EXCEED .010 ON DIA AFTER STRESS RELIEF, EXCEPT THD
(MACH PART ONLY)

QUAL I GRADE TYPE I PER MS 667 E TEST PER MS 1966 CL C
BOTH ALL AREAS

NON-NOTCHED CHARPY IMPACT TEST SPECIMEN-IMPACT TEST PER
MIL-I-6907

MACHINED BAR STRESS RUPTURE TEST SPECIMEN PER MS 000
SMOOTH BAR TENSILE SPECIMEN PER FED STD-151 TY 63
(SELECTION OF TEST BAR LOCATION SHOWN ON P/30307
AND P/30301)

MATL: MS 663 TYPE I WITH ADDED REQUIREMENTS AS FOLLOWS
COMPLETELY ANNEALED MECHANICAL PROPERTIES SHALL
CONFORM TO REQUIREMENTS OF MS 663 TYPE I EXCEPT
TENSILE PROPERTY REQUIREMENTS
TENSILE STRENGTH .... PSI MIN 140,000
WELD STRENGTH AT 0.2% YIELD .... PSI MIN 120,000
ELONGATION PERCENT IN 2 INCHES .... MIN 10
REDUCTION OF AREA PERCENT .... MIN 15
HEAT TREAT PER MIL-H-6875 ANNEALED COND SO-EQL

1

barrels, and, although the centerbodies do differ, the barrels can reasonably be considered to be equal for this phase of machining.

In completing the machining of the spherical barrel, the inner surfaces of each arm are generated by turning about the arm bore centerline. The inside of the spherical barrel centerbody is produced by turning about the barrel centerline.

In the shell barrel, the inner surface of each arm is made by turning about the arm bore centerline. The inner surface of the shell centerbody is generated by contour-milling followed by hand grinding for the final finishing operation.

Each arm bore of the crossed tube barrel is turned about its own centerline to a depth limited by the surface of the crossing tube structure in the 4-blade barrel. The remainder of the arm bore cavity is contour-milled, followed by hand grinding for finishing the milled and turned areas. In the 3-blade crossed tube barrel, each arm bore is completely finished by turning about its own centerline. The inner surface of the crossed tube barrel centerbody is generated by contour-milling and hand grinding to final finish.

The operations of drilling, tapping, and cutting splines are identical for all barrels.

In machining the three different barrels by the traditional method, the spherical barrel is the easiest, followed by the shell barrel, and then the crossed tube barrel.

When the barrels are machined by ECM, the outer surface of the centerbodies can be generated by four passes, right and left for the front and rear, for each arm on a single pass each for the front and rear surface, depending upon the capacity of the equipment available. The inner and outer surfaces of the tailshaft and the aft surface of the rear ring are generated by the same anodes for all the barrels. The outer surface of the centerbody, the tailshaft, and the aft surface of the rear ring are of equal complexity for machining by ECM.

For the shell and spherical barrels, the arm bores are generated about the arm centerline for each arm. The inner surfaces of the centerbodies are produced by anodes inserted through the front ring or arm bores.

The 3-blade crossed tube barrel arm bores can be completely finished in one setup due to the plate configuration of the bottom of the arm bore. The 4-blade crossed tube arm bores require multiple setups to complete the cylindrical portion of the arm and then the outer surface of the crossing cylinder within the arm bore. The inner surfaces of the centerbody require multiple setups for completion of the surfaces of the crossing tubes and the intersections of the crossed tubes.

21

After the completion of the ECM operations, the barrel surfaces requiring close tolerances are finished by traditional-type machining. The minimum tolerance currently attainable with ECM equipment is ±0.005 in., and any tolerance less than this requires a different type of machining. As this condition applies to all barrels, the close-tolerance finishing operations are equal for all barrels.

The spherical barrel is not process-limited, the shell barrel is somewhat more limited, and for practical purposes the crossed tube barrel is limited to ECM processing.

DETERMINATION OF CYCLIC LOADS

In order to evaluate the cyclic loading at a frequency of 1P (one load cycle for each revolution of the propeller), it is necessary to establish certain aerodynamic and geometric characteristics of the aircraft on which the propeller is to be installed. These characteristics are then used to determine the 1P excitation factor (EF)* levels as a function of aircraft weight and airspeed.

Preliminary pertinent details set forth in the final report prepared under Contract DAAJ02-67-C-0073 are as follows:

Aircraft Type	Utility Tilt-Wing V/STOL
Propulsion	2 Engines, 2 Propellers
Engine Rating	2000 shp S.L., Standard Day
Hover Design Point	1400 shp/prop (6000 ft, 95°F)
T/GW Hover	1.07
Disc Loading at Hover	35 psf
Wing Loading	70 psf
Wing Aspect Ratio	8.0
Prop Diameter	14.8 ft
100% Prop rpm	1160
Number of Blades	4
Blade AF	120
Blade IC_{L_i}	0.40
Maximum EF	4.0

From these data, it can be deduced that at the hover design point the ___ ___ gross weight is approximately 11,300 lb. From past experience it was recognized that the maximum operating gross weight could be appreciably higher than this, that the minimum operating weight could be appreciably less, and that the maximum continuous EF would be reached at either the high gross weight/low airspeed condition or the low gross weight/high airspeed condition. Using the design maximum EF of 4.0, comparisons were made of the EF characteristics of three existing tilt-wing V/STOL aircraft designs. This comparison is presented in Figure 10, where EF is plotted versus equivalent airspeed on a squared scale. (It should be noted that the EF level at the zero airspeed intercept on these plots is primarily a function of the wing loading and the slope of the wing lift coefficient

---

$$\text{*EF} = \phi \left(\frac{V_e}{348} \right)^2 = Aq/409$$

where ϕ = angle of thrust axis to airstream at the propeller disc

V_e = aircraft equivalent airspeed - kn

q = airstream dynamic pressure - lb/sq ft
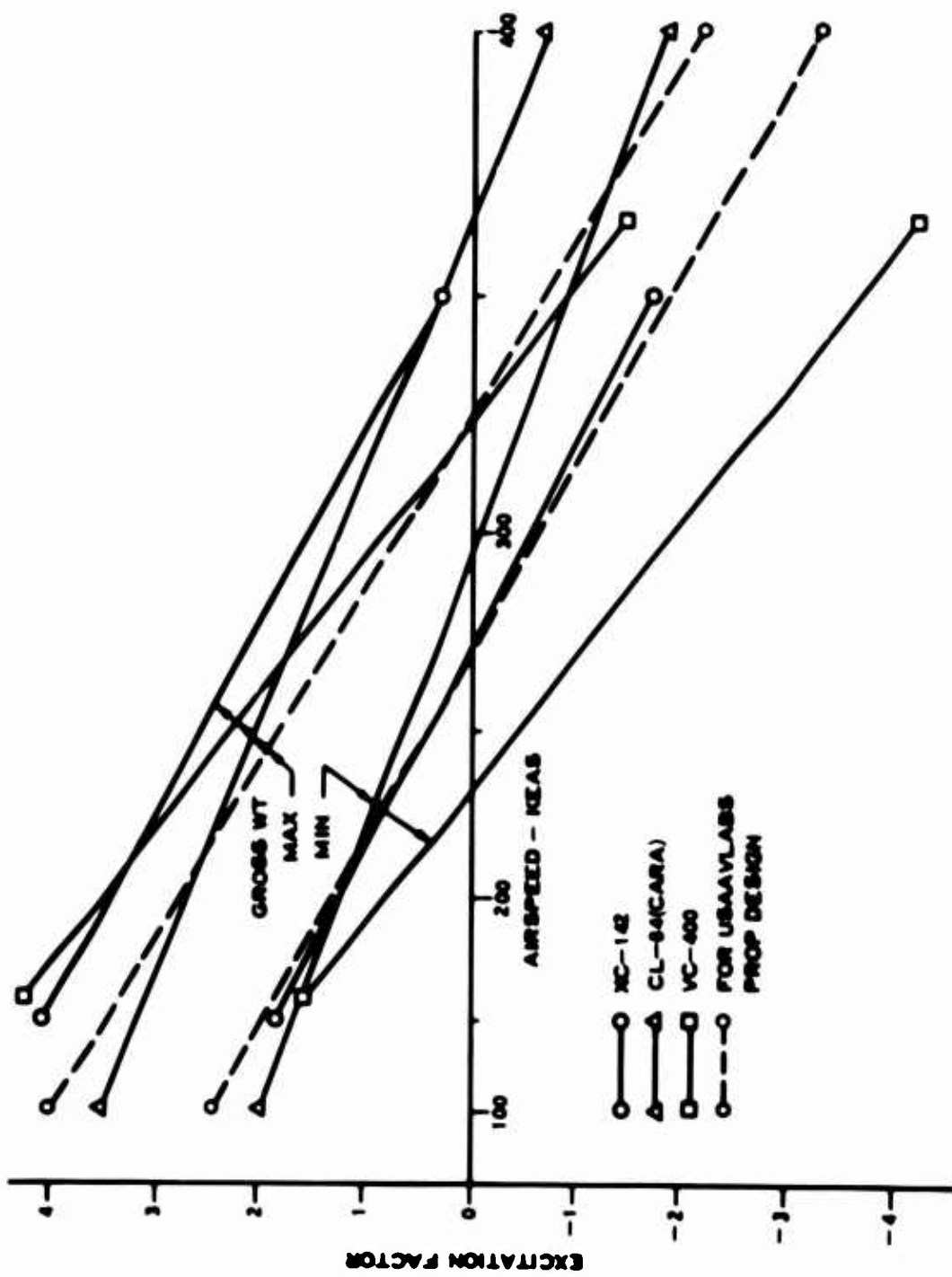
Figure 10. Excitation Factor Diagram for Tilt-Wing, V/STOL Aircraft.

curve $\left(\dfrac{dCL}{d\alpha}\right)$, while the slope of the EF plot is primarily a function of the angle of the propeller thrust line with respect to the zero lift wing (ϕ_t). The excitation factor is positive when the thrust line is angled up with respect to the airstream and is negative for a downward angle. With this background information as a guide, the EF characteristics for this study were estimated and are also shown in Figure 10.

A series of calculations was made to determine the aerodynamic 1P (one load cycle for each revolution of the propeller) shaft moment as a function of EF and airspeed, and, using the moment/EF sensitivities thus derived, the shaft moment levels were calculated and are shown in Figure 11. The shaft moment represents only the out-of-plane component of the blade aerodynamic moments. To determine the maximum blade retention (shank) moment, the blade response moment level and angle, including dynamic effects and operating blade angle, must be considered. Lacking a blade structural definition, calculations made on a blade installed on the XC-142 aircraft were used as a guide in estimating shank moment angles and dynamic magnification as a function of aerodynamic shaft moment. The shank moments thus calculated are shown in Figure 11. It can be seen that for the EF characteristics selected, a good balance is realized in the shank moment levels for the maximum EF cases. For clarity it should be pointed out that the sign convention used in Figure 11 is based on the consideration that when EF changes sign, the shaft moment as seen by the shaft support reverses direction; whereas the shank moment as seen by the retention does not change direction, but the point of maximum loading in the propeller rotational sweeps shifts 180 deg.

After the establishment of a reasonable appearing EF characteristic, it is then possible to develop a more detailed description of the aircraft installation which will also generally fit the previously noted design conditions. Again, data from existing aircraft designs were used as a guide in establishing some of the details of the description. The revised aircraft description is as follows:

Wing Area	175 ft^2
Wing Span	37.5 ft^2
Wing Aspect Ratio	8.0
Slope of Wing Lift Coefficient Curve	0.095
Slope of Upwash Curves	
Wing	0.30
Fuselage	0.10
Nacelle	0.05
Thrust Line to Zero Lift Line Angle	-4.0 deg
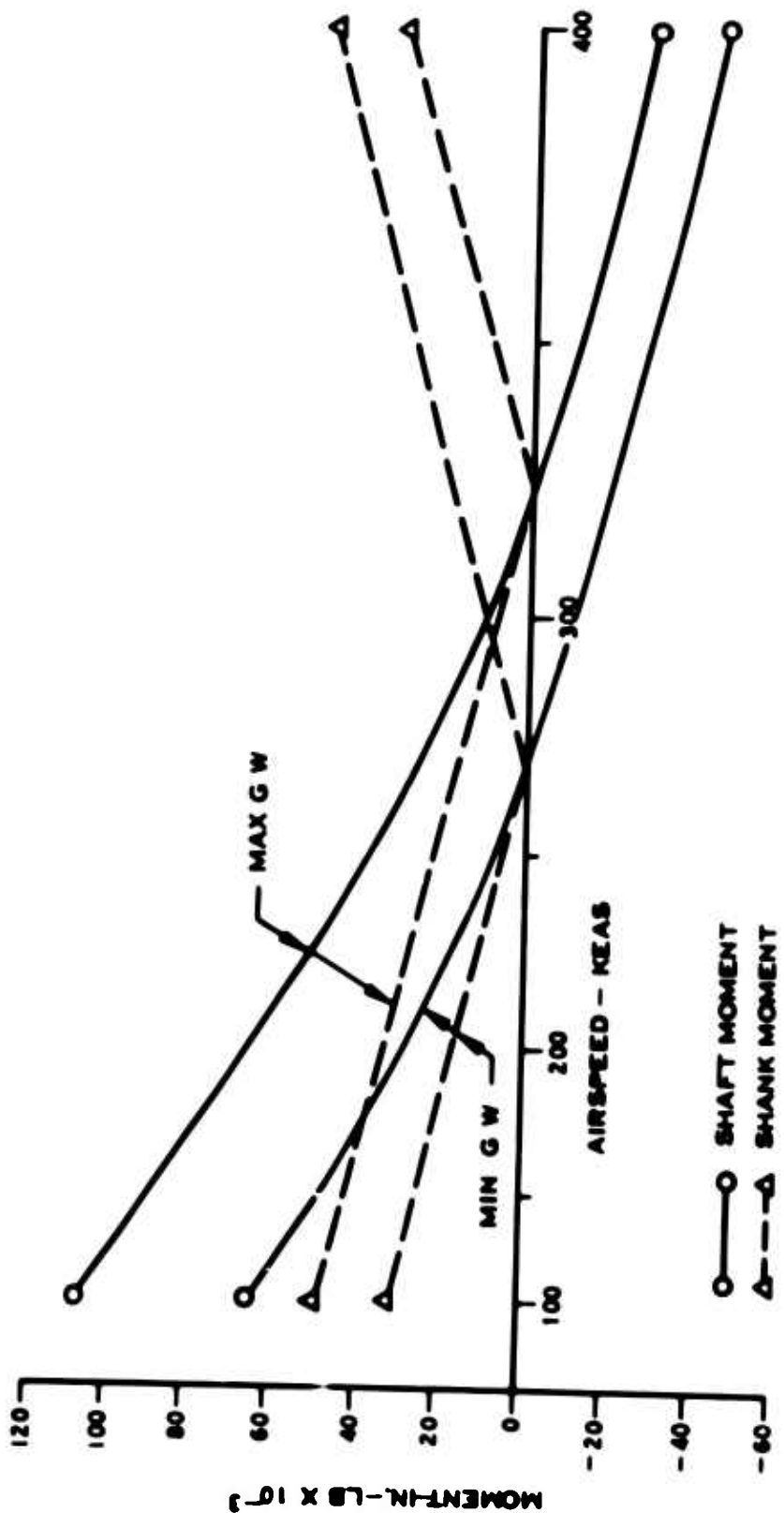
Figure 11. Propeller Shaft and Blade Shank Moments Versus Airspeed.

Gross Weights
   Max Operating (Ferry)   19,000 lb
   Max Design   15,650 lb
   Basic Design and Maneuver
     Spectrum   13,800 lb
   Minimum Operating   9,450 lb

$$EF = (Gross\ Weight/4,400) - 4.23\ (KEAS/348)^2$$

An EF diagram, based on the above aircraft description and covering the significant operating gross weights and maneuver load factors, is shown in Figure 12. The EF characteristics that have been developed do not take into account the propeller slipstream effect on wing lift. For conventional fixed-wing transports, the slipstream effect on resultant EF is small. However, from the aircraft and propeller definitions being used in this study, it is apparent that most of the wing is immersed in the propeller slipstream, as would be expected in this type of aircraft. Under these conditions, the actual EF will be reduced significantly at low airspeeds and high propeller thrust levels. For instance, a simplified analysis based on data presented in NACA Report 1263 shows that at 100 KEAS, the zero power EF of 4 is reduced to 3 with a power of 2000 hp per prop at 1160 rpm. This effect on EF decreases rapidly as the forward speed increases and the ratio of slipstream to free-stream velocities decreases. A more complete analysis of power on EF was not made since the 1P loadings under steady-state operation do not, in general, size the blade and propeller retention areas when the aircraft is expected to be subjected to an appreciable amount of maneuver operation.

In evaluating maneuver loadings, reference was made to specifications MIL-A-8861 and MIL-A-8866, which deal with aircraft strength and rigidity design requirements. The previously adopted aircraft description for use in this study placed the aircraft in the utility category. MIL-A-8861 calls for a design maximum positive load factor of 4.0 at the basic design gross weight for utility aircraft. However, experience with the CL-84 (CARA), XC-142, and VC-400 designs shows that a design load factor of 3.0 has been used for the tilt-wing V/STOL type of aircraft. MIL-A-8866 further describes utility aircraft as having a 7500-hr life, and the aircraft are to be designed for maneuver spectrum C. For a design load factor of 3.0, maneuver spectrum C would be:

Load Factor (N_z)	Occurrences/1000 hr
1.35	10,000
1.65	3,000
1.95	1,000
2.25	300
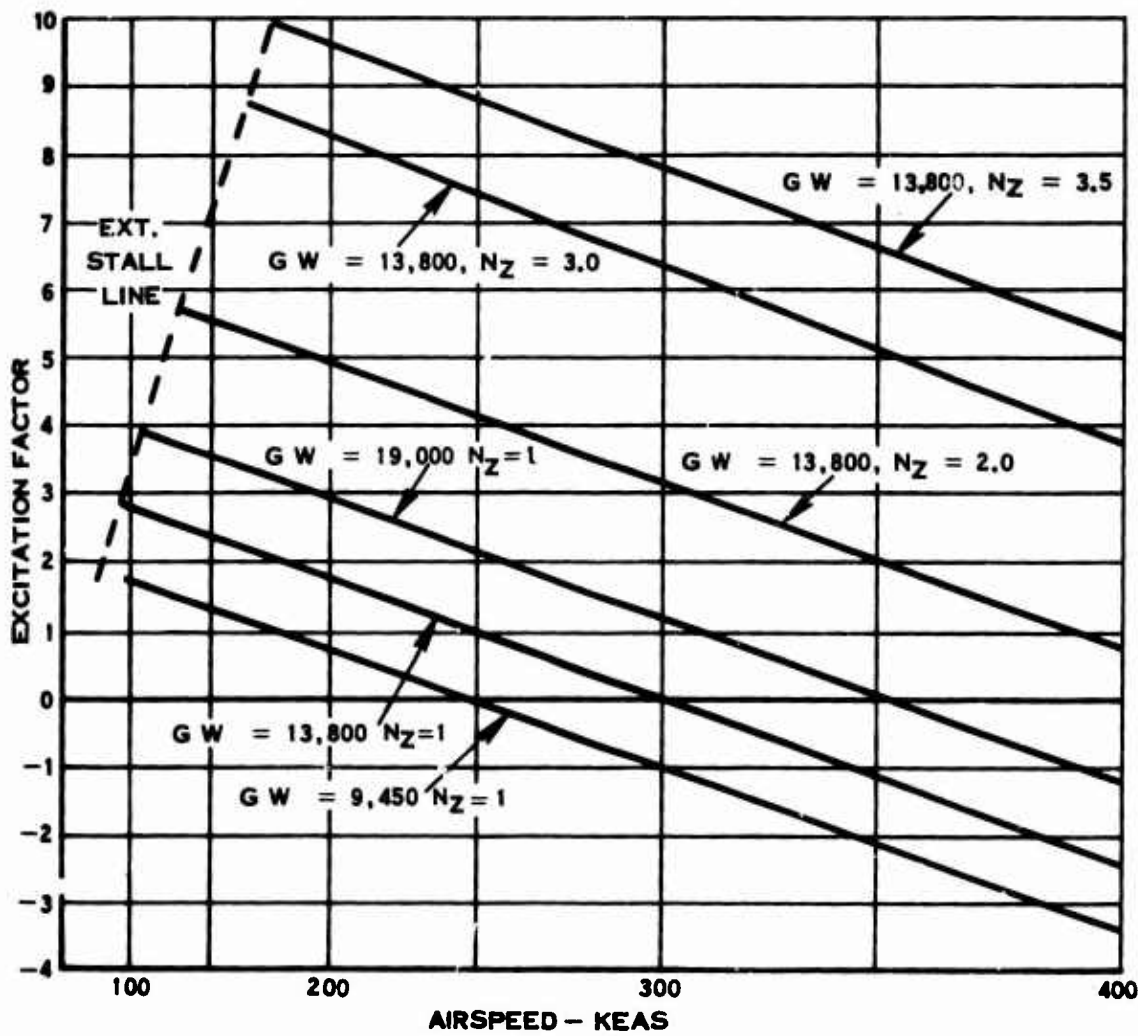
Figure 12. Excitation Factor Versus Airspeed.

28

Load Factor (N_Z)	Occurrences/1000 hr
2.55	100
2.85	30
3.15	10
3.45	3
3.75	2
	14,445/1000 hr

This spectrum description is suitable for aircraft structure fatigue evaluation where each maneuver is one load cycle, the amplitude of which is dependent only on load factor. In order to assess propeller 1P cyclic loadings and fatigue damage, it is necessary to define not only the aircraft load factor but also the airspeed at which the maneuver occurs, the propeller rpm, and the duration of the maneuver. From consideration of other aircraft mission profiles and load factor measurements on in-service aircraft, it appears unlikely that maneuvers of significant duration would occur every 4 minutes as indicated by the above spectrum.

In the course of the CL-84 (CARA) design studies, a detailed assessment of maneuver loadings was made based on the proposed mission profiles. A maneuver was defined as a 90-deg turn or pullout which then establishes the maneuver duration as a function of load factor and airspeed. With this background as a guide, a maneuver spectrum (See Table I) was developed for design purposes.

TABLE I. DESIGN MANEUVER SPECTRUM			
	Maneuvers/1000 hr		
Load Factor (N_Z)	150 KEAS	250 KEAS	350 KEAS
1.5	390'·	2340	1560
2.0	390	234	156
2.5	30	18	12
3.0		14	10
3.5		2	1.5
	4320	2608	1739.5
			Total 8667.5

To complete the definition of maneuver conditions, an average maneuver gross weight of 13,800 lb, an average rpm of 85%, and a propeller design life of 7500 hr were assumed.

Having established the propeller load sensitivities to EF, the aircraft EF characteristics, the maneuver definition, the propeller rpm, the propeller life, and the load level and cycle accumulation were calculated for each of the maneuver conditions. The results are presented in Table II. The loads shown do not include an allowance for vibratory excitations at frequencies other than 1P. This is reasonable at this stage of the design analysis, since for the maneuver analysis the gyroscopic and gravity excitations at 1P, which tend to subtract from the aerodynamic 1P excitation, have also not been included.

Airspeed (KEAS)	Load Factor N_z	EF	Shaft Moment (in.-lb)	Shank Moment (in.-lb)	Cycles $\times 10^{-6}$
TABLE II. 1P CYCLIC LOADINGS FOR USAAVLABS PROPELLER STUDY					
150	1.5	3.92	108,000	49,000	11.92
	2.0	5.51	152,000	69,000	0.593
	2.5	7.06	194,500	88,400	0.031
250	1.5	2.53	52,000	32,900	11.85
	2.0	4.12	84,500	53,500	0.593
	2.5	5.67	117,000	73,800	0.03
	3.0	7.26	149,500	94,500	0.018
	3.5	8.82	181,500	114,000	0.002
350	1.5	0.45	6,050	6,300	11.1
	2.0	2.04	27,500	28,600	0.555
	2.5	3.59	47,500	50,300	0.0295
	3.0	5.18	70,000	72,500	0.018
	3.5	6.74	91,000	94,500	0.0022

The next step was to find barrel stress sensitivities in terms of ±psi/in.-lb moment which, when applied to the loads shown and reflected against the projected fatigue strength (S-N curve) of the barrel material, would result in a cumulative fatigue factor ($\Sigma \frac{n}{N}$) of approximately 0.5. The results of this study showed required sensitivities of 0.25 psi/in.-lb of shaft moment for the rotating propeller attachment and 0.55 psi/in.-lb of shank moment for the retention and barrel areas. Stated differently, the barrel design from a fatigue standpoint should be capable of continuous operation at 130,000 in.-lb shaft moment and 60,000 in.-lb shank moment. It should also be capable of handling transient loadings up to 194,500 in.-lb shaft moment and 114,000 in.-lb shank moment.

Although past experience has indicated that propeller loadings during VTOL transition do not size the propeller structure, calculations of 1P aerodynamic shaft moments were made for the propeller defined for this study. The wing angle versus airspeed schedule used is the landing transition schedule for the XC-142 aircraft.

The results of these calculations are presented in Figure 13. Note that the peak moment level is less than that of some of the steady-state operating conditions examined previously.

One of the sizing criteria set forth in the final report prepared under Contract DAAJ02-67-C-0073 was an EF of 4.0 plus 25% for higher order aerodynamic excitations. Using the loading sensitivities derived in this study, the resultant total moments for this condition would be 134,000 in.-lb at the shaft and 62,500 in.-lb at the shank. The 2P frequency would constitute a major portion of the higher order excitation. Since with a 4-blade propeller the 2P frequency has no reaction on the shaft, it is overly conservative to add 25% for higher orders to the 1P shaft loading. Therefore, the continuous capacity of 130,000 in.-lb derived from the maneuver spectrum analysis should be adequate for purposes of propeller attachment design. The design continuous shank loading will be 62,500 in.-lb, including higher order loadings.

In summary, the vibratory loadings to be used in the r   ller barrel design are:

	Continuous	Maximum
Shaft Moment	130,000 in.-lb	194,500 in.-lb
Shank Moment	62,500 in.-lb	114,000 in.-lb

The previous discussion has been limited to the determination of cyclic loadings. In order to complete the barrel-loading picture, it is necessary to assess the conditions at which the cyclic loadings occur and to determine the steady-state loads that correlate with them.

Based on the use of a boron-aluminum spar-fiberglass shell blade, the blade centrifugal load is 43,000 lb at 1160 prpm.

The continuous shank moment of 62,500 in.-lb was based on a 150-kn climb condition. At this condition, the steady bending moment generated in the blade shank is 35,000 in.-lb. The maximum 1P moment of 114,000 in.-lb occurs at 250 kn 3.5 g maneuver condition (Table II). Using the blade data generated under Contract DAAJ02-67-C-0073, the steady bending moment was assessed for this condition to be 18,000 in.-lb.

31
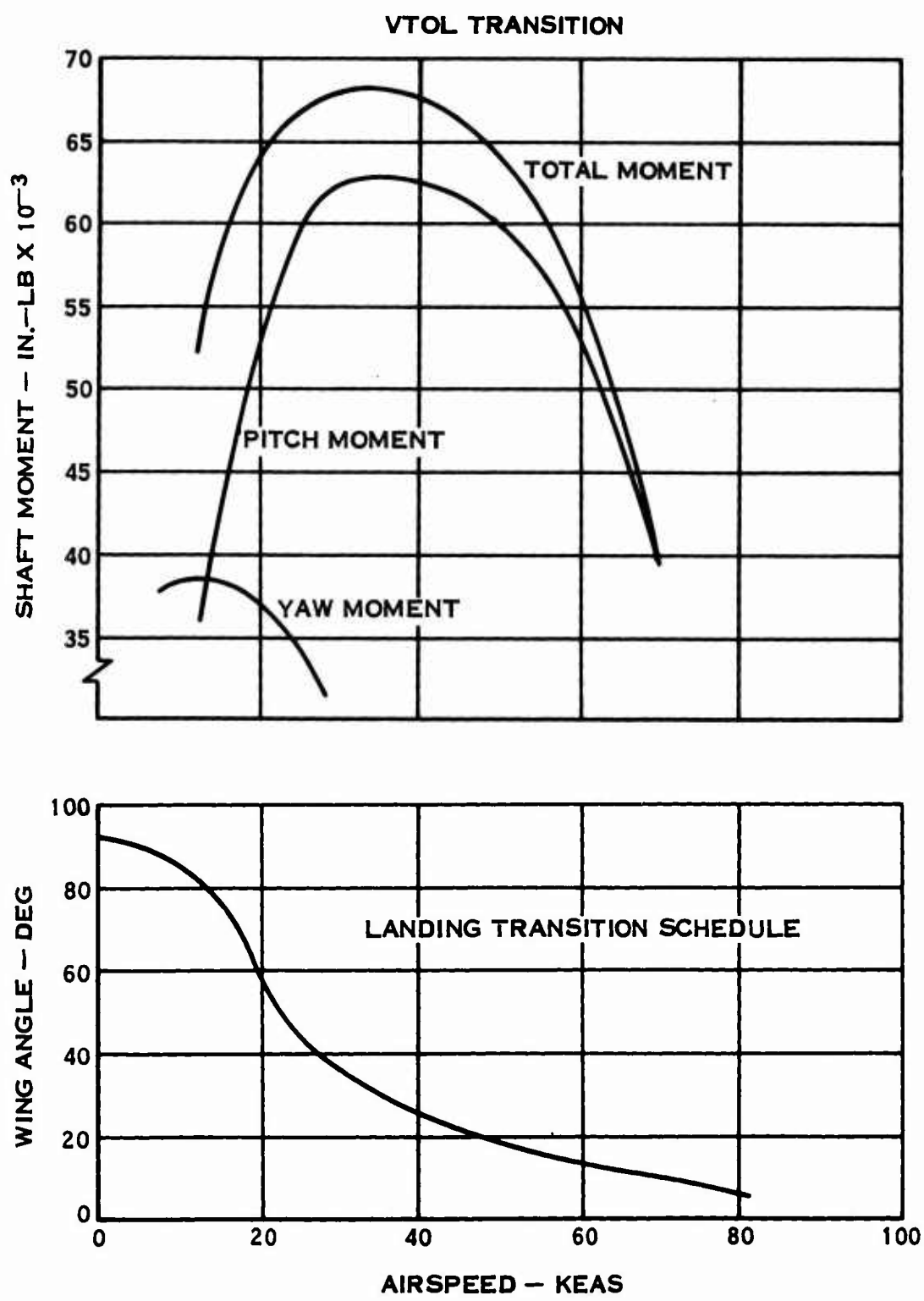
Figure 13. Propeller Shaft Moment and Wing Angle Versus Airspeed.

The following is a summary of the two loading cases (Case 1, Climb, and Case 2, Cruise with 3.5 g maneuver) studied for the 3-blade and 4-blade barrels:

4-Blade Barrels	Case 1	Case 2
Centrifugal Load (lb)	45,000	45,000
Steady Bending Moment (in.-lb)	35,000	18,000
1P Vibratory Moment (in.-lb)	65,000	114,000

The 3-blade barrel loadings were generated by using the same total solidity propeller as for the 4-blade barrel loadings. This has the effect of increasing the aerodynamic loads by a factor of 4/3 per blade. The centrifugal load per blade for the 3-blade barrel loadings was estimated to be 62,000 lb.

A comparison of the two loading cases used in the 3-blade barrel analysis is given below:

3-Blade Barrels	Case 1	Case 2
Centrifugal Load (lb)	62,000	62,000
Steady Bending Moment (in.-lb)	46,700	24,000
1P Vibratory Moment (in.-lb)	86,700	152,000

33

RETENTION AND TAILSHAFT ANALYSIS

Barrel - General

The barrel, which is manufactured from a one-piece titanium forging, is composed of three major structural elements: retention, hub, and tailshaft.

The optimization of a barrel requires an integrated design of the barrel and all items that introduce loads into, or remove loads from, the barrel. This requires designing the blade butt area, actuator, actuator-blade coupling device, bearing, and barrel tailshaft-planet carrier interface for each type of barrel.

The basis for comparison has placed restrictions on both the shell and the spherical barrel concepts. Those restrictions tend to favor the design of a crossed tube concept. Each condition affects the barrels in different ways; these effects are discussed below.

1. A Common Actuator

    The actuator conceived under USAAVLABS Contract DAAJ02-67-C-0073 was for use with the crossed tube barrel concept, with its diameter being determined by the largest size access hole that would not interrupt the cross cylinder intersections. With the selection of this diameter, the two actuator supports were an inherent part of the barrel structure. The shell and spherical barrel designs do not restrict the use of a larger diameter front or rear ring structure. For these two barrel concepts, a separate, lighter part could be inserted in place of the rear plate with an increased rear ring structure in order to retain the barrel stiffness. This use of the actuator has penalized the shell and cross tube barrel.

2. Links

    For the crossed tube barrel concept, the use of links as a means of pitch change was obvious.

    For a cyclic pitch propeller system, the use of links would be desirable independent of the barrel concept; but for a noncyclic pitch propeller, the use of a linkage system in a shell or spherical-type barrel can be questioned.

    The use of a Scotch yoke actuator concept for both the shell and the spherical barrel would allow the reduction of the radial distance from the propeller centerline to the plane of the ball retention. This would

34

reduce the weight of the two 4-blade barrels by approximately 1.7 lb but would add approximately 0.8 lb to the total blade weight.

The deflection limit of 0.008 in. was based on the design of the spherical barrel and produced a gross barrel spring rate out-of-plane of approximately 200 million lb/in. This in effect has penalized the crossed tube barrel design, since neither the 0.008 in.-deflection nor a stress limit could be reached without thinning the crossed tube walls to thicknesses that appear to be beyond the scope of present manufacturing capability. Ignoring this limitation, a deflection match between the centerbody and the front ring can be made which would yield a 0.045-in. tube wall with a 90:10 load split. This theoretical wall thickness would reduce the weight by 3.96 lb.

The actuator loadings have a large effect on the barrel concepts. None of the barrel front rings was stress- or deflection-limited because the added material was required for the attachment of the actuators. This influence will decrease for larger diameter, higher power propeller systems.

Retention

The function of the retention is to hold the blade to the barrel while permitting the pitch change mechanism to rotate the blade about its own centerline with minimal friction. The retention also transfers forces between the blade and the barrel centerbody. Steel inserts are used in the barrel arms to provide a much higher Hertz stress allowable, thereby reducing the pitch diameter of the retention over that needed for a titanium retention. Also, rework of the 4-point retention with integral races would require the insertion of larger rolling elements, thereby creating interchangeability problems.

Outboard of the blade retention races, boron epoxy is wrapped around the barrel arm as a stiffener to minimize the radial deflection from the imposed hoop loading.

Centerbody

The centerbody reacts all retention loads in the plane of rotation and acts as a transfer device between the retention and the barrel tailshaft for all loads not in the plane of rotation. The centerbody is also the reaction area for the pitch change mechanism and serves as the container for the lubricating oil.

35

Tailshaft

The barrel tailshaft is the primary structure for transferring forces between the propeller and the airframe. The tailshaft of the barrel extends into the gearbox and is directly driven through a splined joint by the gear reduction planet carrier. The tailshaft is mounted in a barrel retention bearing such that all forces not in the plane of rotation are reacted by the tailshaft through the retaining bearing into the airframe.

The load carried by the tailshaft is independent of the barrel centerbody shape; therefore, a common tailshaft was used for all the barrels.

The forces transferred by the barrel tailshaft between the barrel and the bearing are the propeller thrust and moment forces. Propeller torque is transmitted directly from the planet carrier into the tailshaft. The propeller retention bearing is a duplex tapered roller pair making a 50-deg angle with the propeller center-line. Figure 14a is a schematic representation of the barrel, bearing, and forces acting on the system.

The thrust force is reacted entirely in the aft bearing, Figure 14b. As the thrust is an axial type of force, the bearing reaction is uniformly distributed around the tailshaft. The angle of the bearing relative to the tailshaft causes the tailshaft to see a uniform axial force for its entire length and also to have a uniform external pressure load around the outside of the tailshaft under the aft bearing.

The moment is reacted across both bearings as shown in Figure 14c. The forces on the aft bearing due to the moment act in the same direction as the thrust reaction forces. The axial component of moment reaction force of the forward bearing is opposite to the axial component of the aft bearing, while the radial component is an external pressure force. Past experience has shown that the bearing reaction forces due to moments can be closely duplicated by a mathematical model of a cosine distribution over one-half of the bearing surface.

In addition to the above forces, it is common practice to assume a gyroscopic moment, with an angular velocity of 0.1 rad/sec, to act continuously and in phase with the 1P shaft moment. The stresses used to determine the margin of safety are thrust for the steady stress and 1P plus gyroscopic moments for the vibratory stress.

One other type of loading is investigated during a tailshaft analysis. This load condition is called the maximum static case and is treated as an ultimate load. The gyroscopic moment is produced by an angular velocity of 2.5 rad/sec. The

36

THRUST

BARREL

I P SHAFT
MOMENT

BEARING

(A)

T

THRUST

T'

(B)

F

I P SHAFT
MOMENT

F'

EFFECTIVE BEARING
SPACING
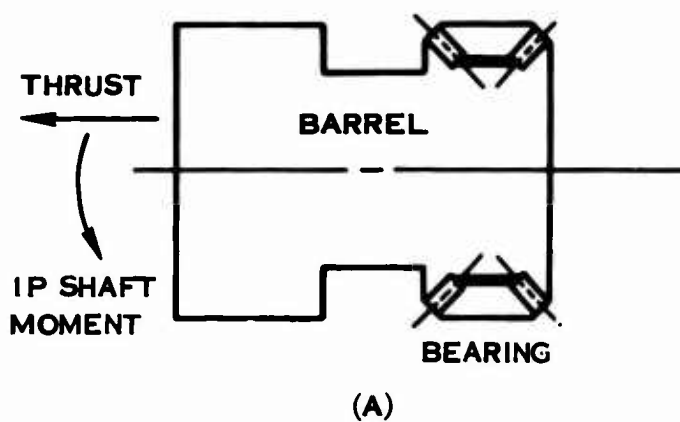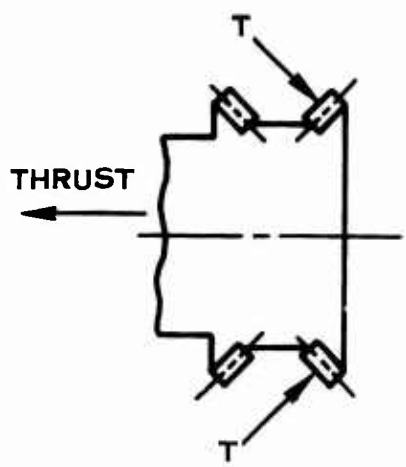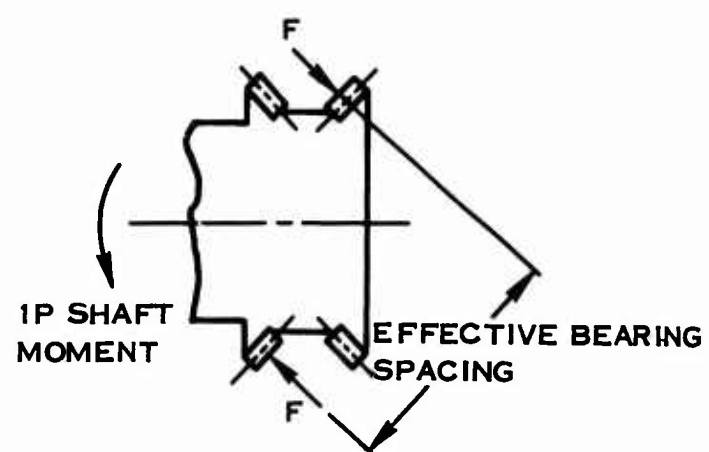
(C)

Figure 14. Schematic Representation of Barrel Loads.

stresses due to thrust, 1P shaft moment, and gyroscopic moment are summed and compared to the tensile yield strength. The stresses must be less than the yield allowable.

The tailshaft was analyzed as a shell of revolution (Figure 15 shows the cross section and applied loads used in the program). At the aft end of the tailshaft, the barrel retaining bearing inner races are pressed on the outside, the planet carrier is pressed on the inside, and the entire assembly is preloaded by a nut. This creates, in effect, a much thicker section for the tailshaft end.

Table III summarizes the maximum stresses in each part of the tailshaft for both loading cases. These stresses are then compared with a Goodman diagram for infinite life, where the margin of safety can be established.

The same two cases are then rerun with the inclusion of the 2.5-rad/sec angular velocity. These resultant total stresses are compared to the yield allowable.

38

PRESS.OVER 180° DUE TO MOMENT

MOMENT REACTION 180°

THRUST REACTION 360°

MOMENT REACTION 180°

PRESS.OVER 180° DUE TO MOMENT

PRESS.OVER 360° DUE TO THRUST
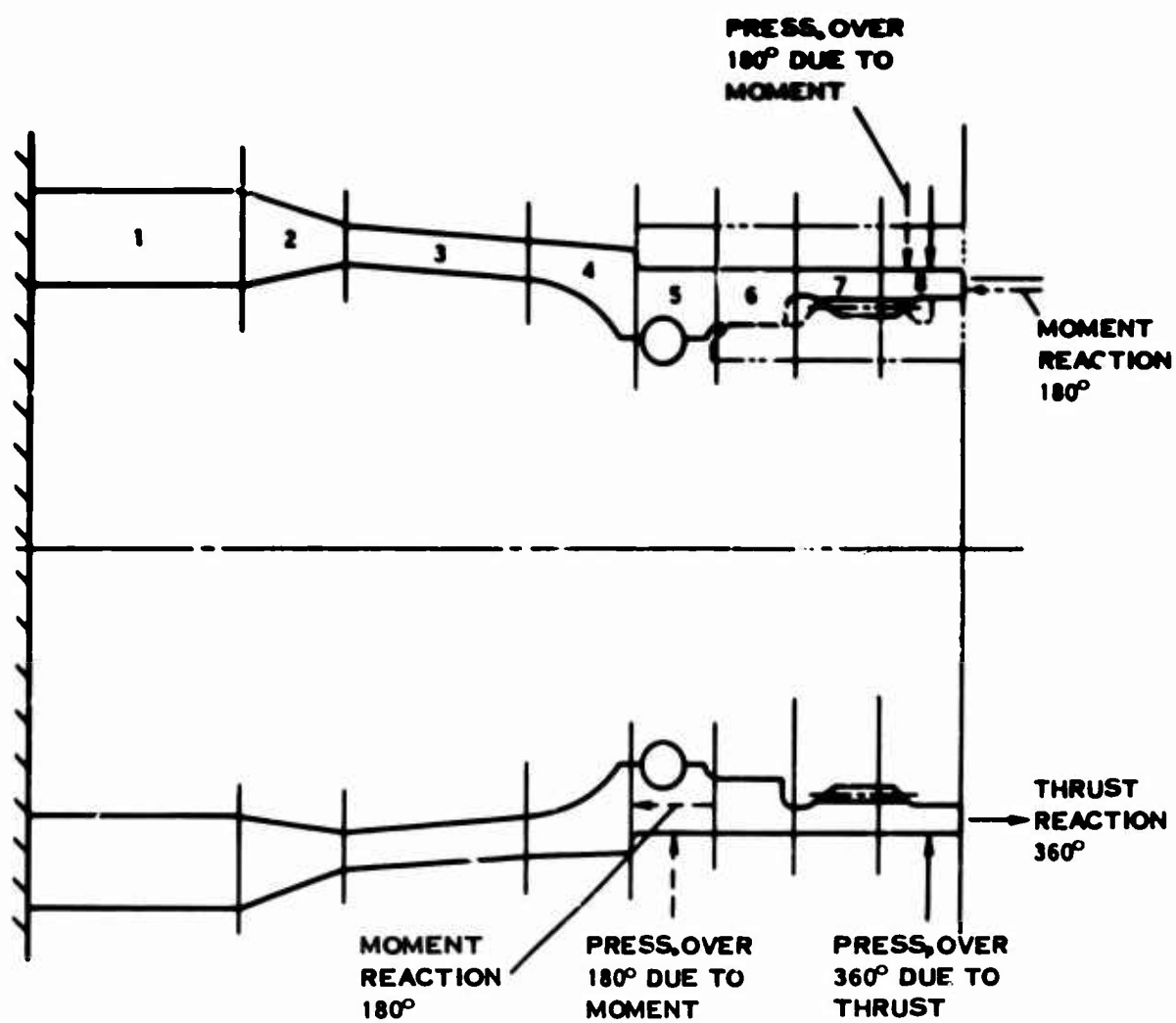
Figure 15. Barrel Tailshaft Cross Section.

TABLE III. TAILSHAFT STRESS SUMMARY

Section	1	2	3	4	5	6	7	8
Case I Stress (psi)								
Axial	11,452 ± 8,286	18,065 ± 6,555	18,103 ±11,219	18,103 ±11,219	5,227 ± 3,731	5,092 ± 2,496	6,797 ± 3,950	4,565 ± 2,543
Hoop	3,436 ±24,860	2,884 ± 2,595	4,812 8,911	4,812 8,911	913 ± 7,812	1,112 ± 4,438	563 7,975	2,439 ±15,884
Shear	0 ±22,625	± 3,819	0 ± 4,402	4,402	0 ± 3,510	0 ± 3,546	0 ± 3,262	± 3,033
Max. Gyro								
Axial	19,737	26,623	31,350	31,350	9,771	6,862	10,160	7,882
Hoop	5,921	6,100	15,240	15,240	9,914	8,185	11,491	16,412
Shear	2,079	3,464	4,166	4,166	934	3,743	3,438	4,217
Case II Stress (psi)								
Axial	11,452 ±12,365	8,070 ±11,754	18,103 ±16,741	18,103 ±16,741	5,228 ± 5,568	2,936 ± 4,474	3,968 ± 6,467	4,565 ± 3,794
Hoop	3,436 3,709	2,884 ± 3,872	4,812 ±13,297	4,812 ±13,297	913 ±11,657	1,615 ± 1,111	1,264 16,111	2,439 23,702
Shear	0 ± 3,376	0 ± 5,699	0 ± 6,569	0 ± 6,569	0 ± 5,237	0 ± 5,291	0 ± 4,868	0 ± 4,525
Max. Gyro								
Axial	23,108	30,112	36,747	36,747	11,622	9,311	12,874	9,234
Hoop	69,325	7,410	19,489	19,489	13,581	11,434	16,687	24,093
Shear	2,925	4,873	5,833	5,833	5,176	5,266	4,838	4,526

Retention

Present-type retentions rely upon the centrifugal load from the blade weight to preload the retention such that the aerodynamic moments will not unload any of the balls in the blade retention races (Figure 16). In the past, the retention diameter required for proper stress levels for the combined aerodynamic and centrifugal loads has been larger than the retention diameter required to prevent unloading.

$$\text{BALL LOAD} = \frac{CF}{2} + \frac{2M}{R} \qquad \text{BALL LOAD} = \frac{CF}{2} - \frac{2M}{R}$$

$$\text{ROCKING OCCURS IF} \quad \frac{2M}{R} > \frac{CF}{2}$$
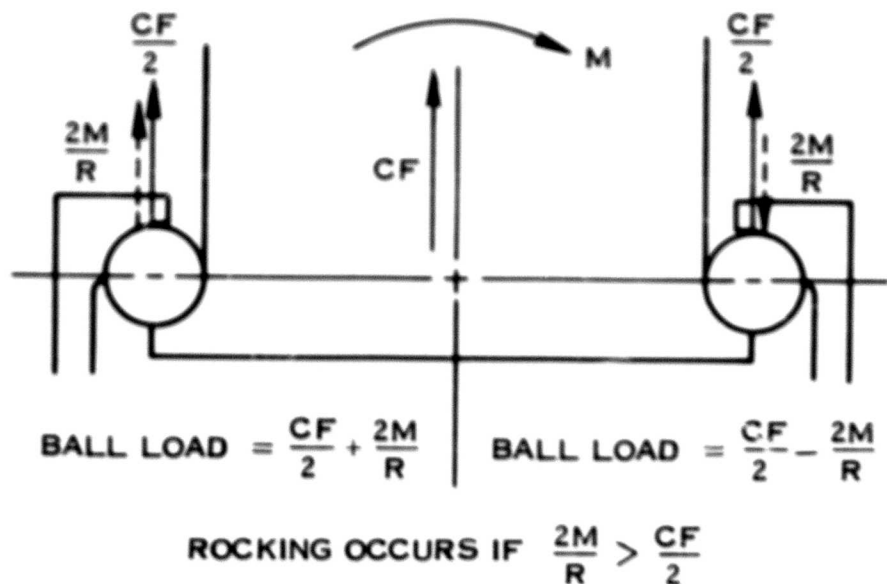
Figure 16. Present-Type Retention.

41

The advent of composite materials for the blade structures requires a change to the presently established retention concepts.

The composite material blade's light weight presents a situation where the centrifugal force is no longer great enough to serve as the preload force to prevent unloading while maintaining a reasonable retention diameter. Therefore, a new type of retention concept is needed. Many types of retentions were considered. Figures 17 and 18 illustrate the various concepts used. From all of these concepts, two were chosen as being the most promising: the crossed roller retention and the 4-point contact or Gothic arch ball bearing retention.

The retention chosen for the 4-blade propeller was 0.625-in.-diameter balls with a 7.405-in. pitch diameter. The 3-blade propeller retention was 0.625-in.-diameter balls with a 9.003-in. pitch diameter. If the retention had not been designed to prevent unloading, then the 4-blade retention would have an 11.600-in. pitch diameter and the 3-blade retention would have an 11.000-in. pitch diameter for a 0.625-in.-diameter ball.

Crossed Rollers

The rollers used in this design are a few thousandths of an inch shorter in length than their diameter in order to maintain rolling contact without any end loading of the rollers. The basic arrangement is to have adjacent rollers "crossed"; that is, with the rolling diameter of one roller at 90 deg to the rolling diameter of the adjacent roller. This arrangement can be varied as required by the relative magnitude of centrifugal plus aerodynamic loads to centrifugal minus aerodynamic loads. Thus, one configuration could be two rollers in the direction of load addition to one roller in the opposite direction; another configuration could be a 3:1 roller ratio, etc.

In order to describe the action of the crossed roller retention, assume a 1:1 roller ratio with the bearing composed of rollers No. 1 reacting forces in the direction of load addition and rollers No. 2 reacting forces in the direction of load subtraction (Figure 17). If the aerodynamic forces are zero, rollers No. 1 take the total load and all values of $F(1)$ are equal. As the moment, M, increases, the left portion of rollers No. 1 carries an increasing force, while the right portion carries a decreasing force; thus, $F(1H)$ left increases as $F(1H)$ right decreases, producing a tendency for the blade to shift to the right. As the blade attempts to shift, rollers No. 2 pick up load until $F(2H)$ right plus $F(1H)$ right equals $F(1H)$ left. As M continues to increase, the above action is continued until $F(1H)$ right is zero and the net force is now carried by rollers No. 2 exclusively on the right portion of the retention. Now, if the centrifugal load is made zero, the only change would be that $F(1) = F(2)$. Thus, the retention is capable of proper operation
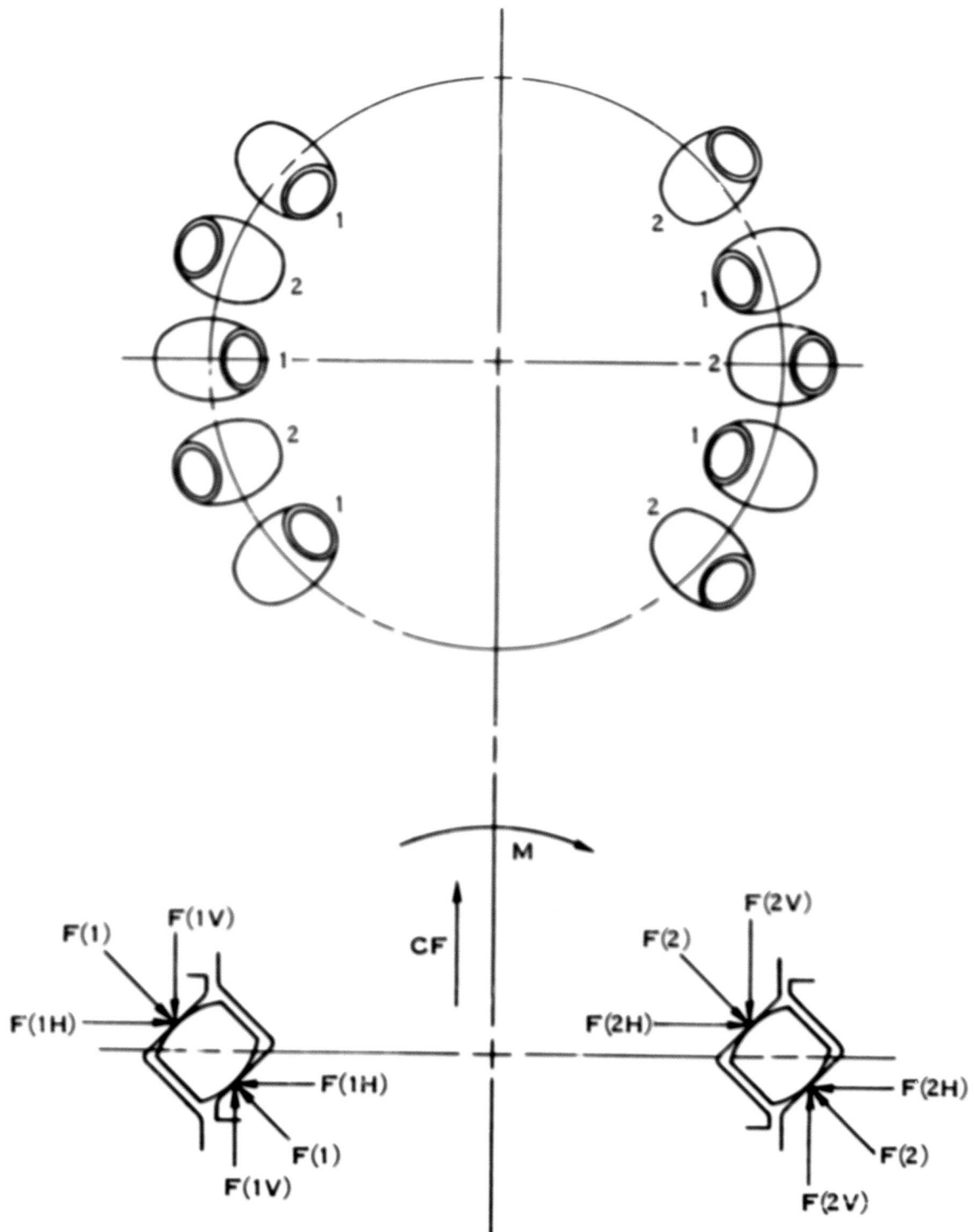
Figure 17. Crossed Roller Retention.

without using centrifugal force as a preloading device, and stresses are the only determining factor in establishing the retention size.

The advantage of the crossed roller retention is the ability to vary the roller ratio to get the optimum use of the rollers in both load directions and the increase in contact area of roller with the race, allowing a greater load per roller than for a ball of the same diameter.

The disadvantage of the crossed roller retention is the necessity to use a constant contact angle and the assembly problem of installing the rollers in the proper sequence. Inspection of the crossed roller bearing installation also presents some problems. Both the assembly and inspection problems are a function of the manner in which the retention is assembled.

Gothic Arch

A Gothic arch ball bearing is a duplex angular contact bearing built into a common race. The groove in the race is generated from two centers so that the two radii cross and do not converge at the center of the groove. A slight clearance is provided between the ball and the race groove to facilitate assembly.

As with any angular contact ball bearing, the contact angle increases as the load increases (Figure 18a). Assume, for an initial load case, that centrifugal force is the only load present; then every ball will have the same contact angle and the bearing will be in complete equilibrium. As the aerodynamic force increases, the load and contact angle in the left portion of the retention increase while the opposite action is occurring in the right portion. As this action continues, the right portion goes to zero load, and the ball is at the no-load or initial contact angle with the upper part of the race and also begins to contact the lower part of the race. Any further increases in aerodynamic moment cause the load to be picked up by the lower part of the race. If it is now assumed that centrifugal load is zero, the only change required is a change in the magnitude of the force and the contact angle of the balls contacting the lower race. Therefore, the retention is capable of proper operation without requiring centrifugal force for a preload, and the only factor determining retention size is the stress limitations.

If the radius were common to both sides of the groove (a semicircular race), the ball could not contact both sides of the groove at the same time. The ball would have to be completely unloaded from the initial, or zero load, contact angle of one side of the groove to the corresponding point on the other side of the groove. Figure 18b illustrates the difference between a Gothic arch and a semicircular race.

44
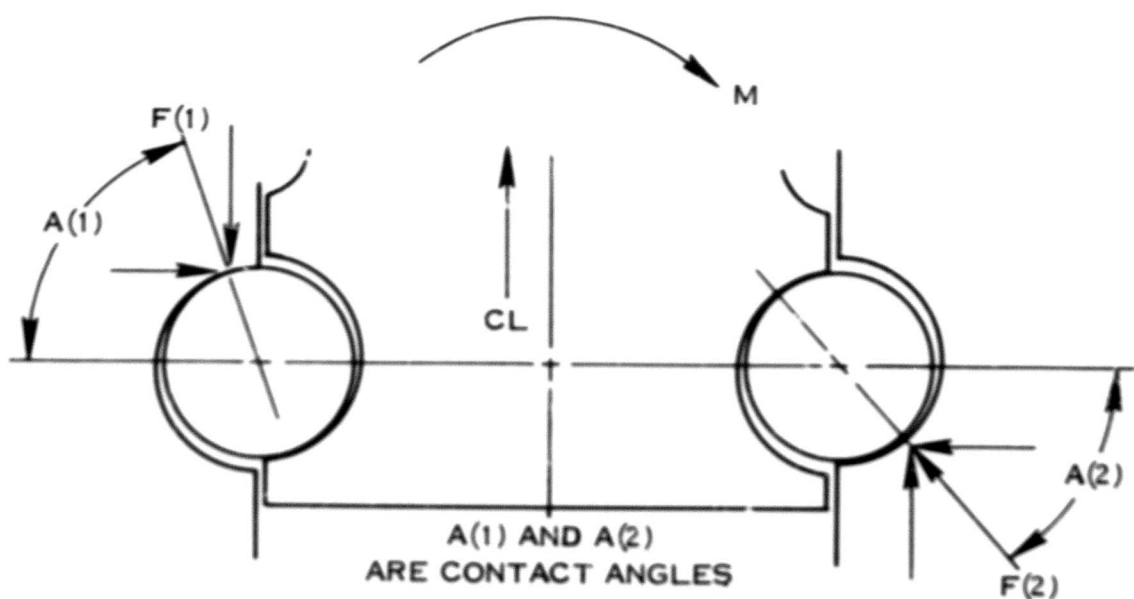
(A) GOTHIC ARCH SHOWING MOMENT CARRYING CAPABILITY
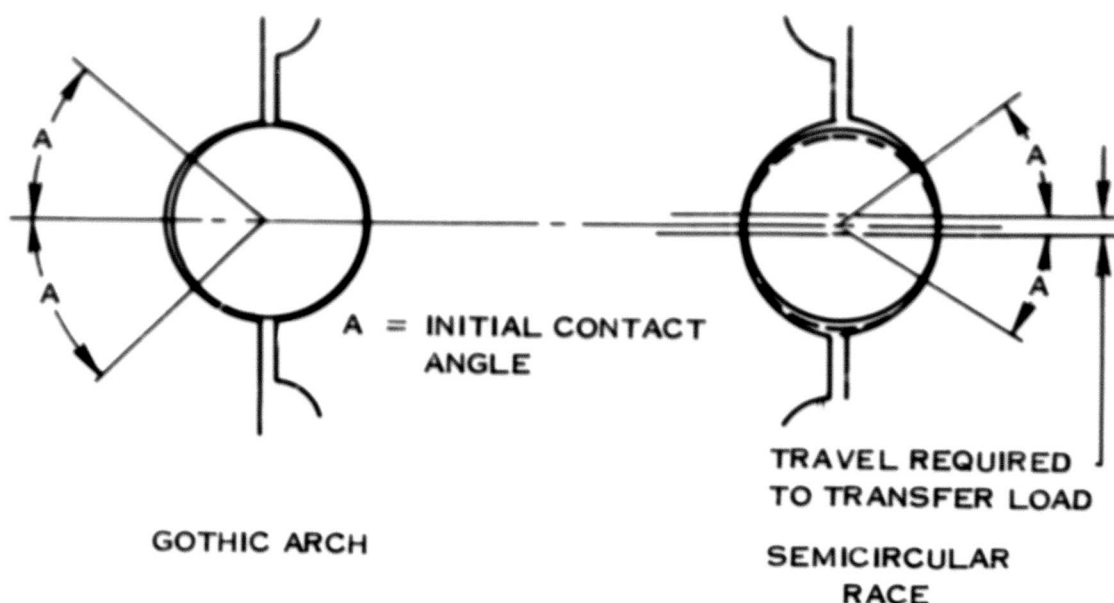
(B) COMPARISON OF GOTHIC ARCH AND SEMICIRCULAR RACES

Figure 18. Gothic Arch 4-Point Retention.

The advantage of the Gothic arch retention is the ease of assembly and inspection. The disadvantage is that no optimization of rolling elements can be obtained. Once the ball diameter and pitch diameter are selected, the general geometry is fixed.

Retention Conclusions

Some of the desirable characteristics of an ideal blade retention are high load-carrying capability, reliability, and ease of assembly.

From the preceding discussions, it is seen that neither the crossed roller retention nor the Gothic arch retention meets all of these characteristics. The two retentions are equal in reliability. The crossed roller is superior in load-carrying capability, while the Gothic arch is superior in ease of assembly. With a composite material blade, the load-carrying capability, in the propeller size being considered, is not of primary importance. Therefore, the Gothic arch retention was selected for its greater ease of assembly.

ANALYSIS OF 4-BLADE BARRELS

Retention Analysis

The retention pitch diameter is determined by calculating (by computer) the maximum Hertz stress for several different pitch diameters using various ball sizes. The results of these calculations are then plotted, and a tentative retention size is selected. This selected pitch diameter and ball size combination is then placed into the computer to calculate the Hertz stresses and deflection for each of the load conditions using a predetermined ball-to-race fit.

Table IV defines the retention geometry for the retention size selected. Also included are (1) the maximum calculated Hertz stress for each loading case (centrifugal load and steady bending moment and vibratory bending moment) and (2) the minimum distance from the edge of contact ellipse relative to the edge of the race.

Barrel Arm Analysis

The barrel arm stresses are independent of the centerbody concept used but are dependent on retention diameter and cylinder length. For this reason, the barrel arm concept is common to the various 4-blade barrel designs. The arm is analyzed as a shell of revolution (cylinder), with the point of connection with the centerbody defined as an infinitely stiff foundation. The cylinder is broken up into as many parts as necessary in order for each part to have a constant thickness (Figure 19). For the imposed loadings, the stresses and deflections are calculated along each part (at preselected points) from the point of fixity to the free end.

The barrel arm outboard of the blade retention area is wrapped with boron-epoxy. The effect of the boron is to stiffen the retention area in the hoop direction such that radial loads from the retention are absorbed by the boron and are not transmitted to the lower portions of the titanium barrel arm. The arm takes the axial portion of the blade loads since the boron is not effective in this direction. The computer program assumes an all-titanium structure and only axial loads for the reasons stated above. Table V summarizes the maximum stresses in each section for both loading conditions.

47

TABLE IV. BLADE RETENTION, 4-BLADE BARRELS

Pitch Diameter	7.40514
Ball Diameter	0.625 ± 0.000025 in.
No. of Balls	37
Ball Matching Radius Outer Race	0.3315 ± 0.003 in.
Ball Matching Radius Inner Race	0.3257 ± 0.0008 in.
Major Diameter Outer Race	8.0318 ± 0.0006 in.
Minor Diameter Inner Race	6.7784 ± 0.0006 in.
Major Diameter Inner Race	7.413 ± 0.001 in.
Minor Diameter Outer Race	7.419 ± 0.001 in.

Case I

    Max Hertz Stress   578,310 psi

    Min Distance From Ellipse Edge Relative to Race Edge, 0.0415 in.

Case II

    Max Hertz Stress   603.820 psi

    Min Distance From Ellipse Edge Relative to Race Edge, 0.0246 in.
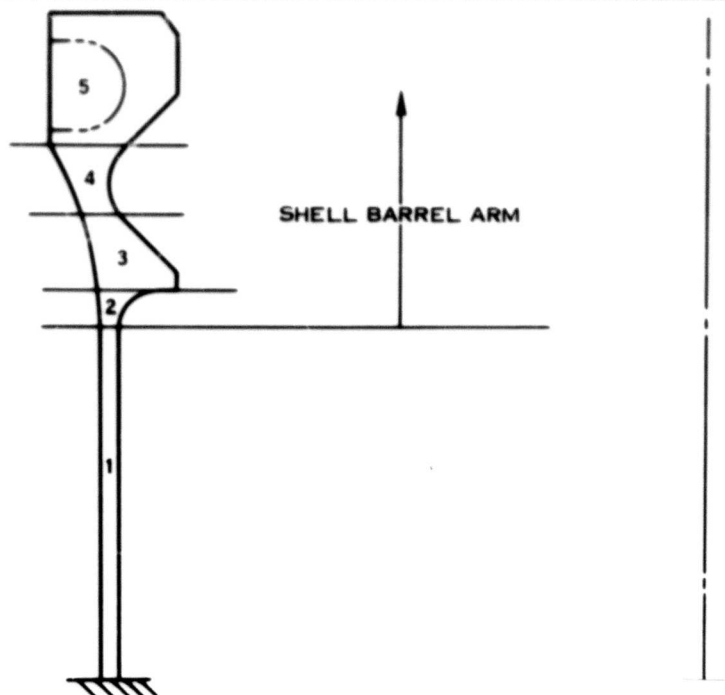
Figure 19. 4-Blade Barrel Arm Section.

TABLE V. BARREL ARM STRESS SUMMARY, 4-BLADE BARREL

Section	1	2	3	4	5
Case I Stress (psi)					
Axial	23,265 ± 11,515	23,265 ± 3,910	19,030 ± 8,749	19,030 ± 8,749	7,620 ± 3,963
Hoop	10,806 ± 5,097	3,153 ± 1,811	12,978 ± 2,785	6,366 ± 2,784	7,279 ± 3,297
Shear	2,759 ± 512	2,697 ± 500	2,140 ± 3,975	515 ± 607	607 ± 1,183
Case II Stress (psi)					
Axial	20,254 ± 20,195	20,254 ± 20,195	16,742 ± 15,344	16,742 ± 15,344	6,584 ± 6,950
Hoop	9,473 ± 8,940	2,679 ± 3,177	5,394 ± 4,884	5,394 ± 4,884	6,417 ± 5,782
Shear	142 ± 899	139 ± 878	110 ± 697	228 ± 1,065	327 ± 2,074

Spherical Barrel

The centerbody of the spherical barrel is generated by taking the 4-blade retaining rings and attaching them to 4 short cylinders. A sphere is used to attach the blade-retaining cylinders to the front ring, and a cone is used to blend the sphere into the rear ring (Figure 20).

The barrel is cut by an imaginary plane through the plane of rotation. That portion of the barrel forward of the plane is the front ring, and that portion aft of the plane and forward of the tailshaft is the rear ring. Each ring, for a 4-blade barrel, is radially symmetrical about 45-deg segments. Each segment is sectioned every 10 deg, as shown in Figure 21. Using a computer program, the section properties are computed for both the front and rear rings. The resultant section properties with each loading condition are used as the input for a computer program entitled Barrel Ring Analysis (deck H 153), which calculates the stresses and deflections for the front and rear rings. Tables VI and VII summarize the total stress and deflection for each 10-deg element. The stresses repeat every 90 deg for each loading case.
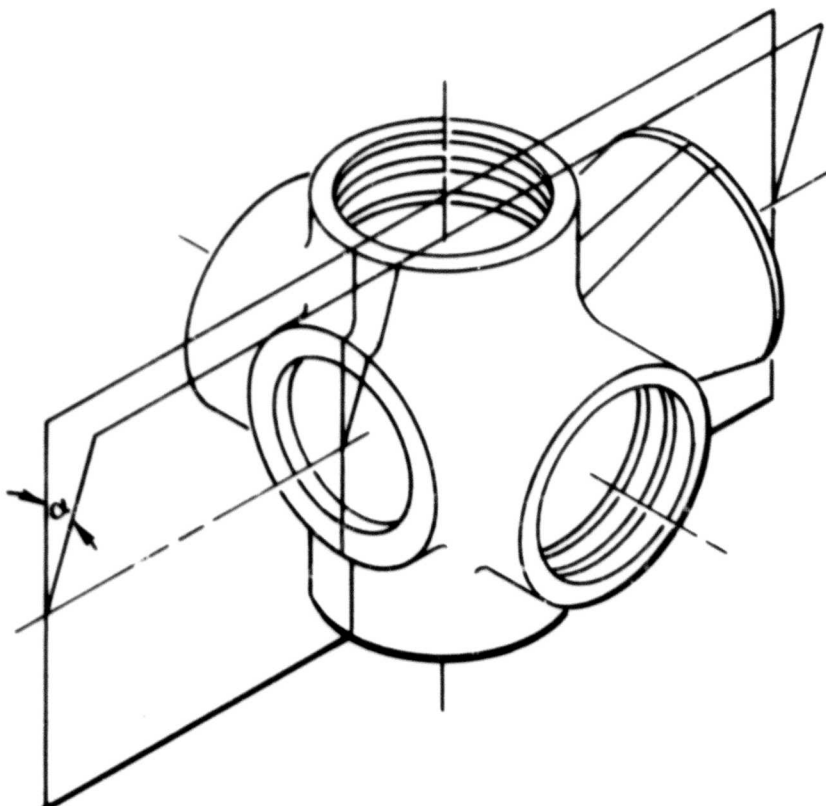
Figure 20. 4-Blade Spherical Barrel.

Figure 21. 4-Blade Spherical Barrel 20° Forward Section.

Shell Barrel

The centerbody of the shell barrel is generated by taking the 4-blade-retaining rings, the front ring, and the rear ring and connecting them by a surface generated by a straight line. The between-arms section of the barrel centerbody is elliptical (Figure 22).

A true shell barrel would have the centerbody elements connect into the blade-retaining rings at a point where the load from the blade enters the ring (Figure 23). The incorporation of the 4-point bearing retention concept required the use of a ball loading hole for assembly purposes. This requirement together with wrapping boron around the barrel arms necessitated the positioning of the centerbody elements inboard of the races, thereby producing secondary stressing in the center-body (Figure 24).

TABLE VI. RING ANALYSIS, 4-BLADE SPHERICAL BARREL

Case I Section Position	Front Ring Outer Surface Stress (psi)	Deflection (in.)	Inner Surface Stress (psi)
0	4,710 ± 2,348	0.0048	5,784 ± 2,548
10	4,662 ± 2,033	0.00488	5,254 ± 3,575
20	4,036 ± 1,652	0.00477	3,734 ± 3,761
30	4,705 ± 1,848	0.00473	4,424 ± 4,596
40	9,669 ± 2,934	0.00467	7,715 ± 5,926
50	8,928 ± 4,680	0.00468	8,611 ± 3,851
60	4,727 ± 2,232	0.00476	5,866 ± 1,107
70	4,074 ± 1,998	0.00481	4,932 ± 102
80	4,649 ± 2,406	0.00483	5,980 ± 1,300

Case I Section Position	Rear Ring Outer Surface Stress (psi)	Deflection (in.)	Inner Surface Stress (psi)
0	7,701 ± 2,681	0.00685	8,029 ± 3,674
10	7,252 ± 2,044	0.00686	8,704 ± 5,224
20	5,418 ± 1,176	0.00686	6,594 ± 5,095
30	6,588 ± 1,409	0.00679	10,229 ± 6,666
40	11,759 ± 2,788	0.00666	15,876 ± 9,695
50	12,400 ± 4,361	0.00666	13,874 ± 6,192
60	6,814 ± 2,469	0.00678	7,714 ± 1,843
70	5,622 ± 2,223	0.00686	4,490 ± 1,847
80	7,409 ± 2,845	0.00689	7,277 ± 2,172

TABLE VII. RING ANALYSIS, 4-BLADE SPHERICAL BARREL

Case II	Front Ring		
Section Position	Outer Surface Stress (psi)	Deflection (in.)	Inner Surface Stress (psi)
0	5,303 ± 4,117	0.00611	6,274 ± 4,473
10	5,227 ± 3,565	0.00611	5,940 ± 6,273
20	4,519 ± 2,897	0.00608	4,481 ± 6,599
30	5,240 ± 3,242	0.00603	5,446 ± 8,064
40	10,296 ± 5,150	0.00594	9,028 ± 10,395
50	9,915 ± 8,214	0.00595	9,489 ± 6,750
60	5,222 ± 3,914	0.00604	6,189 ± 1,937
70	4,538 ± 3,504	0.00612	5,098 ± 183
80	5,221 ± 4,220	0.00615	6,314 ± 2,283

Case II	Rear Ring		
Section Position	Outer Surface Stress (psi)	Deflection (in.)	Inner Surface Stress (psi)
0	7,045 ± 4,702	0.00744	7,637 ± 6,452
10	6,680 ± 3,584	0.00745	7,917 ± 9,170
20	5,028 ± 2,061	0.00745	5,696 ± 8,941
30	6,140 ± 2,471	0.00738	8,814 ± 11,696
40	11,126 ± 4,894	0.00725	13,954 ± 17,006
50	11,456 ± 7,653	0.00725	12,922 ± 10,858
60	6,257 ± 4,368	0.00739	7,519 ± 3,230
70	5,134 ± 3,899	0.00749	4,612 ± 3,245
80	6,760 ± 4,989	0.00752	7,182 ± 3,818
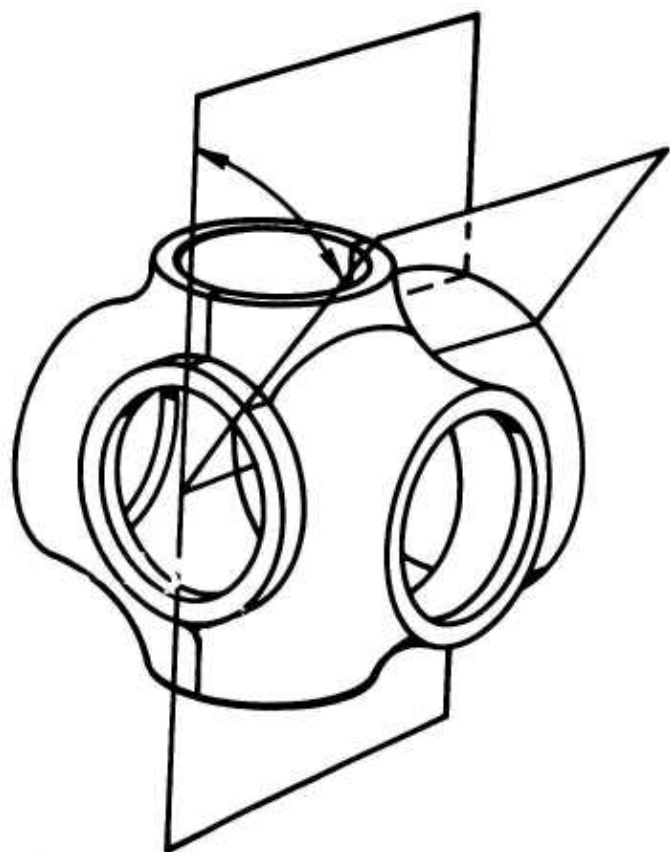
Figure 22. 4-Blade Shell Barrel.
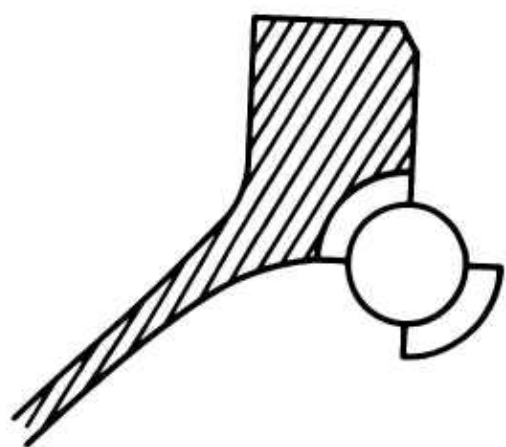
Figure 23. Optimum Shell Barrel Retention Configuration.

54
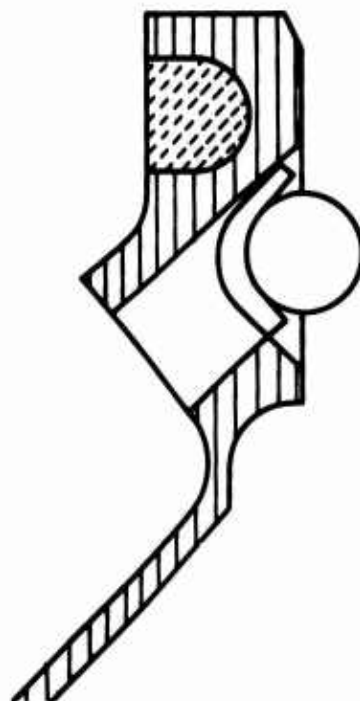
Figure 24. Required Shell Barrel Retention Configuration.

The centerbody is assumed to be divided at the blade centerline, in the plane of rotation, into the front and rear barrel rings. Cross sections are taken every 10 deg from the blade centerline to the between-arms symmetry line for each ring (Figures 25 and 26). The section properties for each section are then determined by use of a computer program entitled Section Properties by Parts (deck P 026A). This output is then used as part of the input for a computer program, Barrel Ring Analysis (H153), which calculates the barrel stresses and deflections (Tables VIII and IX).

The barrel arm does not exist for this configuration. The outboard portions of the spherical barrel arm are used for this ring structure. Figure 19 illustrates the portion used; Figure 19, parts 2 through 5, applies to the shell barrel arm ring.

4-Blade Crossed Tube Barrel Loads

Of the loading conditions, the 3.5 g cruise maneuver condition is used as the design criterion for the 4-blade crossed tube barrel. The axial, in-plane and out-of-plane load distributions are used to determine the analytical approach for the crossed tube concept. The loads themselves are broken down as follows:

55
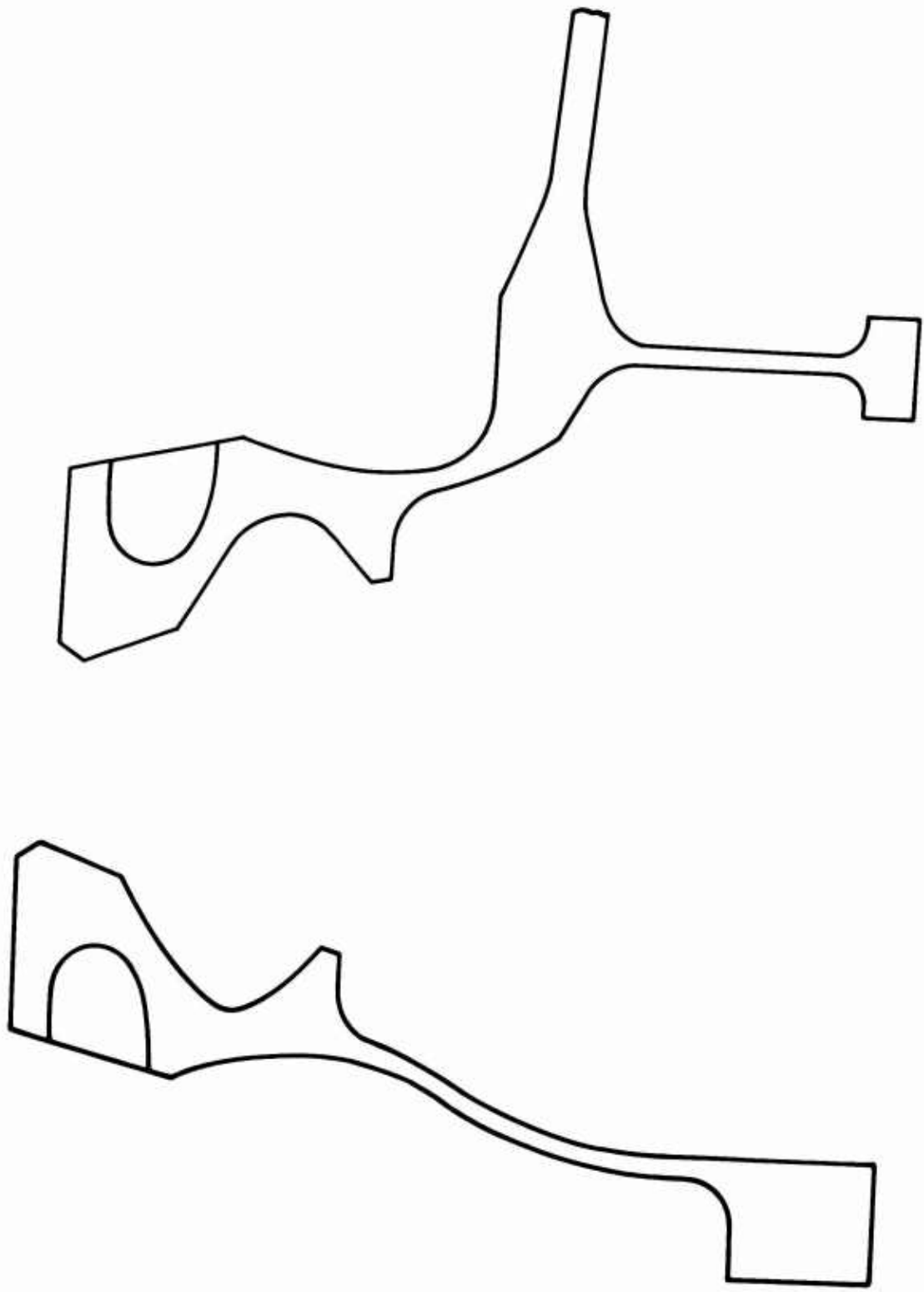
Figure 25. 4-Blade Shell Barrel 20° Forward Section.   Figure 26. 4-Blade Shell Barrel 20° Aft Section.

TABLE VIII. RING ANALYSIS, 4-BLADE SHELL BARREL

Case I	Front Ring		
Section Position	Outer Surface Stress (psi)	Deflection (in.)	Inner Surface Stress (psi)
0	4,984 ± 2,434	0.00602	5,817 ± 2,589
10	5,095 ± 2,226	0.00599	5,535 ± 3,852
20	4,732 ± 1,978	0.00593	4,281 ± 4,493
30	4,030 ± 1,524	0.00584	3,585 ± 4,445
40	11,767 ± 3,731	0.00568	10,253 ± 9,241
50	11,087 ± 5,431	0.0057	11,858 ± 5,880
60	4,011 ± 1,934	0.00588	5,129 ± 1,072
70	4,788 ± 2,287	0.00605	5,778 ± 233
80	5,087 ± 2,569	0.00606	6,362 ± 1,314

Case I	Rear Ring		
Section Position	Outer Surface Stress (psi)	Deflection (in.)	Inner Surface Stress (psi)
0	7,228 ± 2,524	0.00705	7,460 ± 3,564
10	7,375 ± 2,083	0.00706	8,912 ± 5,226
20	6,233 ± 1,453	0.00704	7,431 ± 5,484
30	6,106 ± 1,448	0.00698	10,288 ± 6,918
40	11,429 ± 2,705	0.00685	15,125 ± 8,491
50	12,130 ± 4,388	0.00684	13,486 ± 5,394
60	6,222 ± 2,159	0.00697	7,622 ± 2,015
70	6,393 ± 2,415	0.00704	5,217 ± 1,776
80	7,520 ± 2,853	0.00708	7,501 ± 2,100

57

TABLE IX.
RING ANALYSIS,
4-BLADE SHELL BARREL

Case II		Front Ring	
Section Position	Outer Surface Stress (psi)	Deflection (in.)	Inner Surface Stress (psi)
0	5,601 ± 4,268	0.00767	6,297 ± 4,546
10	5,708 ± 3,904	0.00764	6,272 ± 6,760
20	5,298 ± 3,468	0.00757	5,176 ± 7,884
30	4,478 ± 2,673	0.00745	4,552 ± 7,799
40	12,656 ± 6,547	0.00724	12,213 ± 16,210
50	12,306 ± 9,530	0.00725	13,038 ± 10,309
60	4,465 ± 3,393	0.00748	5,347 ± 1,876
70	5,327 ± 4,012	0.00762	5,947 ± 411
80	5,704 ± 4,506	0.00772	6,697 ± 2,309

Case II		Rear Ring	
Section Position	Outer Surface Stress (psi)	Deflection (in.)	Inner Surface Stress (psi)
0	6,635 ± 4,443	0.00767	7,033 ± 6,239
10	6,798 ± 3,651	0.00767	8,012 ± 9,138
20	5,776 ± 2,539	0.00765	6,394 ± 9,622
30	5,629 ± 2,505	0.00759	8,718 ± 12,085
40	10,778 ± 4,714	0.00745	13,545 ± 14,939
50	11,137 ± 7,658	0.00745	12,705 ± 9,505
60	5,691 ± 3,774	0.00760	7,341 ± 3,572
70	5,863 ± 4,250	0.00769	5,245 ± 3,178
80	6,875 ± 5,019	0.00774	7,281 ± 3,701

1. Centrifugal loading is considered to be constant and evenly distributed about all four barrel arms (Figure 27).

2. Moment loading, both steady and vibratory, is considered to act as shown in Figure 28. It is taken as being symmetrical about a neutral axis and distributed around the arm on a cosine curve.

Analysis and Logic

The analytical approach was determined from the configuration of barrel arm loads and from the geometrical characteristics of the crossed tube design. This approach was applied in essentially three parts:

1. The elemental analysis of the continuous cylinder centerbody area neglecting the effects of the front and rear rings.

2. The analysis of the front and rear rings by spherical barrel analytical approach neglecting the effects of the centerbody.

3. The combination of parts 1 and 2. In order to relate part 1 to part 2, a stiffness comparison is made, which in turn determines the percentage of load absorbed by the front and rear rings as opposed to the centerbody. This percentage load split is determined by matching deflections at a point on the barrel common to both of the analyses.

The Elemental Analysis of the Continuous Cylinder Centerbody Area

Due to the geometrical complexity of the crossed tube design, the standard analytical approach for barrel analysis cannot be used. Instead, a thin strip or "element" analysis is employed in which slices are cut through the barrel parallel to the in-plane axis. A typical element configuration is shown in Figure 29.

The barrel loading is symmetrically distributed around the barrel arm. In the barrel analysis these distributed loads are further defined as acting at point locations around the arms, and these point locations coincide with the ends of the in-plane section elements cut (Figure 30). Because the moment loading is a function of θ, it becomes necessary to define these section elements with respect to θ. This is done by, first, considering the areas of continuous cylinders as effective only to 45 deg either side of the in-plane axis of barrel symmetry and, second, assuming that the in-plane section elements cut are of even radial distribution (Figure 31) with identical section properties from 0 to 40 deg.

59
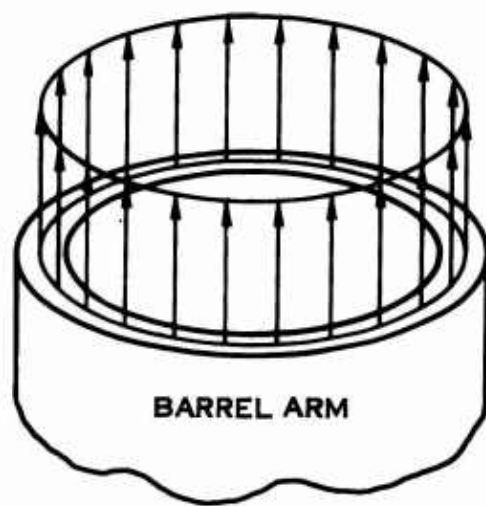
BARREL ARM

Figure 27. Moment Load Distribution.
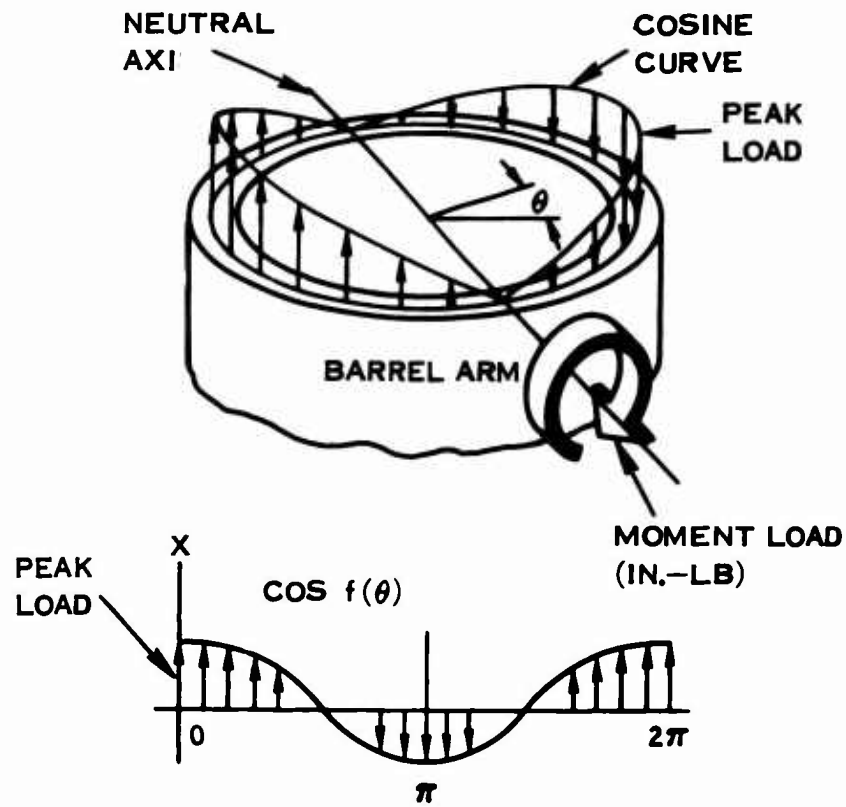
Figure 28. Centrifugal Load Distribution.

AXIS OF BARREL SYMMETRY(IN—PLANE)

LOAD AXIS OF SYMMETRY

AREA OF CONTINUOUS CYLINDERS

OUT—OF—PLANE AXIS

ENGINE SHAFT ℄

RANDOM SECTION PLANE

RANDOM ELEMENT SECTION (TYPICAL)
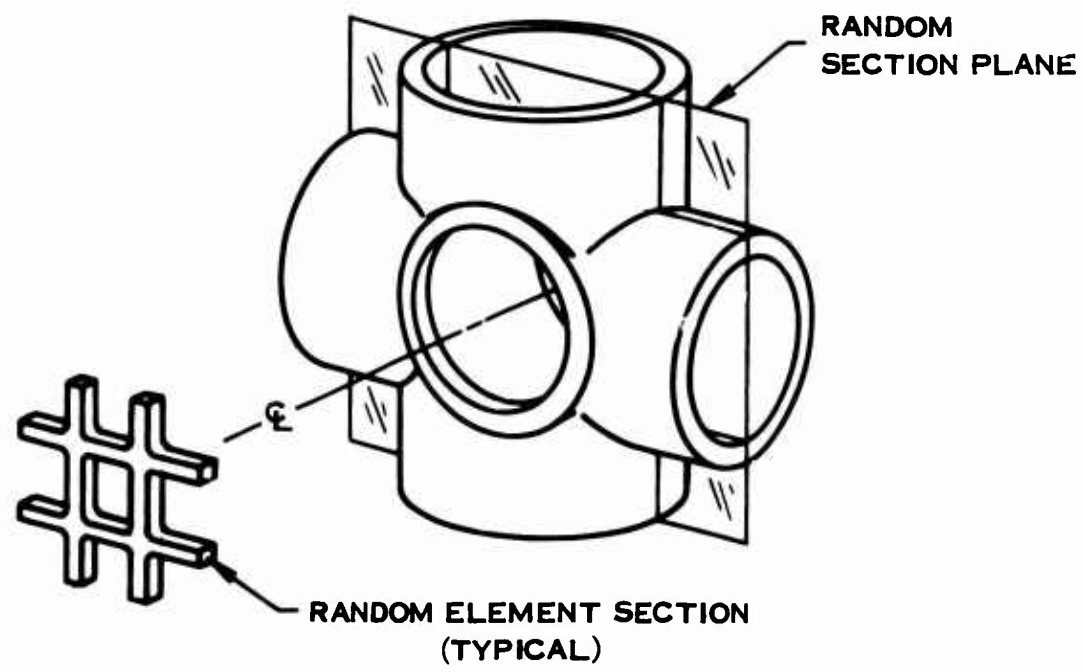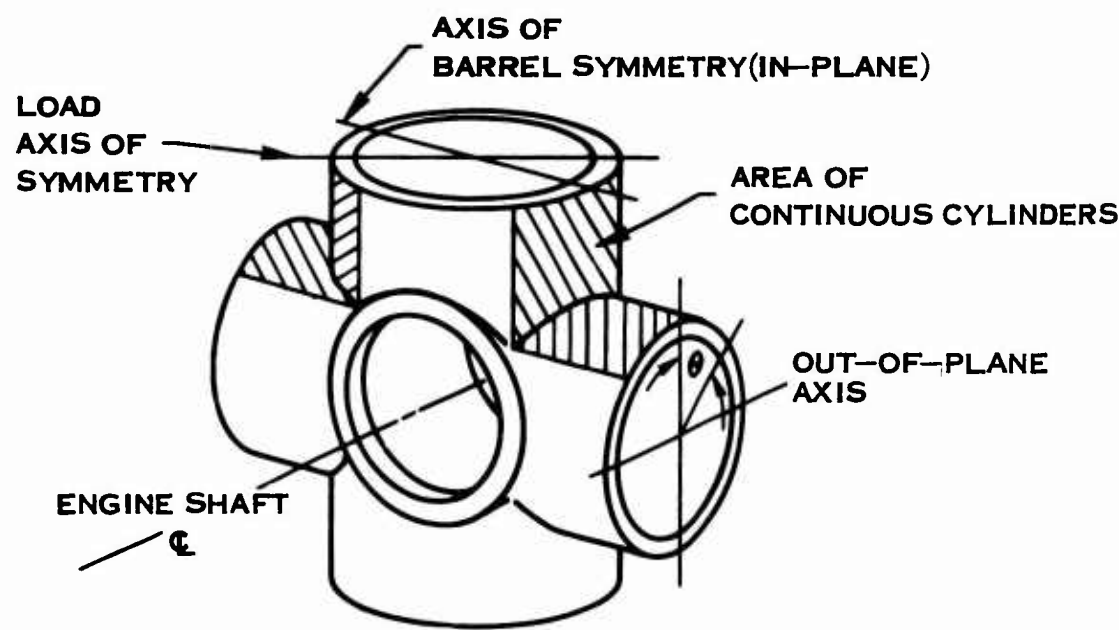
Figure 29. Typical Element of Continuous Cylinder Centerbody Area.

61
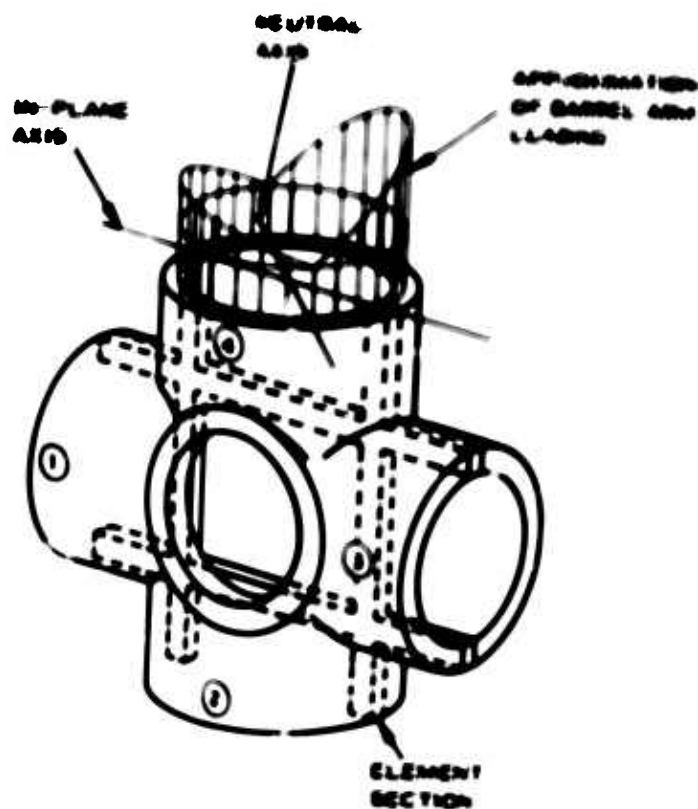
Figure 30. Typical Element Configuration
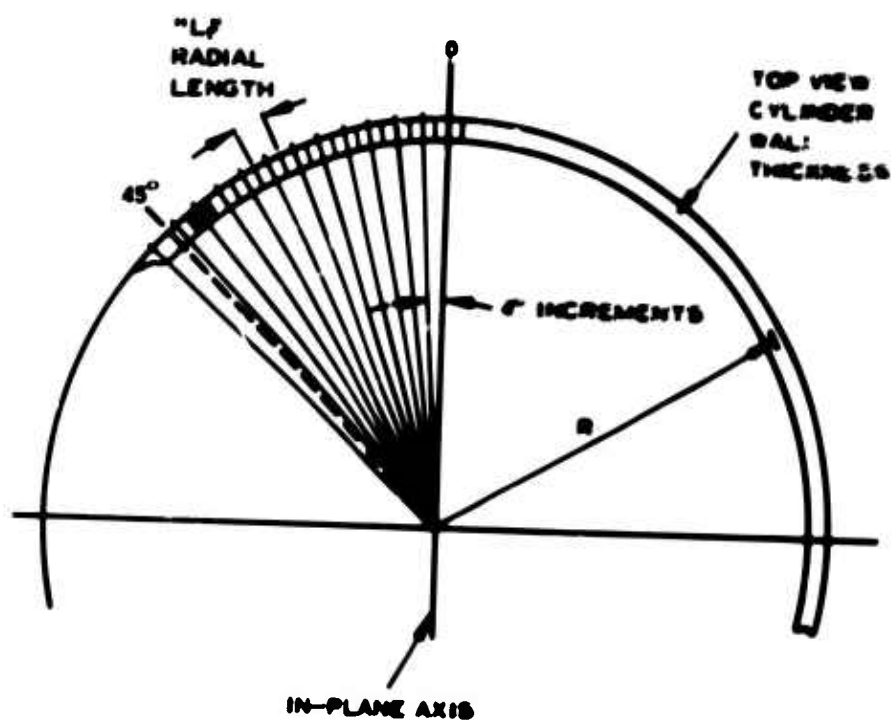
Figure 31. In-Plane Barrel Arm Section Elements.

The more section elements that are taken in the 0- to -40-deg area, the more accurate the analysis will be. If N, the number of elements, equals infinity, a partial differential equation for the system can be written from which, theoretically, the stress and deflection equations can be integrated. This case would be mathematically impossible because of the complex geometry; therefore, a set of equations is derived for the general section configuration, and a summation of a definite number of sections is made. The number of section elements to be considered is arbitrarily selected at 20. The radial distribution increment is then calculated from

$$\text{DEG/ELEMENT} = \frac{2\ (40\ \text{DEG})}{(20\ \text{ELEMENTS})}$$

$$\underline{\text{DEG/ELEMENT} = 4.0}$$

Figure 31 shows the 4-deg increments measured from the center of one element to those adjacent to it. This allows an approximate area calculation using the radial length of an element times its thickness or

$$A = t\,(L_r)$$

where

$$L_r = \frac{2\ (40)\ \pi\ R}{360} \tag{1}$$

Given the following loads, the relationships of the loads to the elements can be written:

CF = centrifugal force
SBINP = steady bending moment in plane
SBOOP = steady bending moment out of plane
1PINP = 1P vibratory moment in plane
1POOP = 1P vibratory moment out of plane
2PINP = 2P vibratory moment in plane
2POOP = 2P vibratory moment out of plane

An equation for any element is

$$CF_{ELE} = \frac{40\ (CF)}{360} \tag{2}$$

For the moment loads, the peak load of the distribution is found from the standard formula of

$$P = \frac{2M}{R} \tag{3}$$

and the load at any point for in-plane loads is

$$P_{IN} = \frac{2M}{R} \, (\cos \theta) \tag{4}$$

For out-of-plane loads, which are 90 deg out of phase to the in-plane moment,

$$P_{OUT} = \frac{2M}{R} \, (\sin \theta) \tag{5}$$

Substituting the respective moments and their signs for MOMENT and summing the results produce the final element load. For the determination of the proper sign, an investigation into 4-blade barrel loading is necessary.

Assuming that on barrel arm No. 1 (Figure 30) the vibratory moments 1P and 2P are in phase (i.e., when 1P is a positive moment), the total barrel load picture would appear as shown in Figure 32, where a force directed toward the center of barrel rotation and clockwise moments is considered to be negative. θ is positive forward of the "Y" axis.

Having calculated the total load on the end of each element, it is now possible to analyze each section as an independent system.

In Figure 33, a section is drawn with loads P_1 and P_2 shown on one barrel arm only. It is assumed that the location of AXIS B is unchanged. An elongation of A and A' over the length L will then cause hoop and bending stresses in B because B is part of a cylinder (see the deflection sketch in Figure 33). These stresses are of a secondary bending nature and cause a hoop restraint on the elongation of A and A', effectively reducing the load transmitted into length L_1 and L_2. The stress in L_1 and L_2 is tensile and a function of the load transmitted. It now becomes necessary to define the hoop restraint of B. This is done by considering the intersecting cylinder, of which B is an element, with all the barrel arm loads of one-half cylinder A transmitted to its end normal to its meridian (Figure 34). These transmitted loads are a combination of the centrifugal load and moment loads. If their magnitudes are plotted along

64
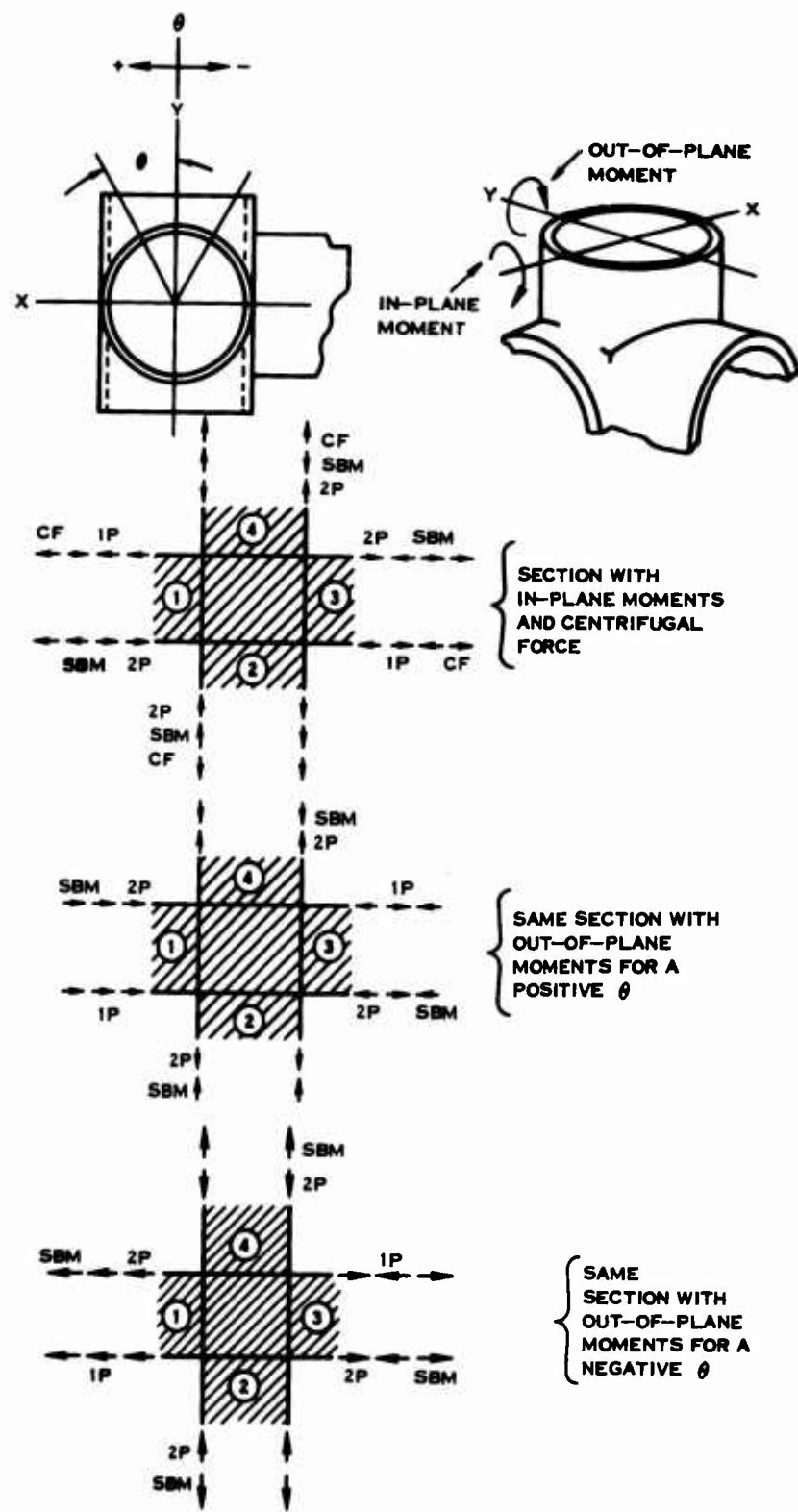
Figure 32. Loading Diagrams.
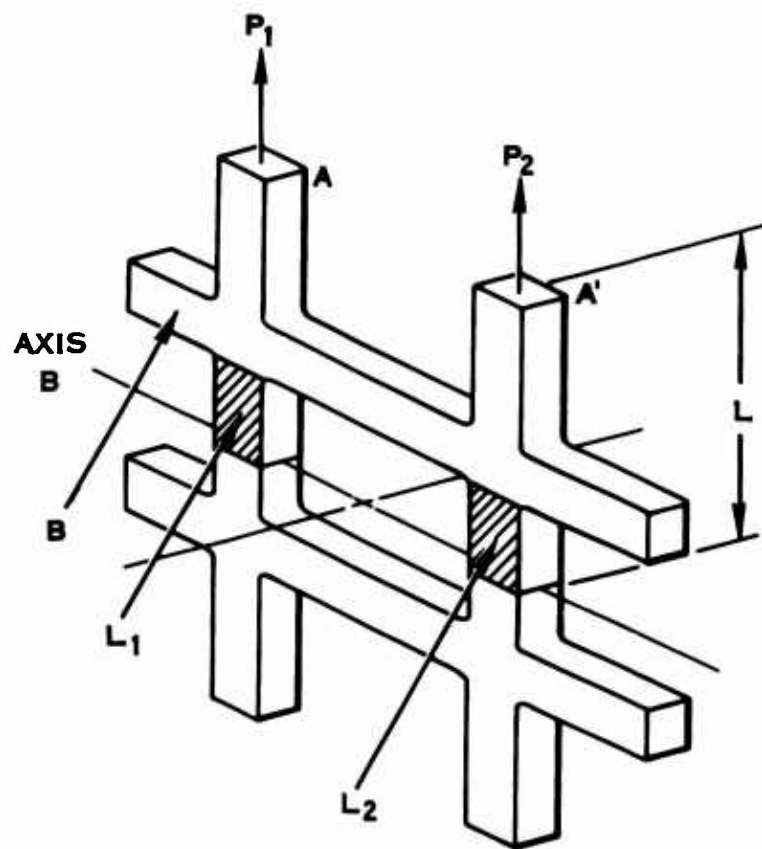
FOR THE CENTER SECTION ELEMENT

A1 AND A1' = R . ALL OTHERS ARE R COS ϕ

DEFLECTION
SKETCH
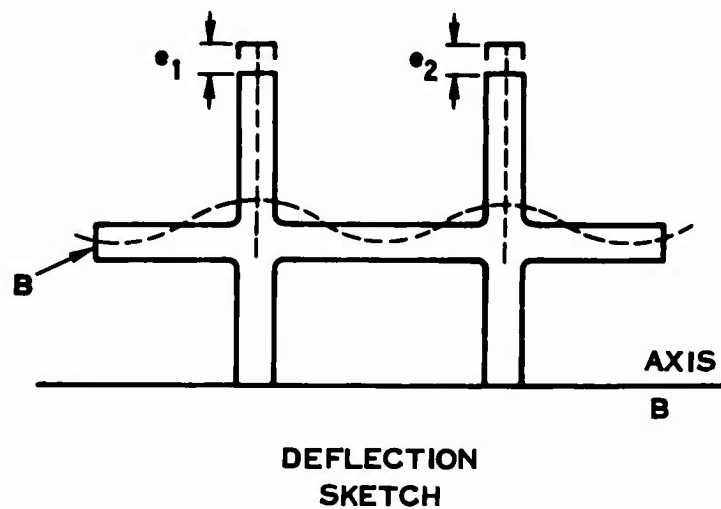
Figure 33. 4-Blade Crossed Tube Barrel Section Elements.

CYLINDER B
ARM
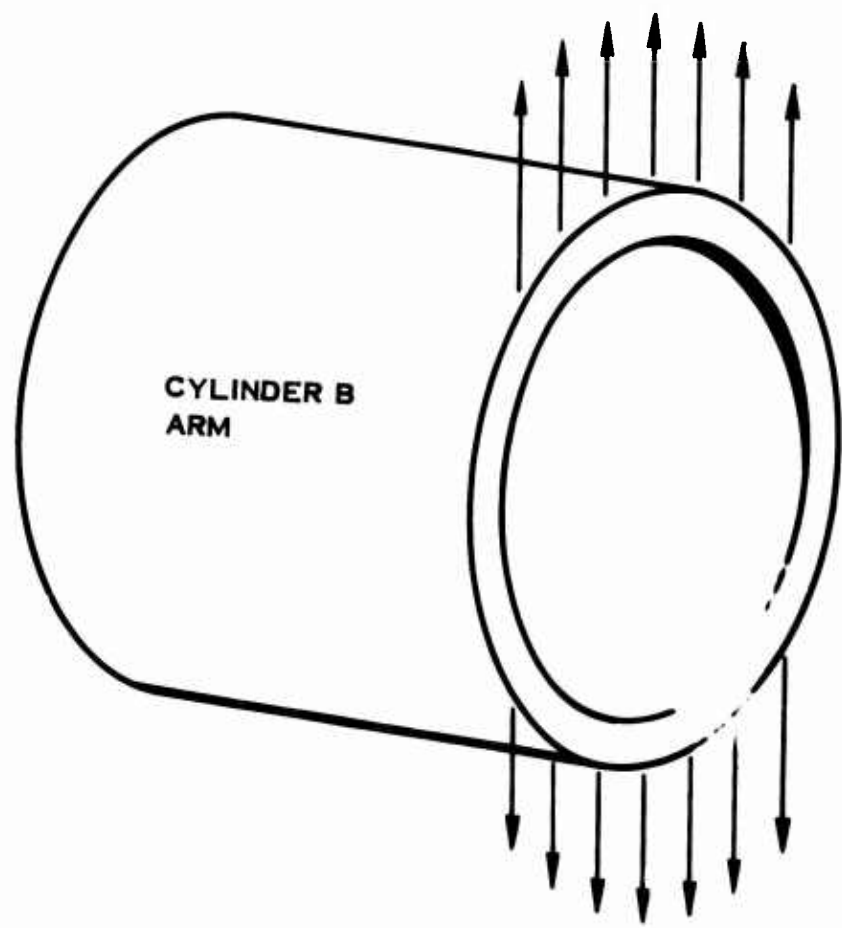
Figure 34. Barrel Arm Loading.

67

one-half the circumferential linear length of B, the combination can be defined as a Fourier harmonic (Figure 35). The harmonic combination at the mean line is then the zero Fourier harmonic and second Fourier harmonic.

At this point it becomes beneficial to employ the computer program entitled Thin Shells of Revolution (deck HO88) to determine the effective stiffness, or spring rate, of the cylinder. This spring rate can be determined quite easily once the relationship between deflection and load is obtained. A theoretical load ΔP is applied to the center section element of cylinder A, and an elongation of L_1 is calculated from the equation

$$e = \frac{\Delta P \, L_1}{E \, A} \tag{6}$$

where E = modulus of elasticity.

This elongation, or deflection, is common to both the element and the cylinder B (Figure 36); therefore, the load necessary to cause the δ is a portion of ΔP and will be called P_{CYL}, so that

$$\Delta P - P_{CYL} = P_{ELE} \tag{7}$$

where P_{ELE} = load on the section element

P_{ELE} can then be used to recalculate e.

Through this iterative process, the spring rate of the cylinder, once determined, is constant; therefore, using the theoretical e to calculate it is correct.

Introducing the geometry of cylinder B along with the deflection e produces a load, P_{CYL}, necessary to cause e. The spring rate is then

$$S_L R_L = \frac{P_{CYL}}{e} \tag{8}$$

It is assumed that the section of cylinder B which is part of the center-body is identical to ARM B in restraint; therefore, the spring rate is effectively doubled or

$$SR_1 = \frac{2 \, P_{CYL}}{e} \tag{9}$$

68
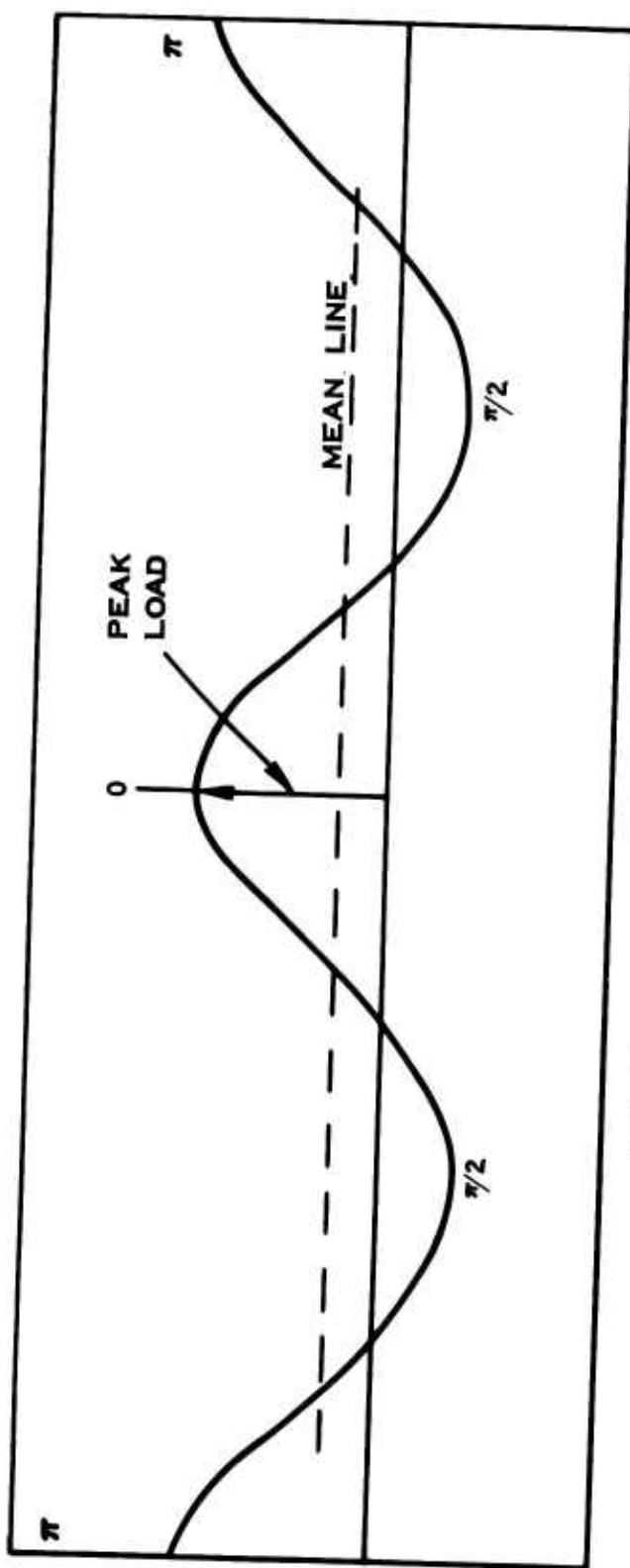
THIS PLOT IS OF CENTRIFUGAL AND STEADY
BENDING ONLY BUT IS REPRESENTATIVE OF
ALL THE LOADING.

Figure 35. Barrel Arm Loads Defined as a Fourier Harmonic.

69
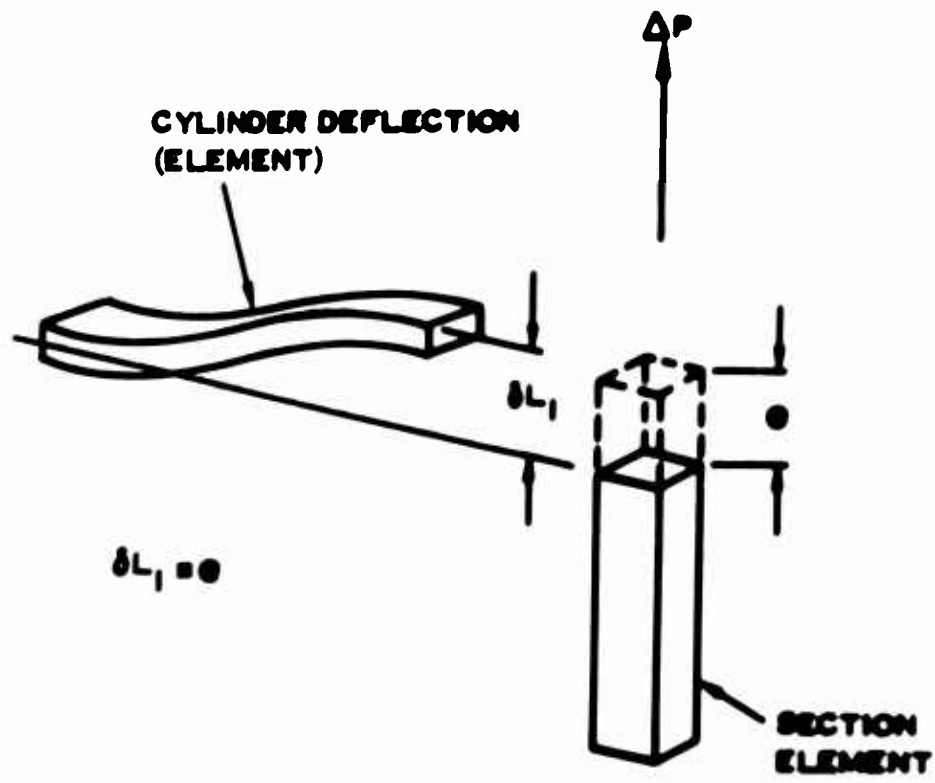
Figure 36. Interaction of Cylinder Elements.

MOSS also calculates the hoop and bending stresses in cylinder B caused by P_{CYL}. These stresses are also ratioed to the force P_{CYL} to produce stress factors.

$$SF = \frac{f}{P_{CYL}} \tag{10}$$

Because P_{CYL} and P_{ELE} are derived from the theoretical load ΔP, the relationship of the actual load P must be defined. This is done by the spring rate comparison that follows.

The deflection of the section element L_1 is

$$\delta L_1 = \frac{PL_1}{EA} \tag{11}$$

where $L_1 = R \cos \theta$, length of any θ element

The spring rate of the section element A1 is

$$SR_{ELE} = \frac{EA}{L_1} \tag{12}$$

The deflections of the cylinder and the section element are common, so

$$\delta L_1 = \delta_{CYL} \tag{13}$$

Therefore,

$$\frac{P_{CYL} (ACT)}{SR} = \frac{P_{ELE} (ACT)}{SR_{ELE}} \tag{14}$$

(ACT) indicates actual applied loads

$$P_{CYL (ACT)} = P - P_{ELE (ACT)} \tag{15}$$

Solving equation (14) for $P_{ELE (ACT)}$,

$$P_{ELE (ACT)} = \frac{(P_{CYL (ACT)}) (SR_{ELE})}{SR} \tag{16}$$

71

Combining equations (8), (12), and (15) produces

$$P_{ELE} \text{ (ACT)} = \frac{P^2}{P_{CYL} + P} \qquad (17)$$

Tensile stresses in the section element are obtained from

$$f_{ELE} = \frac{P_{ELE} \text{ (ACT)}}{A} \qquad (18)$$

and secondary stresses are obtained from

$$f_{SEC} = P_{CYL} \text{ (ACT)} \quad SF \qquad (19)$$

Deflections are recalculated using the actual loads.

This entire calculation is further complicated by vibratory loading and changes in the A1 length as sections are cut progressively farther away from the in-plane axis of symmetry. Because of the need for repetitive calculations, a computer program is written to expedite these calculations and to allow for the iterations to determine wall thicknesses.

Figure 37 is a reproduction of the actual program entitled Crossed Cylinder Barrel Analysis (deck H999) to which the above analysis can be compared.

Figure 38 shows the cylinder intersection area of the 4-blade crossed tube barrel. From the barrel, a section is taken to describe the geometry that is used as input to the program deck H088 (Figure 39). A deflection (see the deflection parameters in Figure 39), using the centrifugal and steady bending loads only, is calculated by standard formulas. This deflection is also part of the H088 input and is broken down into two parts:

1. The deflection caused by the centrifugal load (the zero Fourier harmonic), and

2. The deflection caused by the steady bending moment (the second Fourier harmonic). H088 is then used to calculate the load necessary to produce this deflection. This is the load P which is used to determine the spring rate of the barrel arm.

72

```
•  XQT CUR
   INF HSSUBS
•IP FOR H999
C                          CROSSED CYLINDER BARREL ANALYSIS
C
C                                  INPUT DATA
C
C LOC       SYMBOL      DESCRIPTION                                    DIMENSION
C
C   1           R       MEAN RADIUS OF BARREL ARM CYLINDER                 IN
C   2           T       CYLINDER WALL THICKNESS                            IN
C   3           E       MODULUS OF ELASTICITY                             PSI
C   4          CF       CENTRIFUGAL LOAD                                   LB
C   5        SBMINP     STEADY BENDING MOMENT IN PLANE                  IN LB
C   6        SBMOOP     STEADY BENDING MOMENT OUT OF PLANE              IN LB
C   7        VBM1IP     1P VIBRATORY BENDING MOMENT IN PLANE            IN LB
C   8        VBM1OP     1P VIBRATORY BENDING MOMENT OUT OF PLANE        IN LB
C   9        VBM2IP     2P VIBRATORY BENDING MOMENT IN PLANE            IN LB
C  10        VBM2OP     2P VIBRATORY BENDING MOMENT OUT OF PLANE        IN LB
C  11         DEFL      MAX DEFLECTION OF CYLINDER AT THE PEAK LOAD
C                       FROM HO 88                                         IN
C  12        QLOAD      TOTAL Q LOAD FROM FIRST AND SECOND HARMONIC
C                       OF HO 88                                       LB/IN
C  13      SPHI/BOT     TOTAL BOTTOM FIBER MERID BENDING STRESS  HO 88    PSI
C  14      SPHI/TOP     TOTAL TOP FIBER MERID BENDING STRESS HO 88        PSI
C  15      STHET/BOT    TOTAL BOTTOM FIBER HOOP STRESS  HO 88             PSI
C  16      STHET/TOP    TOTAL TOP FIBER HOOP STRESS  HO 88                PSI
C  17      SFITH/BOT    TOTAL BOTTOM FIBER SHEAR STRESS HO 88             PSI
C  18      SFITH/TOP    TOTAL TOP FIBER SHEAR STRESS  HO 88               PSI
C  19
C      FOR A TRACTOR PROP IN FORWARD FLIGHT SBM.1P VBM.2P VBM ARE POSITIVE
C      WITH RESPECT TO THE FRONT RING
C      2P STRESSES AND DEFLECTIONS ARE CALCULATED WHEN A VALUE OF 2P IS
C      IN LOCATION 10
C
C      A NEGATIVE STRESS DENOTES COMPRESSION -ITEMS 11THRU 18 ARE TAKEN
C      FROM HO 88 OUTPUT
C
C                                 OUTPUT DATA
C                                STRESS SECTION
C LOC        SYMBOL      DESCRIPTION                                    DIMENSION
C           STATION     LOCATION OF STRESSES                              NONE
C             CF        STRESS DUE TO CENTRIFUGAL LOAD                     PSI
C           SBMINP      STRESS DUE TO SBM IN PLANE                         PSI
C           SBMOOP      STRESS DUE TO SBM OUT OF PLANE                     PSI
C           1P INP      STRESS DUE TO 1P VBM IN PLANE                      PSI
C           1P OOP      STRESS DUE TO 1P VBM OUT OF PLANE                  PSI
C           2P INP      STRESS DUE TO 2P VBM IN PLANE                      PSI
C           2P OOP      STRESS DUE TO 2P VBM OUT OF PLANE                  PSI
C      STEADY TOTAL     SUM OF CF + SBMINP + SBMOOP STRESSES              PSI
C      1P VBM TOTAL     SUM OF 1P VBM STRESSES                            PSI
C
C                               DEFLECTION SECTION
C
C           STATION     LOCATION OF DEFLECTIONS
C             CF        DEFLECTION DUE TO CENTRIFUGAL LOAD                 IN
C           SBMINP      DEFLECTION DUE TO SBM IN PLANE                     IN
C           SBMOOP      DEFLECTION DUE TO SBM OUT OF PLANE                 IN
C           1P INP      DEFLECTION DUE TO 1P VBM IN PLANE                  IN
```

Figure 37.   USAAVLABS Barrel Stress Analysis.

73

```
C          IP OOP      DEFLECTION DUE TO IP VBM OUT OF PLANE              IN
C          2P INP      DEFLECTION DUE TO 2P VBM IN PLANE                  IN
C          2P OOP      DEFLECTION DUE TO 2P VBM OUT OF PLANE              IN
C          TOTAL       SUM OF ALL DEFLECTIONS SHOWN                       IN
      DIMENSION DATA(20),PELIP(46),PELOP(46),PELII(46),PELIO(46),PEL2I
     2(46),PEL2O(46),STSIP(46),STSOP(46),STSII(46),STSIO(46),STS2I(46),
     3STS2O(46),DEL1(46),DEL2(46),DEL3(46),DEL4(46),DEL6(46),DEL7(46),
     4DELT(46),STST(46),STVT(46),CFSTB(46),CFSTT(46),SBMIB(46),
     5SBMOB(46),SBMOT(46),SBMIT(46),VB1IB(46),VB1IT(46),VB1OB(46)
      DIMENSION VB1OT(46),VB2IB(46),VB2IT(46),VB2OB(46),VB2OT(46),
     2SUMSB(46),SUMST(46),SUMVB(46),SUMVT(46),DELS(46)
      EQUIVALENCE (DATA(1),R),(DATA(2),T),(DATA(3),E),(DATA(4),CF),
     2(DATA(5),SMINP),(DATA(6),SMOOP),(DATA(7),VM1IP),(DATA(8),VM1OP),
     3(DATA(9),VM2IP),(DATA(10),VM2OP),(DATA(11),DEFL),(DATA(12),QLOAD)
     4,(DATA(13),SPHIB),(DATA(14),SPHIT),(DATA(15),STHEB),(DATA(16),STH
     5ET),(DATA(17),SFITB),(DATA(18),SFITT)
      IO=6
    1 CALL START
      CALL LOAD(DATA)
      WRITE (IO,2)
    2 FORMAT(//40X,40H CROSSED CYLINDER BARREL ANALYSIS            //
     250X,17H INPUT DATA        /)
      WRITE (IO,3)R,T,DEFL,QLOAD,E,CF,SMINP,SMOOP,VM1IP,VM1OP,VM2IP,
     2VM2OP,SPHIB,SPHIT
    3 FORMAT(10X,3HR =E12.6,6H   T =E12.6,9H   DEFL =E12.6,11H   QLOAD =
     2 E12.6,6H   E =E12.6//10X,4HCF =E12.6,11H   SBMINP =E12.6,12H   S
     3BMOOP =E12.6,11H   IP INP =E12.6,11H   IP OOP =E12.6//10X,9H 2P IN
     4P =E12.6,11H   2P OOP =E12.6,13H   SPHI/BOT =E12.6,13H   SPHI/TOP
     5=E12.6.//)
      WRITE(IO,16)STHEB,STHET,SFITB,SFITT
   16 FORMAT(10X,11HSTHET/BOT =E12.6,14H   STHET/TOP =E12.6,14H   SFITH/
     2BOT =E12.6,14H   SFITH/TOP =E12.6//45X,16H STRESS SECTION //45X,1
     36H  OUTSIDE FIBER     )
      WRITE (IO,4)
    4 FORMAT(6X,4H STA,5X,3H CF,7X,7H SBMINP,5X,7H SBMOOP,5X,7H IP INP,
     25X,7H IP OOP,5X,7H 2P INP,5X,7H 2P OOP  //)
      Q=2.0*QLOAD*2.0*3.14159*R/90.0
      SPR=Q/DEFL
      PCON=CF/90.0
      AREA=2.0*R*T*3.141592/90.0
      CA=Q/PCON
      PELCO=PCON/(CA+1)
      J=1
      DO 8 I=4,92,4
      AI=(I-4)
      THET=AI/57.29579
      PELIP(J)=2.0*SMINP*COS(THET)/(R*(CA+1)*90.0)
      PELOP(J)=2.0*SMOOP*SIN(THET)/(R*(CA+1)*90.0)
      PELII(J)=2.0*VM1IP*COS(THET)/(R*(CA+1)*90.0)
      PELIO(J)=2.0*VM1OP*SIN(THET)/(R*(CA+1)*90.0)
      PEL2I(J)=2.0*VM2IP*COS(THET)/(R*(CA+1)*90.0)
      PEL2O(J)=2.0*VM2OP*SIN(THET)/(R*(CA+1)*90.0)
      STSIP(J)=PELIP(J)/AREA
      STSOP(J)=PELOP(J)/AREA
      STSII(J)=PELII(J)/AREA
      STSIO(J)=PELIO(J)/AREA
      STS2I(J)=PEL2I(J)/AREA
      STS2O(J)=PEL2O(J)/AREA
      DEL1(J)=(PELCO*R*COS(THET))/(E*AREA)
      DEL2(J)=(PELIP(J)*R*COS(THET))/(E*AREA)
```

Figure 37. USAAVLABS Barrel Stress Analysis (Continued).

```
          DEL3(J)=(PELOP(J)*R*COS(THET))/(E*AREA)
          DEL4(J)=(PEL11(J)*R*COS(THET))/(E*AREA)
          DEL5(J)=(PEL10(J)*R*COS(THET))/(E*AREA)
          DEL6(J)=(PEL21(J)*R*COS(THET))/(E*AREA)
          DEL7(J)=(PEL20(J)*R*COS(THET))/(E*AREA)
          J=J+1
       8 CONTINUE
          STSCO=PELCO/AREA
          DO 9   J=1,23
          L=24-J
          K=23+J
          DEL1(K)=DEL1(L)
          DEL2(K)=-DEL2(L)
          DEL3(K)=DEL3(L)
          DEL4(K)=-DEL4(L)
          DEL5(K)=DEL5(L)
          DEL6(K)=-DEL6(L)
          DEL7(K)=DEL7(L)
          STSIP(K)=-STSIP(L)
          STSOP(K)=STSOP(L)
          STS11(K)=-STS11(L)
          STS10(K)=STS10(L)
          STS21(K)=-STS21(L)
          STS20(K)=STS20(L)
       9 CONTINUE
C         DELT=SUM OF ALL THE DEFLECTIONS SHOWN
C         STST=TOTAL STEADY LOAD AXIAL STRESS
C         STVT=TOTAL IP VIBRATORY LOAD AXIAL STRESS
          DO 10   J=1,46
          DELT(J)=DEL1(J)+DEL2(J)+DEL3(J)+DEL4(J)+DEL5(J)+DEL6(J)+DEL7(J)
          STST(J)=STSCO+STSIP(J)+STSOP(J)
          STVT(J)=STS11(J)+STS10(J)
      10 CONTINUE
C         THE FOLLOWING SBS NUMBERS ARE CONSTANT -STRESS / INCH DEFLECTION
          SBSA=SPHIB/DEFL
          SBSB=SPHIT/DEFL
          SBSC=STHEB/DEFL
          SBSD=STHET/DEFL
          SBSE=SFITB/DEFL
          SBSG=SFITT/DEFL
C         STRESSES DUE TO STEADY LOADS
          DO 11   J=1,46
          CFSTB(J)=STSCO+SBSA*(DEL1(J))
          CFSTT(J)=STSCO+SBSB*(DEL1(J))
          SBMIB(J)=STSIP(J)+SBSA*(DEL2(J))
          SBMIT(J)=STSIP(J)+SBSB*(DEL2(J))
          SBMOB(J)=STSOP(J)+SBSA*(DEL3(J))
          SBMOT(J)=STSOP(J)+SBSB*(DEL3(J))
C         STRESS DUE TO VIBRATORY LOADS
          VB11B(J)=STS11(J)+SBSA*(DEL4(J))
          VB11T(J)=STS11(J)+SBSB*(DEL4(J))
          VB10B(J)=STS10(J)+SBSA*(DEL5(J))
          VB10T(J)=STS10(J)+SBSB*(DEL5(J))
          VB21B(J)=STS21(J)+SBSA*(DEL6(J))
          VB21T(J)=STS21(J)+SBSB*(DEL6(J))
          VB20B(J)=STS20(J)+SBSA*(DEL7(J))
          VB20T(J)=STS20(J)+SBSB*(DEL7(J))
          SUMSB(J)=CFSTB(J)+SBMIB(J)+SBMOB(J)
          SUMST(J)=CFSTT(J)+SBMIT(J)+SBMOT(J)
          SUMVB(J)=VB11B(J)+VB10B(J)
```

Figure 37. USAAVLABS Barrel Stress Analysis (Continued).

75

```
      SUMVT(J)=VB11T(J)+VB1OT(J)
   11 CONTINUE
      WRITE(IO,5)(J,CFSTT(J),SBMIT(J),SBMOT(J),VB11T(J),VB1OT(J),VB21
     2T(J),VB2OT(J), J=1,45)
    5 FORMAT(5X,I5,7F12.2)
      WRITE(IO,6)
    6 FORMAT(///,44X,15H INSIDE FIBER  //)
      WRITE (IO,4)
      WRITE(IO,7)(J,CFSTB(J),SBMIB(J),SBMOB(J),VB11B(J),VB1OB(J),
     2VB21B(J),VB2OB(J),J=1,45)
    7 FORMAT(5X,I5,7F12.2)
      WRITE(IO,12)
   12 FORMAT(///44X,20HDEFLECTION SECTION  //)
      WRITE (IO,4)
      WRITE(IO,13)(J,DEL1(J),DEL2(J),DEL3(J),DEL4(J),DEL5(J),DEL6(J),
     2DEL7(J),J=1,45)
   13 FORMAT(5X,I5,7F12.9)
      WRITE(IO,14)
   14 FORMAT(///41X,35H TOTAL DEFLECTIONS AND STRESSES     //92H
     2 STA    STEADY STS/OUT    VBM STS/OUT     STEADY STS/IN    VBM STS/IN
     3      DEFLECT TOT    //)
      WRITE(IO,15)(J,SUMST(J),SUMVT(J),SUMSB(J),SUMVB(J),DELT(J),J=1,45
     2)
   15 FORMAT(5X15,5F15.5)
      GO TO 1
      END
'N XQT H999
```

Figure 37.   USAAVLABS Barrel Stress Analysis (Continued)
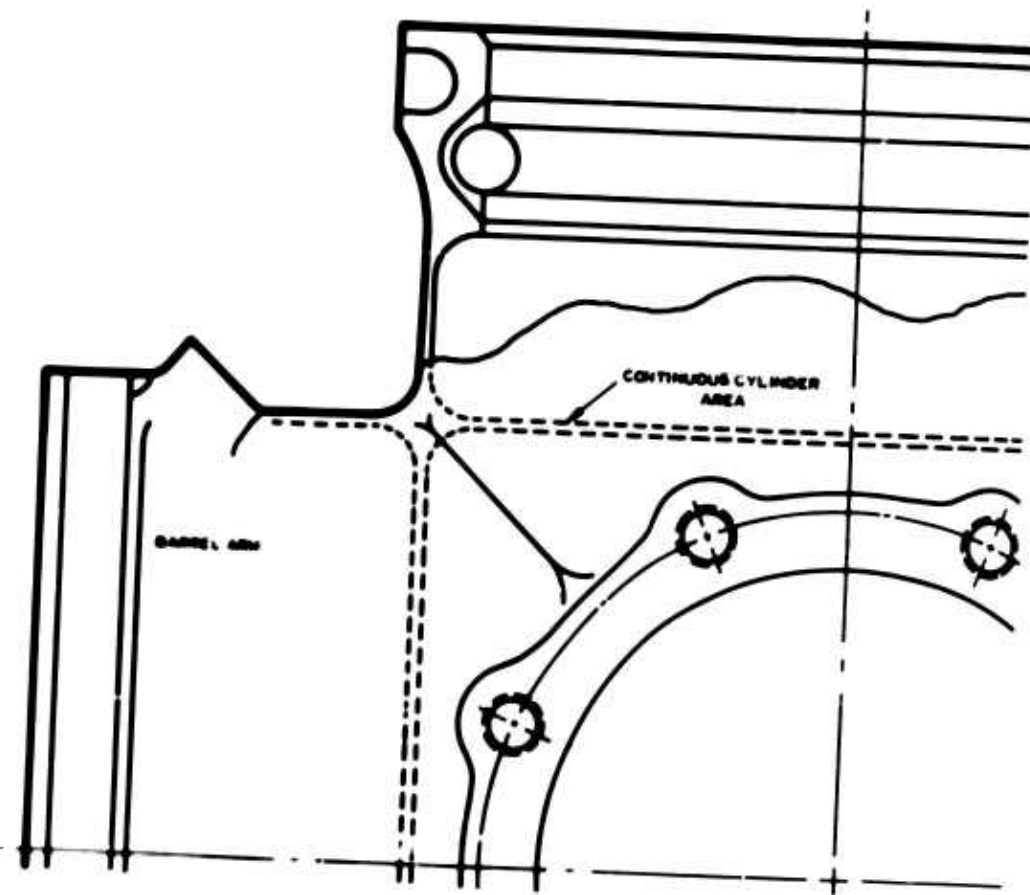
Figure 38. Cylinder Intersection.

77
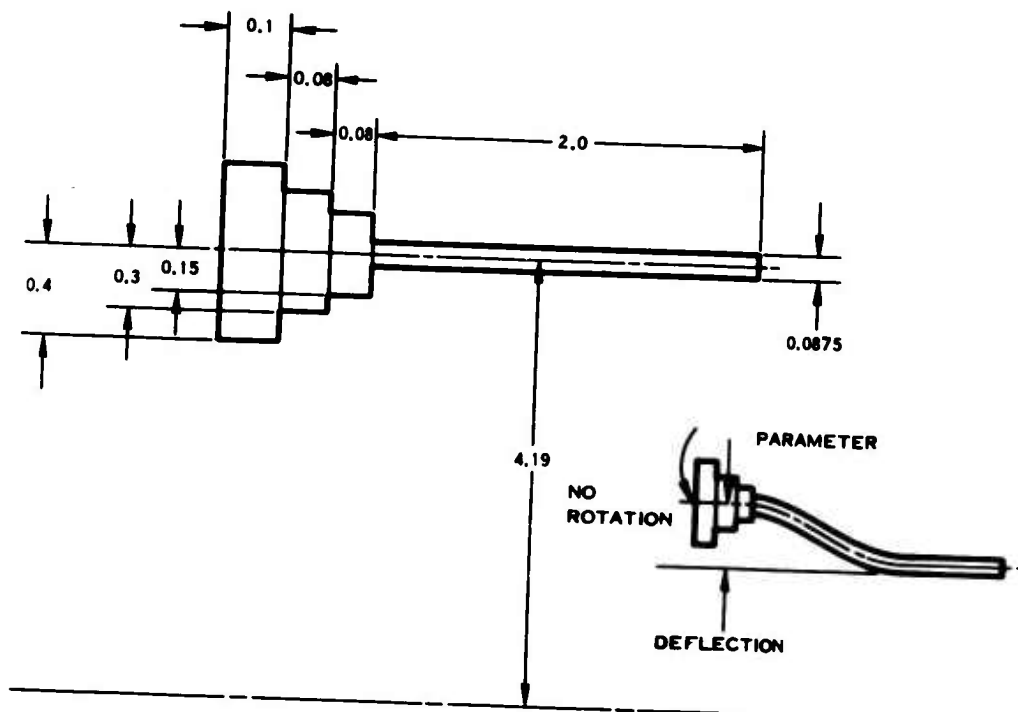
Figure 39. Analytical Model of Fillets.

From the computer run, the following information is collected and a summation is made:

HARMONIC	0	2	SUM
LOAD P	-148.	-285.	-433.
SPHI/BOT	-420.	-842.	-1262.
SPHI/TOP	420.	643.	1063.
STHET/BOT	2198.	2587.	4785.
STHET/TOP	2453.	666.	666.
SFITH/BOT	0	-629.	-629.
SFITH/TOP	0	-764.	-764.

Along with these data, the loads are collected and are used as the input for the crossed tube barrel program. The loads used in the actual program run are identical to those given for run H153. The maximum stress calculated is

$$f_b = 17,324 \pm 17,413 \text{ psi} \tag{20}$$

This stress meets the stress limitation required.

The Front and Rear Ring Analysis by Conventional Analytical Approach

Neglecting the material that comprises the continuous cylinder center-body area (investigated in Item 1), the barrel is assumed to have a configuration similar to the spherical barrel. This permits application of the standard barrel program deck H153, which will be used to size the front and rear rings.

The total loads introduced are as follows:

CF	=	45,000 lb
SBINP	=	12,720 in.-lb
SBOOP	=	13,780 in.-lb
1PINP	=	73,400 in.-lb
1POOP	=	87,500 in.-lb
2PINP	=	10,000 in.-lb
2POOP	=	10,000 in.-lb

These total loads are used along with the geometrical sections cut to produce the maximum stress and deflections. The actual run produced a maximum stress of

79

$$f_b = 7,130 \pm 8,250 \text{ psi} \tag{21}$$

on the 100-deg section, and the maximum deflection of

$$\delta = 0.5785 \text{ in.} \tag{22}$$

occurred at the 50-deg section.

Combination of Parts 1 and 2

In order to relate the calculations made in parts 1 and 2, it becomes necessary to divide the loads applied to the barrel arms into some proportion between the continuous cylinder centerbody area and the front and rear rings. To facilitate finding this proportion, the deflections of the center area must match with those of the front and rear ring at some common point. This common point is determined from inspection of the crossed tube barrel geometry.

If a point is rotated from the in-plane axis of symmetry toward the front of the barrel, at an area between 40 and 45 deg, the continuous cylinder configuration begins to diminish, and the front ring interface area originates. At this location, then, the effect of loads on the front ring and on the continuous cylinder should produce equal deflections. Study of the loads applied versus deflection in the H999 run of part 1 reveals that two-thirds of the deflections caused in the cylinder are caused by centrifugal load; therefore, the centrifugal load is varied proportionately between the cylinder and ring analysis. The in-plane and out-of-plane moment loading is not quite as effective, and a ratio of 60 to 40% will be arbitrarily used to spread the total loading between the two analyses; i.e., 60% of all in-plane moments are effective on the continuous cylinder centerbody and 40% on the front and rear rings, while 40% of all out-of-plane moments are effective on the continuous cylinder centerbody and 60% on the front and rear rings.

The centrifugal load is divided into 10% increments between programs H999 and H153 so that the sum of the two loads equals the total centrifugal load, i.e., 10% to H153 and 90% to H999, etc.

From the computer runs made, the deflections at 45 deg are plotted versus the load percentage combination for both of the programs (Figure 40). Their common point is determined to be approximately 52% to the front and rear ring and 48% to the centerbody. Stresses and deflections can be used from the 50-50% load share printouts with only slight error.

80
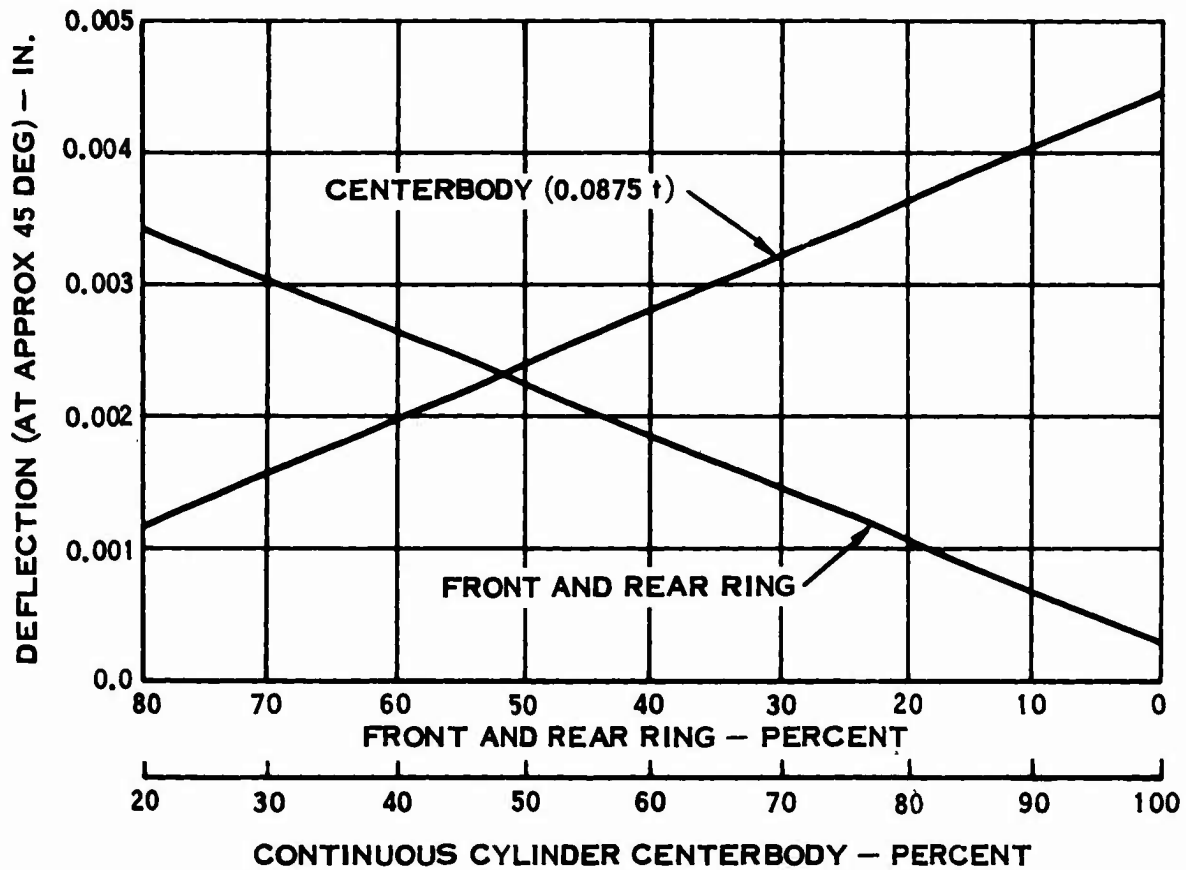
Figure 40. CF Distribution Versus Deflections.

The maximum stresses for the front and rear rings are negligible. However, the centerbody stresses are printed for the inside edge of the barrel arm cylinder (Figure 41), which is not the point of maximum stress. This maximum stress occurs at the end of the cylinder blend fillet where the cylinder thickness becomes constant (Figure 41).

To determine this stress, a relationship of the deflections and stresses from the H088 run to the stress given in H999 for the end of the barrel arm is necessary. This relationship is as follows:

The deflection at the barrel arm edge from H088 is

$$\delta_{E88} = 0.001745 \text{ in.} \tag{23}$$

The deflection at the fillet end from H088 is

$$\delta_{F88} = 0.001733 \text{ in.} \tag{24}$$

81

The ratio of these deflections is

$$\frac{\delta \text{ E88}}{\delta \text{ F88}} = 1.006 \text{ in./in.} \tag{25}$$

The steady load deflection from H999 at the barrel arm edge is

$$\delta \text{ SE99} = 0.00108 + 0.00015 + 0.000067 = 0.0013 \text{ in.} \tag{26}$$

The vibratory load deflection from H999 at the barrel arm edge is

$$\delta \text{ VE99} = 0.000853 + 0.000424 + 0.000116 + 0.0000485 = 0.00143 \text{ in.} \tag{27}$$

The deflections at the fillet end can then be found from

$$\frac{\delta \text{ VE99}}{1.006} = \delta \text{ SF99} \tag{28}$$

$$\frac{\delta \text{ VE99}}{1.006} = \delta \text{ VF99} \tag{29}$$
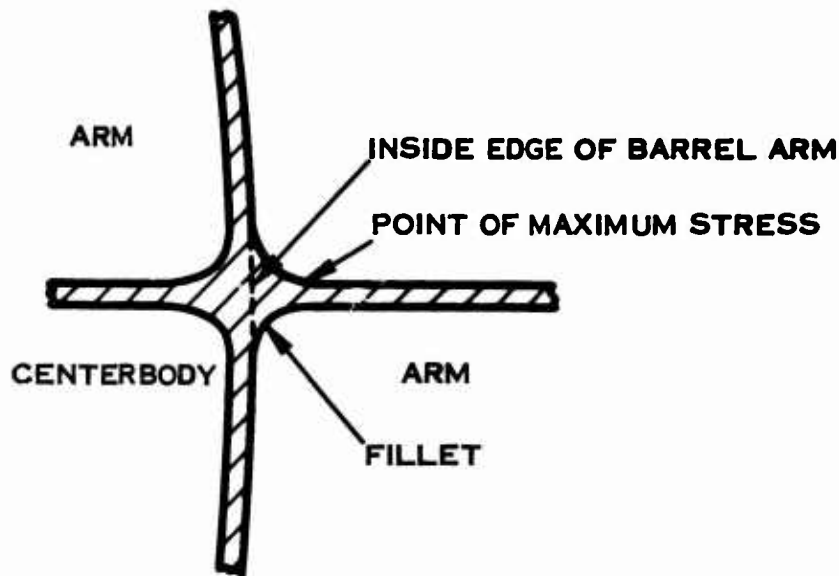
Figure 41. Barrel Arm Fillets.

82

$$\delta_{SF99} = 0.001292 \text{ in.} \tag{30}$$

$$\delta_{VF99} = 0.00142 \text{ in.} \tag{31}$$

The bending stress at the fillet end from H088 is

$$f_{F88} = 10,210 \text{ psi} \tag{32}$$

It is now possible to determine a factor of stress per in. of deflection at the fillet end.

$$SF = \frac{10,210}{0.001733} = 5.9 \times 10^6 \text{ psi/in.} \tag{33}$$

The stress at the fillet end is then determined from

$$f_F = (\delta_{SF99} \pm \delta_{VF99}) (SF) \tag{34}$$

$$f_F = 7,640 \pm 8,390 \text{ psi} \tag{35}$$

Stress concentration factor (Reference 7)

$$K_t = 1.0$$

$$f_F = 7,640 \pm 9,220 \text{ psi} \tag{36}$$

This maximum stress provides an ample margin of safety.

The maximum radial deflection of the barrel arm race is approximated by an observation that, in addition to the centerbody deflection, there exists an elongation of the barrel arm. Calculations of the formula

$$e = \frac{PL}{EA} \tag{37}$$

show the effect of this elongation on the total radial deflection to be 30%. The total radial deflection is then given by

83

$$\delta_{rad} = (\delta_{VE99} + \delta_{SE99})\ (1.3)$$

$$\delta_{rad} = 0.00355 \text{ in. (average)} \tag{38}$$

Neither the deflection limitation nor the stress limitation has been met by these calculations. However, the wall thickness of 0.0875 in. is a definite manufacturing limitation.

If there were no manufacturing limitations, the centerbody walls could, theoretically, be made thinner, thereby optimizing the use of the walls and reducing the weight of the barrel. This theoretical thickness is determined by plotting the data available in deflection versus load share and the maximum radial deflection versus thickness curves, then extrapolating a possible range in which a deflection match could be maintained at 45 deg. Along with maintaining this range, the maximum deflection is held to 0.007-0.008 in. The range of possible thicknesses is found to be from 0.0475 to 0.0425 in. For the theoretical weight calculation, the mean thickness of 0.045 in. is used.

It should be noted that, although this thickness is theoretical for the barrel configuration designed, a proportion of thickness for a larger barrel design could meet any manufacturing limitations if provided with the same proportionate reduction on the total barrel weight.

ANALYSIS OF 3-BLADE BARRELS

Another requirement of this program was to design a 3-blade barrel and to compare it for structure and fabricability with the 4-blade designs. To make a meaningful comparison, it was necessary to analyze all three of the basic concepts to ascertain which concept was the best design and then to base the comparison on the optimum barrel from each category.

The following text summarizes the structural analysis of the three barrels designed.

Retention Analysis

The basis for the analysis for the 3-blade retention is identical to that of the 4-blade retention. The increased loadings necessitated that the pitch diameter be increased to 9.003 in. Table X summarizes the race geometry for these barrels and the maximum Hertz stress for each loading condition.

Barrel Arm Analysis

The method of analysis for the 3-blade barrel arm is identical to that of the 4-blade barrel arm. The increased blade loads resulted in enlarging the retention pitch diameter, thereby changing the barrel arm geometry.

Figure 42 describes the elements into which the arm has been sectioned. Table XI gives the stress summary for the 3-blade barrel arm analysis.

TABLE X. BLADE RETENTION, 3-BLADE BAhRELS

Pitch Diameter	9.003 in.
Ball Diameter	0.625 ± 0.000025 in.
No. of Balls	45
Ball Matching Radius Outer Race	0.3315 ± 0.003 in.
Ball Matching Radius Inner Race	0.3257 ± 0.0008 in.
Major Diameter Outer Race	9.6295 ± 0.0007 in.
Minor Diameter Inner Race	8.3761 ± 0.0006 in.
Major Diameter Inner Race	9.010 ± 0.001 in.
Minor Diameter Outer Race	9.017 ± 0.001 in.

Case I
    Max Hertz Stress   576,660 psi
    Min Distance From Ellipse Edge Relative to Race Edge, 0.033 in.

Case II
    Max Hertz Stress   599,620 psi
    Min Distance From Ellipse Edge Relative to Race Edge, 0.0178 in.

SHELL BARREL ARM
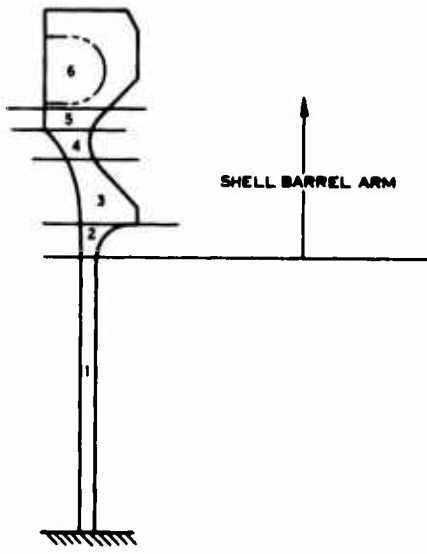
Figure 42. 3-Blade Barrel Arm Section.

TABLE XI. BARREL ARM STRESS SUMMARY, 3-BLADE BARREL

Section	1	2	3	4	5	6
Case I Stress (psi)						
Axial	23,831 ±10,821	22,563 ±10,306	20,075 ±8,413	20,075 ±8,413	6,940 ±3,050	11,155 ±4,947
Hoop	7,149 ± 3,246	6,390 ± 2,619	3,813 ±1,569	7,302 ±2,551	8,326 ±3,317	11,219 ±4,206
Shear	142 ± 265	288 ± 535	346 ± 643	630 ±1,16°	673 ±1,249	797 ±1,450
Case II Stress (psi)						
Axial	19,865 ±18,068	19,865 ±18,068	17,873 ±14,749	17,873 ±14,749	6,142 ±5,347	9,860 ±8,672
Hoop	6,299 ± 5,691	10,279 ± 8,562	3,402 ± 2,751	4,230 ± 4,473	7,458 ±5,816	6,201 ±4,866
Shear	733 ± 464	148 ± 938	178 ± 1,127	324 ± 2,050	346 ±2,190	409 ±2,596

Spherical Barrel

The centerbody of the spherical barrel is generated by taking the three blade-retaining rings and attaching them to short cylinders. A sphere is used to attach the blade-retaining cylinders to the front ring, and a cone is used to blend the sphere into the rear ring (Figure 43).
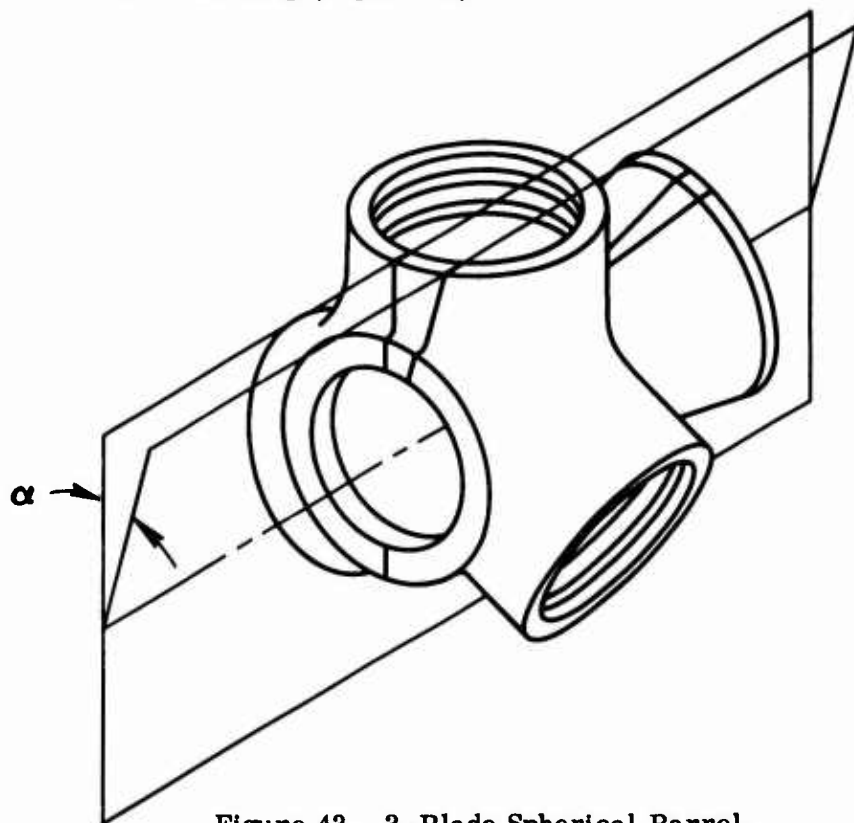
Figure 43. 3-Blade Spherical Barrel.

Each ring, for the 3-blade barrel, is radially symmetrical about 60-deg segments. Each segment is sectioned every 10 deg, as shown in Figures 44 and 45.

The method of analysis for a 3-blade and a 4-blade barrel is identical from this point on, and all comments made for the 3-blade spherical barrel apply to the 4-blade spherical barrel.

The stresses and deflections are summarized in Tables XII and XIII for each 10-deg section. The stress distribution is repeated for each 120 deg.
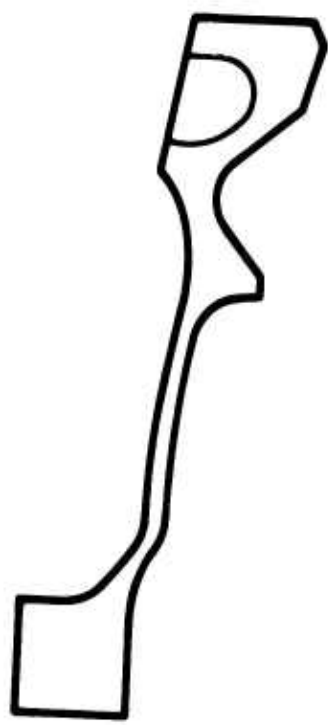
Figure 44. 3-Blade Spherical Barrel 20° Forward Section.
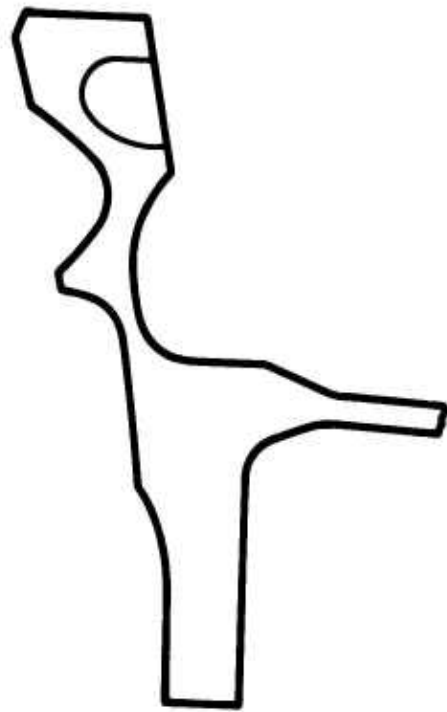
Figure 45. 3-Blade Spherical Barrel 20° Aft Section.

89

TABLE XII. RING ANALYSIS, 3-BLADE SPHERICAL BARREL

Case I		Front Ring	
Section Position	Outer Surface Stress (psi)	Deflection (in.)	Inner Surface Stress (psi)
0	4,523 ± 2,585	0.0044	3,285 ± 3,616
10	4,468 ± 1,961	0.00441	2,796 ± 4,443
20	4,121 ± 1.247	0.00444	2,434 ± 4,822
30	4,098 ± 923	0.00446	2,761 ± 5,357
40	6,793 ± 686	0.00446	5,063 ± 7,553
50	7,517 ± 2,032	0.00445	9,840 ± 7,332
60	6,489 ± 2,995	0.00447	11,267 ± 6,347
70	6,527 ± 4,340	0.0045	10,943 ± 4,925
80	6,373 ± 3,659	0.00455	7,801 ± 3,759
90	4,024 ± 2,118	0.00457	4,833 ± 2,742
100	3,980 ± 2,397	0.00455	4,078 ± 2,748
110	4,339 ± 2,713	0.0045	3,768 ± 3,122

Case I		Rear Ring	
Section Position	Outer Surface Stress (psi)	Deflection (in.)	Inner Surface Stress (psi)
0	6,339 ± 2,934	0.0052	1,859 ± 5,360
10	5,991 ± 2,199	0.0052	2,888 ± 5,851
20	5,101 ± 1,261	0.0052	3,953 ± 5,849
30	4,803 ± 547	0.0053	5,660 ± 5,975
40	7,827 ± 1,200	0.0052	11,245 ± 8,677
50	5,835 ± 2,475	0.0052	16,301 ± 9,931
60	5,521 ± 3,075	0.0052	17,239 ± 8,594
70	6,921 ± 4,258	0.0053	14,455 ± 7,001
80	9,417 ± 4,809	0.0053	8,407 ± 5,034
90	5,113 ± 2,320	0.0053	3,197 ± 3,811
100	5,455 ± 2,728	0.0053	1,830 ± 4,349
110	6,244 ± 3,104	0.0053	1,579 ± 4,950

TABLE XIII. RING ANALYSIS, 3-BLADE SPHERICAL BARREL

Case II	Front Ring		
Section Position	Outer Surface Stress (psi)	Deflection (in.)	Inner Surface Stress (psi)
0	5,022 ± 4,529	0.00546	3,404 ± 6,250
10	4,911 ± 3,448	0.00547	3,180 ± 7,695
20	4,503 ± 2,203	0.0055	3,069 ± 8,369
30	4,476 ± 1,632	0.00555	3,656 ± 9,306
40	7,275 ± 1,199	0.00556	6,503 ± 13,143
50	7,746 ± 3,458	0.00556	11,141 ± 12,803
60	6,912 ± 5,151	0.00559	12,375 ± 11,119
70	7,237 ± 7,503	0.00565	11,707 ± 8,660
80	7,060 ± 6,353	0.00571	7,910 ± 6,585
90	4,438 ± 3,690	0.00574	4,720 ± 4,773
100	4,430 ± 4,182	0.00571	3,914 ± 4,763
110	4,845 ± 4,742	0.00565	3,679 ± 5,395

Case II	Rear Ring		
Section Position	Outer Surface Stress (psi)	Deflection (in.)	Inner Surface Stress (psi)
0	5,840 ± 5,135	0.0056	1,929 ± 9,293
10	5,582 ± 3,863	0.0056	2,580 ± 10,148
20	4,800 ± 2,229	0.0056	3,309 ± 10,152
30	4,537 ± 988	0.0057	4,732 ± 10,379
40	7,745 ± 2,020	0.0056	9,799 ± 15,102
50	5,800 ± 4,245	0.0056	14,703 ± 17,326
60	5,276 ± 5,298	0.0057	15,972 ± 15,039
70	6,359 ± 7,362	0.0057	13,753 ± 12,276
80	8,562 ± 8,333	0.0058	8,338 ± 8,804
90	4,697 ± 4,037	0.0058	3,466 ± 6,625
100	4,982 ± 4,755	0.0058	2,218 ± 7,547
110	5,712 ± 5,421	0.0057	1,907 ± 8,582

Shell Barrel

The centerbody of the shell barrel is generated by taking the 3-blade-retaining rings, the front ring, and the rear ring, and connecting them by a surface generated by a straight line.

The barrel is radially symmetrical about 60-deg segments. Each segment is sectioned every 10 deg, as shown in Figures 46 and 47.

As the method of analysis for a 3-blade and a 4-blade barrel is now identical, all comments made for the 4-blade shell barrel apply to the 3-blade shell barrel.

The shell barrel stress and deflection summary is contained in Tables XIV and XV.

Barrel Description 3-Blade Crossed Tube

The 3-blade crossed tube barrel can be described as follows: one cylinder is considered to be the base, and another cylinder is passed through the base at a 120-deg angle between cylinder center lines. A third cylinder is then passed through the intersection in the same plane as the first two cylinders. Each point around the cylinder wall is extended until it intersects one of the other cylinder walls. The final picture is outlined in Figure 48. The cylinder intersection peak requires a large length of barrel arm for proper clearance of the trunnion assembly, and this length is not compatible with the shell and spherical barrel designs. Therefore, a slight alteration in the crossed tube concept is unavoidable. This alteration amounts to replacing the cylinder intersection peak with a flat disc as shown in Figure 49.

3-Blade Crossed Tube Loads

The 3.5 g cruise maneuver condition is again used as the loading criterion for the 3-blade crossed tube design. The total load is applied to the 3-blade crossed tube in the same way that the total barrel load is applied to the 4-blade crossed tube design and, similarly, is used to determine the analytical approach. All of the loading distributions are proportional to those described in the 4-blade analysis, where the ratio of proportionality is the total 3-blade load to the total 4-blade load being described.

3-Blade Crossed Tube Analysis and Logic

The analytical approach is determined from the configuration of barrel arm loads and from the geometrical characteristics of the 3-blade crossed tube design. The configuration of the barrel arm loads is identical to that of the 4-blade analysis,
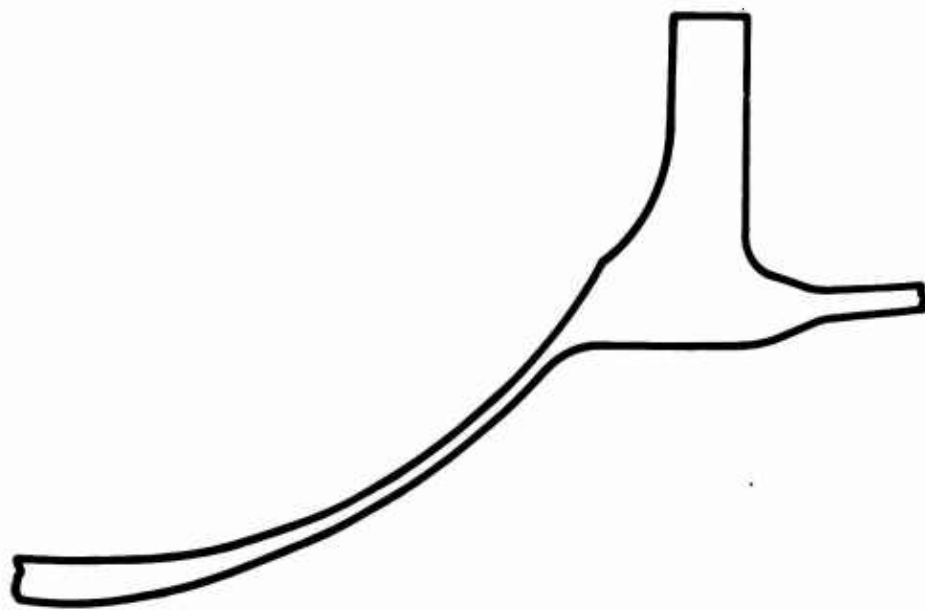
Figure 46. 3-Blade Crossed Tube Barrel 40° Aft Section.
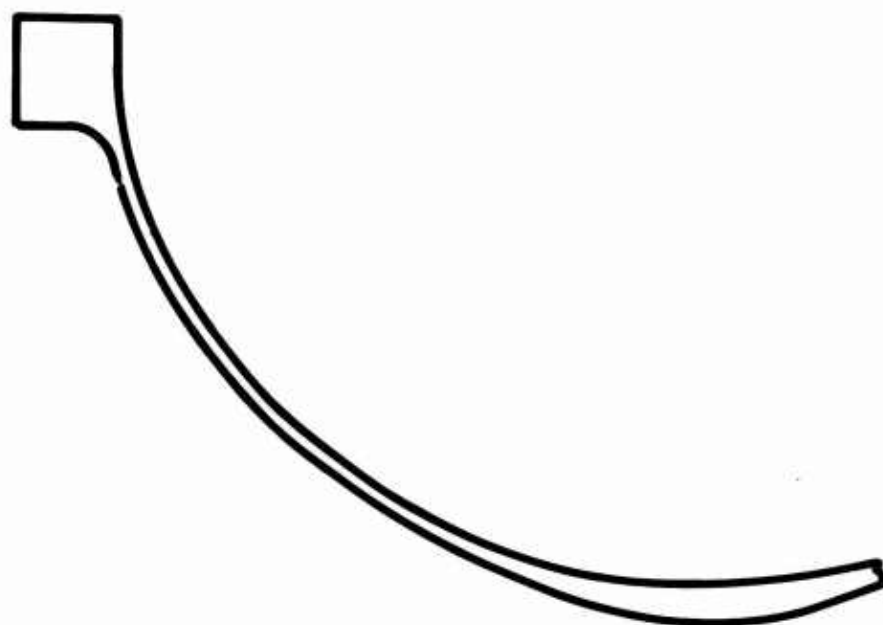
Figure 47. 3-Blade Crossed Tube Barrel 40° Forward Section.

93

TABLE XIV. RING ANALYSIS, 3-BLADE SHELL BARREL			

Case I		Front Ring	
	Outer Surface		Inner Surface
Section	Stress	Deflection	Stress
Position	(psi)	(in.)	(psi)
0	$4,218 \pm 2,445$	0.0043	$2,937 \pm 3,354$
10	$4,376 \pm 1,912$	0.0042	$2,719 \pm 4,108$
20	$4,346 \pm 1,328$	0.0043	$2,849 \pm 4,929$
30	$3,146 \pm 865$	0.0043	$2,329 \pm 4,689$
40	$6,589 \pm 772$	0.0043	$4,973 \pm 7,364$
50	$7,960 \pm 1,940$	0.0043	$10,342 \pm 7,217$
60	$6,984 \pm 2,979$	0.0043	$11,680 \pm 6,276$
70	$7,013 \pm 4,336$	0.0043	$11,357 \pm 4,862$
80	$6,224 \pm 3,463$	0.0044	$7,646 \pm 3,658$
90	$3,170 \pm 1,473$	0.0044	$4,159 \pm 2,454$
100	$4,243 \pm 2,401$	0.0044	$4,519 \pm 2,575$
110	$4,248 \pm 2,643$	0.0043	$3,626 \pm 2,824$

Case I		Rear Ring	
	Outer Surface		Inner Surface
Section	Stress	Deflection	Stress
Position	(psi)	(in.)	(psi)
0	$5,662 \pm 2,729$	0.0043	$1,802 \pm 4,405$
10	$5,411 \pm 2,061$	0.0043	$2,797 \pm 4,804$
20	$5,266 \pm 1,231$	0.0043	$4,635 \pm 5,334$
30	$3,857 \pm 561$	0.0043	$4,874 \pm 4,713$
40	$5,553 \pm 728$	0.0043	$8,311 \pm 7,564$
50	$5,980 \pm 2,336$	0.0043	$14,002 \pm 8,418$
60	$4,685 \pm 2,830$	0.0043	$14,793 \pm 7,282$
70	$5,982 \pm 3,874$	0.0043	$12,451 \pm 5,911$
80	$6,376 \pm 3,462$	0.0044	$5,315 \pm 4,734$
90	$3,966 \pm 1,555$	0.0044	$2,966 \pm 2,808$
100	$5,563 \pm 2,637$	0.0044	$2,745 \pm 3,494$
110	$5,662 \pm 2,906$	0.0043	$1,722 \pm 3,943$

TABLE XV. RING ANALYSIS, 3-BLADE SHELL BARREL

Case II	Front Ring		
	Outer Surface		Inner Surface
Section	Stress	Deflection	Stress
Position	(psi)	(in.)	(psi)
0	4,685 ± 4,283	0.0052	3,037 ± 5,798
10	4,808 ± 3,362	0.0053	3,091 ± 7,116
20	4,758 ± 2,344	0.0053	3,535 ± 8,552
30	3,459 ± 1,521	0.0054	3,110 ± 8,146
40	7,071 ± 1,352	0.0054	6,382 ± 12,813
50	8,245 ± 3,298	0.0054	11,649 ± 12,606
60	7,456 ± 5,124	0.0054	12,810 ± 10,996
70	7,758 ± 7,496	0.0054	12,170 ± 8,553
80	6,884 ± 6,014	0.0055	7,755 ± 6,410
90	3,472 ± 2,569	0.0055	4,050 ± 4,272
100	4,705 ± 4,190	0.0055	4,393 ± 4,459
110	4,742 ± 4,619	0.0054	3,557 ± 4,878

Case II	Rear Ring		
	Outer Surface		Inner Surface
Section	Stress	Deflection	Stress
Position	(psi)	(in.)	(psi)
0	5,212 ± 4,777	0.0046	1,842 ± 7,635
10	5,043 ± 3,620	0.0046	2,514 ± 8,330
20	4,944 ± 2,179	0.0046	3,984 ± 9,256
30	3,612 ± 996	0.0047	4,121 ± 8,188
40	5,392 ± 1,234	0.0047	6,984 ± 13,152
50	4,973 ± 4,012	0.0047	12,641 ± 14,688
60	4,485 ± 4,879	0.0047	13,709 ± 12,743
70	5,488 ± 6,699	0.0047	11,843 ± 10,365
80	5,815 ± 6,004	0.0048	5,444 ± 8,252
90	3,668 ± 2,708	0.0048	3,141 ± 4,883
100	5,096 ± 4,597	0.0048	3,012 ± 6,060
110	5,172 ± 5,074	0.0047	1,961 ± 6,833
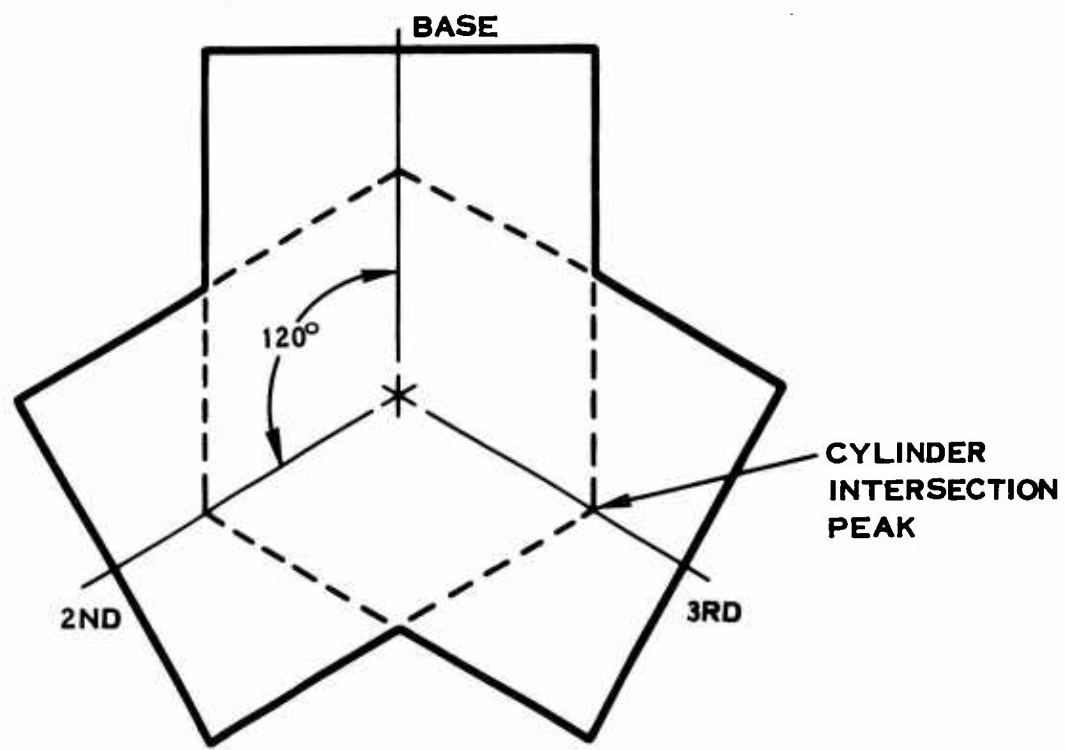
Figure 48. 3-Blade Crossed Tube Barrel Schematic, Intersecting Cylinders.
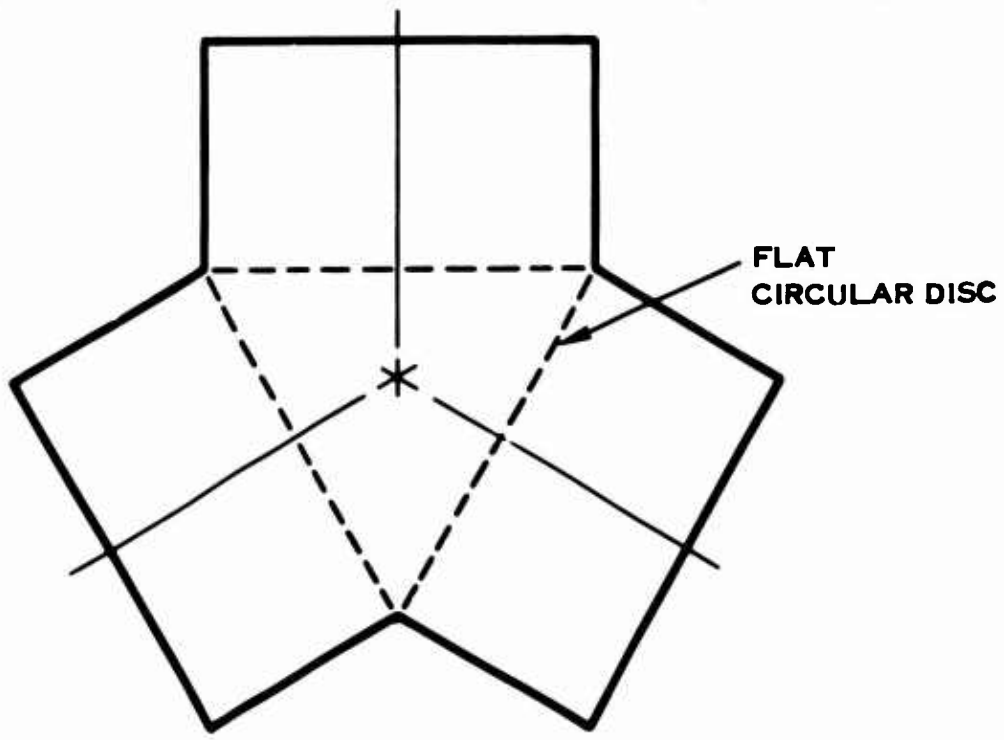
Figure 49. 3-Blade Crossed Tube Barrel Schematic With Flat Circular Disc.

96

where the magnitude of any one given load is found by:

3-blade load mag = (4-blade load) (3-blade total load)/(4-blade total load)

The analysis is approached in the same three steps as before:

1. The elemental analysis of the centerbody area neglecting the effects of the front and rear rings.

2. The analysis of the front and rear rings neglecting the centerbody.

3. The combination of 1 and 2 in a load share for a final result.

This analysis is not as involved as the 4-blade analysis, and assumptions for correlation to the 4-blade analysis are made for simplification.

These assumptions are:

1. The point of maximum load (i.e., the maximum loaded element) occurs at the same radial displacement as the 4-blade concept (roughly 34 deg from the in-plane axis of symmetry).

2. All of the sign conventions and directions established in the 4-blade analysis remain the same.

3. The load share between the front and rear rings and the centerbody is approximately the same order of magnitude as the 4-blade analysis.

4. Sections are cut in plane under the same specifications as in the 4-blade analysis.

The Element Analysis of the Centerbody

Figure 50 shows a typical in-plane element with a load applied. One-third of this element is considered to be in equilibrium, so the following equations from statics apply:

$$\Sigma F_x = 0 \text{ and } \Sigma F_y = 0 \tag{39}$$

$$P_1 \cos 30 + F_1 \cos 60 = P_2 \cos 30 + F_2 \cos 60 \tag{40}$$

$$P_1 \sin 30 + P_2 \sin 30 = F_1 \sin 60 + F_2 \sin 60 \tag{41}$$

97
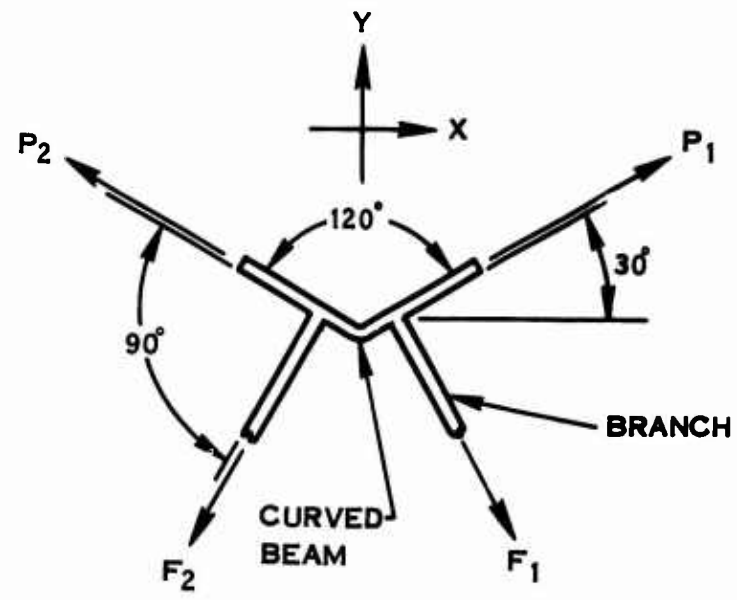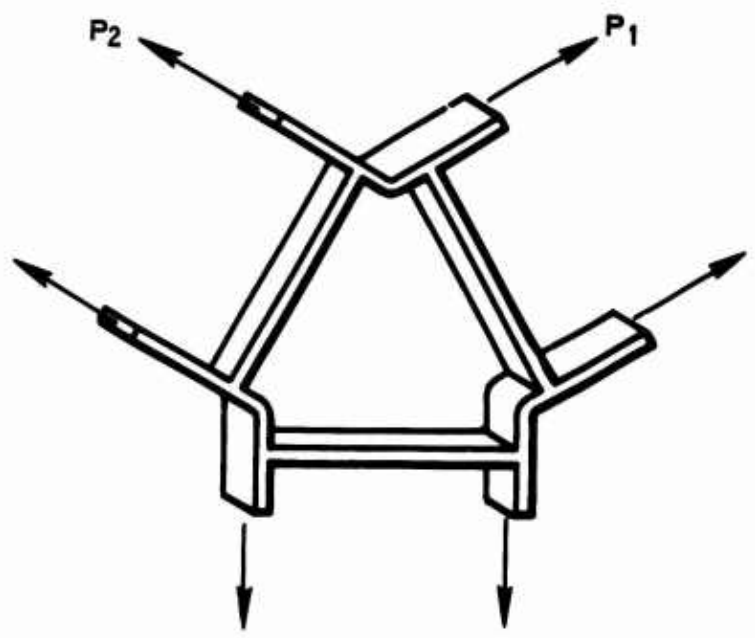
Figure 50. Typical In-Plane Element.

98

An investigation of the loading conditions for 1P and 2P vibratory in phase on one barrel arm gives the combinations of total loads represented by P_1 and P_2 in Figure 50. The investigation is identical to that of the 4-blade barrel, and the general case is shown in Figure 51. The magnitudes of these loads for any given element are calculated using the same equations given in the 4-blade barrel analysis and are a function of θ.

From assumption 1 of the 3-Blade Crossed Tube Barrel Analysis and Logic section, these loads are calculated for θ equal to 34 deg. Their values are as follows:

$$P\ (CF) = 690\ lb$$
$$P\ (SBMIP) = 64\ lb$$
$$P\ (SBMOP) = 46.6\ lb$$
$$P\ (1P1NP) = \pm\ 378\ lb$$
$$P\ (1\ POOP) = \pm\ 296\ lb$$

Summing these values according to the configuration established in Figure 51 produces the following calculations:

FRONT

When in-plane and out-of-plane 1P (CCW) moments are negative at barrel arm No. 1,

P_a = CF - SBM - 1P - SBMOP + 1POOP 690 - 64
    - 378 - 46.6 + 296   =   400 lb

P_b = CF + SBM - 1P/2 - SBMOP - 1POOP/2
    690 + 64 - 189 - 46.6 - 148   =   370 lb

P_c = CF - SBM + 1P/2 - SBMOOP - 1POOP/2
    690 - 64 + 189 - 46.6 - 148   =   620 lb

P_d = CF + SBM - 1P/2 - SPMOOP - 1POOP/2
    690 + 64 - 189 - 46.6 - 148   =   370 lb

P_e = CF - SBM + 1P/2 - SPMOOP - 1POOP/2
    690 - 64 + 189 - 46.6 - 148   =   620 lb

P_f = CF + SBM + 1P - SPMOOP + 1POOP
    690 + 64 + 378 - 46.6 + 296   =   1128 lb

OUT-OF-PLANE LOADING FRONT AND REAR
GENERAL CASE

FRONT OUT OF PLANE

REAR OUT OF PLANE

IN-PLANE FRONT AND REAR
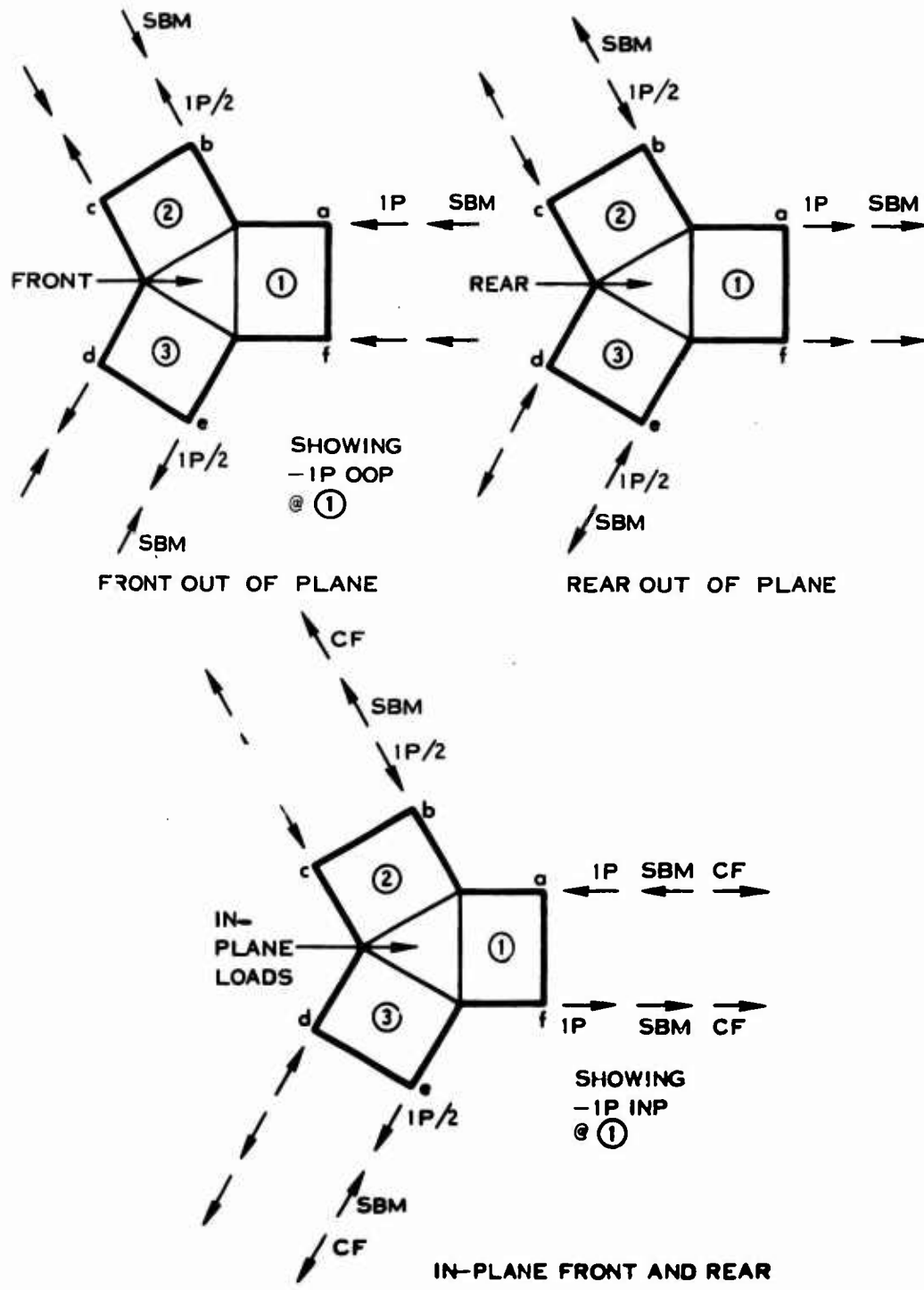
Figure 51. Load Schematics.

FRONT

When in-plane and out-of-plane 1P (CW) moments are positive at barrel arm No. 1,

P_a = CF - SBM + 1PINP - SBMOP - 1POOP
690 - 64 + 378 - 46.6 - 296 = 660 lb

P_b = CF + SBM + 1P/2 - SBMOP + 1POOP/2
690 + 64 + 189 - 46.6 + 148 = 1044 lb

P_c = CF - SBM - 1P/2 - SBMOP + 1POOP/2
690 - 64 - 189 - 46.6 + 148 = 438 lb

P_d = CF + SBM + 1P/2 - SBMOP + 1POOP/2
690 + 64 + 189 - 46.6 + 148 = 1044 lb

P_e = CF - SBM - 1P/2 - SBMOP + 1POOP/2
690 - 64 - 189 - 46.6 + 148 = 438 lb

P_f = CF + SBM - 1P - SBMOP - 1POOP
690 + 64 - 378 - 46.6 - 296 = -66 lb

REAR

When the 1P in-plane moment is negative at barrel arm No. 1,

P_a = CF - SBM - 1P + SBMOP + 1POOP
690 - 64 - 378 + 46.6 + 296 = 590 lb

P_b = CF + SBM - 1P/2 + SBMOP - 1POOP/2
690 + 64 = 189 + 46.6 - 148 = 463 lb

P_c = CF - SBM + 1P/2 + SBMOP - 1POOP/2
690 - 64 + 189 + 46.6 - 148 = 714 lb

P_d = CF + SBM - 1P/2 + SBMOOP - 1POOP/2
690 + 64 - 189 + 46.6 - 148 = 463 lb

P_e = CF - SBM + 1P/2 + SBMOOP - 1POOP/2
690 - 64 + 189 + 46.6 - 148 = 714 lb

P_f = CF + SBM + 1P + SBMOOP + 1POOP
690 + 64 + 378 + 46.6 + 296 = 1475 lb

101

REAR

When the 1P moment is positive at barrel arm No. 1,

P_a = CF - SBM + 1P + SBMOP - 1POOP
690 - 64 + 378 + 46.6 - 296 = 745 lb

P_b = CF + SBM + 1P/2 + SBMOP + 1POOP/2
690 + 64 + 189 + 46.6 + 148 = 1173 lb

P_c = CF - SBM - 1P/2 + SBMOP + 1POOP/2
690 - 64 - 189 + 46.6 + 148 = 632 lb

P_d = CF + SBM + 1P/2 + SBMOP + 1POOP/2
690 + 64 + 189 + 46.6 + 148 = 1173 lb

P_e = CF = SBM - 1P/2 + SBMOP + 1POOP/2
690 - 64 - 189 + 46.6 + 148 = 632 lb

P_f = CF + SBM - 1P + SBMOP - 1POOP
690 + 64 - 378 + 46.6 - 296 = 136 lb

These summation totals are illustrated in Figures 52 and 53.

Taking these loads and solving for F_1 and F_2 and resolving them along with P_1 and P_2 into forces in the X and Y directions allows an investigation of the curved beam between the branches in Figure 50.

The area of section (A-A) in Figure 54 is given by

$$A \approx 2 \pi Rd \tag{42}$$

The neutral axis is found from

$$h = \frac{R - d}{\log \left(\frac{R + c}{R - c}\right)} \quad \text{(Reference 2)} \tag{43}$$

where h = distance from the centroid to the neutral axis.

The bending stress is given by

$$f_b = K \frac{MY}{I} \tag{44}$$

102
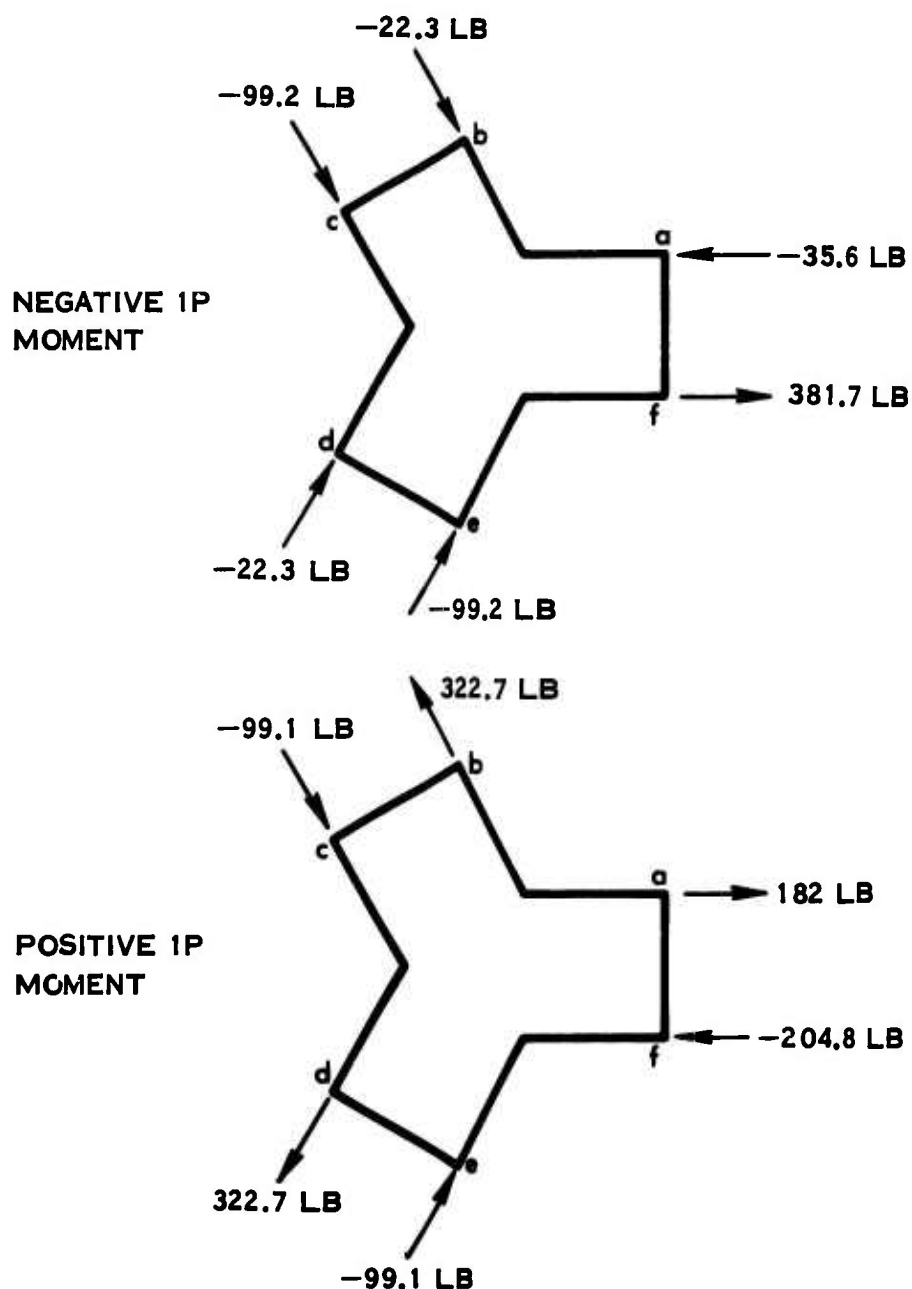
Figure 52. 3-Blade Crossed Tube Barrel Front Section Element.

103
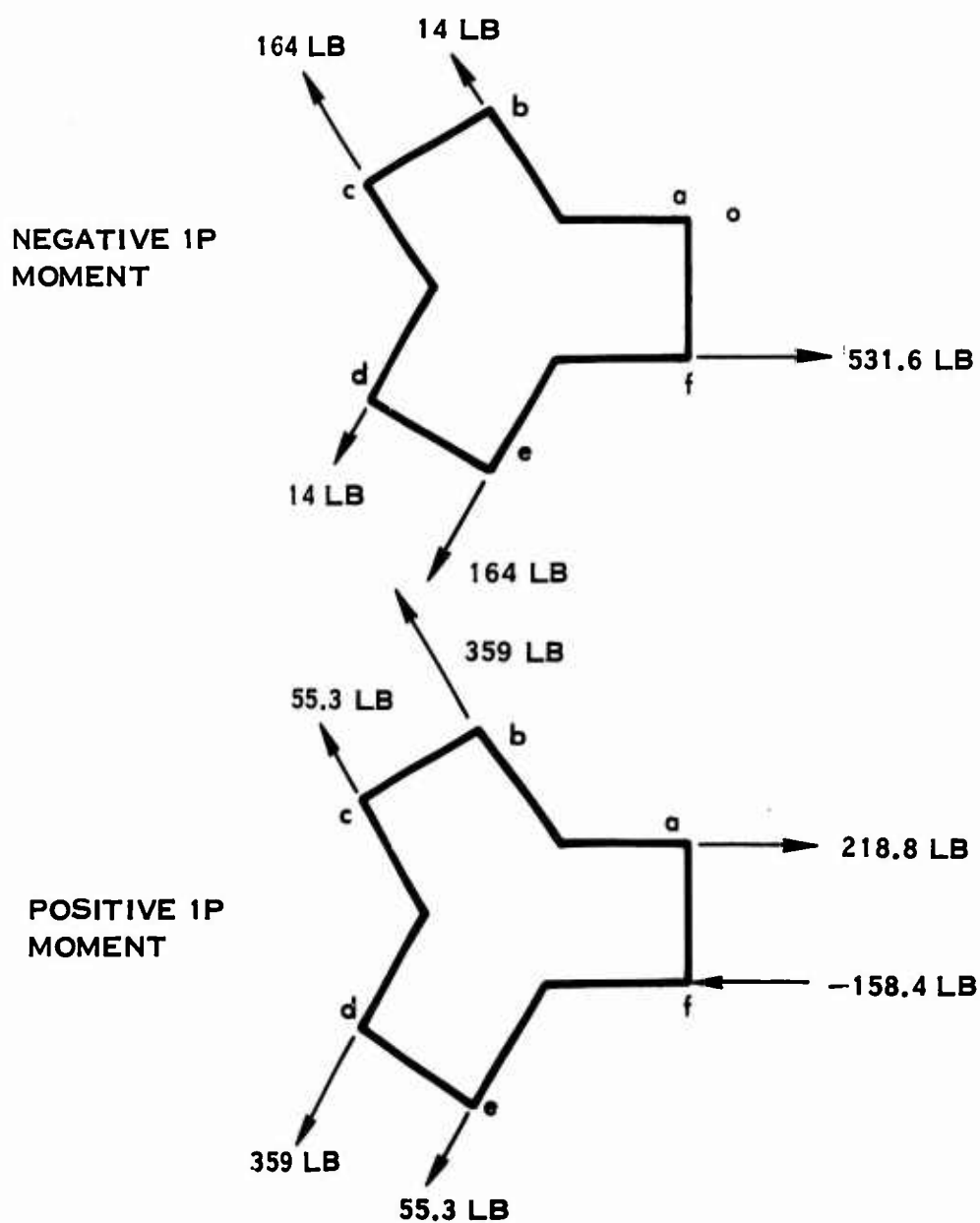
Figure 53. 3-Blade Crossed Tube Barrel Rear Section Element.

104
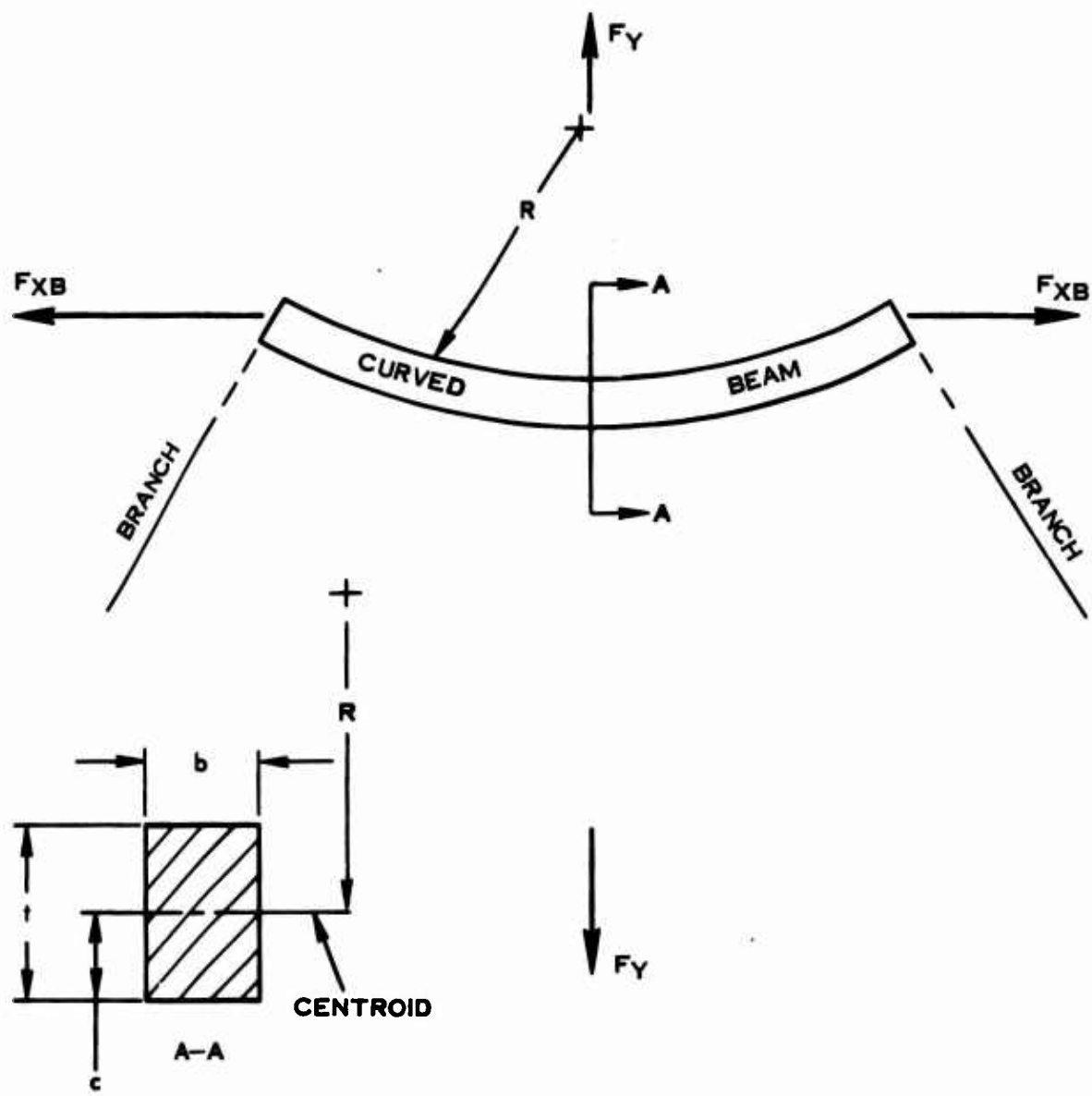
Figure 54.   Curved Beam Load Schematic.

where K = curved beam factor

$$I = I_c + A\ (h^2) \tag{45}$$

$$y = h + c = h + \frac{t}{2} \tag{46}$$

Upon substitution in equation (44),

$$f_b = K\ \frac{12\ M\ (h + 0.5t)}{bt^3} + \frac{2P_1\ Rt\ h^2}{90} \tag{47}$$

To determine the load distribution between the curved beam and the center disc, a spring rate comparison is made and the applied load is divided accordingly.

The disc is considered to be a flat plate fixed on one end and a load applied in one corner (Figure 55). The deflection of this plate in the "X" direction is a combination of bending and torsional deflection and is given by

$$\delta = \frac{F_X\ L^3}{3EI} + \frac{b}{2}\ \sin\ \frac{ML}{\beta bt^3\ G} \qquad \text{(Reference 1)} \tag{48}$$

where (β) is the correction factor for twist of a rectangular beam.

The spring rate of the disc is then

$$SR_D = \frac{F_X}{\delta} \tag{49}$$

The curved beam spring rate is determined by standard curved beam analysis and is given by

$$\delta_B = \int \frac{M}{EI}\ xdx \qquad \text{(Reference 2)} \tag{50}$$

which, for the geometry, reduces to

$$\delta_B = \frac{0.142\ F_{XB}\ R^3}{EI} \tag{51}$$
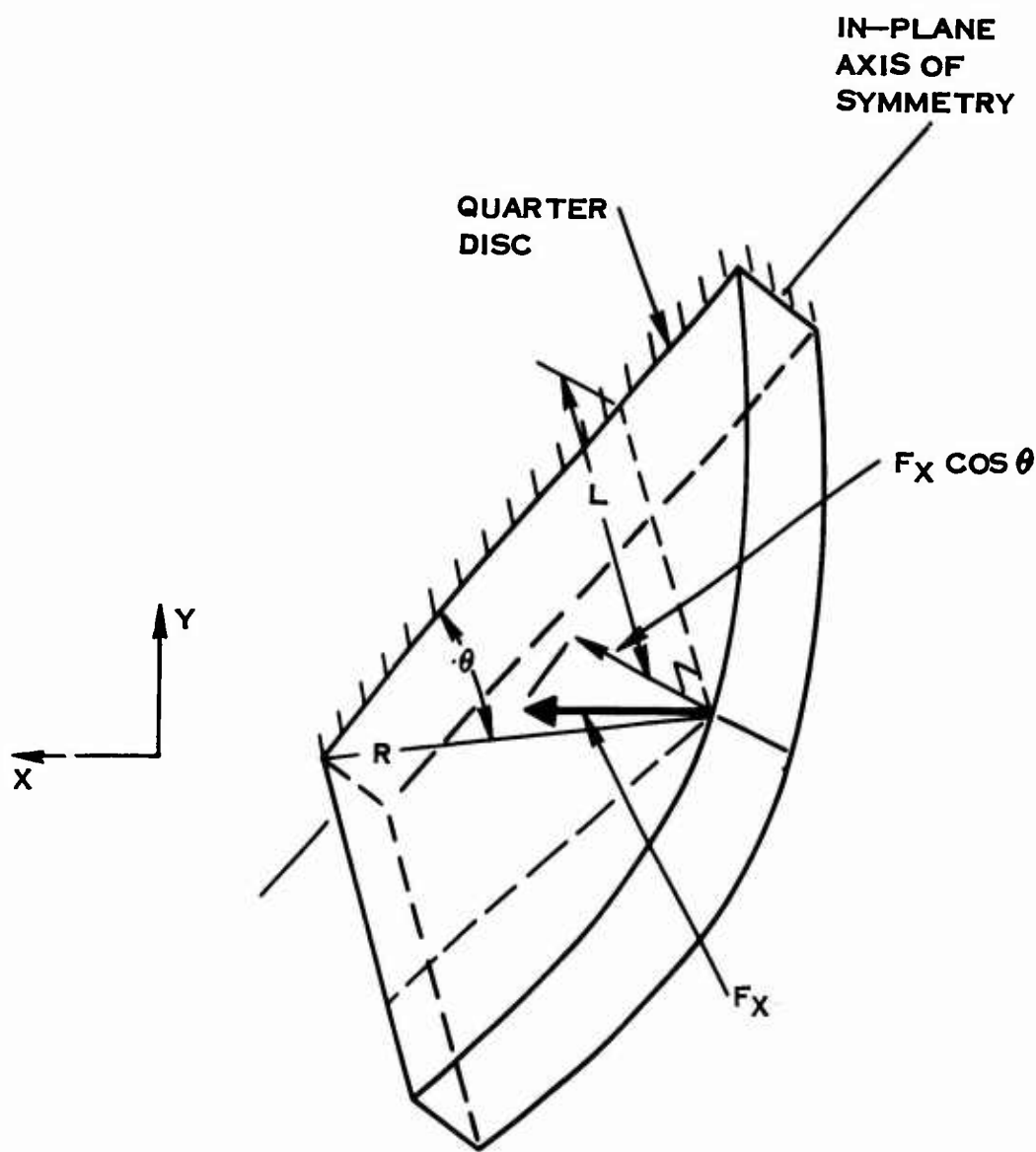
Figure 55. Center Disc Loading Diagram.

$$SR_B = \frac{F_{XB}}{\delta B} \tag{52}$$

The distribution of loads between the disc and beam is then found by

$$F_{X(TOT)} = F_X + F_{XB} \tag{53}$$

where

$$\frac{F_X}{SR_D} = \frac{F_{XB}}{SR_B} \tag{56}$$

These equations can now be used to determine the load that causes the moment in equation (44).

Analysis of the Front and Rear Rings

Because of time limitations on the amount of analysis that can be done, the 3-blade crossed tube barrel was not analyzed by H153. Instead, the data acquired for the 3-blade spherical barrel are used, introducing only a slight error because of minor geometry differences. The values of stresses given for the spherical barrel design are intuitively lower than those that would be found for the crossed tube when full loads are applied; however, there will be a load share in the crossed tube which effectively reduces the stress loads. This load share is discussed in the next section. It is assumed, then, that the stress level for the front and rear rings of the crossed tube barrel is approximately equal to that of the spherical barrel (see the 3-Blade Spherical Barrel Values Analysis section).

The Load Share of the Centerbody to the Front and Rear Rings

Figure 56 is a plot of spring rate ratios versus load share between the rings and centerbody from the 4-blade crossed tube analysis. The spring rate ratio is the spring rate of the centerbody divided by the spring rate of the intersecting barrel arm. From assumption 3, this curve is applied to the 3-blade barrel analysis.
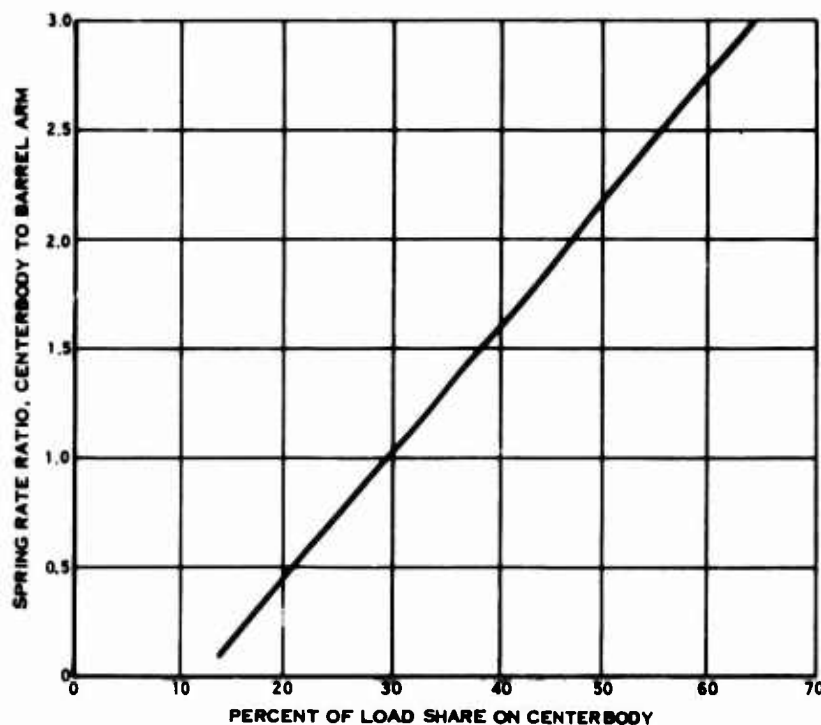
Figure 56. Load Sharing of Barrel Centerbody.

The ratio of

$$\frac{SR_D}{SR_B} = 0.5 \tag{57}$$

so that the load share is then approximately a 20-80% combination. (20% of the centrifugal load is assumed to be effective on the centerbody and 80% on the front and rear rings. The in-plane/out-of-plane load split is kept the same as in the 4-blade barrel analysis, 60% in-plane and 40% out-of-plane effective.) The total loads are now revised to reflect this share:

P (CF)	=	130 lb
P (SBMIP)	=	38.4 lb
P (SBMOP)	=	18.2 lb
P (1PINP)	=	± 227 lb
P (1POOP)	=	± 118 lb

109

Summing as before to obtain the various combinations, Figures 52 and 53 are revised as shown. The maximum combination is

$$P_1 = 219 \text{ lb}$$
$$P_2 = 359 \text{ lb}$$

which gives forces

$$F_1 = 359 \text{ lb}$$
$$F_2 = 25 \text{ lb}$$
$$F_x = 289 \text{ lb}$$
$$F_y = 289 \text{ lb}$$

Referring to Figure 57, F_x is applied to the curved beam and the stress is calculated from equation (47),

where
$$M = F_x Y = 10.1 \text{ in.} - \text{lb}$$
$$Y = R - R \cos 30$$
$$K = 1.1 \text{ (Reference 3)}$$
$$h = 0.008 \text{ in.}$$
$$t = 0.135 \text{ in.}$$
$$b = 0.35 \text{ in.}$$
$$I = 0000716 \text{ in.}^4$$
$$A = 0.04725 \text{ in.}^2$$
$$I \text{ (NA)} = 0.0000746 \text{ in.}^4$$

Then,

$$f_b = 11,000 \text{ psi max} \qquad (56)$$

The minimum stress is calculated the same way using

$$P_1 = -204.8 \text{ lb}$$
$$P_2 = -99.0 \text{ lb}$$

From equation (44),

$$f_b = -4600 \text{ psi min} \qquad (57)$$

110

The total stress is then

$$f_b = 3200 \pm 7800 \text{ psi at the centerbody} \tag{58}$$

The margin of safety is ample.

The approximate maximum stress in the front ring is then

$$f_b = 15,000 \pm 15,000 \text{ psi} \tag{59}$$

(This stress is approximated from the 3-blade spherical barrel analysis.)

The margin of safety (MS) for this stress is

$$MS = (26,000/15,000) -1 = 0.735 \tag{60}$$

The barrel arm analyses are common to all of the 3-blade barrel designs.
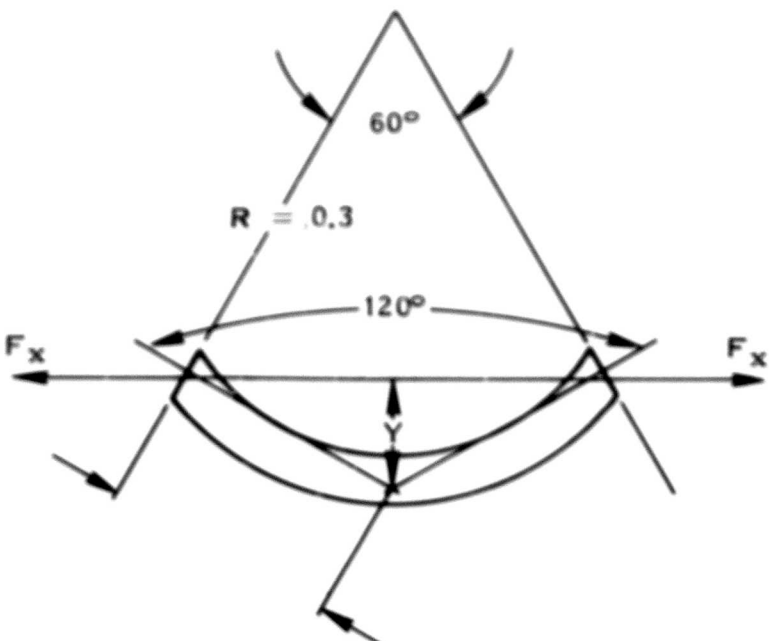
Figure 57. Curved Beam Load Schematic.

As previously stated, the deflection limit of 0.008 in. was based on producing a gross barrel spring rate, out of plane, of approximately 200 million lb/in. Local barrel arm and retention ball effects have reduced the barrel spring rate to about 300 million lb/in. Since a boron blade has not been designed in conjunction with the barrels, a specific spring rate requirement can not be determined. In the subsequent design of a blade, it may be necessary to add material to the barrel arms to obtain the foundation stiffness required for the blade.

The results of the design of the six barrels are summarized in Table XVI in terms of minimum margins of safety, weight, spring rate, relative machinability, and relative forgeability.

TABLE XVI. BARREL SUMMARY

| | Min. Margin of Safety* | | | Weight | Spring Rate | Relative** | Relative** |
	Arm	Centerbody	Tailshaft	(lb)	(in.-lb/rad)	Machinability	Forgeability
4-Blade Barrel							
Spherical	0.240	0.572	0.558	33.9	29.2×10^6	1	1
Shell	0.240	0.687	0.558	33.7	38.8×10^6	2	1
Crossed Tube	0.240	3.46	0.558	34.5	32.6×10^6	3	2
3-Blade Barrel							
Spherical	0.301	0.538	0.558	38.0	28×10^6	1	1
Shell	0.301	0.855	0.558	38.9	32.7×10^6	2	1
Crossed Tube	0.301	0.735	0.558	39.8	32.0×10^6	3	2

* Min. Margin of Safety = $\dfrac{\text{Actual Stress}}{\text{Working Stress}} - 1$

** Numbers (1, 2, and 3) indicate the relative ease associated with fabricating the various barrel configurations. The higher the number, the more difficult the particular operation.

MAIN BEARING DESIGN AND ANALYSIS

The stiffness of the propeller mounting system, which, in part, is influenced by the tailshaft and main bearing assembly, is a very important design consideration. The overall stiffness is used to define the whirl - flutter divergence speed of the aircraft as well as the critical speed behavior of the propeller-test-rig assembly. In addition, the mounting stiffness is influential in defining the propeller blade critical speeds which are not reactionless. This includes the whirl and symmetrical modes of the propeller disc.

To establish a lightweight bearing and housing combination, it is necessary to design both items simultaneously in a reiterative process. The basic bearing configuration, a high-contact-angle back-to-back tapered roller bearing, was chosen because of its ability to support the loads and to be lighter than other bearing arrangements. The housing was also made lightweight by tailoring it to the bearing loads.

The bearing and housing are exposed to a variety of loading conditions, which had to be resolved into basic loads to facilitate a bearing life calculation. The spectrum of loads is due to the shaft 1P moments for several flight modes (Table XVII).

To determine an equivalent moment due to the various flight modes, which are moments that vary in magnitude but not in direction, the following equation was used:

$$M_{ME} = \sqrt[3]{\Sigma M^3 t / \Sigma t} \qquad (61)$$

where M_{ME} is the mean effective shaft 1P moment (in.-lb), M is the moment (in.-lb), and t is the duration of the moment in sec.

The development of the mean effective shaft 1P moment can be seen in Table XVII. From Table XVII, it also can be seen that the maximum shaft 1P moment is 194,500 in.-lb.

The other load that was used in conjunction with the shaft 1P moment is the thrust load. Due to the lack of thrust data for the USAAVLABS propeller, an approximation had to be made. This was done with thrust data from the XC-142 aircraft, which has a flight envelope compatible with that of the USAAVLABS aircraft, in the following manner:

114

TABLE XVII. DETERMINATION OF MEAN EFFECTIVE SHAFT 1P MOMENT

Maneuver Shaft 1P Moments

Airspeed (KEAS)	Load Factor N_z	Shaft Moment (in. -lb)	Cycles x 10^6
150	1.5 g	108,000	11.92
	2.0 g	152,000	0.593
	2.5 g	194,500	0.031
	1.5 g	52,000	11.85
	2.0 g	84,500	0.593
250	2.5 g	117,000	0.03
	3.0 g	149,500	0.018
	3.5 g	181,500	0.002
	1.5 g	6,050	11.1
	2.0 g	27,500	0.555
350	2.5 g	47,500	0.0295
	3.0 g	70,000	0.018
	3.5 g	91,000	0.0022

Mean Effective Maneuver Shaft 1P Moment = 80,900 in. -lb.

Flight Mode	1P Shaft Moment (in. -lb)	Duration (% Time)
Climb	107,000	7
Cruise	35,000	65
High-Speed Cruise	20,000	8
Maneuver	80,000	8
Dive	43,000	2
Ground Handling		10

Mean Effective Shaft 1P Moment = 56,000 in. -lb.

8,590 lb = USAAVLABS max takeoff thrust

9,000 lb = XC-142 max takeoff thrust

4,560 lb = XC-142 mean effective thrust

Q_{ME} = $(4,560/9,000)(8,590)$

Q_{ME} = 4,350 lb USAAVLABS mean effective thrust

Table XVIII shows all the loads used to size the barrel retention bearing and the support housing.

TABLE XVIII. SIZING LOADS		
Load Condition	Max Load	Mean Effective Load
Thrust	8,590 lb	4,350 lb
Shaft 1 P Moment	194,500 in.-lb	56,000 in.-lb

The propeller retention bearings size was established by using the Anti Friction Bearing Manufactures Association (AFBMA) calculation, a computer program for ball and roller bearings[4], and the following parameters.

A bearing B10 vacuum melt life of 3000 hr was the basic design consideration. The size and location of the barrel tailshaft and the gear train limited the pitch diameter of the bearing to between 11 and 12 in. One parameter that greatly increased the reiterative bearing calculation was the desire to minimize housing deflections, due to the bearing loads, with as little weight penalty as possible. This combination of light weight and low deflections was accomplished by separating the rows of rollers to enable the bearing load lines to intersect at, or near, the combined bearing and bearing support housing center of gravity, thereby lowering the moment that is induced into the housing by the bearing loads. This can be seen in Figure 58.

.10-.08

.10-.08 30 PLACES
EQUALLY SPACED

SECTION A-A

PROPELLER
¢

.46-.48

		NUT-RETAINER					
6	1	NUT-RETAINER					
5	1	CUP-LOCKING					
4	1	PIN-HEADLESS					
3	1	LINER-HOUSING					
2	1	BEARING ASSY					
1	1	HOUSING			6AL-4V TITANIUM FORGING		
		PART NAME	PART NUMBER	REQ OF	MATERIAL AND HEAT TREAT	WT PER ASSY LB	REMARKS

NOTES

1. FIT BETWEEN HOUSING AND LINER 0.0020 IN. (L) TO 0.0020 IN. (T)
2. FIT BETWEEN BEARING AND LINER 0.0020 IN. (L) TO 0.0020 IN. (T)
3. FIT BETWEEN BEARING AND BARREL 0.0005 IN. (T) TO 0.0025 IN. (T)

Figure 58. Main Propeller Retention Assembly.

117

Figure 59 shows the last reiteration of the bearing calculation using the AFBMA method.
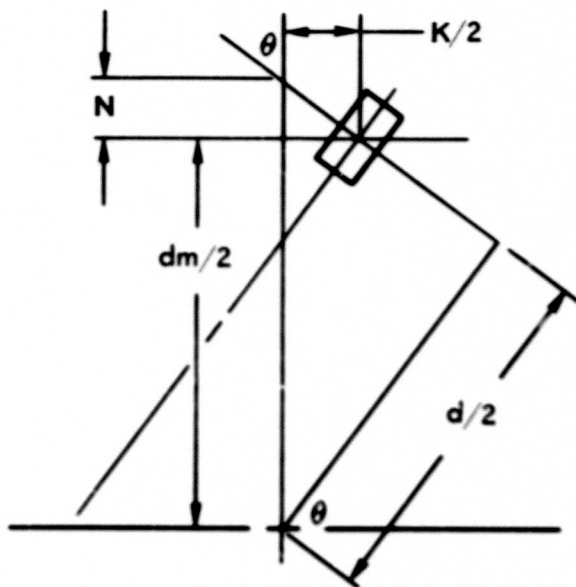
Figure 59. Determination of Equivalent Radial Load.

θ = bearing contact angle
dm = bearing pitch diameter
K = distance between rollers at the pitch diameter

From Figure 59, the following can be derived:

$$Q_e = (M/d) \cos (90 - \theta) + Q \qquad (62)$$
$$\text{and}$$
$$P_r = (M/d) \sin (90 - \theta) \qquad (63)$$

From previous reiteration, let the following be true:

θ = 50 deg   dm = 11.56 in.
K = 1.12 in.   M = 56,000 in. -lb
Q = 4,350 lb

From equations (62) and (63),

$$Q_e = 8,830 \text{ lb} \qquad P_r = 3,760 \text{ lb}$$

The AFBMA equation for effective radial load is as follows:

$$P_e = XVP_r + YQ \tag{64}$$

Since Q_e/P_r is greater than, or equal to, $1.5 \tan\theta$, equation (64) should be rewritten as follows:

$$P_e = (0.4)(1.0) \, P_r + (0.4)(\cot\theta) Q_e \tag{65}$$

By substituting in equation (65),

$$P_e = 4,460 \text{ lb}$$

Bearing Dynamic Capacity

From previous reiteration, let the following be true:

$$
\begin{aligned}
D &= 0.3996 \text{ in. (roller mean diameter)} \\
L_e &= 0.45 \text{ in. (roller effective length)} \\
Z &= 69 \text{ (number of rollers)} \\
I &= 1 \text{ (number of rows)} \\
\theta &= 50°
\end{aligned}
$$

Since $D \cos\theta / dm = 0.022$,
then $F_c = 4100$, per AFBMA curve.

The AFBMA dynamic capacity equation is as follows:

$$CB = F_c (I L_e \cos\theta)^{0.778} \; Z^{0.75} \; D^{1.075} \tag{66}$$

By substituting in equation (66),

$$CB = 13,930 \text{ lb}$$

The AFBMA life equation for roller bearings is

$$L_i = (CB/P)^{3.33} (16,667/\text{rpm}) \tag{67}$$

By substituting in equation (67),

$$L_i = 630 \text{ hr (B10 air melt highest loaded row)}$$

119

Using a factor of 5 for consumable vacuum melt material, the bearing life is 3150 hr.

A bearing computer program[4] was used also to bracket the bearing life. The program yielded a 755-hr B10 air melt life for the highest loaded row.
The difference in the two lives is due to the computer's giving a more exacting calculation than the general bearing equation, and the former also takes into account housing stiffness.

The preceding bearing lives were estimated, assuming that the proper amount of lubrication would be present to carry away the heat generated by the bearing. The power loss in a bearing is a function of the torque required to rotate a bearing in both its loaded and unloaded state. This is the basis for the following calculation:

$$T_0 = f_0 \, P \, (dm)^3 (n\omega/P)^{0.66} \quad \text{(Reference 5)} \tag{68}$$

where
T_0 = torque required to rotate an unloaded bearing
f_0 = 3-4 (per row) = bearing and lubrication factor
P = 0.01035 kg/mm^2 = difference between atmospheric pressure and the vaporization pressure of oil
dm = 293.5 mm = bearing pitch diameter
n = 3.405×10^{-10} kg/sec/mm^2 = dynamic viscosity of oil
ω = 122 rad/sec = angular velocity of bearing

By substituting in equation (68),

$$T_0 = 23.6 \text{ in.-lb per row} \tag{69}$$

also
$$T_1 = f_1 \, g_1 \, P_0 \, dm$$

where
T_1 = torque required to rotate a loaded bearing
f_1 = 0.0004-0.0005 = bearing design factor
g_1 = 1.68 = loading factor
P_0 = 1593 kg = static equivalent load

By substituting in equation (69),

T_1 = 34.1 in.-lb (highest loaded row)

T_1 = 17.3 in.-lb (lightest loaded row)

$$HP = T \, (N/63,000) \tag{70}$$

where
HP = horsepower required to rotate bearing
T = total torque = 98.6 in.-lb
N = 1165 rpm

The horsepower loss is obtained from equation (70),

$$HP - 1.63$$

1. 63 horsepower - 77. 5 Btu/min

In one minute, a quart of MIL-L-7808 at 225° F will absorb 48 Btu, for a 50° F temperature rise.

Required oil flow = 1.6 qt/min

An investigation was made to establish a bearing material. Two materials were found to be acceptable, 52CB and E9310, both of which are consumable electrode vacuum melt steel. The E9310 material was chosen as the final bearing material because of its being a case-hardened steel and its availability. A case-hardened material will prevent the propagation of surface cracks, because of the hardness difference between the surface and core material. Due to this bearing's having a small cross section and a large diameter, the bearing races under a load will tend to distort; a case-hardened steel will take more of this distortion, without being over-stressed, than a through-hardened steel.

Bearing roller retainer material was also investigated. Among the materials studied were beryllium copper and stamped silver-plated steel. The stamped silver-plated steel cage was chosen over the beryllium copper based on the recommendation of the proposed bearing manufacturer. The bearing will have to be test-ed with the silver-plated steel cage to establish its adequacy. From the manufac-turer's experience, it is believed that this cage is adequate for this bearing instal-lation. The results of the bearing study can be seen in Figure 60, which is com-posed of the basic details of the bearing geometry and environment.

The bearing support housing, as shown in Figure 60, consists basically of a ring supported by a ribbed cone. This housing could be analyzed by Hamilton Standard's Shells of Revolution program, HO88, as if there were no ribs on the cone. To be able to use HO88, the housing was modified to eliminate the ribs but to maintain the support that they provide. This was accomplished by taking a representative section of cone and rib and determining its moment of inertia and neutral axis. The rib was then removed, and the cone was thickened until it had the same moment of inertia as the ribbed section. The thickened cone was then repositioned so that its neutral axis coincided with that of the ribbed section. The housing was then further modified by breaking it up into simple geometric parts. The results of the housing modification can be seen in Figure 61, which shows the housing configuration used in HO88 to compute the housing deflections and stresses.

121

NOTES

1. BEARING MATERIAL—E9310 CONSUMABLE VACUUM MELT STEEL
2. RETAINER MATERIAL — SILVER-PLATED AISI—1050 STEEL
3. LUBRICATION — MIL—L—7808D
4. TEMPERATURE RANGE — -65°F TO +275°F
5. THRUST LOAD — 430 LB MEAN EFFECTIVE
6. APPLIED MOMENT — 56000 IN.-LB MEAN EFFECTIVE
7. RADIAL LOAD — 4460 LB EQUIVALENT
8. BEARING SYSTEM LIFE — 600 HR B10 AIR MELT
9. CONTACT ANGLE — 50°
10. NO. OF ROLLERS — 69
11. ROLLER MEAN DIA — 0.3996 IN.
12. ROLLER LENGTH — 0.50 IN. TOTAL 0.44 IN. EFFECTIVE
13. PITCH DIA — 11.56 IN.
14. CONE ROTATES AT 990 RPM
15. LOAD LINES TO INTERSECT APPROXIMATELY AT BEARING O.D.
16. 6 HOLES 0.03125 DIA EG SP 2 PLACES
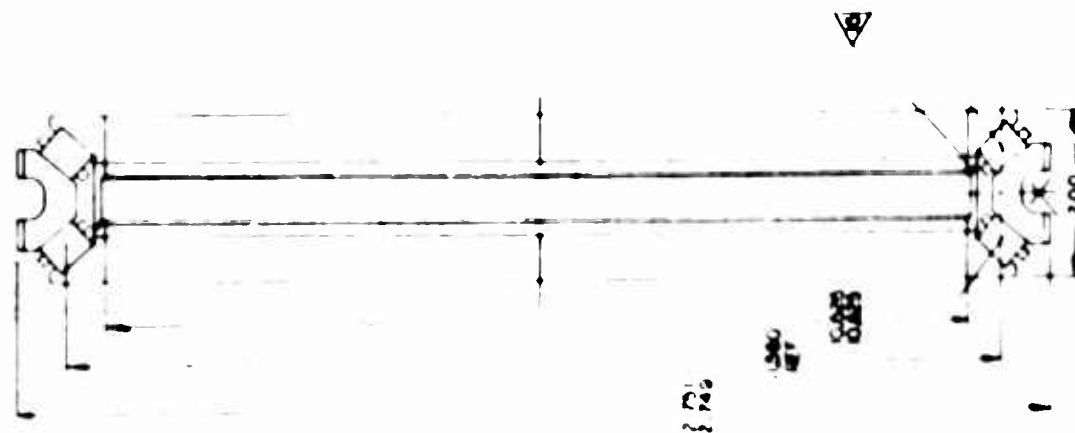
Figure 60. Retention Bearing.

PART 1

PART 4

LOAD
LINE

5.78 IN.
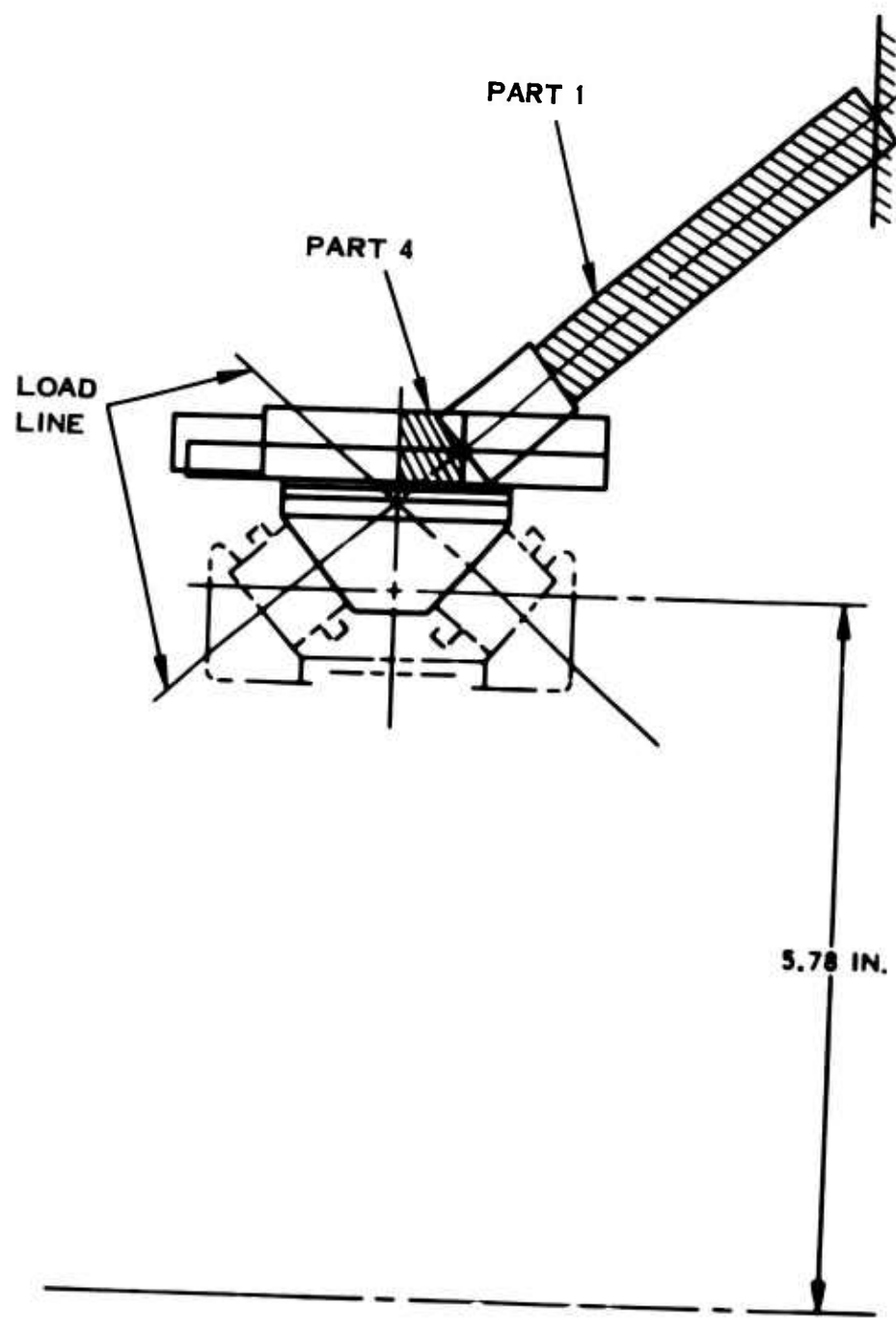
Figure 61. Housing Geometry for HO88.

To apply the loads to the housing in a manner that is acceptable to HO88, the loads had to be represented by Fourier series harmonics in the axial or radial direction.

The thrust load produces a uniform axial and radial load around the housing at the load line intersection point, which was represented by the 0th harmonic in the axial and radial direction, the magnitude of which was determined as follows:

$$Q = 8590\text{-lb max takeoff thrust}$$
$$R = 6.25\text{-in. distance from housing to intersection of load line}$$
$$\theta = 50\text{-deg bearing contact angle}$$
$$C = \text{circumference at load line intersection point}$$
$$Q/C = 219\text{-lb/in. axial component}$$
$$N\theta = Z/\tan\theta = 183\text{-lb/in. radial component}$$

The moment also produces axial and radial loads around the housing, at the load line intersection point, but they are not uniform as in the case of the thrust.

The axial component of the moment is represented by a cosine distribution which is the 1st harmonic type of load. The radial component is not any basic distribution; it is a back-to-back cosine distribution which is represented by superimposing a 0th harmonic upon the 2nd harmonic. Figures 62, 63, 64, and 65 give a graphical representation of these loads. The magnitude of moment loads was determined as follows:

$$M = 194,500\text{-in.-lb max shaft 1P moment}$$
$$P_0 = \text{max load in a cosine distribution}$$
$$P_0 = 2\ (M/R)$$
$$P_a = P_0/R\ 1,585\text{-lb/in. axial component}$$
$$N\theta = P_a/\tan\theta = 1,322\text{-lb/in. radial component}$$

The modification of the housing geometry and the loads enabled the running of the thin Shells of Revolution program (deck HO88).

From the method in which the loads were inputed, it can be seen that the restraint due to the bearing inner race and the barrel tailshaft was not taken into account; this was the next step in establishing the proper bearing housing configuration.

The HO88 program was run with the moment and thrust loads to determine how much the housing would deflect without the inner race and tailshaft restraint. From this run it was found that the stresses, in the cone area, were high. A deflection curve was plotted for the radial deflection (Figure 66), from which it can be seen

124
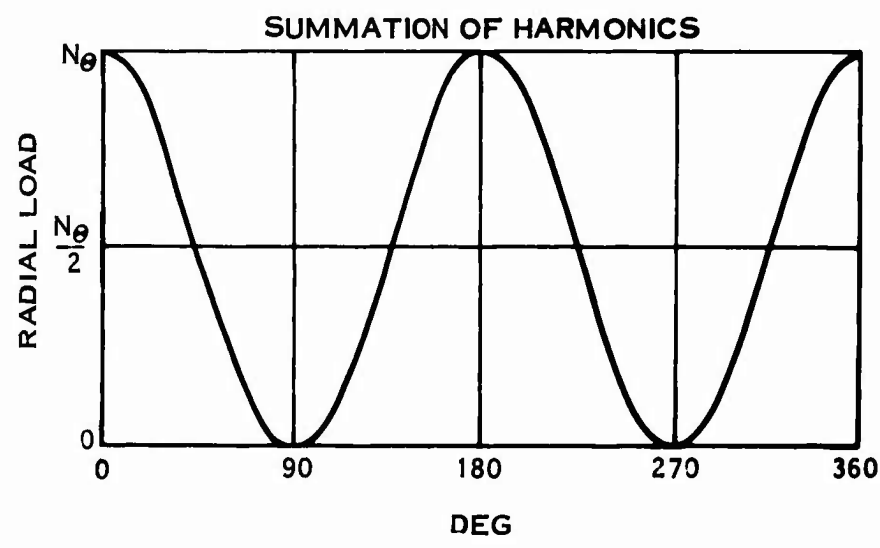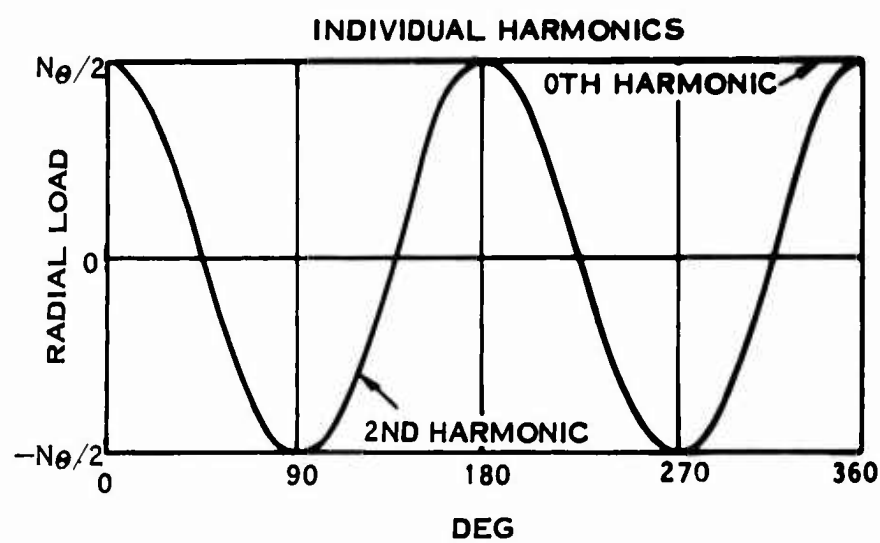
Figure 62. Development of the Radial Component of the Moment Load.

125
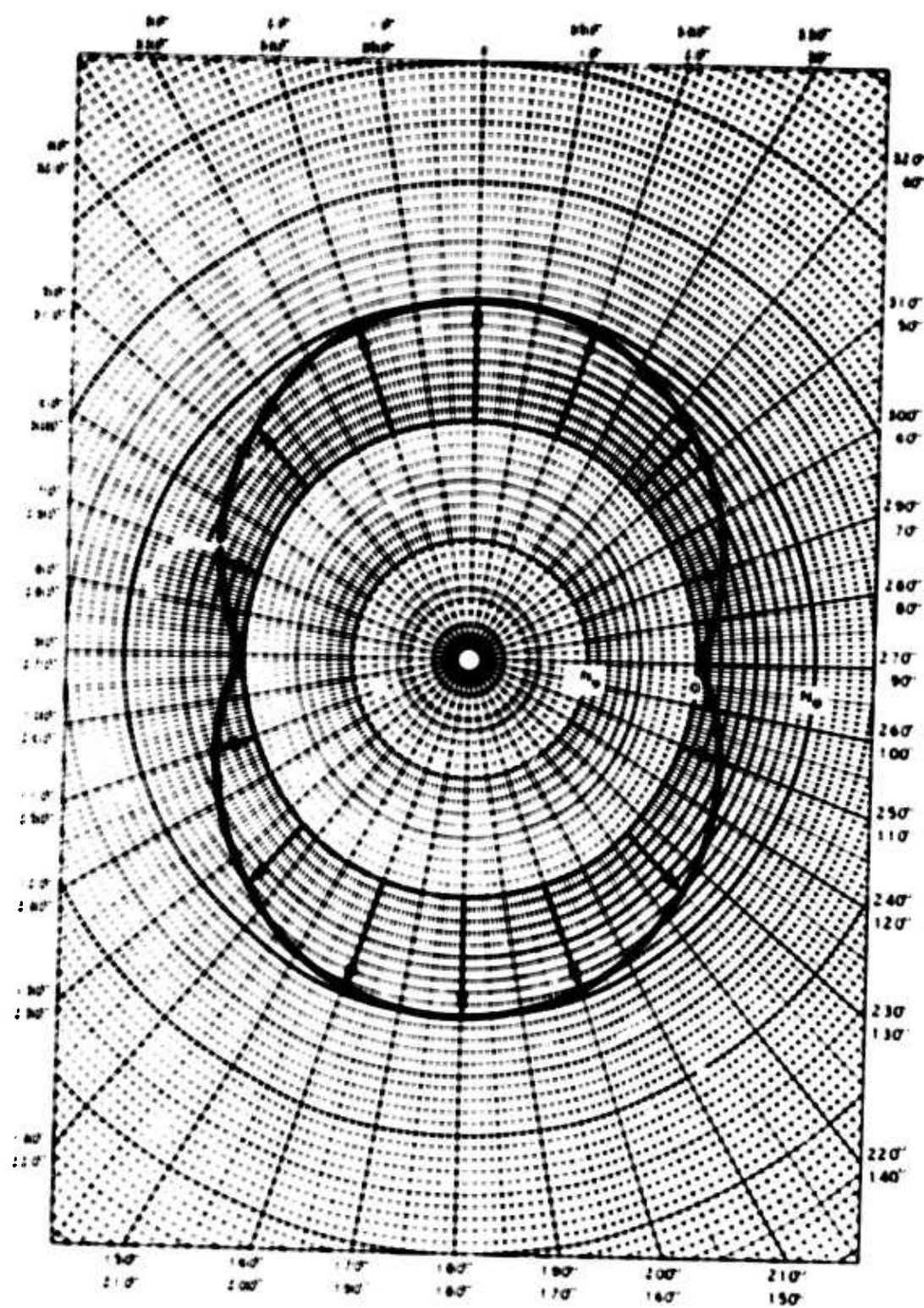
Figure 63. Radial Load Distribution Due to the Moment.

126
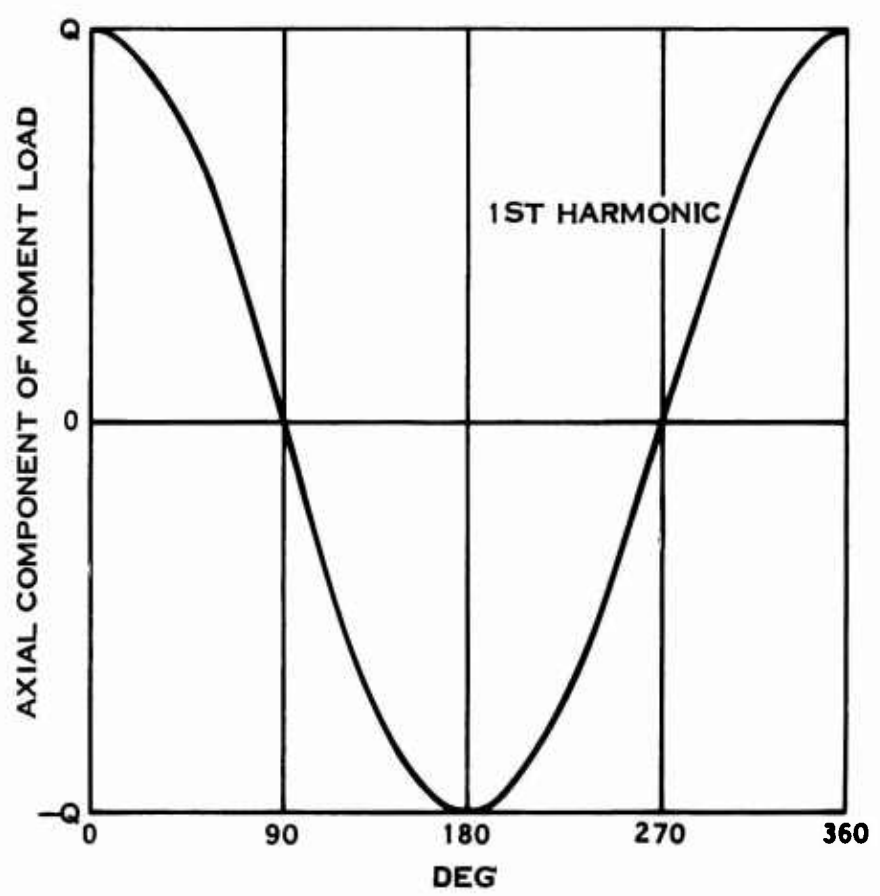
Figure 64. Development of the Axial Component of the Moment Load.

127
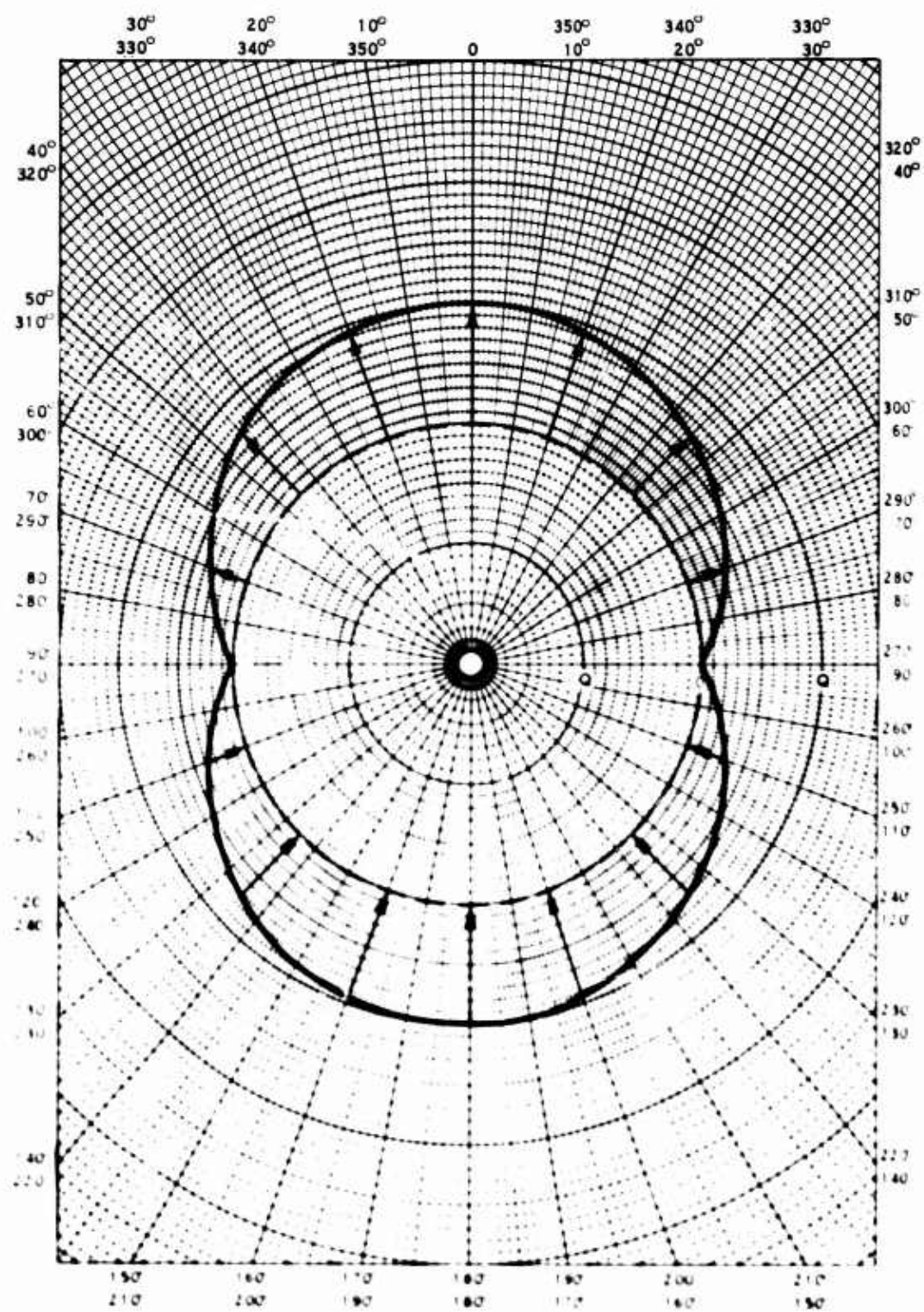
Figure 65. Axial Load Distribution Due to the Moment.
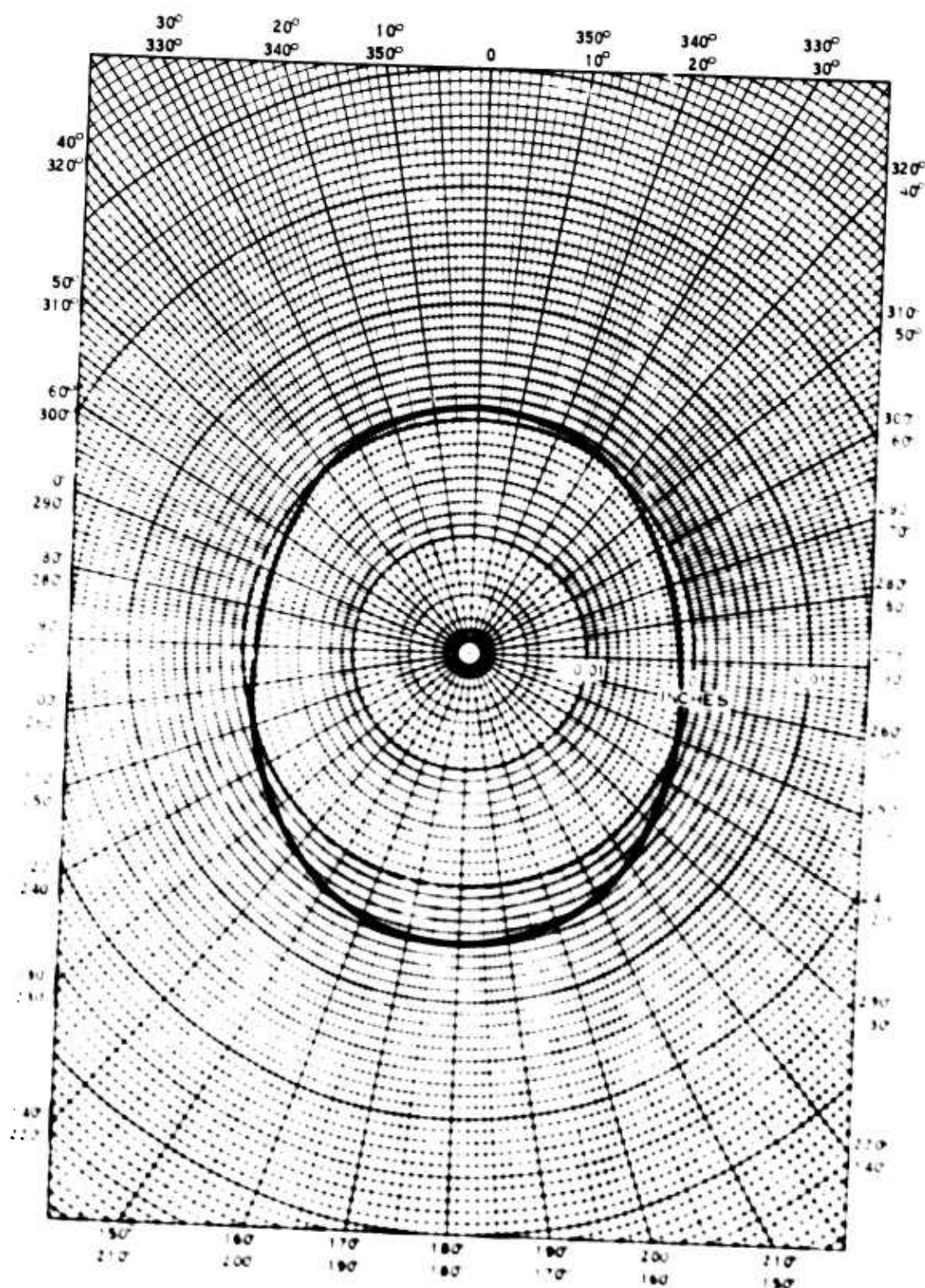
Figure 66. Radial Housing Deflection (at end of part 4), No Inner Race Support.

129

that the housing has a radially inward deflection in a plane approximately 90 deg away from the plane in which the moment load is applied. A curve was also plotted for the axial deflection (Figure 67). Since there is the inner race and tailshaft restraint on the housing, this radially inward deflection should be nonexistent or a much smaller value.

To accomplish this, a restraining load was applied to the housing 90 deg away from the actual loading. The magnitude of this load was determined by knowing the deflection required and the system spring rate. The effect of including this restraining force was to reduce the stresses and deflections in the main housing.

Figure 68 illustrates the radial housing deflection with the inner race and tailshaft restraint. Figures 69 and 67 represent the axial deflections with and without the restraint, in the ring area of the housing.

To determine the actual stresses in the cone area of the housing, the results from HO88 have to be modified to account for the difference in geometry between what was used in HO8. nd the actual housing geometry. Figure 70 shows the difference between the actual housing and the HO88 geometry for part 1 (see Figure 61).
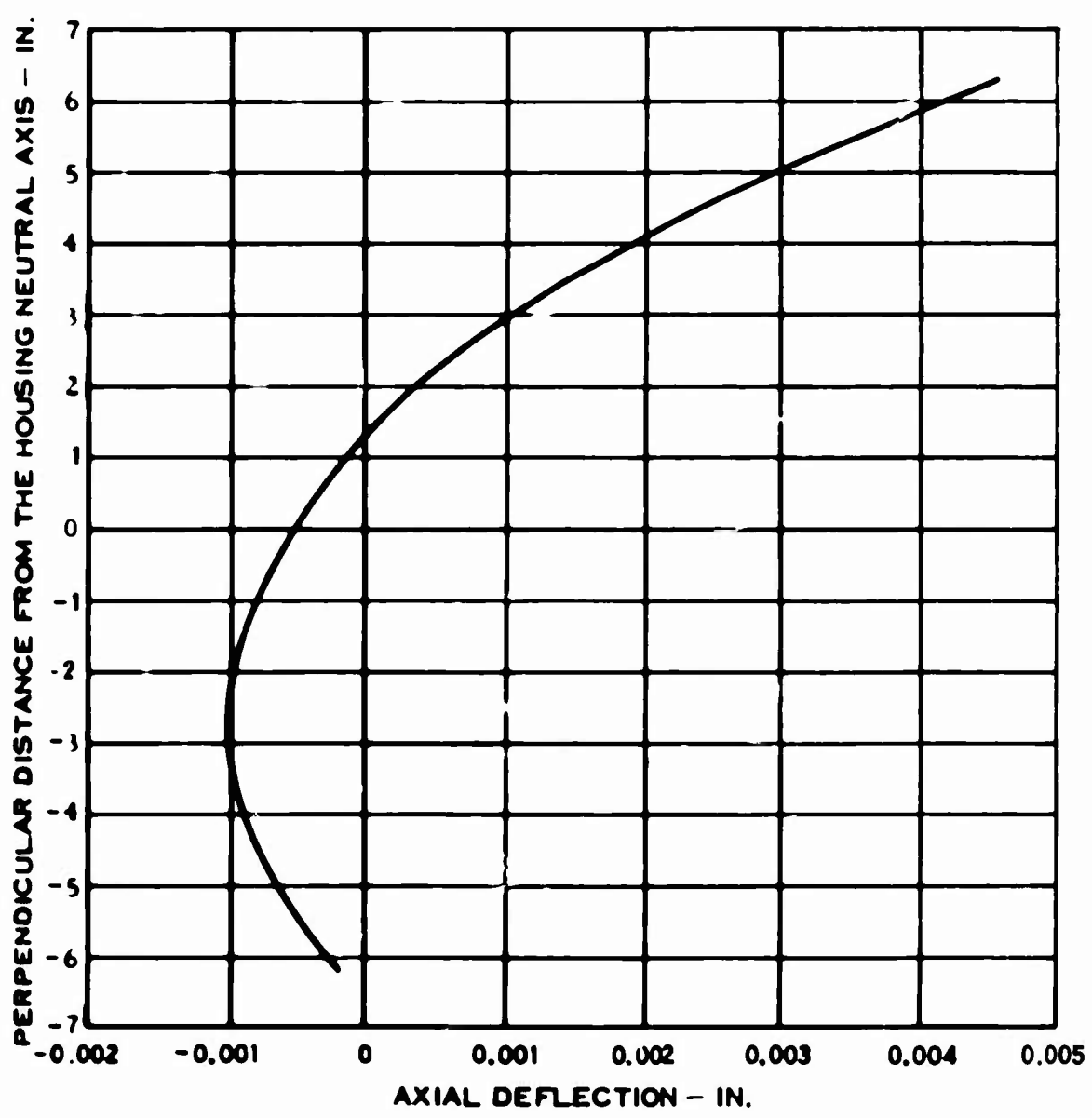
Figure 67. Axial Housing Deflection (at end of part 4), No Inner 'ace Support.

131
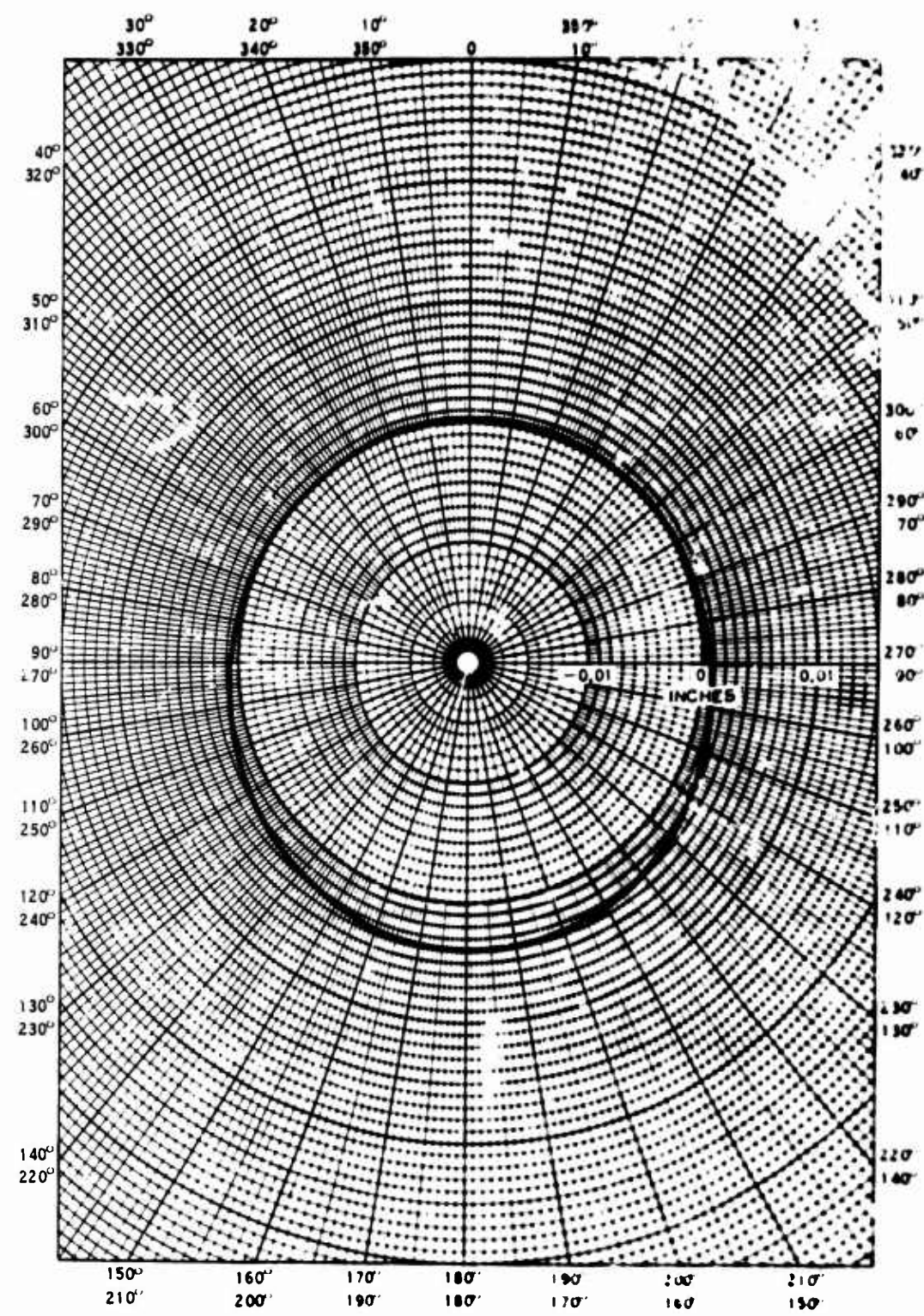
Figure 68. Radial Housing Deflection (at end of part 4), Inner Race Support Included.

132
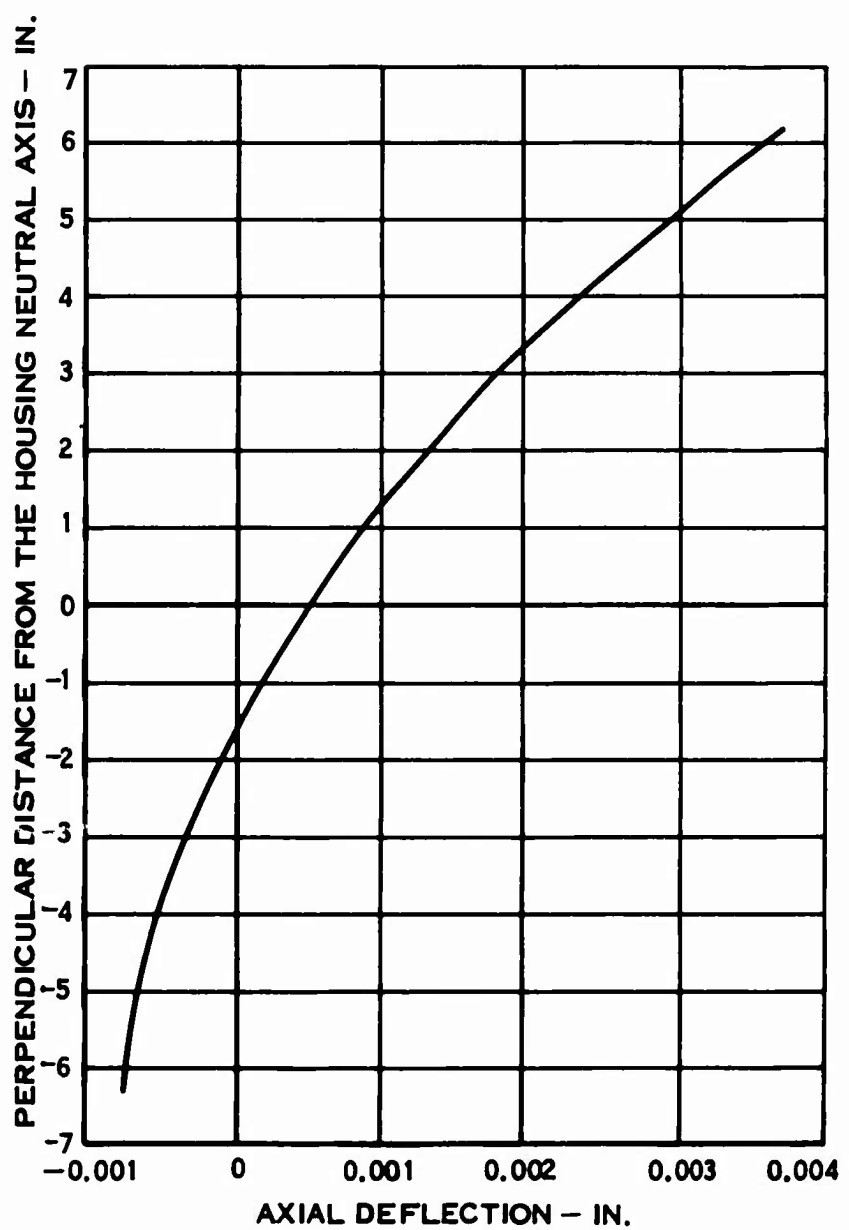
Figure 69. Axial Housing Deflection (at end of part 4), Inner Race Support Included.

133
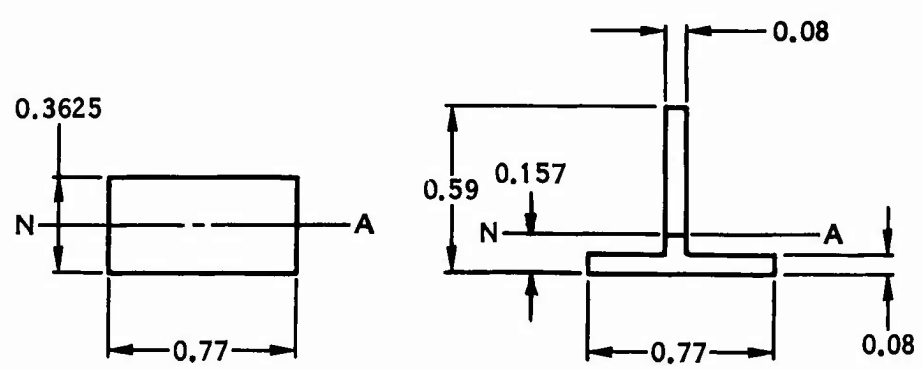
Figure 70.   Cross Section of Part I.

The actual combined bending and tensile stresses in the outer fiber of the T-section can be related to the simulated section used in the Shells of Revolution program. Since an equivalent moment of inertia section was used, the longitudinal stress is directly proportional to the distance from the neutral axis; this assumes that the pure tension loading also increases with this same relationship, which it does not, thus imposing an 8% error on this assumption.

The maximum longitudinal stress on the outer fiber is calculated to be 17,100 psi at the end of part 1.

The stresses on the bottom of this section also have to be adjusted. The bottom fibers of the housing are subjected to hoop, shear, and longitudinal stresses.

The stresses on the outermost bottom fiber per HO88 are
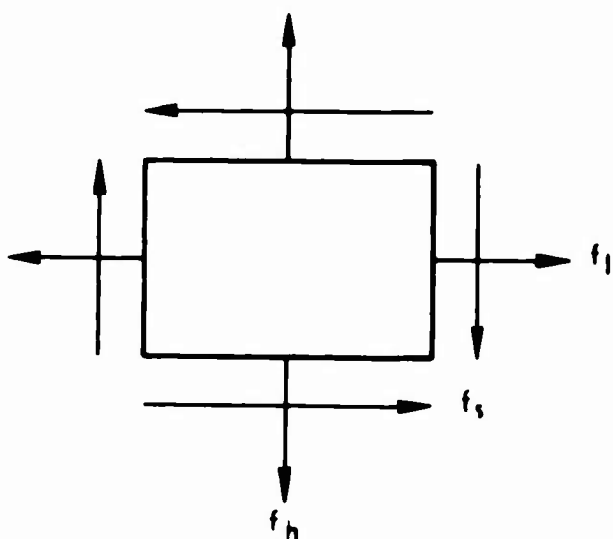
$$f_1 = 2,767 \text{ psi}$$
$$f_h = 2,859 \text{ psi}$$
$$f_s = 3,743 \text{ psi}$$

The c ratio for the bottom is 0.866.

Since both shear and hoop are dependent on the thickness of the section, they should be adjusted by the thickness ratio, which is 2.27.

The actual stresses on the bottom of the housing are

$$f_1 = 2,400 \text{ psi}$$

135

$$f_h = 6,490 \text{ psi}$$
$$f_s = 8,500 \text{ psi}$$

at the end of part 1.

By plotting these stresses on Mohr's Circle, the maximum stress of 13,100 psi is obtained. For conservatism, a stress concentration factor of 3 is said to exist in the area of concern. This results in a maximum stress in the housing of $f = 6,500 \pm 19,700$ psi with a margin of safety of 0.46.

Bearing Design Summary

The main propeller mount bearing life has been analyzed by three separate methods. The first method was by a computer program which analyzes the maximum loaded roller in determining the resultant bearing life. The second method was by use of the AFBMA tapered roller bearing analysis, and the third analysis was conducted by the proposed bearing manufacturer.

Table XIX summarizes the B10 vacuum melt life for the bearing as calculated by each method.

TABLE XIX. B10 LIFE OF MAIN BEARING	
Method	Life (hr)
Computer Program	3780
AFBMA	3150
Manufacturers	3300

The housing was designed to withstand the maximum loads imposed and has a resultant margin of safety of 0.46. The analysis has confirmed the existence of a nonlinear deflection which is occurring across the bearing. A static test would ascertain whether the magnitude of this nonlinearity will have any effect on each roller pattern.

The design criterion selected for the mount bearings was to use a minimum B10 life of 3000 hr, based on the AFBMA life calculation adjusted by a factor of 5.

TITANIUM GEAR TOOTH COATING INVESTIGATION

INTRODUCTION

From September 1965 through June 1968, Hamilton Standard conducted a development program to determine the feasibility of utilizing titanium as a construction material for aircraft power gearing. A wear protective coating evolved out of this work which demonstrated promise of enabling titanium gear teeth to withstand Hertz stresses, bending stresses, and sliding velocities comparable to those operating environments associated with conventional carburized steel power gearing.

The basic coating consisted of a number of titanium-nickel intermetallic layers which were formed on the surfaces of titanium gear teeth via the thermal diffusion of a thin layer of electroless nickel. At the end of this program it was believed that the coating parameters (thickness of applied electroless nickel, diffusion temperature, and diffusion time) associated with the electroless nickel process had been optimized and that significant modifications to the coating technique would be necessary if load-carrying capacity were to be improved.

Endurance testing of coated gears showed a Hertz stress limit of 85,000 to 90,000 psi with a finite life of approximately 200 hr (350 million cycles). The eventual breakdown of the coating was attributed to high phosphorus-rich zones (15-16%) which formed within the titanium-nickel intermetallic layers during the diffusion process. The presence of phosphorus (7-9%) is inherent in the electroless nickel during the plating process.

In June 1968, USAAVLABS sponsored a component feasibility program to investigate two proposed approaches for developing an improved wear coating. Both proposed approaches involved elimination of the element of phosphorus from the coating system and were to be investigated concurrently over a 7-month period.

One approach involved applying a layer of pure (phosphorus-free) nickel to the gear teeth and using a thermal diffusion process similar to that employed during previous development work with electroless nickel. The second approach made use of an ion-sputtering coating technique which would permit direct deposition of the titanium-nickel intermetallic compounds on titanium gear teeth, thereby avoiding the requirements of high thermal treatments after coating.

The terms "electroless nickel" and "electrolytic nickel" have reference to the type of plating process used to provide a layer of nickel on the surfaces of the titanium gear teeth. Nickel that is applied using the electrolytic plating process is essentially deposited as pure nickel.

137

Nickel that is applied using the electroless plating process inherently contains from 7 to 9 percent phosphorus in the nickel coating due to the composition requirements for the electroless nickel plating bath.

BACKGROUND OF TEST PROGRAM

Gear Design

Two spur gear designs were employed to evaluate potential wear coatings. All test gears were 2.5-in. pitch diameter with a 0.25-in. face width. Both 8-pitch (20-tooth) and 12-pitch (30-tooth) gears were employed. The 8-pitch gear had a high ratio of Hertz stress to bending stress, while this ratio for the 12-pitch gear was more representative of actual full-scale gearing. The two gear configurations permitted Hertz stress and bending stress capacity to be evaluated independently. Detailed drawings of the test gearing are shown in Figures 71 and 72. Both types of test gearing incorporated involute profile modifications based on a torque loading that would produce a Hertz stress of 100,000 psi. (This Hertz stress corresponds to a tooth load of 240 lb/in. for the 8-pitch gear and 227 lb/in. for the 12-pitch gear).

Test Gear Load Data

Load data for the test gearing are plotted in Figure 73. Note that Hertz stress for the steel gearing is greater than that for the titanium gearing for a given torque loading. This is due to the difference in moduli between the two materials. The method used to calculate tooth loads is given in Appendix I.

Test Facility

A detailed description of the test rig used for evaluating the test gearing is given in the Plan of Test (see Appendix II). Photographs of the test facility are shown in Figures 74 and 75. The rig was designed such that the loading conditions Hertz stress, bending stress, and pitch line velocity of full-scale power gearing would be simulated using the 2.5-in. pitch diameter test gearing.

COATING INVESTIGATION

Investigation of a Phosphorus-Free Diffused Nickel Coating

Plating

Prior to initiating work reported herein, Hamilton Standard had developed a technique of applying a well-bonded layer of pure nickel on a flat titanium surface using an electrolytic plating process. This technique was

138
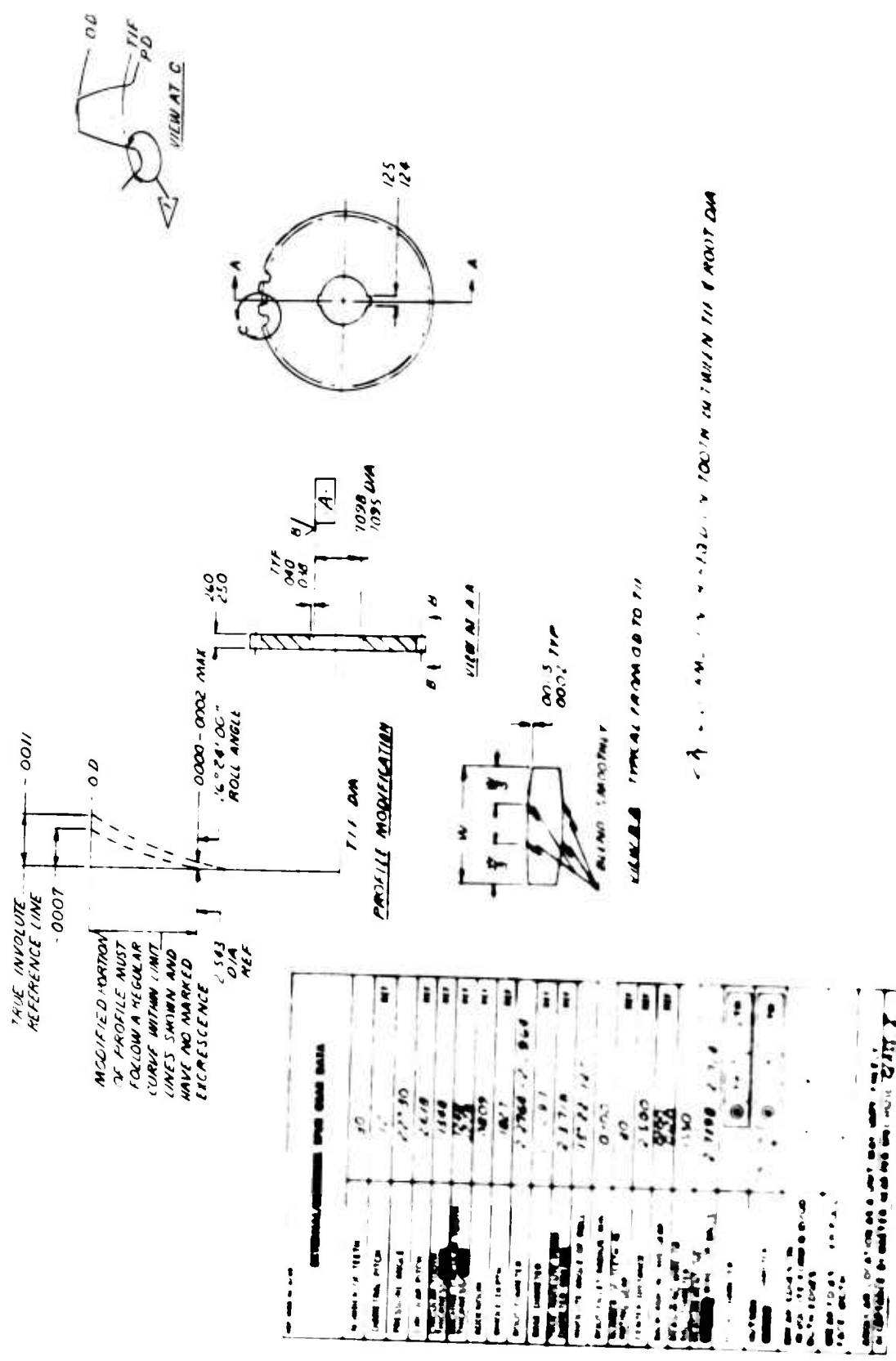
Figure 71. 12-Pitch Titanium Test Gear
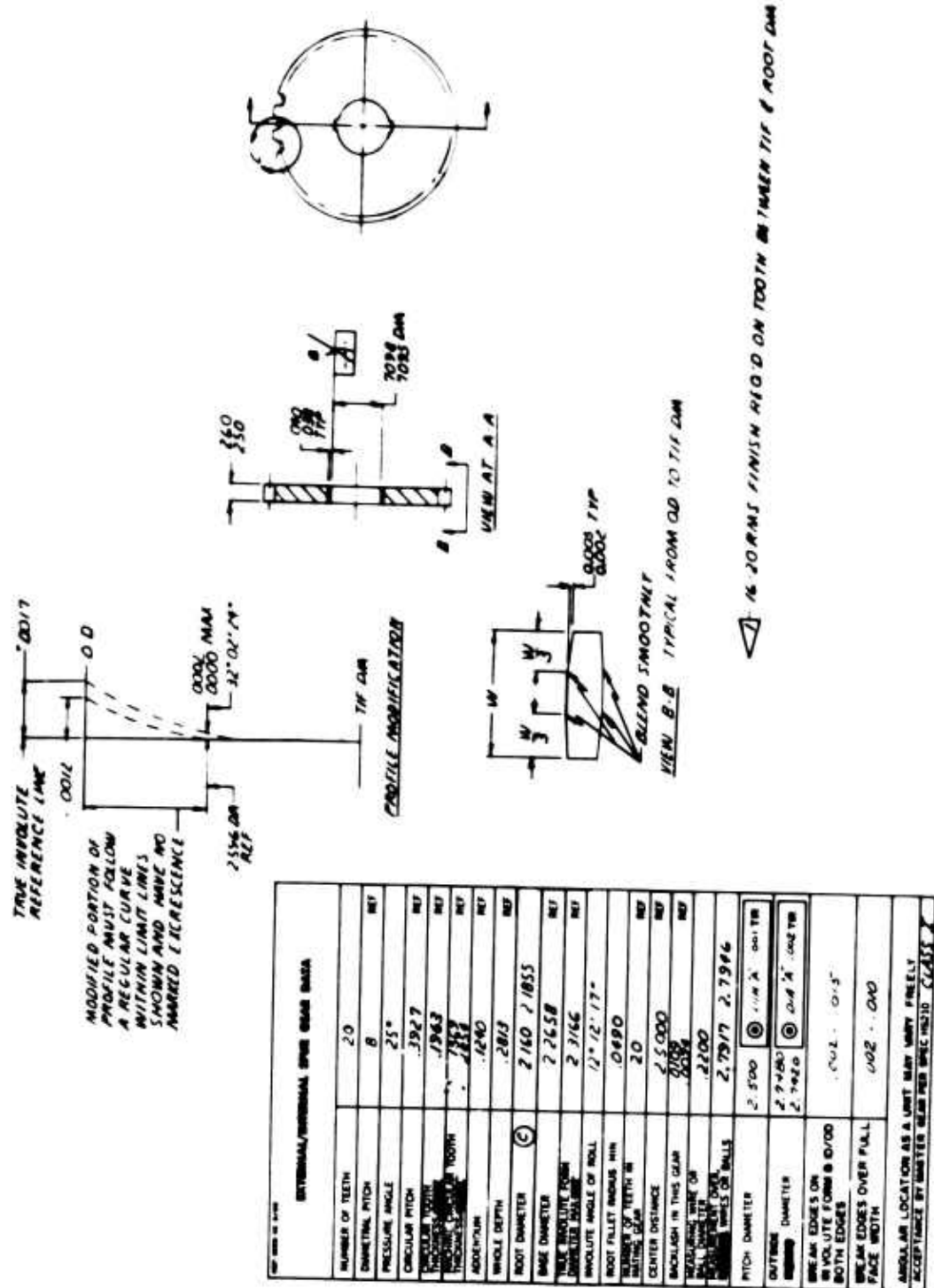
Figure 72. 8-Pitch Titanium Test Gear
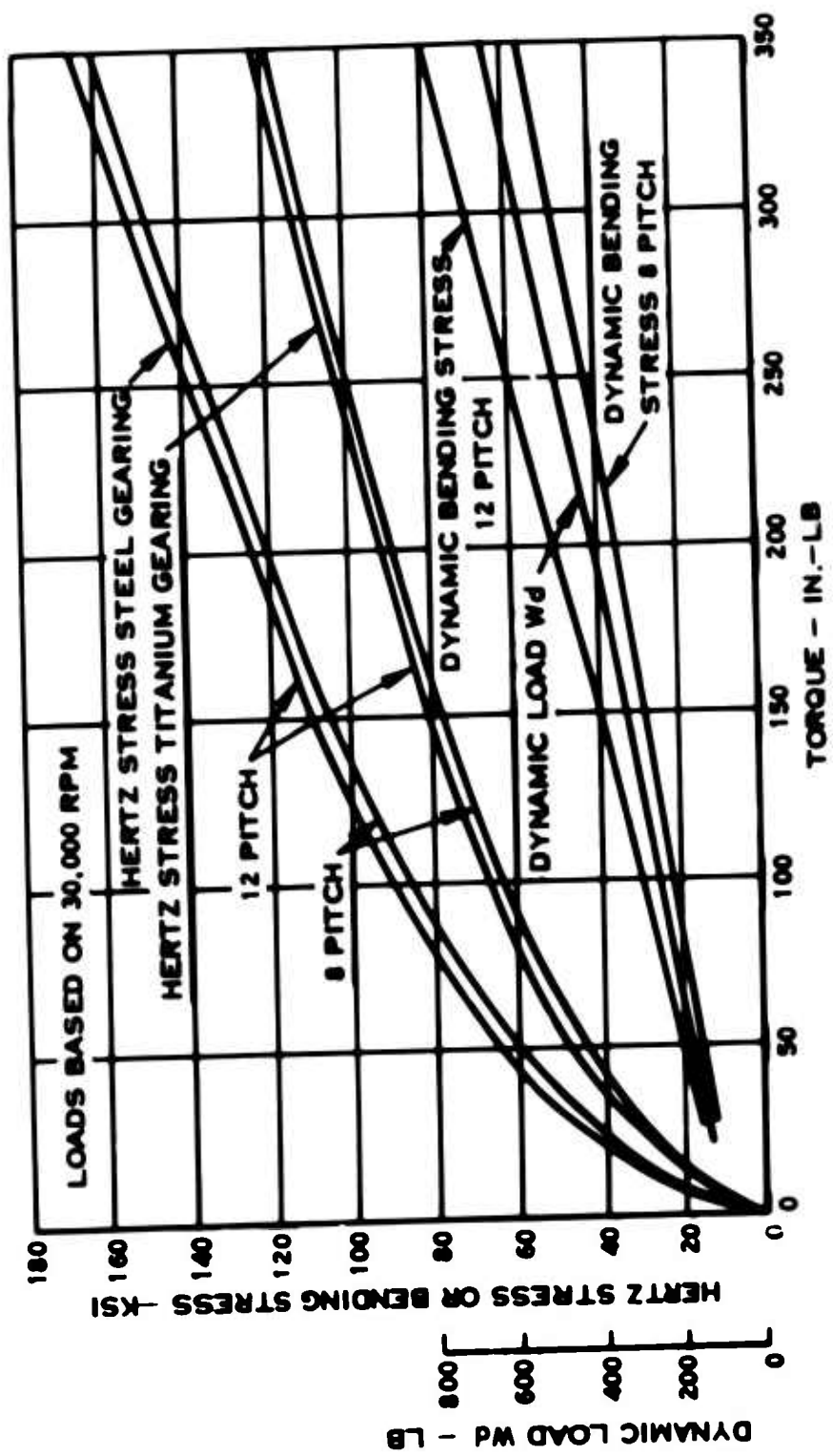
Figure 73. Test Gear Load Data.

141
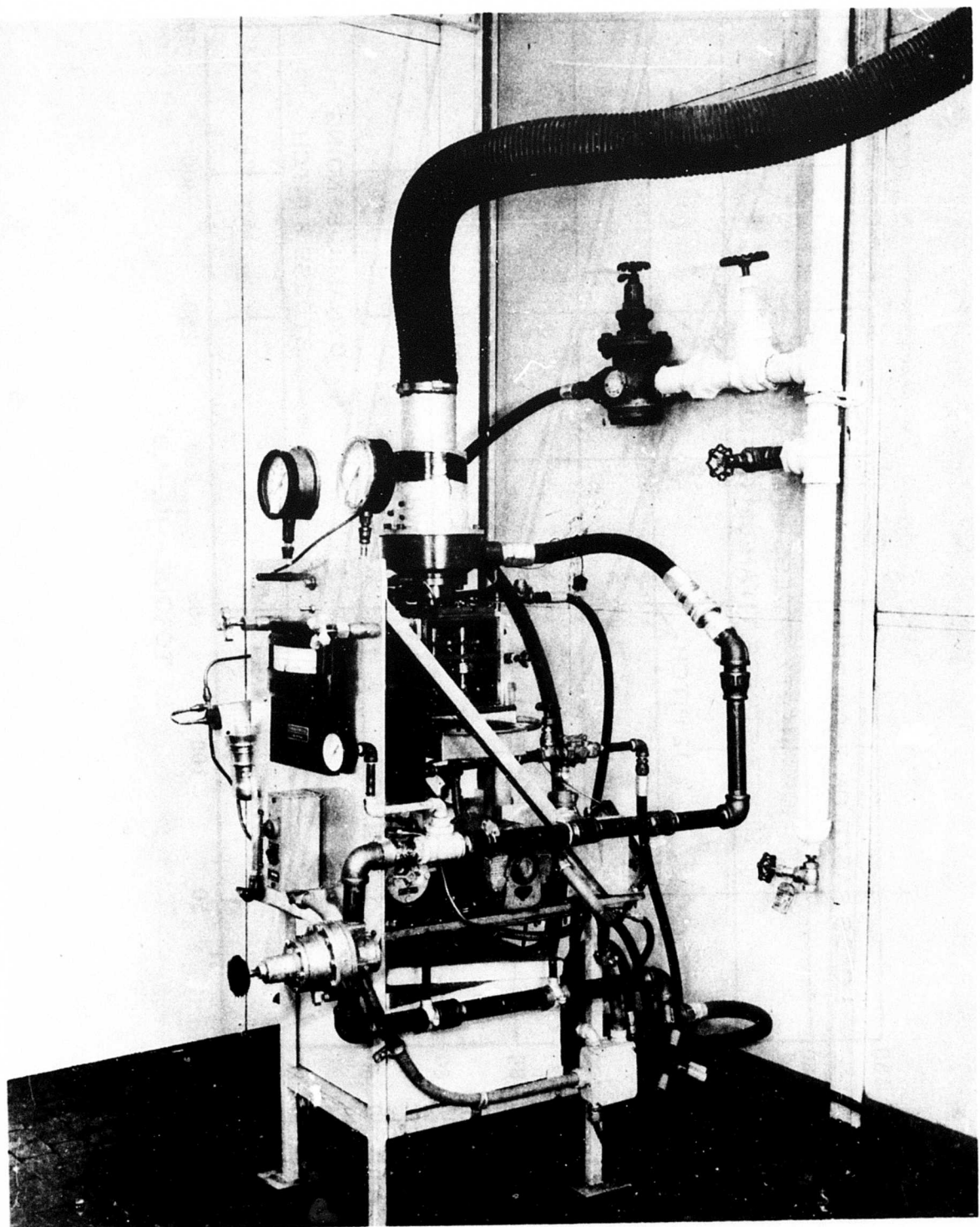
Figure 74. Four-Square Gear Tester.
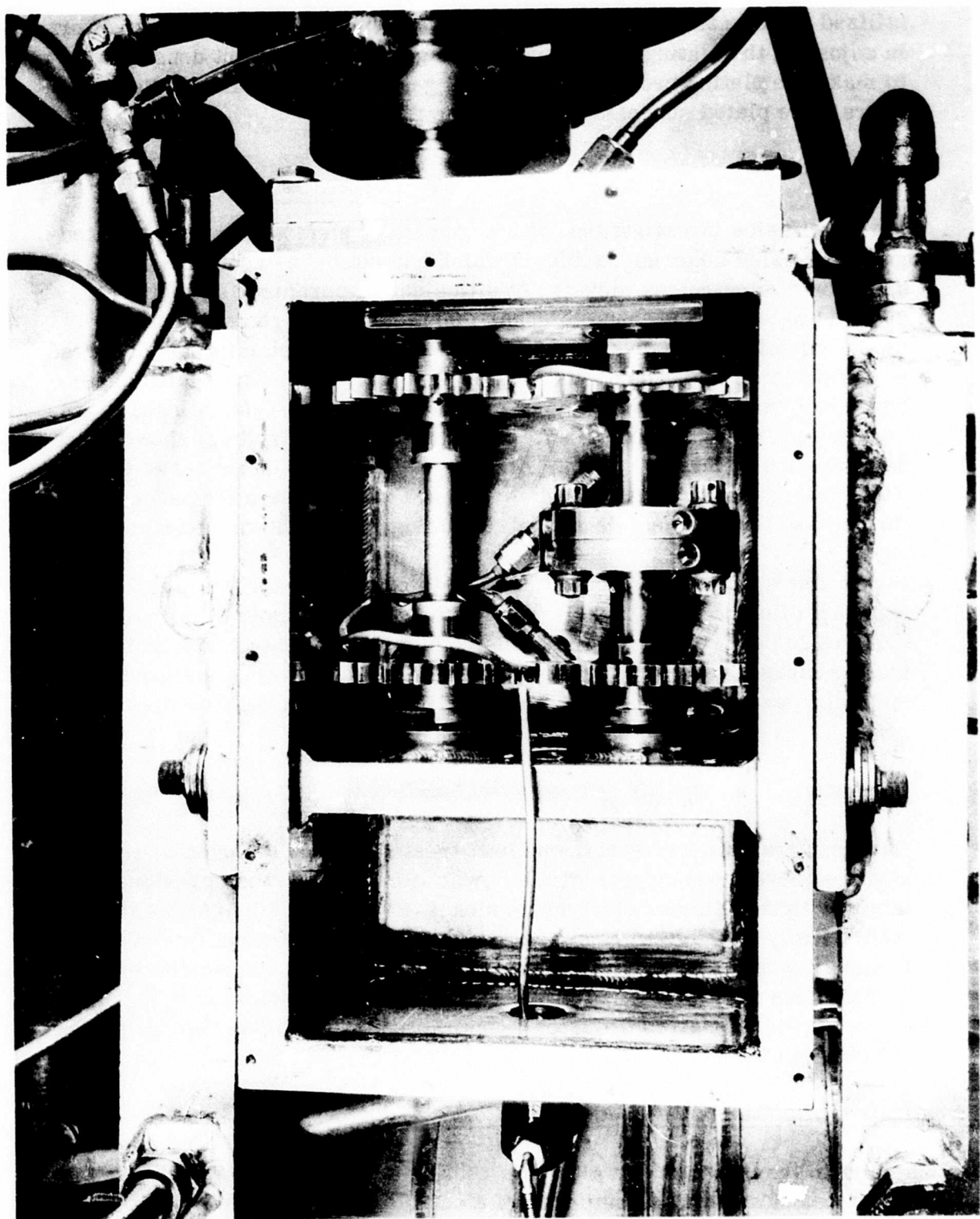
Figure 75.   Four-Square Gear Tester.

utilized to plate titanium gear teeth and required some development effort
in adjusting the plating conditions (anode geometry, current density, etc.)
to make the plating process suitable for gear teeth application. Several
gears were plated successfully with pure nickel.

Diffusion

Initial diffusion investigations with segments of electrolytic nickel-plated
gears revealed adhesion problems which had not been encountered with the
diffusion of electroless nickel. At diffusion temperatures up to 1550°F,
severe blistering was found to occur primarily in the roots of the gear
teeth. Metallurgical investigations showed that the delamination occurred
at some point during the diffusion process; i.e., the intermetallic layers
began to form but not in sufficient magnitude to prevent delamination. In-
vestigations of higher diffusion temperatures (1650°F and up) showed that
delamination could be avoided. At 1650°F, sufficient thickness of the
Ti_2Ni intermetallic layer (which forms next to the base material) could be
formed and thus prevent delamination during the cooldown cycle.

It was also apparent that the diffusion rate of pure nickel was much slower
than that of electroless nickel. This difference in the rate of diffusion is
believed to be a result of phosphorus' combining with the nickel (in the elec-
troless nickel process) to cause exothermal reactions and thus produce
spike temperatures within the intermetallic layers during the diffusion pro-
cess.

Hardness

Hardness traverses of specimens heat treated at 1650°F revealed that the
hardness levels were considerably lower (Rc 30) than those previously ob-
tained with the diffused electroless nickel (Rc 60 - Rc 70). Although it was
theoretically possible to raise the hardness of the intermetallics after dif-
fusion, it was deemed to be not practical because of the necessity to heat
coated parts in a vacuum (to prevent oxidation of the titanium) to a temper-
ature above the desired diffusion temperature (1650°F) and then to quench
the part in oil.

Investigation of a Duplex Diffused Nickel Coating

At this point in the program, an alternate coating approach was investigated
which consisted of applying a thin layer of electroless nickel and then a layer of
pure (electrolytic) nickel to the gear teeth prior to diffusion. The reasoning be-
hind this approach was that the electroless nickel would provide good adhesion
and hardness for the intermetallic layers during diffusion, the layer of pure nickel

144

would absorb some of the phosphorus in the electroless nickel during diffusion and thus would provide a means of reducing the overall phosphorus content of the intermetallic coating.

Selection of Coating Parameters for Duplex Diffused Nickel Coating

A scrap 30-tooth titanium gear was plated using the duplex system (0.4 mil of electroless nickel plus 1.0 mil of pure nickel). An as-plated gear tooth is shown in Figure 76. It should be noted that the thickness of electroless nickel is quite uniform, while the thickness of pure nickel varies from approximately 1.2 mils at the root to 1.6 mils at the tip. The variation in thickness of the pure nickel is due to the fact that it is deposited "electrolytically". This would be expected in plating a gear tooth shape using this type of plating technique. However, the rate at which the intermetallic layers form during diffusion is independent of the thickness of pure nickel (as long as the supply of nickel on the gear tooth surfaces is not exhausted); therefore, a uniform intermetallic coating is produced. Excess (undiffused) nickel is removed after the diffusion cycle.

Hardness of Duplex Diffused Nickel Coating

Segments cut from a duplex-nickel-plated 30-tooth gear were subjected to diffusion cycles of 1450°F for 4 hr and 1550°F for 1 hr. The results of this investigation revealed excellent adhesion and substantially higher hardnesses than previously experienced with the diffusion of pure nickel alone into titanium. Hardness rose from Rc 30 with pure nickel to Rc 44 at a diffusion temperature of 1450°F and to Rc 58 at a diffusion temperature of 1550°F with the duplex-coating approach.

A duplex nickel-plated gear tooth segment diffused at 1550°F for 1 hr is shown in Figure 77. Note layer identification and hardness.

Additional investigations (using titanium tab specimens) were made to evaluate hardness and layer formations resulting from various combinations of plating thicknesses and diffusion cycles. From this study, three sets of coating parameters were chosen for evaluation on actual test gearing. The specific coating procedures used for the initial test gear evaluations are discussed in a later section on Process Optimization Testing.

Removal of Excess (Undiffused) Nickel

All of the thermally diffused nickel-coating processes investigated by Hamilton Standard have had one thing in common. A thin layer of nickel remains on the surface after the diffusion process, and it has been found necessary

145

50X

PURE NICKEL

ELECTROLESS NICKEL
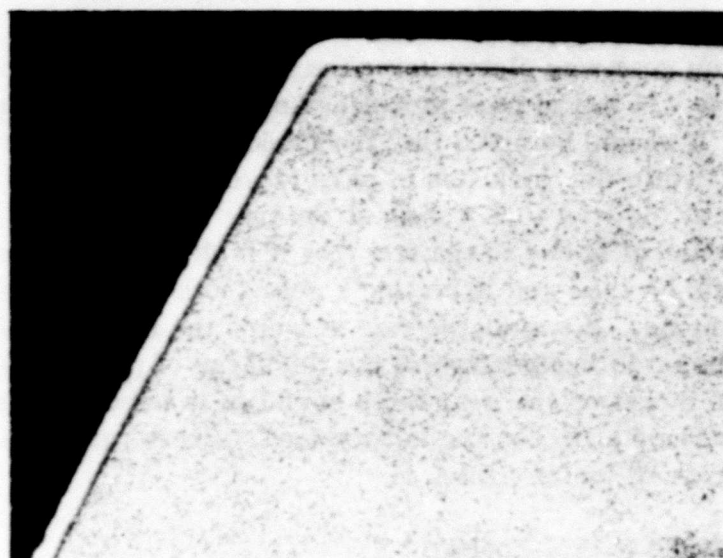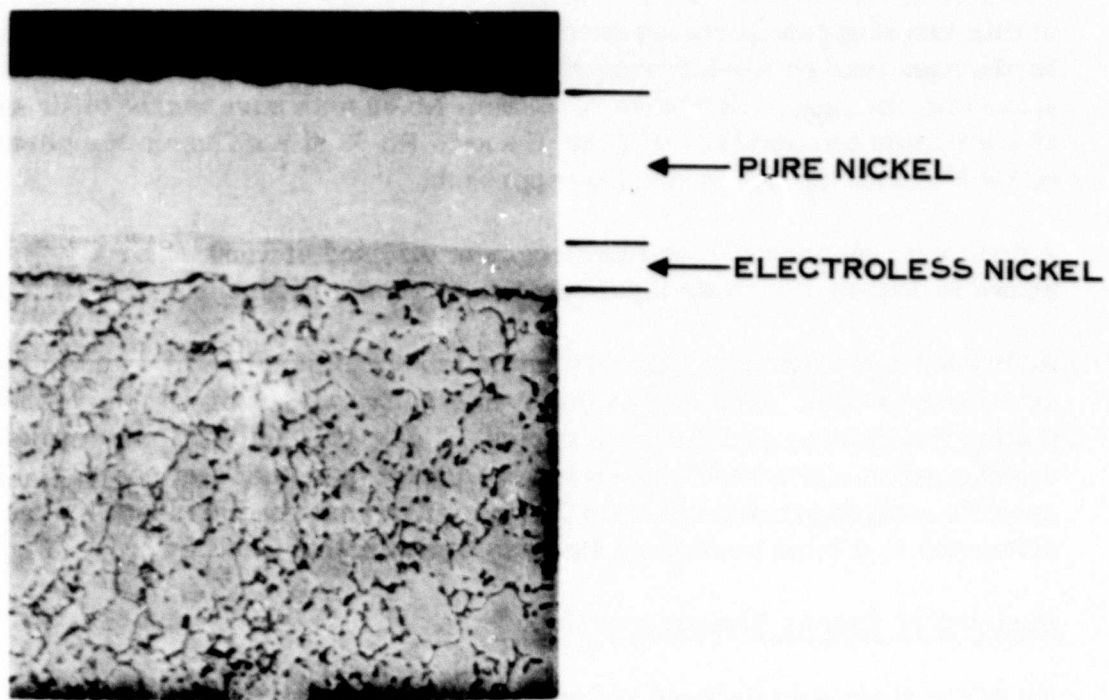
500X

Figure 76. Duplex Nickel-Plated Gear Segment.

146

50X

←— HARD NICKEL SHELL
←— INTERMETALLIC ZONE

←— EXCESS NICKEL

←— TiNi3 } 58.5 RC
←— TiNi }
←— Ti2Ni } 56.5 RC
←— TRANSFORMED BETA 42.0 RC

←— $\alpha + \beta$ 32.0 RC

500X
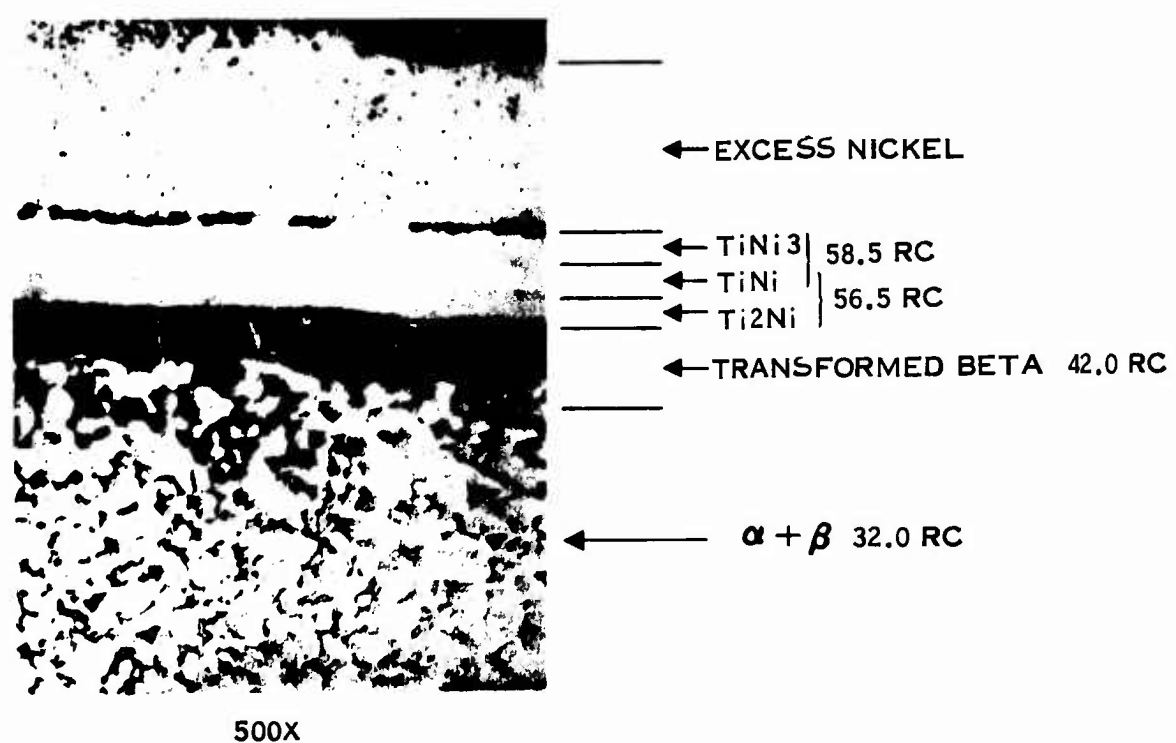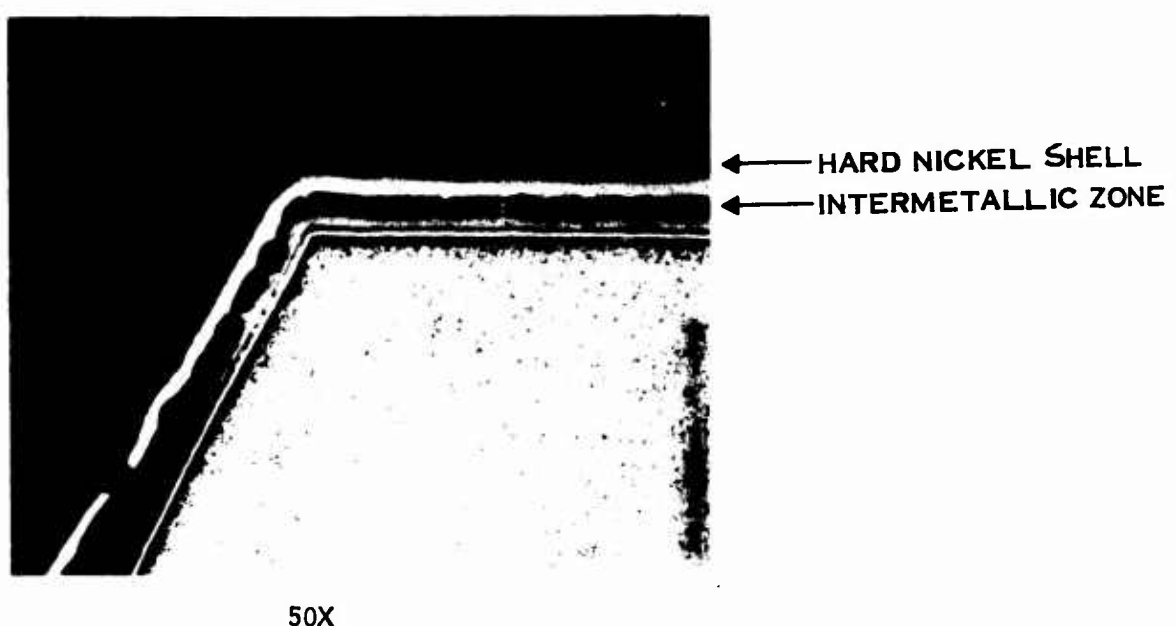
Figure 77.   Duplex Nickel-Plated Gear Segment - 1550°F, 1 Hour.

147

to remove this outer layer in order to have the titanium-nickel intermetallic layers serve as the wearing surface. With the electroless nickel process, the excess nickel was hard and brittle and could be adequately removed by shot peening. With the electrolytic (pure) nickel, the excess nickel was relatively soft and had to be removed chemically. The duplex nickel process, being a combination of both, led to an investigation of both shot peening and chemical etching in order to determine the best method of removing excess nickel with this coating process.

The investigation for removing excess nickel was carried out simultaneously with the preparation of the initial set of test gearing. Gears S/N 214 and S/N 215 were coated with 0.4 mil of electroless nickel plus 1.0 mil of pure nickel and were subjected to a 1550°F 1-hr diffusion cycle. A gear segment consisting of 3 teeth (see Figure 78) was processed simultaneously with these gears to serve as a test piece for determining the best method of removing the excess nickel.
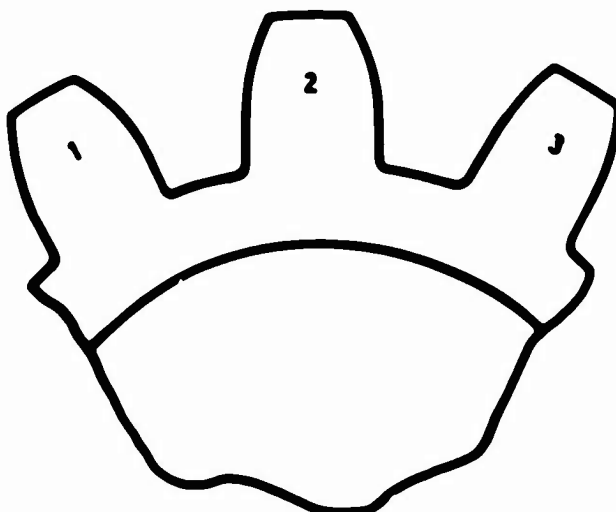
Figure 78. Sketch of a Gear Segment.

Tooth No. 3 in Figure 78 was shot-peened (0.010-in.-diameter steel shot at 80 psi) for approximately 10 min. This resulted in complete removal of the excess nickel on the sides; however, a small patch of nickel remained at the center of the wearing surface of the tooth which could not be removed. Tooth No. 1 and tooth No. 2 were etched in 40% HNO_3 for 2 hr and 4 hr, respectively.

A photomicrograph of this gear segment revealed that both the 2-hr and 4-hr etching cycles removed all excess nickel while leaving the intermetallic layers intact. A corner of tooth No. 2 after etching is shown in Figure 79a. That portion of tooth No. 3 that retained some excess nickel after
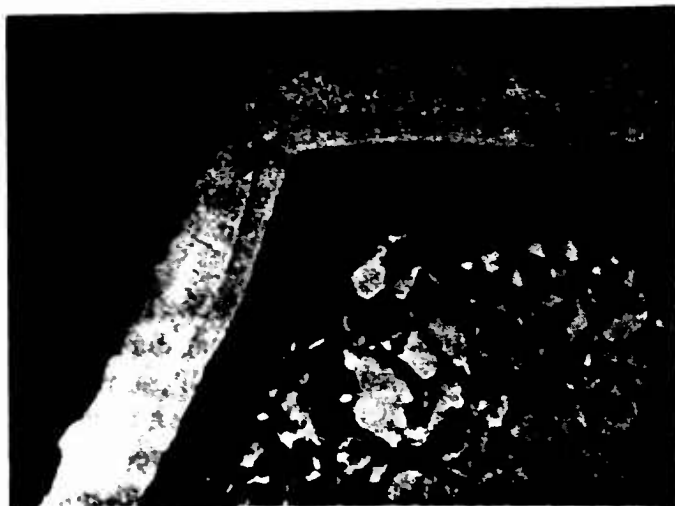
(a)
Titanium gear segment - Etched
4 hr in 40% HNO3 to remove
excess (undiffused) nickel after
1550°F 1-hour heat treatment.
(500X)

(b)
Titanium gear segment. Excess
nickel partially removed by
peening after 1550°F 1-hour
heat treatment.
(500X)
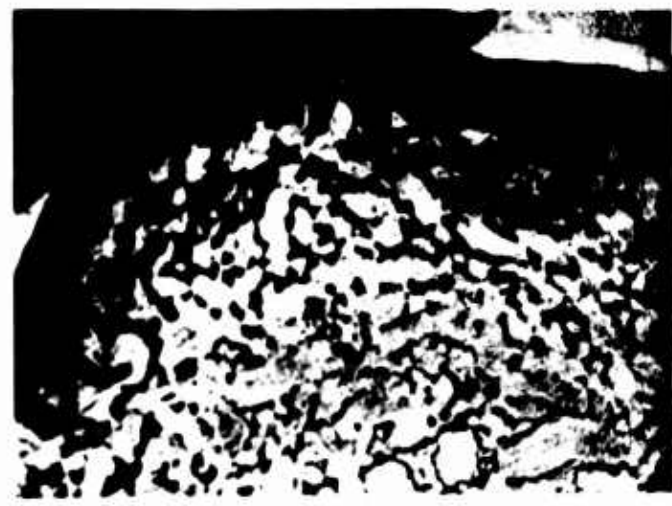
(c)
Titanium gear segment. Corner
of tooth broken thru intermetal-
lic layers after peening to
remove excess nickel.
(500X)

Figure 79. Removal of Excess Nickel After Diffusing

149

peening is shown in Figure 79b. (The apparent separation of the patch of excess nickel is due to preparation of the microsection of the gear tooth.) A corner of tooth No. 3 after peening is shown in Figure 79c. Comparing Figures 79a and 79c, it is noted that the intermetallic coating was broken away from the corners of the peened gear tooth, while the coating on the corners of the etched teeth was undamaged.

Based on the above investiagtion, the excess nickel on gears S/N 214 and S/N 215 was removed chemically using the 2-hr etch. All subsequent duplex nickel-plated gears were processed similarly. After etching, all gears were shot-peened (0.010-in.-diameter steel shot at 45 psi) in order to retain the benefit of improved fatigue strength. However, note that the peening intensity was reduced from that normally used for removing excess nickel in order to avoid damage to the intermetallic layers at the corners of the gear teeth.

A detailed description of the coating procedure used to coat test gearing is given in Appendixes III and IV.

Investigation of Ion-Sputtered Titanium-Nickel Intermetallic Coatings

A coating technique known as "ion sputtering" offered a means of coating titanium with the same titanium-nickel intermetallic compounds as obtained via the thermal diffusion of nickel plate. The following potential advantages of the ion-sputtering approach made it desirable to evaluate this type of coating process:

1. High thermal treatments (which degrade base material fatigue strength) could be avoided.

2. Coating thickness would not necessarily be limited to 0.001 in. as is the case with diffused nickel.

3. The intermetallics would be compositionally correct and could be applied individually or in combinations to gear tooth surfaces.

4. Phosphorus would not be present in the coating.

How Ion Sputtering Works

The schematic of an ion-sputtering facility shown in Figure 80 provides a basic description of how the process works. A chamber is evacuated. Argon is then introduced into the chamber, providing a partial atmosphere of the gas. A target (coating material) and a substrate (titanium gear)

150
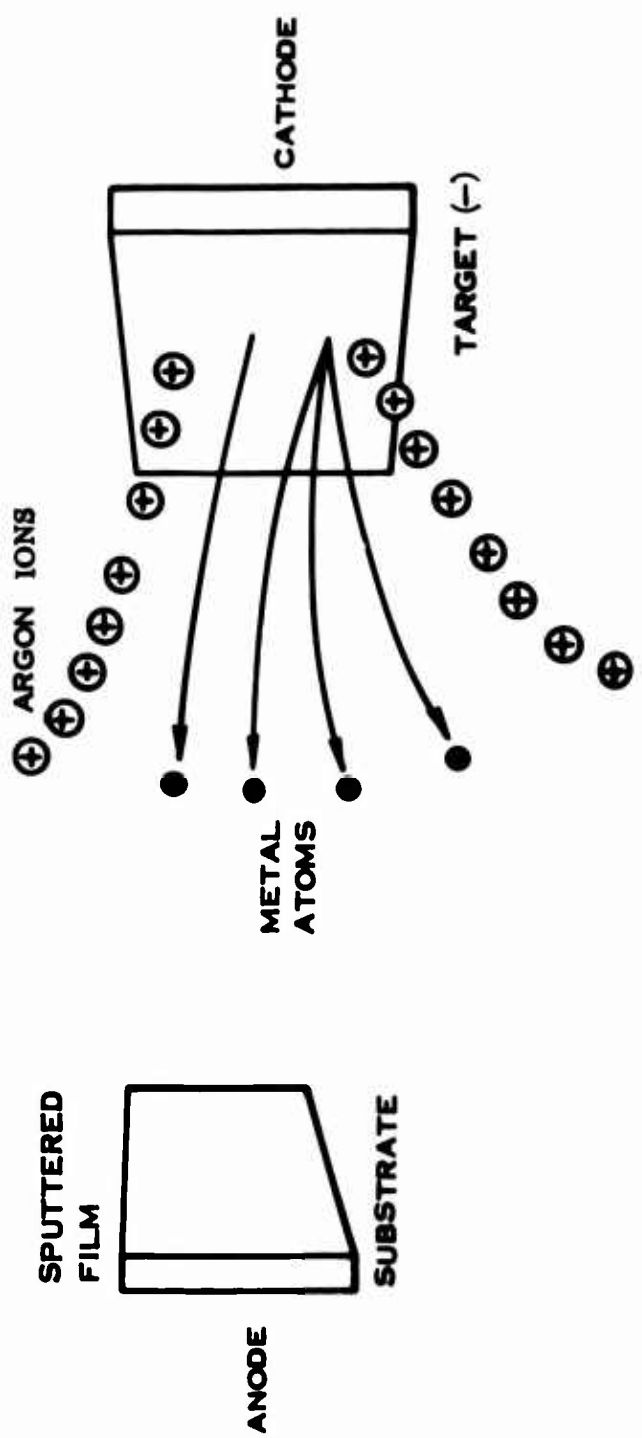
Figure 90. Schematic of an RF Sputtering System.

151

have been placed in the chamber. A voltage potential is placed between the target (cathode) and the substrate (anode). Electrons are drawn from the target material which collide with, and ionize, the argon atoms, giving them a positive charge. The positively charged argon atoms strike the target material with sufficient velocity to dislodge atoms of the target material. The dislodged target atoms in turn move toward the substrate (titanium gear) and strike the substrate with sufficient momentum to effect excellent adhesion to the substrate. The result is a well-bonded, uniform, dense layer of target material formed on the substrate.

Tab Studies

Titanium tabs (2.5 in. x 0.5 in. x 0.04 in. thick) were utilized to establish sputtering rates for the titanium-nickel intermetallic compounds and also served to evaluate coating hardness. Bond strength of ion-sputtered coatings was evaluated via standard bend tests.

The target materials used for the initial development work were in the form of hot-pressed powdered discs (4-in. dia x 0.25 in. thick). The characteristics of the three intermetallics when applied to titanium tabs are summarized in Table XX.

TABLE XX.   CHARACTERISTICS OF ION-SPUTTERED COATINGS

Intermetallic Coating	Hardness Rc	*Bond Strength	Thickness (mil)
$TiNi_3$	30	Excellent	0.95
Ti_2Ni	52	Excellent	0.94
TiNi	60	**Good	0.80

*Bond strength considered to be excellent if no cracking of the coated tab specimen occurred when bent through an angle of 105 deg.

**Fine cracking observed with these specimens after bending through 105 deg.

Coating of Test Gears

Based on the evaluations of ion-sputtered tabs, four gears were processed for rig evaluation. One set (S/N 116 and S/N 121) was coated with Ti_2Ni. The second set (S/N 117 and S/N 120) was coated with TiNi. The $TiNi_3$ was felt to be too soft to justify its evaluation on actual test gearing.

With the exception of the Ti_2Ni, the target materials used in the hot-pressed powered form tended to disintegrate after prolonged use in the sputtering chamber. Therefore, the gears coated with TiNi were coated using a target

152

manufactured by electron beam melting procedures. No postcoating heat treatments were employed in the evaluation of ion-sputtered coated gears.

The specific technique employed to coat gears using the ion-sputtering process was restricted due to the limitations imposed by the facilities available at the time to coat gears. The facilities available during this program were considered adequate for an initial feasibility study of ion-sputtered coated gears. For coating work conducted under this program, a flat target (shape) had to be utilized. This required that the gear to be coated be rotated perpendicular to the target during the coating procedure. This arrangement is shown in Figure 81.
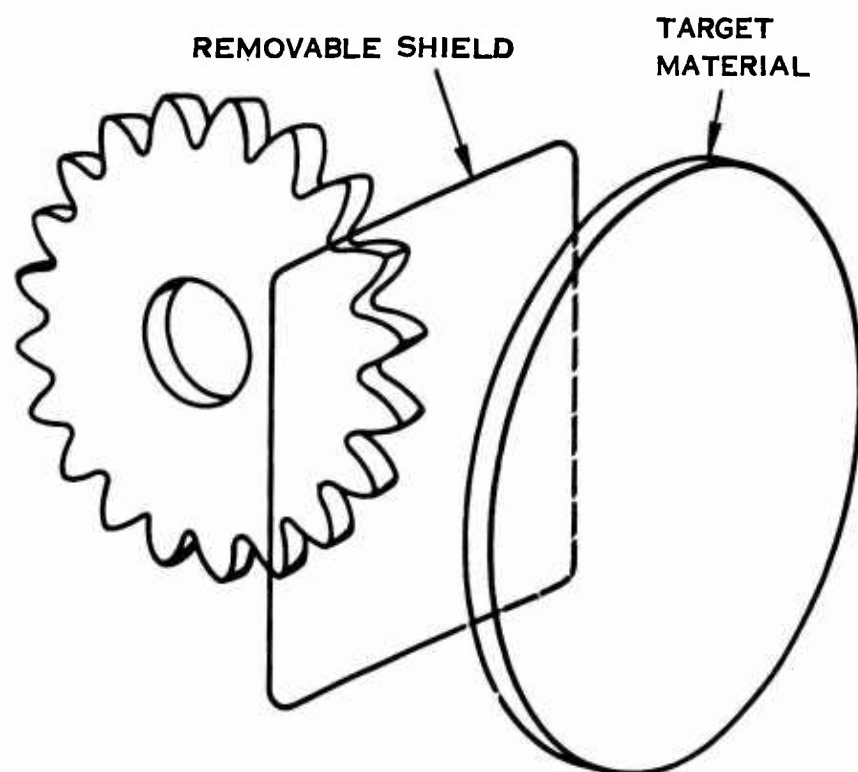
Figure 81. Arrangement Used To Sputter-Coat Gears.

During the initial sputtering work with tab specimens, it was found that sputter cleaning (reverse sputtering) was essential for titanium (due to its instantaneous oxidation characteristics) in order to ensure that the coating would adhere well to the titanium substrate. Sputter cleaning was accomplished by placing a shield between the titanium and the target material such that the titanium could be atomically cleaned prior to being coated.

153

Once the desired cleaning had been accomplished, the shield would be removed, polarity would be reversed, and the coating procedure would be initiated.

With the titanium tab specimens, this cleaning procedure worked quite well because all of the major components were stationary. The same cleaning procedure was used in coating the actual gears, but it was not as effective due to the requirement to rotate the gear during both the cleaning process and the coating process.

The sputtering rate was such that it took approximately 4 hr to deposit 1 mil of the coating on the titanium gear teeth, whereas an equivalent coating thickness could be deposited on stationary tabs in 90 min. The difference in sputtering rate is due to stationary versus rotating substrates and is theoretically affected by a factor of π as shown by the following series of equations.

The sputtering diagram shown in Figure 82 is useful in analyzing the difference in sputtering rates for stationary and rotating substrates.
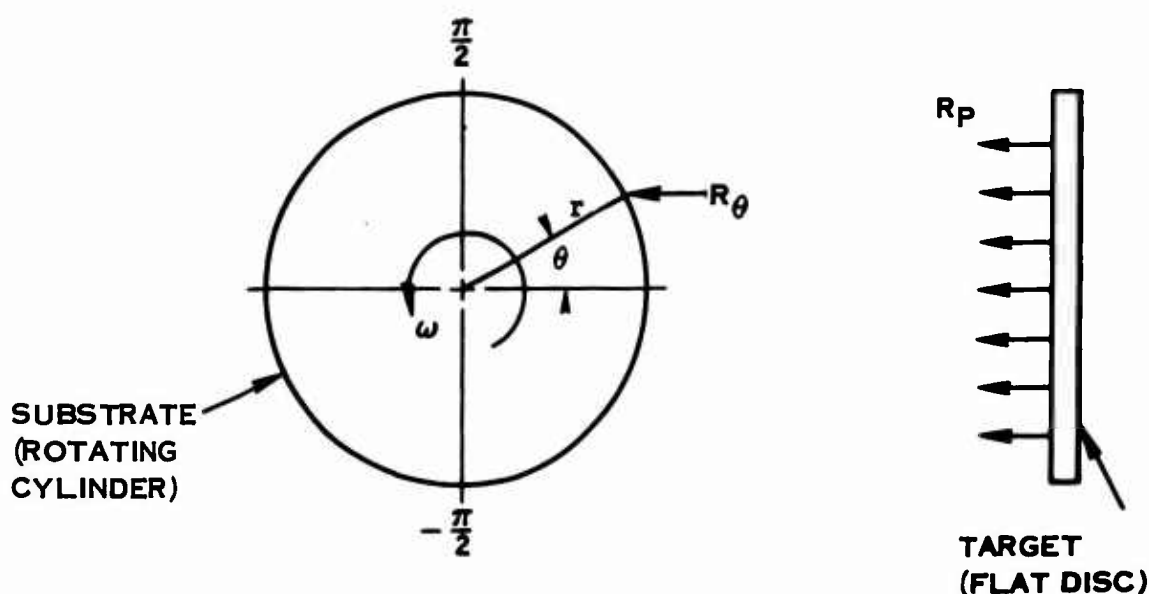
Figure 82. Sputtering Rate Diagram.

In Figure 82,

R_p = sputtering rate measured using a flat target with a cylindrical rotating substrate (in./min)

R_Θ = sputtering rate measured at any point on the surface of the rotating cylinder (in./min)

ω = angular velocity of the cylinder (rad/min)

r = radius of the cylinder (in.)

Θ = angle of rotation (rad)

The relationship between R_Θ and R_p is expressed as

$$R_\Theta = R_p \cos \Theta \tag{71}$$

The total thickness of coating T_1, deposited at the angle Θ, for a time t, for 1 revolution is

$$T_1 = R_\Theta \, t \tag{72}$$

For an extremely small coating thickness,

$$dT_1 = R_p \cos \Theta \; dt \tag{73}$$

where

$$dt = \frac{r\,d\Theta}{2\pi\,r\,\omega} \tag{74}$$

Substituting in equation (73),

$$dT_1 = \frac{R_p \cos \Theta \; d\Theta}{2\pi\,\omega} \tag{75}$$

The thickness of coating obtained during one revolution is found by integrating equation (75),

$$T_1 = \int_{-\frac{\pi}{2}}^{-\frac{\pi}{2}} \frac{R_p \cos \Theta \, d\Theta}{2\pi\,\omega} = \frac{R_p}{\pi} \tag{76}$$

155

The total thickness of coating T_N for many revolutions would be

$$T_N = T_1 \Theta_T \qquad (77)$$

where $\qquad \Theta_T$ = the total angle of rotation (rad)

The total angle of rotation is then expressed as

$$\Theta_T = \omega t_T \qquad (78)$$

where $\qquad t_T$ = total time (sec)

Substituting in equations (76) and (77), the total coating thickness for a rotating substrate is found to be

$$T_N = \frac{R_p \ t_T}{\pi} \qquad (79)$$

An alternate method (not used during this program) of sputter coating gears is illustrated in Figure 83. This type of an arrangement would be used for any future work with ion-sputtered coated titanium gearing.

The sputtering arrangement shown in Figure 83 uses a cylindrical target material shape that surrounds the gear to be coated. A removable cylindrical shield is placed between the target and gear to permit sputter cleaning to be accomplished. Several improvements (such as those listed below) would be expected using this type of sputtering arrangement compared to the actual arrangement that was used.

1. Sputtering rates could be oj'imized. (Sputtering would be accomplished in a radial directio: thus eliminating the need for rotating the part to be coated.)

2. Sputter cleaning could be effectively accomplished in that all portions of the gear to be coated would be simultaneously subjected to the cleaning process. The coating of the gear teeth would be initiated in a similar fashion.

3. Depending on the particular gear configuration, several gears could be coated simultaneously.

156

REMOVABLE
CYLINDRICAL
SHIELD

CYLINDRICAL
TARGET

GEAR

STATIONARY SHAFT
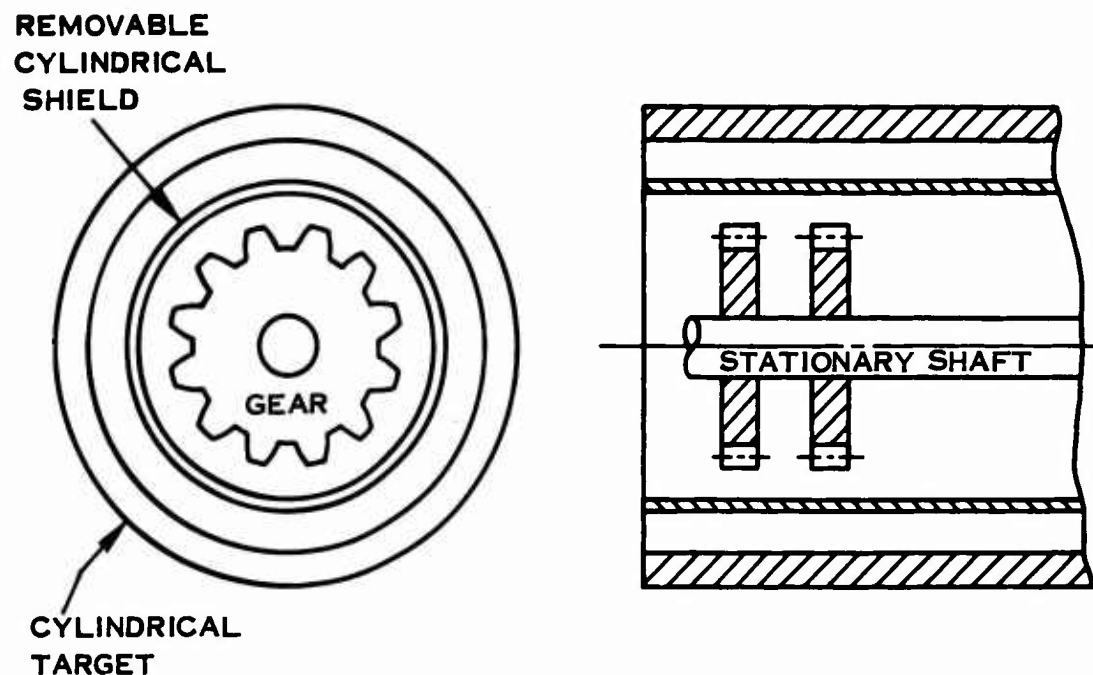
Figure 83. Recommended Arrangement for Sputter Coating Gear Teeth.

LABORATORY TESTING

General Test Requirements

Coating Selection

1. Duplex Diffused Nickel Coating – In order to establish a basis for selecting specific combinations of plating thickness and diffusion heat treatments for subsequent evaluation of this type of coating process on actual titanium gearing, a metallurgical investigation was conducted using titanium test panels to determine the effects

157

of these process variables on the characteristics of the inter-
metallic coating. For this study, two combinations of duplex
nickel-plating thickness were used.

    a.   0.4 mil of electroless nickel plus 1.0 mil of pure nickel

    b.   1.0 mil of electroless nickel plus 1.0 mil of pure nickel

Photomicrographs of titanium tabs in the as-plated condition prior
to diffusion are shown in Figure 84.

Titanium test panels with the above combinations of nickel plating
were subjected to diffusion temperatures of 1450°F, 1550°F,
1650°F, and 1750°F. At the 1450°F diffusion temperature, diffu-
sion times of 4 hr, 8 hr, and 12 hr were investigated. The
diffusion rate becomes quite rapid at temperatures above 1450°F;
therefore, the diffusion time investigated for diffusion tempera-
tures above 1450°F was maintained at 1 hr. Figures 85, 86, 87,
and 88 contain photomicrographs of the various microsections
made of the coated titanium tabs after diffusion.

A study of the hardness gradient as well as the general appearance
of the diffusion zone obtained with titanium tab specimens provided
the basis for selection of specific process parameters for subse-
quent gear evaluations. Maximum hardness at the surface with a
steadily decreasing hardness in a direction toward the base mater-
ial was desirable. In several cases, a soft intermediate zone was
found to exist within the coating such as shown in Figure 85b. At
diffusion temperatures of 1650°F and 1750°F, a substantial
amount of transformed beta material had formed (see Figures 87
and 88). This was considered undesirable for a gear tooth coating.
Those coatings shown in Figures 86, 87a, and 88a were selected
for evaluation on actual test gearing.

2.   <u>Ion-Sputtered Coatings</u> - Specific titanium-nickel intermetallic
    compounds were chosen for evaluation on actual gearing based on
    the thickness, hardness, and adherence of the coating as sputtered
    on titanium test panels.

<u>Inspection of Test Gearing</u>

Inspection records of each gear as machined and after coating were
maintained. Involute profiles, measurement over wires, tooth-to-tooth

ELECTROLESS NICKEL

PURE NICKEL

(B) 1 MIL OF ELECTROLESS NICKEL PLUS 1 MIL OF PURE NICKEL

ELECTROLESS NICKEL

PURE NICKEL

(A) 4 MIL OF ELECTROLESS NICKEL PLUS 1 MIL OF PURE NICKEL
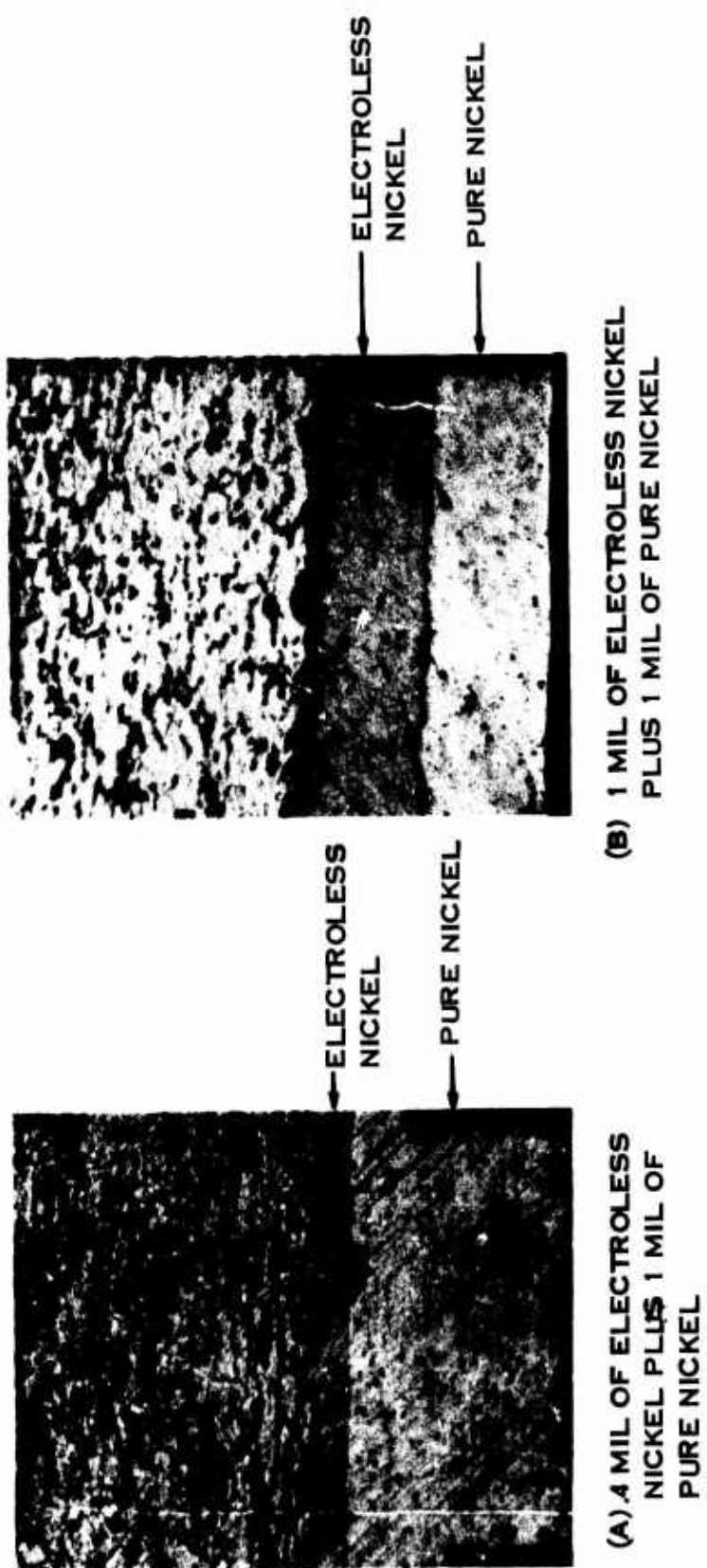
Figure 84. Duplex Nickel-Plated Titanium Tabs Specimens Prior to Diffusion (500X).

159
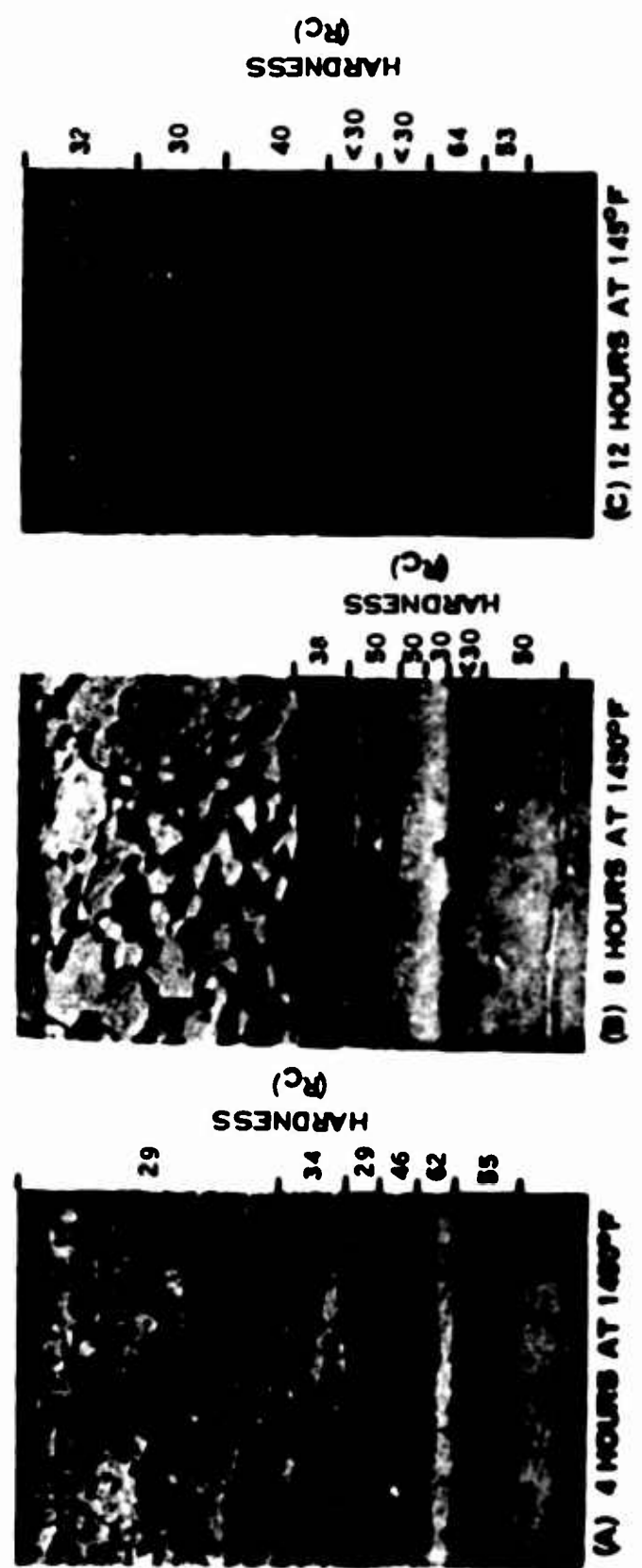
Figure 85. Effect of Diffusion Time on Duplex Nickel-Plated (1 Mil of Electroless Nickel Plus 1 Mil of Pure Nickel) Titanium Tabs at a Diffusion Temperature of 1450°F (500X).
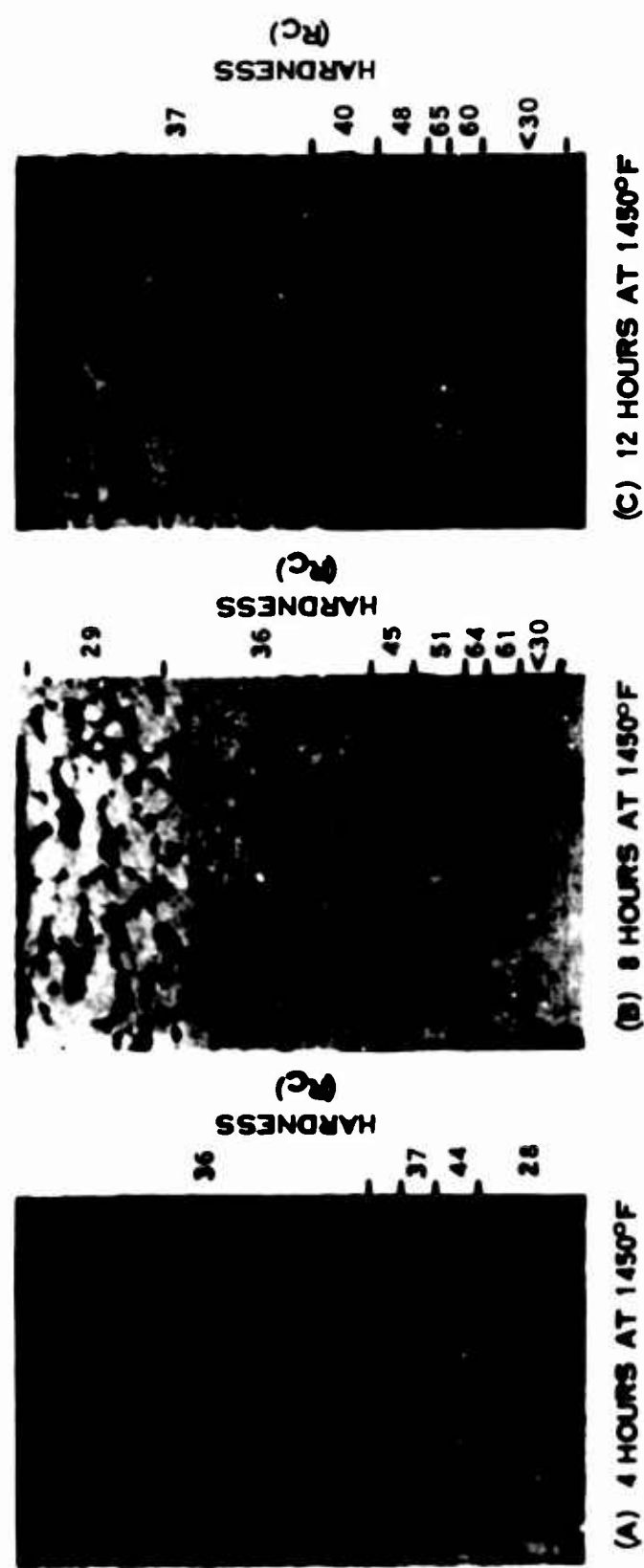
Figure 96. Effect of Diffusion Time on Duplex Nickel-Plated (0.4 Mil of Electroless Nickel Plus 1 Mil of Pure Nickel) Titanium Tabs at a Diffusion Temperature of 1450°F (500X).

Figure 87. Effect of Diffusion Temperature on Duplex Nickel-Plated (0.4 Mil of Electroless Nickel Plus 1 Mil of Pure Nickel) Titanium Tabs (500X).

162
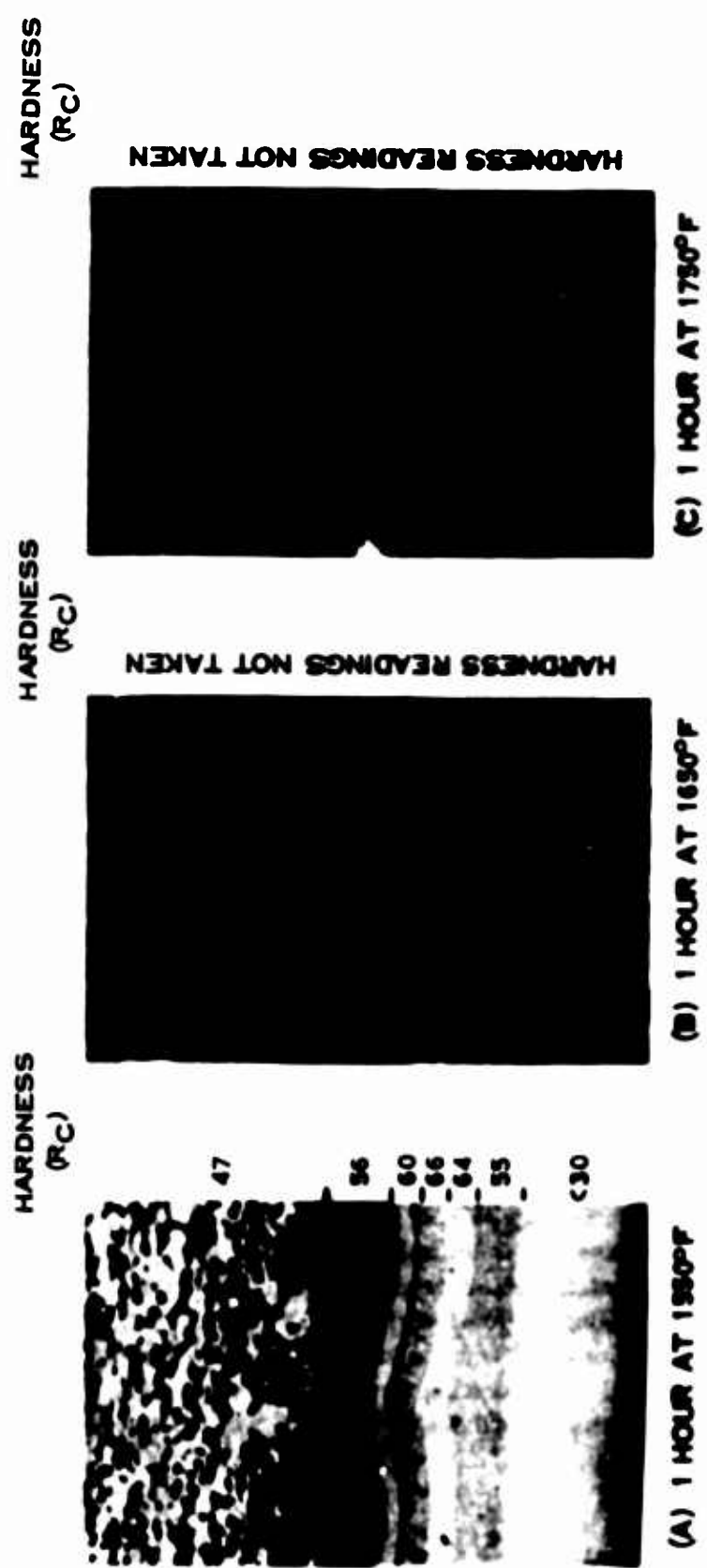
Figure 88. Effect of Diffusion Temperature on Duplex Nickel-Plated (1 Mil of Electroless Nickel Plus 1 Mil of Pure Nickel) Titanium Tube (500X).

spacing error, and root diameter were recorded using 4 teeth randomly selected for each gear. The high and low points (pitch runout) were also recorded. Corresponding high and low points for mating gears were matched (when possible) during assembly of the gears for testing. The method used to calculate tooth loads is given in Appendix I.

Method Used To Monitor Tooth Load

After applying the torque necessary to provide the desired Hertz stress loading and after operating the test gears under load for specified periods of time, the frictional torque (the torque required to set the gears in motion) was measured. This provided a means of ensuring that the torque initially applied to the gears prior to testing had not changed during testing. Since the frictional torque could vary slightly due to temperature changes and oil film thickness on the gear teeth, it was necessary to measure the frictional torque at as many locations as possible and to use the average frictional torque as a means of monitoring the applied torque. For the 8-pitch gears, 12 frictional readings were taken; for the 12-pitch gears, 16 readings were used.

Gross changes in the average frictional torque after running a set of gears would indicate that a corresponding change in the initially applied torque had occurred during running. A criterion was set up whereby a test level would be discounted if the average frictional torque dropped by more than 5% during the test run. (If the actual torque on the gears dropped 5% after testing, the corresponding change in Hertz stress would be $\sqrt{100\%} - \sqrt{95\%}$.) If the 5% limit were exceeded, the gears would be retorqued after testing, and a new average frictional torque would be recorded. The percentage of change would then be based on the new frictional torque reading.

Process Optimization Testing (120 Hours)

Purpose

The purpose of this phase of testing was to establish the optimum procedure for placing a titanium-nickel intermetallic coating on titanium gear teeth. This investigation included evaluation of the effect of coating process variations (for both a diffusion-type coating and an ion-sputtered-type coating) on load-carrying capacity. This testing would provide the basis for selecting a specific coating process for subsequent endurance testing.

164

Evaluation of Duplex Diffused Nickel-Plated Gears

Based on the metallurgical investigations of titanium tab specimens incorporating a duplex thermally diffused nickel coating, three pairs of gears were processed for rig evaluation using the coating parameters shown in Table XXI.

		Plating Thickness		
Set Number	Test Gear S/N	Electroless Nickel (mils)	Pure Nickel (mils)	Heat Treatment
1	214 215	0.4	1.0	1,550°F, 1 hr
2	220 223	0.4	1.0	1,450°F, 8 hr
3	221 222	0.1	1.0	1,550°F, 1 hr

TABLE XXI. COATING PREPARATION FOR INITIAL TEST GEARS

The initial set of gears (S/N 214 and S/N 215) was processed through paragraph 4.1 of the Plan of Test (Appendix II). Successful 10-million-cycle tests were completed at Hertz stress levels of 85,000, 95,000, 105,000, and 115,000 psi. A coating failure was encountered after completion of 3.6 million cycles at the 125,000-psi Hertz stress level. All test levels were accomplished at 30,000 rpm. Total test time (including initial break-in running) on these gears was 24.8 hr.

Photographs of gears S/N 214 and S/N 215 after testing are shown in Figures 89 and 90. It should be noted that at the last load level, the steel (drive) gearing had to be replaced with a set of previously tested titanium gears (S/N 200 and S/N 201), due to excessive scoring of the steel gears at this load level. It is believed that the lack of involute profile modification of the steel gears contributed to the scoring at the higher load levels. The steel gears were also exposed to a Hertz stress level of 169,000 psi at this torque level. (Hertz stress for steel is 1.35 times greater than the Hertz stress for titanium for a given torque level.)

Figure 89.   Gear S/N 214 After Testing (5X).
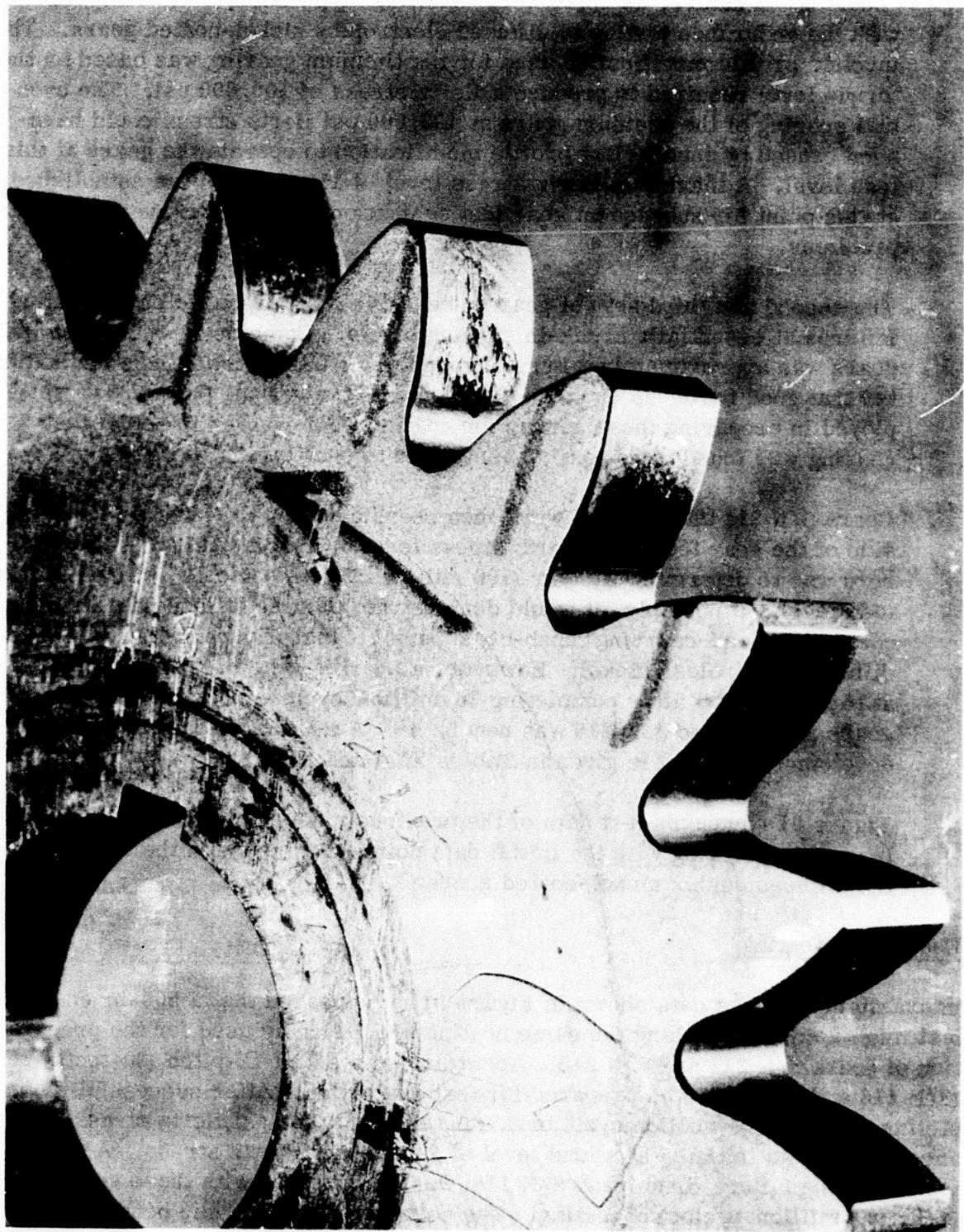
Figure 90. Gear S/N 215 After Testing (5X).

The coating failure encountered with gears S/N 214 and S/N 215 was "scoring" in nature, as opposed to "spalling"-type failures encountered with the endurance testing of diffused electroless nickel-coated gears. The involute profile modification used for the titanium gearing was based on the torque level required to produce a Hertz stress of 100,000 psi. The eventual scoring of the titanium gears at 125,000 psi Hertz stress could have been caused by insufficient profile modification to operate the gears at this load level. A maximum Hertz stress level of 110,000 psi was established at this point for subsequent gear test evaluations in order to avoid scoring problems.

The second and third sets of gears (see Table XXI) produced early coating failures at essentially break-in running levels. Combined test time on these gears was approximately 2 hr. Although prior tab investigations had indicated that good hardness could be obtained with the coating parameters employed in preparing these gears, the coating when applied to actual test gearing was found to be easily susceptible to scuffing and wear.

Gears S/N 214 and S/N 215 were then reevaluated on the reverse (untested) side of the gear teeth at a Hertz stress level of 110,000 psi. The intent here was to determine if 50 hr (100 million cycles) could be attained at this load level. If possible, it would demonstrate that the diffused duplex nickel coating had load-carrying capability superior to that of the previously developed diffused electroless nickel. However, a scoring-type failure was encountered at this load level after completing 36 million cycles. Total test time on gears S/N 214 and S/N 215 was now 52 hr. A summary of all the preliminary development testing is given in Tables XXII and XXIII.

Figure 91 compares test data of the previously developed diffused electroless nickel coating with the initial data points obtained with the testing of the diffused duplex nickel-coated gears.

Endurance Testing

In examining the test data shown in Figure 91, it appeared that a 500-hr endurance test might be feasible using the same coating procedure as used for the preparation of gears S/N 214 and S/N 215. Accordingly, a set of 12-pitch (30-tooth) gears (S/N 118 and S/N 119) was prepared for test evaluation. After successfully completing an initial 10-million-cycle break-in test at 85,000-psi Hertz stress, endurance testing was initiated at a load level of 100,000-psi Hertz stress. A single-tooth-bending failure (from gear S/N 118) was encountered with these gears after 66 hr (80 million cycles) of testing. The corresponding dynamic bending stress

168

Set No.	Gear S/N	*Total Test Time (hr)	Coating Description
1	214–215	57.1	**
2	221–222	1.7	1-mil electroless nickel plus 1.0-mil pure nickel 1550°F 1 hr
3	220–223	0.5	0.4-mil electroless nickel plus 1.0-mil pure nickel 1450°F 8 hr
4	118–119	68.0	
5	117–120	***	Ion-Sputtered 0.8 mil TiNi
6	116–121	***	Ion-Sputtered 0.6 mil Ti_2Ni
7	218–219	***	**
8	216–217	***	**
9	113–114	14.0	**

TABLE XXII. SUMMARY OF PRELIMINARY GEAR TESTING

*Total combined test time is 141.3 hr.

**Coating description for these gears is as follows:
0.4-mil electroless nickel and 1.0-mil pure nickel, diffuse
1550°F 1 hr, 2-hr etch in 40% nitric acid and shot-peen.

***These gears failed at essentially break-in load levels; therefore,
no test time is indicated.

at this load level was 56,000 psi. A photomicrograph of the failed gear tooth is shown in Figure 92. An examination of this photomicrograph showed that there was virtually no coating wear. However, several cracks were observed in the coating near the fractured surface. These cracks were observed on both the tensile and compressive sides of the tooth, although the tooth had been loaded in only one direction. These cracks are shown in Figures 93 and 94.

Examination of other teeth from gear S/N 118 revealed the same type of cracking near the roots of the teeth. All cracks were found to be confined to the coating and were identified as pure fatigue cracks developed from operating the gears at 56,000-psi dynamic bending stress.

Fatigue cracks as such cannot develop from purely compressive (cyclic) stressing. The fatigue cracks that were observed on what would normally be considered the compressive sides of the teeth (because of the direction of loading) were actually caused by cyclic tensile stressing in these areas. Tensile stresses can be imposed

169

| Gear S/N	Hertz Stress (ksi)	Bending Stress (ksi)	Torque (in.-lb)	Cycles x10^6	Time (Min)	Mode of Failure
TABLE XXIII. PRELIMINARY GEAR TEST RESULTS						
214-215 (Side A) vs Steel Gears	75	25.5	126	0.9	30	Wore through coating on two teeth of each gear.
	85	30.3	162	11.8	394	
	95	36.0	205	10.0	334	
	105	42.0	250	9.7	323	
	115	48.0	297	10.0	334	
	125	55.0	351	3.6	120	
214-215 (Side B) vs 221-222 (Side A)	60	20.0	92	0.9	30	Wore through coating on all teeth of gears S/N 221 and S/N 222.
	75	25.5	126	0.7	25	
	85	30.3	162	0.3	10	
221-222 (Side B) vs 220-223 (Side A)	60	20.0	92	0.9	30	Wore through coating on all gear teeth.
	75	25.5	126	0.2	7	
214-215 (Side B) vs 200-201	75	25.5	126	0.7	25	Gear S/N 200 failed from fatigue crack that initiated a keyway.
	85	30.3	162	10.0	334	
	95	36.0	205	7.4	247	
214-215 (Side B) vs Steel Gears	110	48.0	300	36.8	1220	Wore through coating on two teeth of each gear.
*118-119 (Side B) vs Steel Gears	75	37.0	133	0.6	30	Bending fatigue failure on one tooth of gear S/N 118. No coating wear.
	85	46.0	175	0.6	30	
	100	56.2	231	79.3	3960	
*113-114 (Side A) vs Steel Gears	80	40	150	16.8	840	Bending fatigue failure on one tooth of gear S/N 113. No coating wear.
* These gears tested at 20,000 rpm; all other gears tested at 30,000 rpm.						
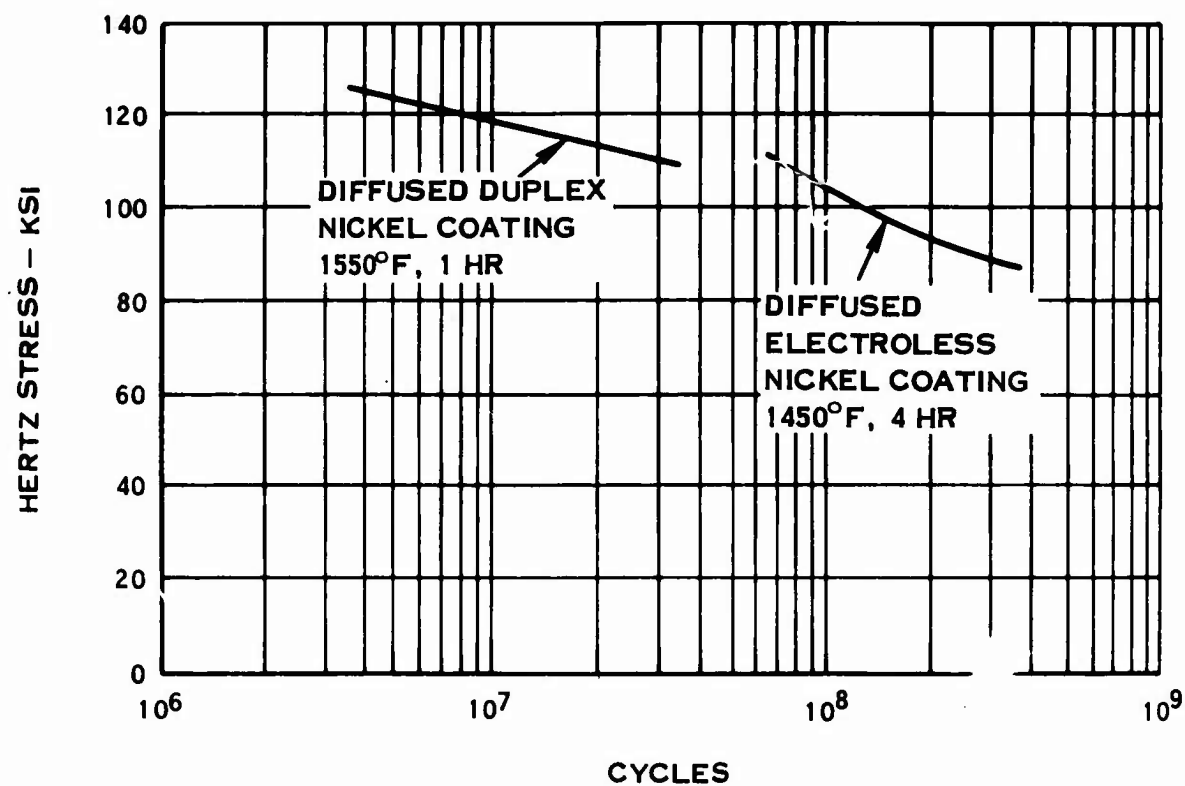
Figure 91. S/N Curve, Titanium Gear Testing.

171
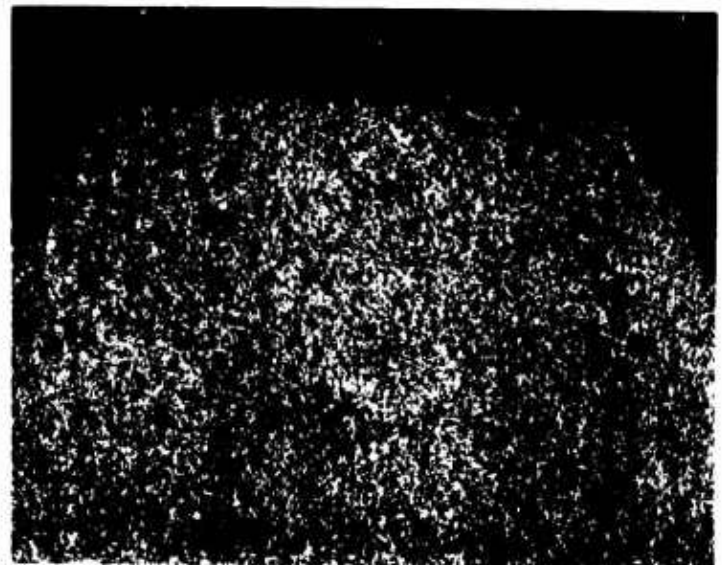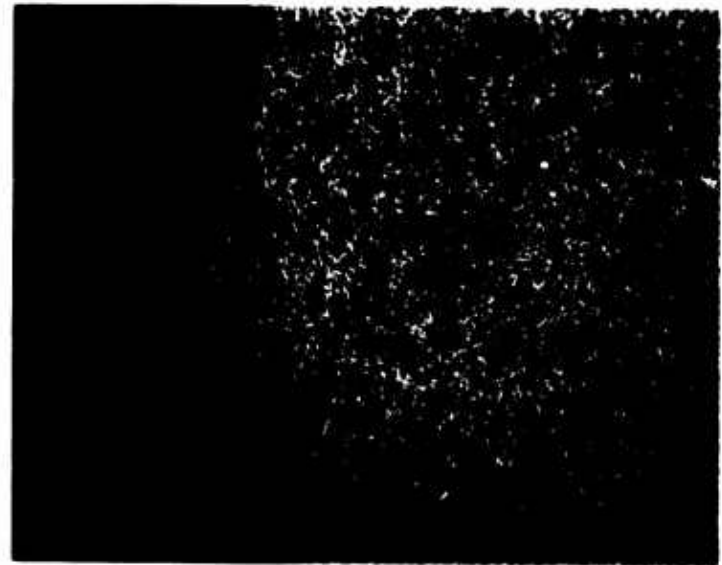
Figure 92. Failed Gear Tooth Showing
Negligible Coating Wear (50X).

172
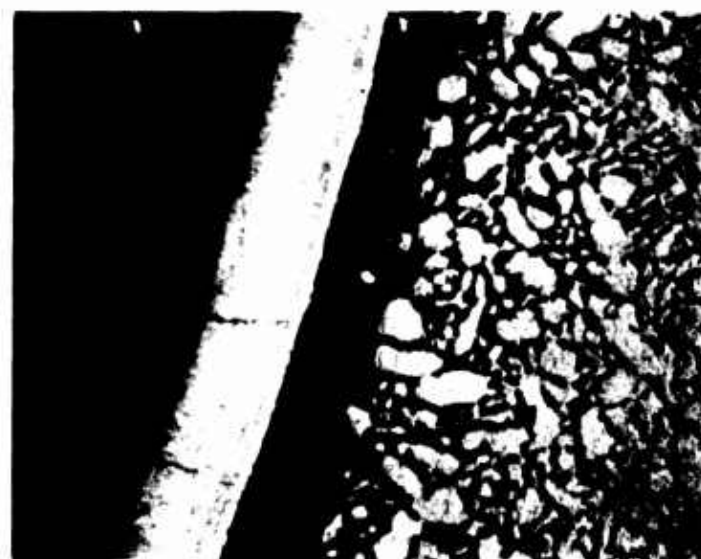
Figure 93. Cracks in Coating on Tensile
Side Near the Root of the
Failed Gear Tooth (500X).

Figure 94. Crack in Coating on Compressive Side
Near the Root of the Failed Gear Tooth
(500X).

by two phenomena: (1) a particular gear tooth can "spring back" as soon as the tooth load is removed and thus can deflect to some point beyond its normal position, which in effect would impose completely reverse bending on the gear tooth, even though it is transmitting load in only one direction; (2) the tensile stress distribution at the root of the particular tooth under load is such that it is possible to have tensile loading completely around the root. However, the magnitude of the tensile stress imposed in this manner would be insignificant and therefore is not included in the analysis. The magnitude of the tensile stress imposed by the "spring-back" phenomenon is a function of the dynamics of the particular system and as such is difficult to analyze with any accuracy. It is believed that in this particular case, the tensile stressing was great enough to promote fatigue cracking on the unloaded sides of the gear teeth.

A second set of 30-tooth gears (S/N 113 and S/N 114) was prepared for testing employing the same coating procedure as used with gears S/N 118 and S/N 119 and was endurance-tested at a load level of 86,000-psi Hertz stress (45,000-psi dynamic bending stress). This was the same load level as used previously for the endurance testing of diffused electroless nickel-coated gears. A coating failure was encountered after 252 hr (333 million cycles) of testing at this load level. Endurance test results are summarized in Table XXIV.

TABLE XXIV. ENDURANCE TEST RESULTS					
Gear S/N	Hertz Stress (ksi)	Bending Stress (ksi)	Torque (in.-lb)	Time (hr)	Speed (rpm x 1000)
113-114	75	37.0	133	-	20.0
(Side B)	86	45.0	175	100	20.0
vs	86	45.0	175	100	22.5
Steel	86	45.0	175	52	25.0
Gears					

Figure 95 shows the S/N relationship for Hertz stress that has been determined from the endurance testing of titanium gears with a diffused nickel coating. Separate curves have been drawn for the diffused electroless-type coating and the duplex diffused nickel-type coating. Both of these coating approaches show an approximate infinite-life Hertzian capacity of 80,000 psi. The endurance testing has also shown that infinite-life bending-stress capacity is approximately 45,000 psi.

174
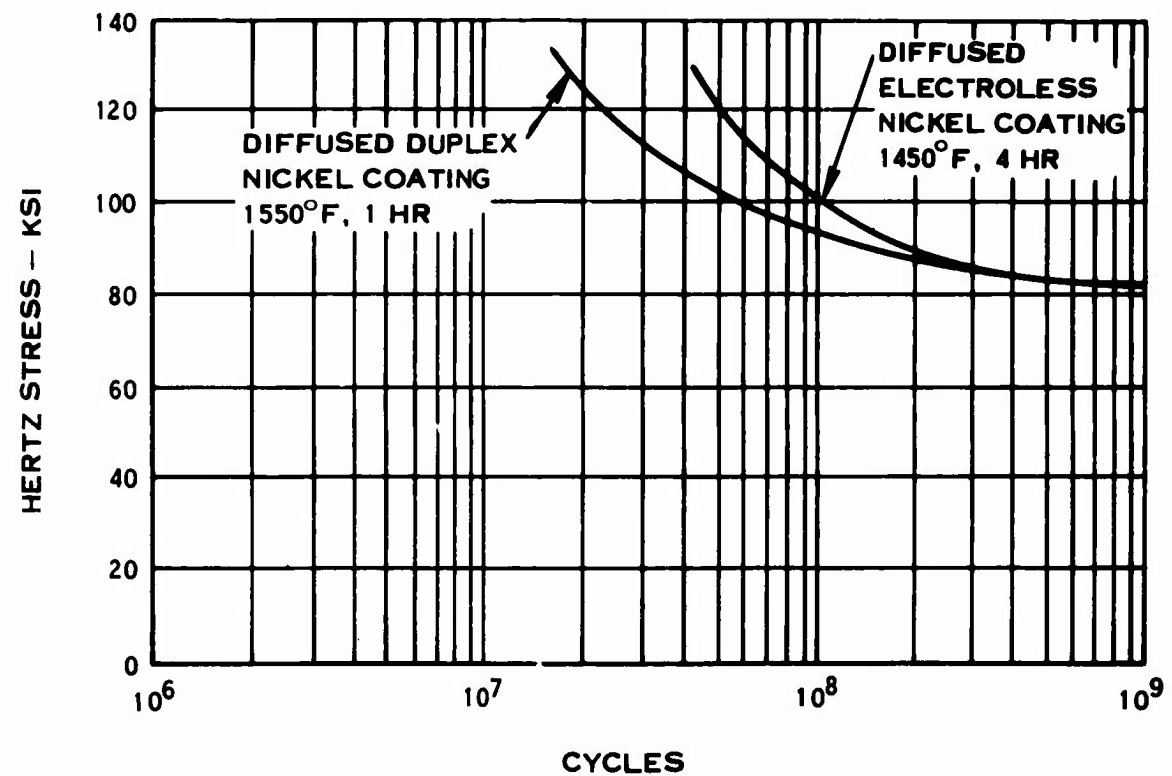
Figure 95. S/N Curve, Titanium Gear Testing.

From the curves in Figure 95, it is evident that the maximum operating Hertz stress for titanium gearing is approximately 85,000 psi, with a finite life of approximately 350 million cycles, using either the diffused electroless nickel coating or the duplex diffused nickel coating. The results are fairly consistent with 4 high-time data points clustered in this area. The infinite-life operating Hertz stress limit is estimated at 80,000 psi based on the limited amount of endurance testing conducted to date.

Design Trade-Off Study

A design trade-off study was conducted whereby relative weights of a study gearbox were calculated using assumed design allowables for titanium and steel gearing. For this study, the design allowables chosen for steel gearing were 150,000-psi Hertz stress and 65,000-psi dynamic bending stress. These values were based on Hamilton Standard's past experience with steel gearing and were considered to be representative of what the maximum infinite-life load-carrying capacity of steel gearing would be during the 1975 time period. Present-day infinite-life steel allowables are 140,000-psi Hertz stress and 60,000-psi dynamic bending stress. The design allowables chosen for titanium gearing were 100,000-psi Hertz stress and 50,000-psi bending stress. The study showed that a 20% weight advantage could be expected if the above design allowables were found to be realistic. A drawing of the study gearbox is shown in Figure 96. A gear weight summary for the study gearbox (using the above design criteria) is given in Table XXV.

The endurance testing of titanium gears performed herein has revealed that infinite-life Hertz stress capacity is something less than 85,000 psi, with a bending-stress limit of approximately 45,000 psi. With these limitations on load-carrying capacity for titanium gearing, the weight saving afforded by titanium versus steel would be insignificant.

It should be noted that the above weight comparison was based on assumed (1975) design allowables for steel gearing. If today's steel allowables were maintained, a weight saving of approximately 15% could be possible with titanium gearing. There are also those transmission systems (such as planetary reductions) where titanium gears could be considered because of the existence of relatively lower Hertz stress requirements.

176
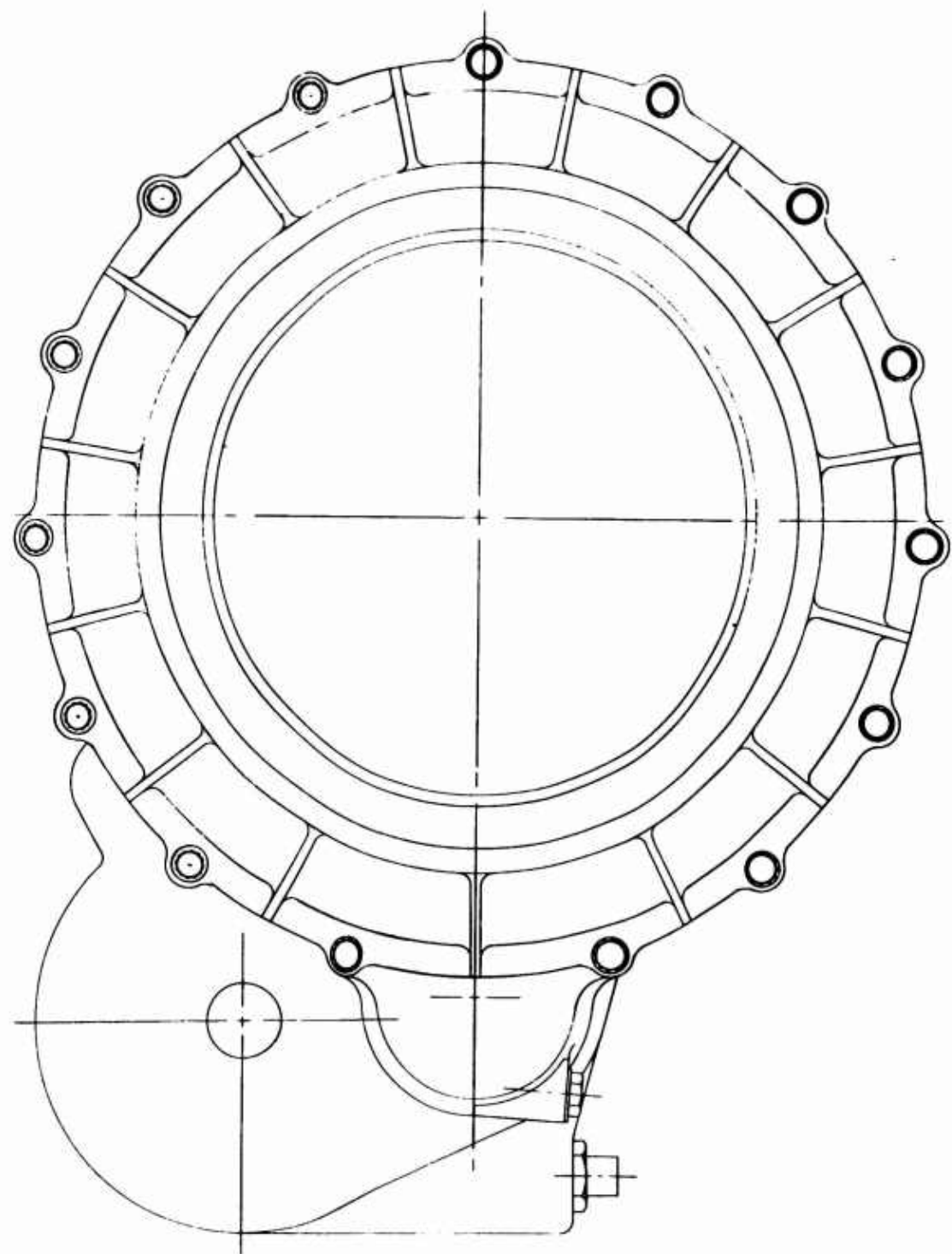
Figure 96.   Integral Gearbox for Steel Gearing.
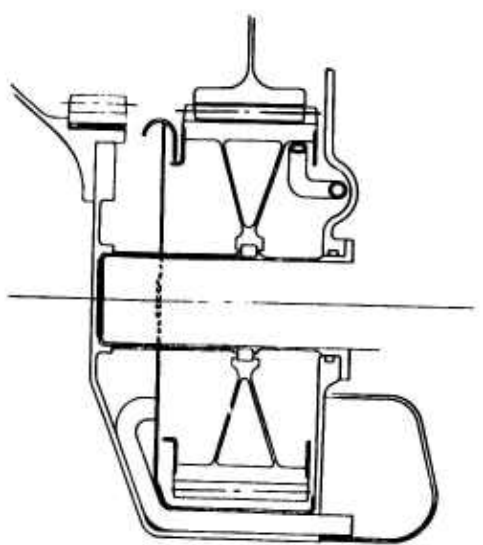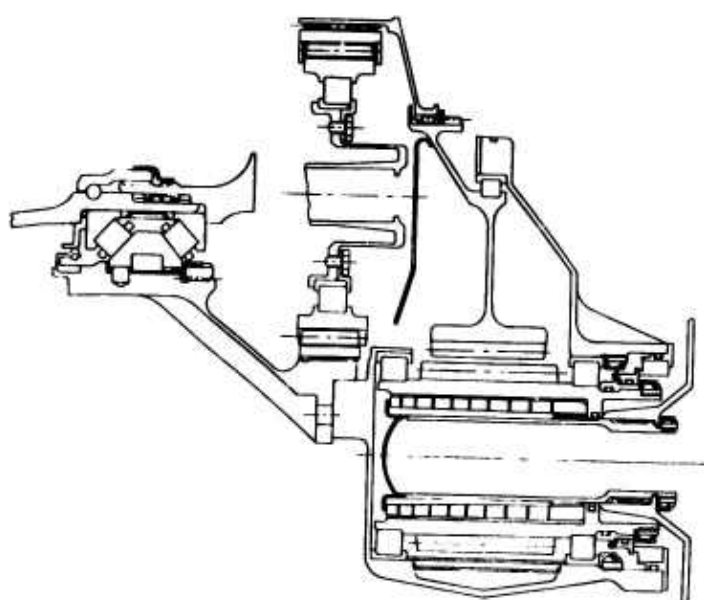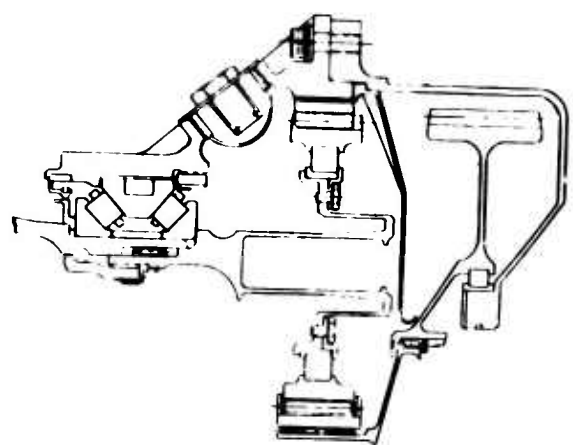
	TABLE XXV. STUDY GEARBOX - GEAR WEIGHT SUMMARY*				
	Steel		Titanium		
Hertz Stress (psi)	150,000	140,000	100,000	86,000	80,000
Bending Stress (psi)	65,000	60,000	55,000	45,000	40,000
Gears:					
Pinion	3.50	3.65	2.99	3.84	4.21
Idler	5.53	5.83	4.87	6.01	6.80
Bull	14.20	14.52	10.98	13.18	14.75
Sun	2.60	2.75	2.08	2.22	2.44
Planets	10.80	12.08	7.72	9.16	11.60
Ring	5.66	6.02	3.90	4.43	5.13
Housing Weight Diff	-1.93	-.93	***	1.16	1.80
Total	40.36**	43.92	32.54	40.00	46.73
Percent Weight Saving	-		19.40	0.89	-15.80

*Weights listed are based on the complete gear train as shown in Figure 96.

**Percent weight saving is based on this total weight.

***Housing weight based on these conditions is 16.5 lb.

179

BORSIC® ALUMINUM BLADE RETENTION INVESTIGATION

INTRODUCTION

Blades represent 35% of the total weight of one of today's advanced propeller/gear-box systems. Blade weight also sets the design loads for other major components such as barrel, actuator, gearbox, and support structure. It thus represents the single, most determining factor on total system weight. Therefore, in seeking to define the maximum weight-reduction potential for a 1970-1975 propeller system, prime attention must be directed toward blade weight reduction. This requires not only the evaluation of those new materials that appear to be feasible for use in that time period, but also a detailed evaluation of composite blade structures to best utilize the advanced material properties. Toward this end, the present contract is intended to provide fabrication development and design data for the retention area which will lead to development of full-scale advanced composite hardware. The requirements for the present contract were to design, fabricate, and tensile-test two reduced-size Borsic® aluminum specimens representative of an advanced propeller system. The design study resulted in the selection of the two configurations shown in Figure 97.

RETENTION TEST SPECIMEN DESIGN

The design of the blade stub presents the problem of transferring a concentrated load into a composite structure. The retention load is a uniform ring force acting at a 45-deg contact angle. The collapsing component of the load was reacted by placing a flat plate inside the composite cone. Two methods of transferring the axial component of the load into the composite were tried.

The first design (Configuration I) consisted of a uniform wall thickness cone of Borsic® aluminum with aluminum pieces on both sides of the lower portion of the cone. The axial force is transferred into the composite by shear at the composite-aluminum braze joint plus some compression caused by the wedging action of the two aluminum sides on the composite cone.

The second design (Configuration II) utilized the same construction as the first design for the inner part of the cone and the inner aluminum piece. The Borsic® aluminum cone was built up to one-third of the final thickness, and an aluminum wedge was added at the bottom.

Another third of the composite cone was built up, and a second aluminum wedge was added to the bottom of the cone. The composite cone was completed, and the final outer surface of aluminum was added.

180
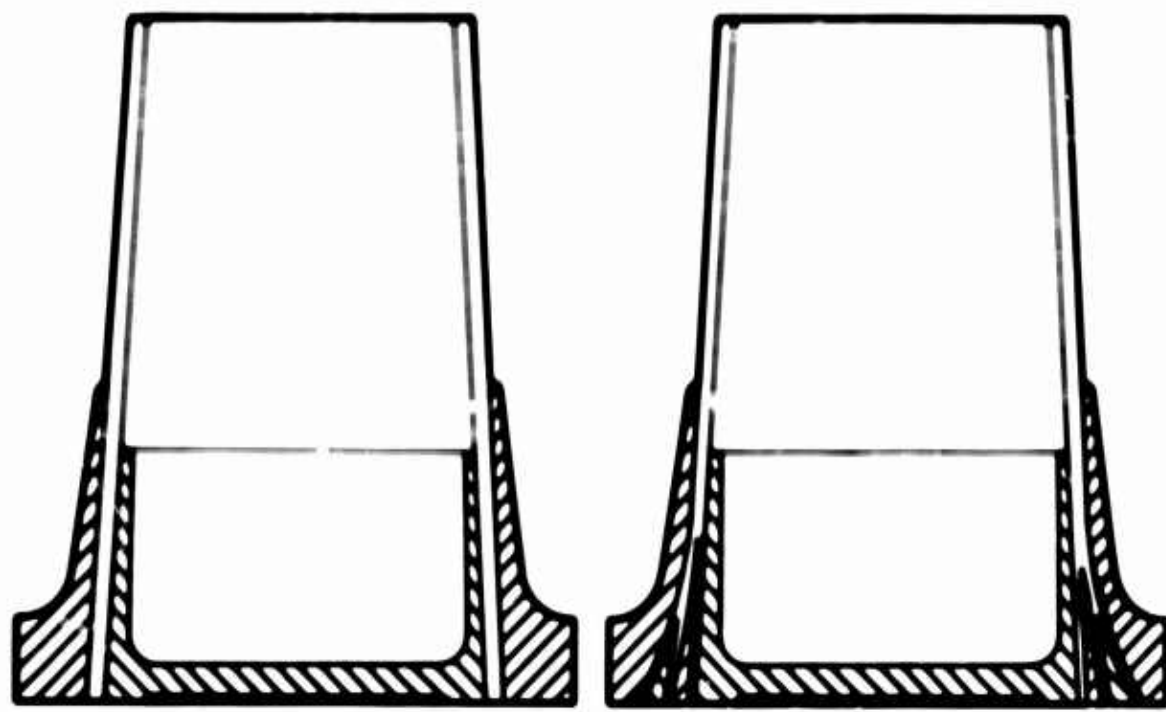
CONFIGURATION I – CONSTANT WALL
THICKNESS BORSIC° ALUMINUM

CONFIGURATION II – SPLIT LAYERS
OF BORSIC° ALUMINUM

Figure 97. USAAVLABS Retention Tensile Specimens.

181

The second design requires more parts and has more surfaces to be matched. Both designs were considered to be of equal load-carrying capacity in the analysis.

A computer program,[12] "Analysis of Shells of Revolution Subjected to Symmetrical and Non-symmetrical Loads," was used to analyze the test specimen. The program is usable for a multilayer orthotropic structure having different properties in each layer. The program calculates the deflections as uniform for all layers, and the stresses are then based on the properties of the individual layers. The preceding statements indicate that the program is a good mathematical model for a composite structure. The average tensile strength of Borsic® aluminum test panels at the time the retention test specimens were fabricated was 120,000 psi. The predicted failure load for this stress was calculated to be 141,000 lb.

A detailed drawing of the two specimen configurations is shown in Figure 98.

Fabrication

The test specimens were fabricated using metal matrix braze foil tape as the basic building block. This tape is made by collimation of the Borsic® fibers over a 1-mil-thickness 713 aluminum alloy braze foil and then plasma-sprayed with 6061 alloy to hold the fibers in place and to make up the remainder of the aluminum matrix required. The tape has approximately 175 fibers/in. tape width, and the Borsic® fiber represents approximately 50% of the tape weight.

The tape-cutting and lay-up procedure is illustrated in Figure 99. The tapes are cut to patterns which are sized to make up one complete layer with two pieces when they are wrapped around the mandrel and butted. The patterns are changed as required to allow for the increasing diameter as the part is built up. In the case of Configuration I, all of the layers are built up by tack welding of each layer to the layer below along the butt joints which are staggered from layer to layer. A total of thirty layers was assembled to have a final wall thickness of 0.150 in. This produces a finished fiber volume fraction of about 48%.

The cutting and lay-up procedure for Configuration II is the same as that described above except that the lower ends of the tapes are split at about .125-in. intervals to allow the tapes to fan out over the aluminum wedges. This is illustrated in Figure 100.

After lay-ups of the tape over the inner mandrel, the outer die is fitted and the entire assembly is placed in the Abar vacuum furnace shown in Figure 101. This furnace is capable of a vacuum of 10^{-5} torr at the braze bond temperature. The bonding and compaction of the matrix are accomplished by the relative motion between the two dies. They are designed in such a way that the final dimensions are reached when the bottom surfaces of both the mandrel and the outer die are in the
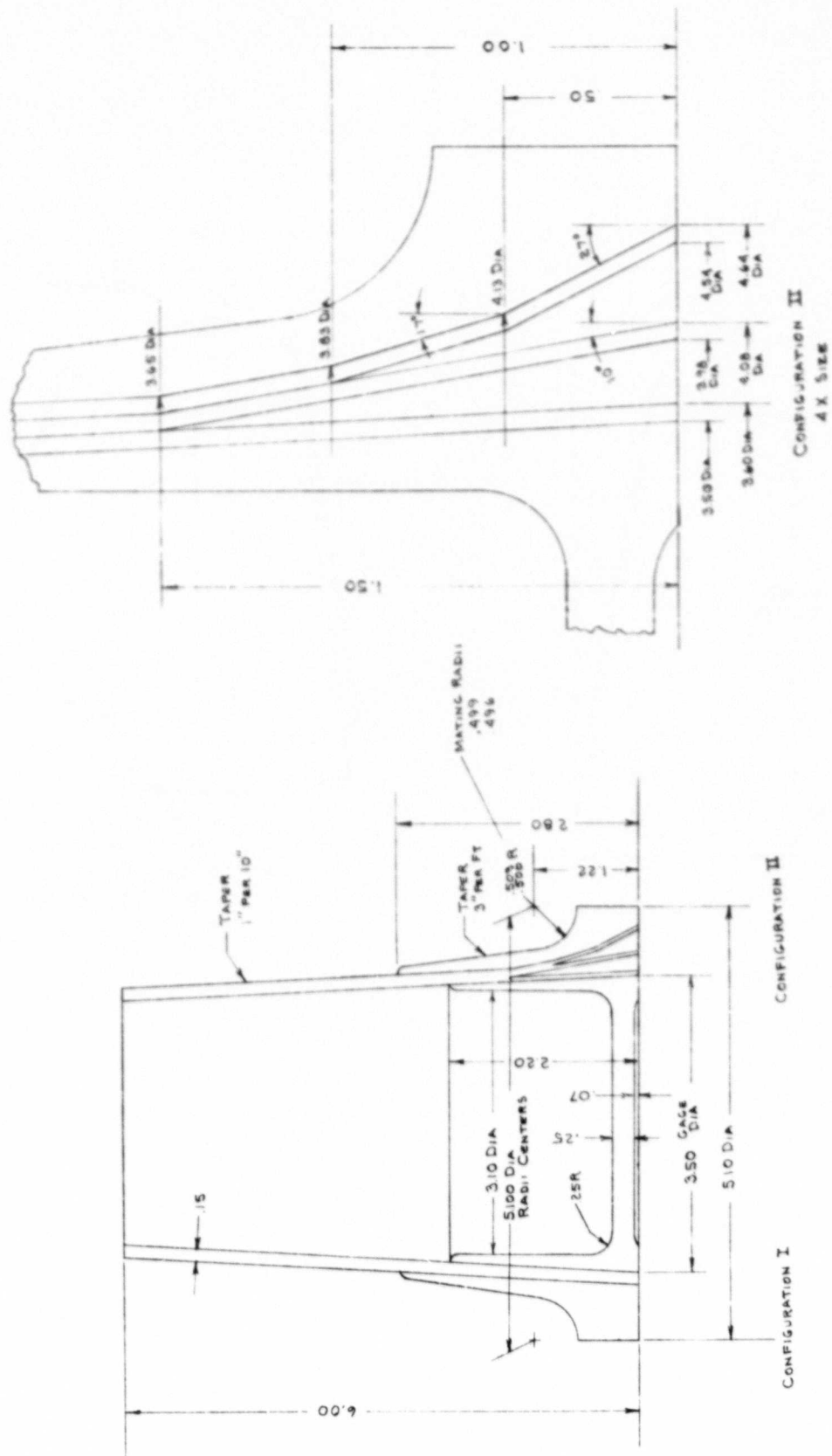
Figure 98. Detailed Drawing of Retention Test Specimens.
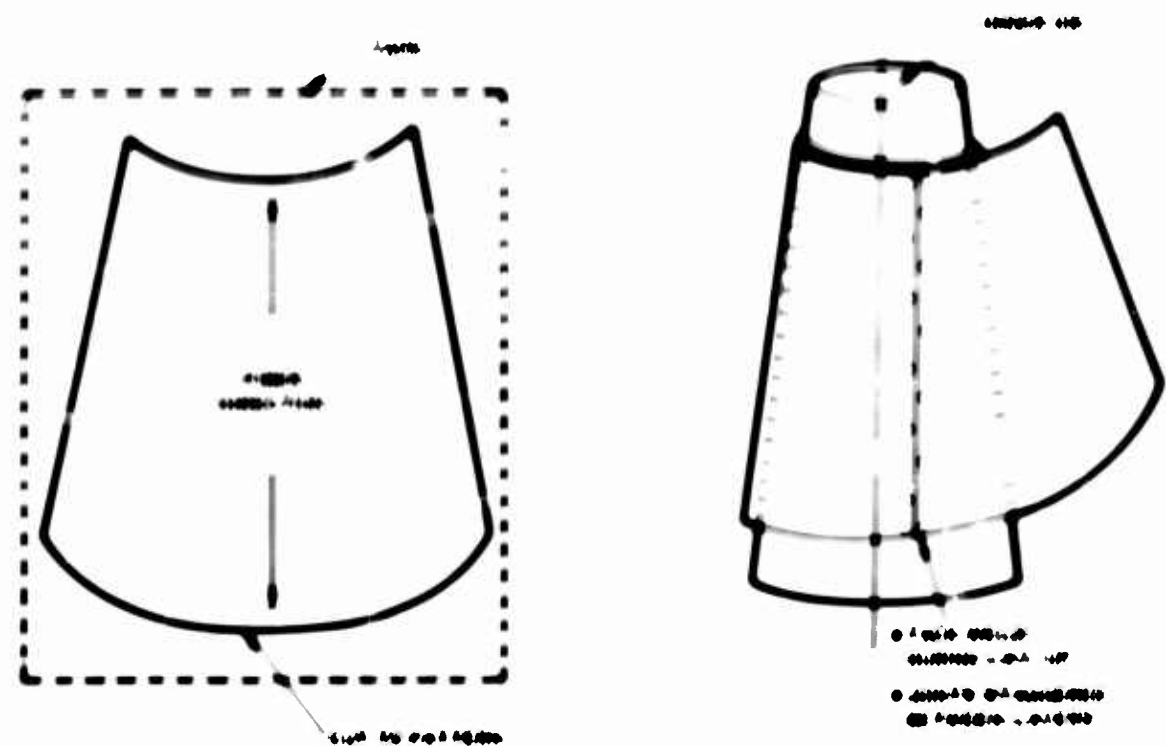
Figure 99. Tape-Cutting and Lay-up Procedure.
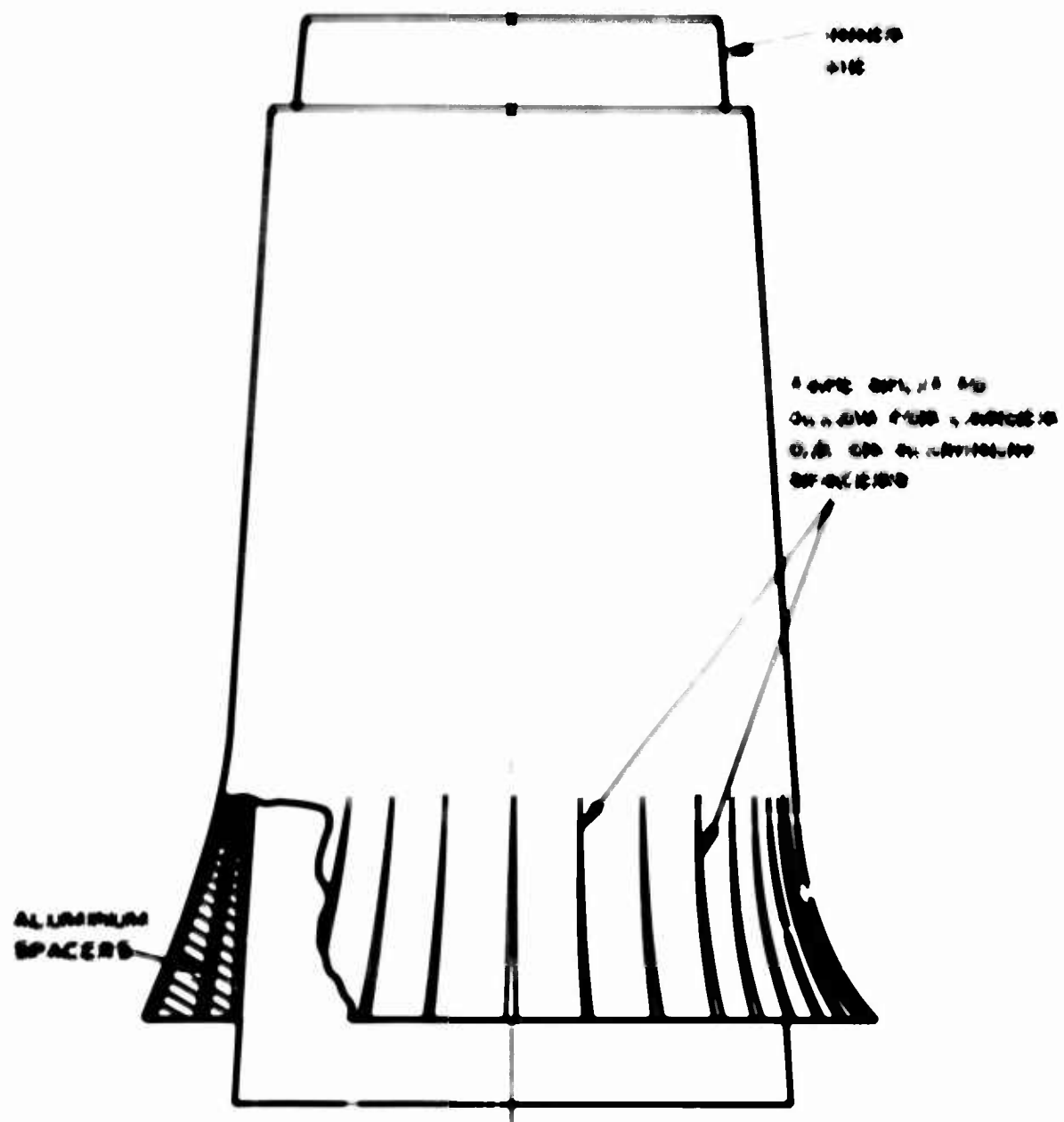
Figure 100. Tape Cutting and Lay-Up of Configuration II.

same plane (the bottom of the furnace). The inner mandrel is the same for both specimen configurations, but the outer die is larger at the base to allow for the flare of the Configuration II specimen. The driving force used to produce the relative motion is the weight of the outer die. The braze bond setup is shown schematically in Figure 102.

After completion of the braze-bonding operation, it is necessary to braze the inner support and a block of aluminum, which is later machined to final dimensions, to the basic Borsic® aluminum cone. This was accomplished as shown in Figure 102. Both pieces were brazed in one operation. The inner support and the aluminum block were carefully fitted to the Borsic® aluminum cone and then assembled with braze foil to provide the filler material. The inner support rested on a pedestal based on the base of the furnace, and a steel weight was added to the aluminum block to assure proper positioning of the parts during the braze cycle. The brazing was also carried out in the Abar vacuum furnace using 718 aluminum alloy braze so that the temperature used was well below the braze-bonding temperature used in forming the cone. Both the inner support and the aluminum block are 6061 aluminum alloy which was heat-treated to the T-6 condition after brazing to the Borsic aluminum cones. Final machining of the outside of the specimen was done after the heat-treating cycle. Photographs of the finished specimens are shown in Figure 103. The differences in the two configurations can be clearly seen at the base of the retention.

Testing

Tensile testing of the two specimens was required for this phase of the program and was conducted in the test setup shown in Figure 104. The tensile machine used was a Baldwin Southwork machine of 200,000 lb capacity. The test fixture was designed as shown in Figure 105. The lower portion of the fixture simulates a barrel retention and loads the base of the specimen at an angle of approximately 45 deg. The upper tensile load is applied through a steel cone that is inserted into the top of the specimen. Three soft aluminum chuck sections are placed between the cone and the inner wall of the specimen. Load is transferred through the wall of the specimen to the heavy steel ring which is adhesively bonded to the outside of the specimen. The ends of the chucks are tapered, as is the wall thickness of the steel ring, so as not to pick up the load abruptly at the edge of the fixture. The top plate which is bolted to the support ring provides additional strength to the ring and prevents motion of the chucks with respect to the inner wall of the specimen. The fixture ring performed well during testing of both specimens.

The tensile test of Configuration II was conducted first and resulted in three distinct steps to final fracture of the specimen. The three loads were 25,000, 30,000, and 41,300 lb, respectively. At each step, the load increased steadily until a distinct fracture was heard and a sudden drop-off of load was noted.
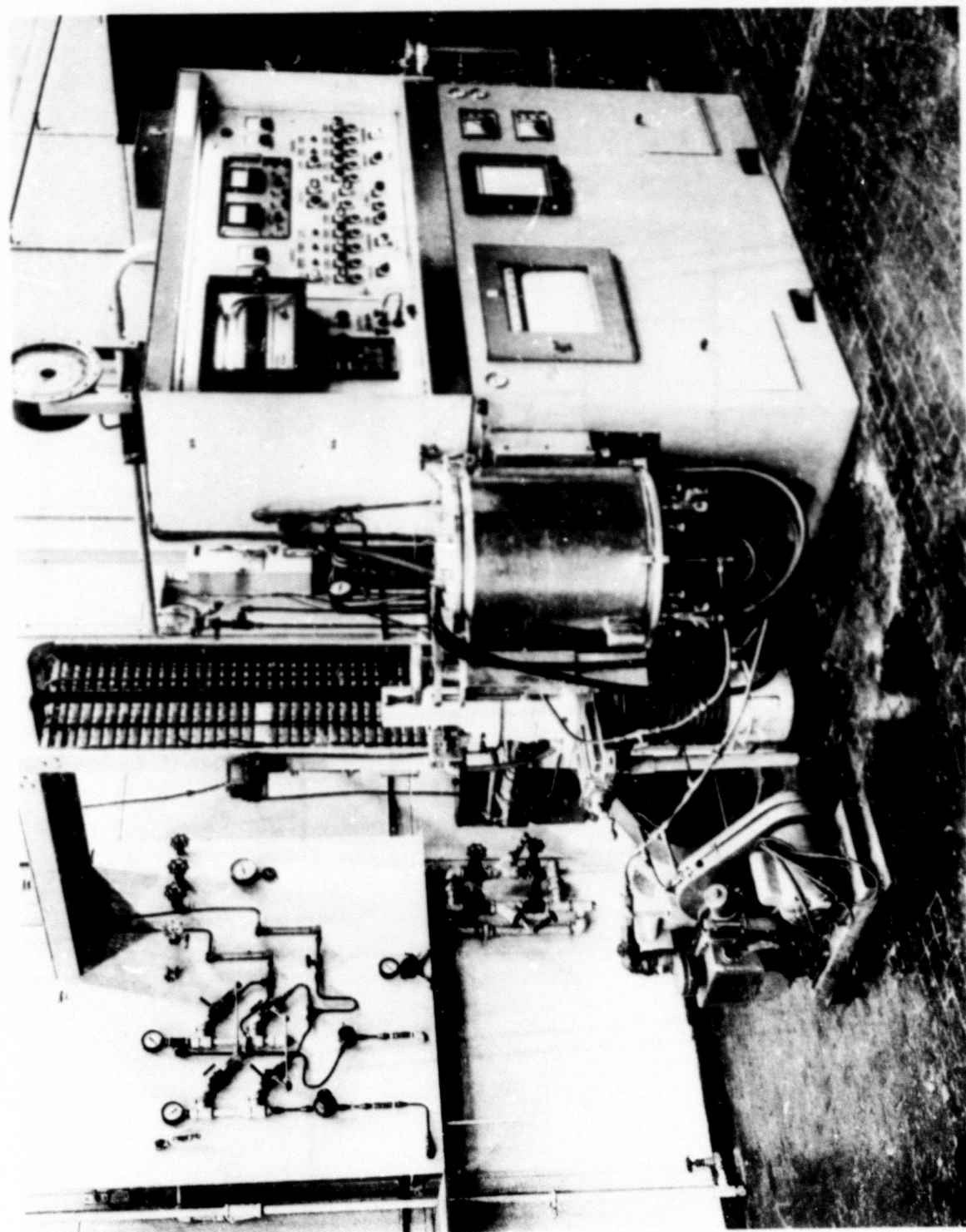
Figure 101. Abar Vacuum Furnace.

187
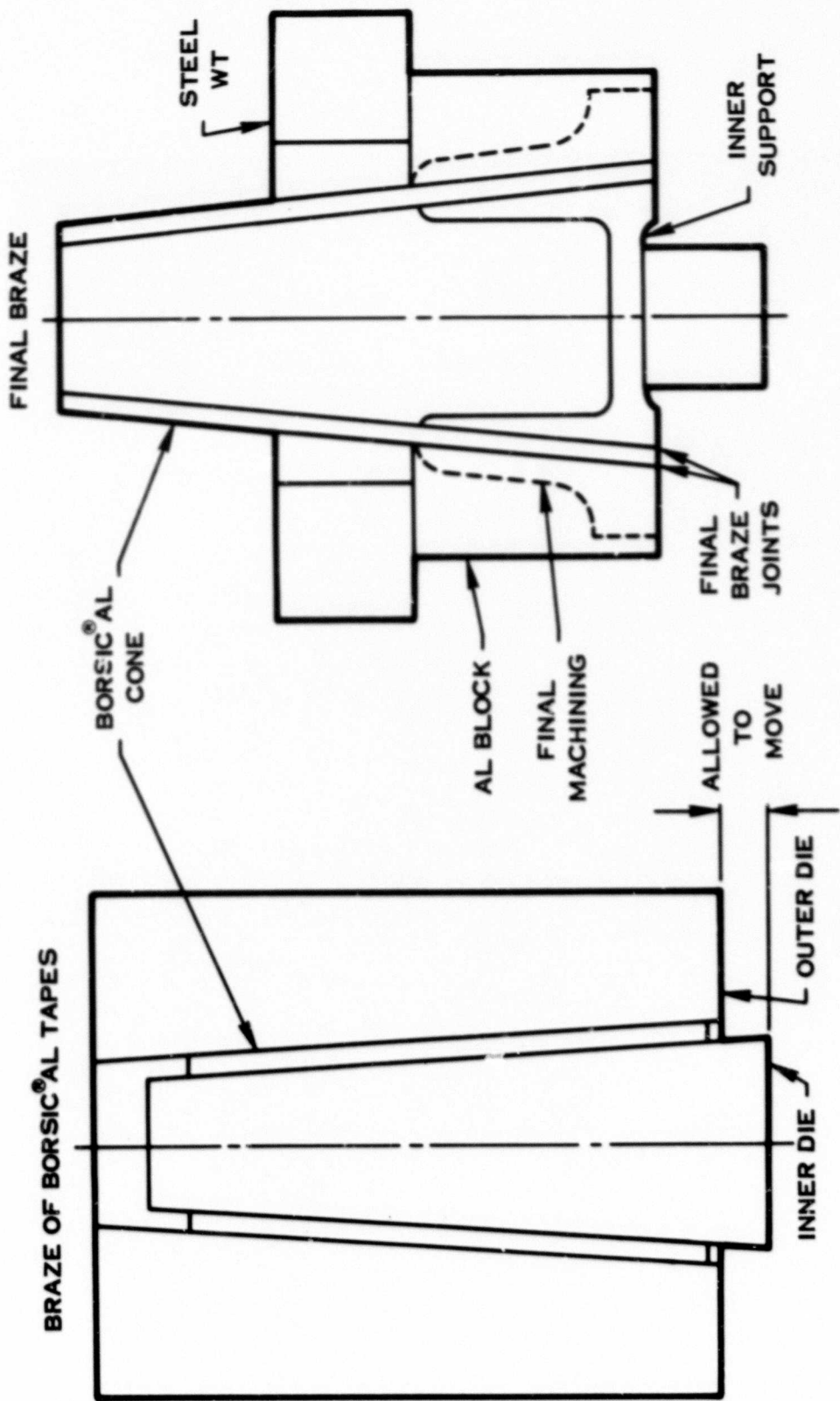
Figure 102. Braze Bond Tooling.

188

Figure 103. Finished Specimens.
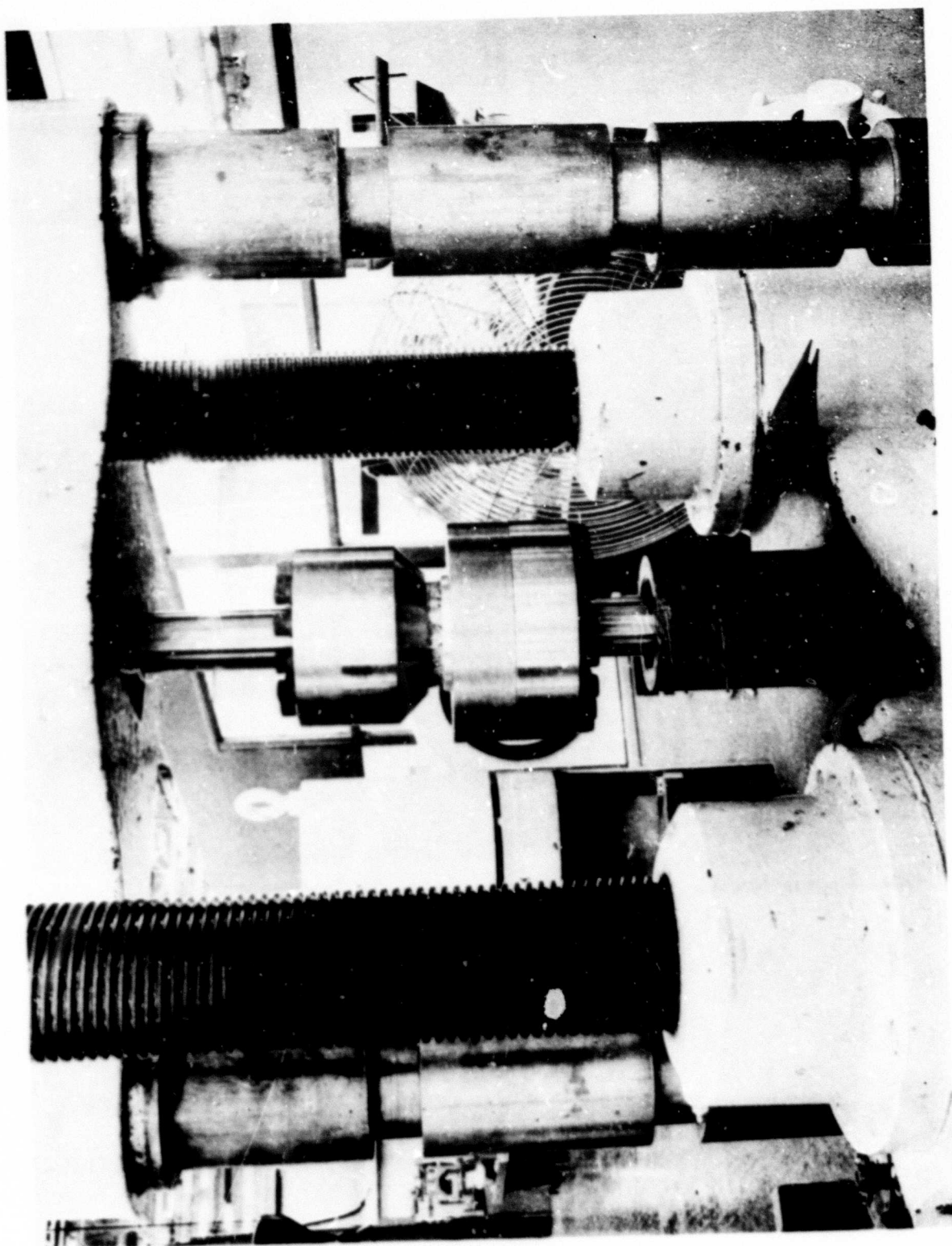
Figure 104. Retention Specimen Test Setup.

190
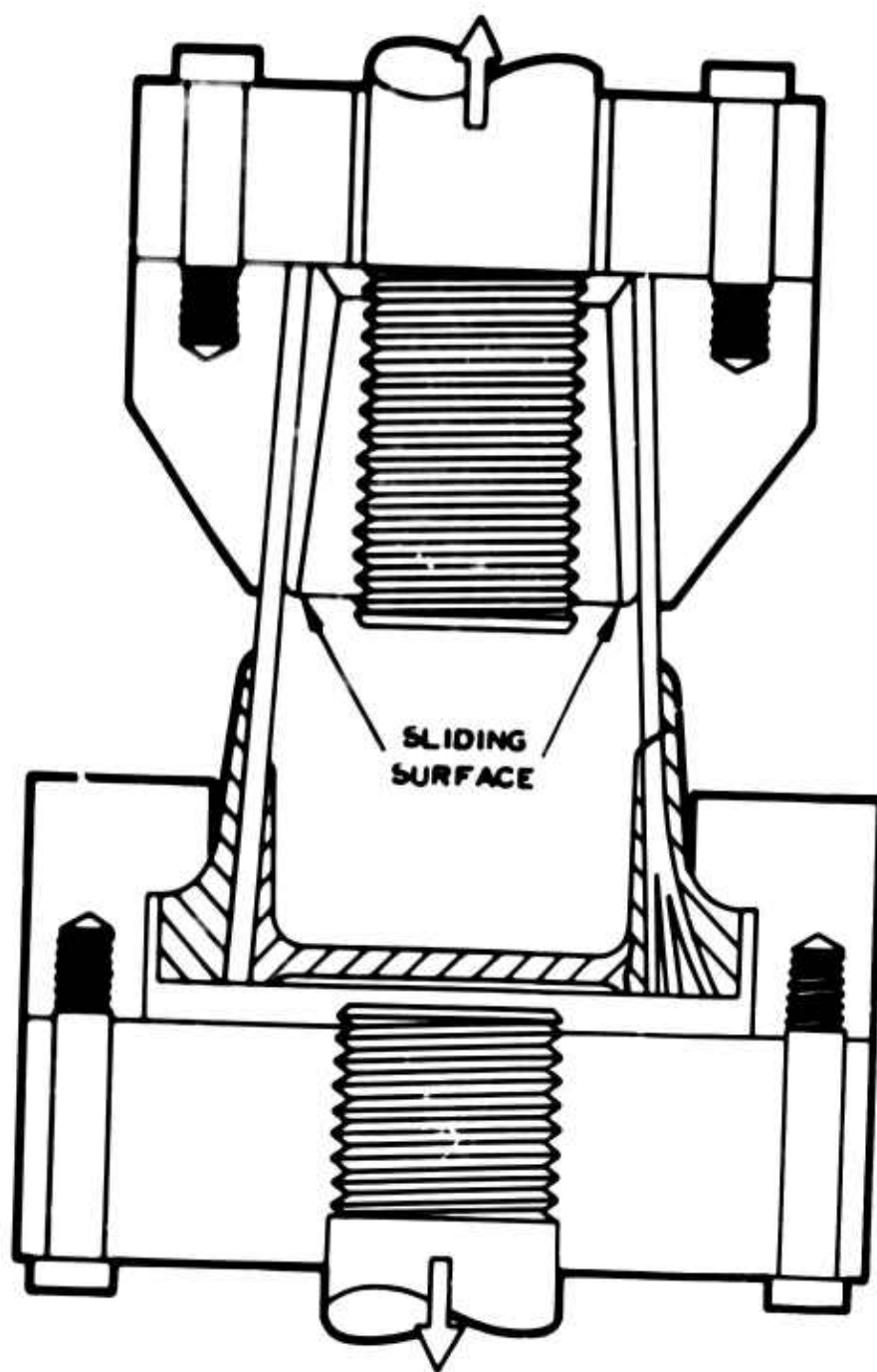
Figure 105. Tensile Test Fixturing.

191

The specimen would then pick up load again until the next step was reached, at which time the same sequence was repeated. Photographs of the fractured specimen are shown in Figure 106. It can be clearly seen both in the base of the specimen and in the wall that the three layers of fibers into which the wall had been divided by the wedges had fractured separately rather than causing the load to be evenly distributed. The sequence of failure was that the outer layer of fibers picked up the load first, due to its greater angle to the load, and carried the major portion of the load until its ultimate strength was reached. The load then transferred to the next layer until the same process was repeated, and the load finally transferred to the innermost layer. The reason for this behavior and the inability of the structure to distribute the load are due to the total elastic behavior of the boron fibers. Since there is no plastic elongation that can occur in these fibers, there is no redistribution as would occur in conventional materials by the process of yielding.

The Configuration I specimen was tested in the same setup as described above, but in this case the specimen carried the steadily increasing load to an abrupt fracture at 123,000 lb. The fractured specimen is shown in Figure 107. It should be noted that this fracture alternated between the grip area and the top of the retention and showed no sign of delamination as noted in the Configuration II specimen. It should also be noted that the failure load is very nearly three times the maximum load carried by the innermost layer of Configuration II, which is at the same angle as the total wall thickness of Configuration I. The failure load of 123,000 lb is about 13% lower than that predicted by the design computer program. However, the program did not indicate high stresses in the base of the retention, and it was noted that the base of the specimen was permanently dished. This would indicate a different loading than was assumed for the calculations and could account for the deviation from the predicted value.

192
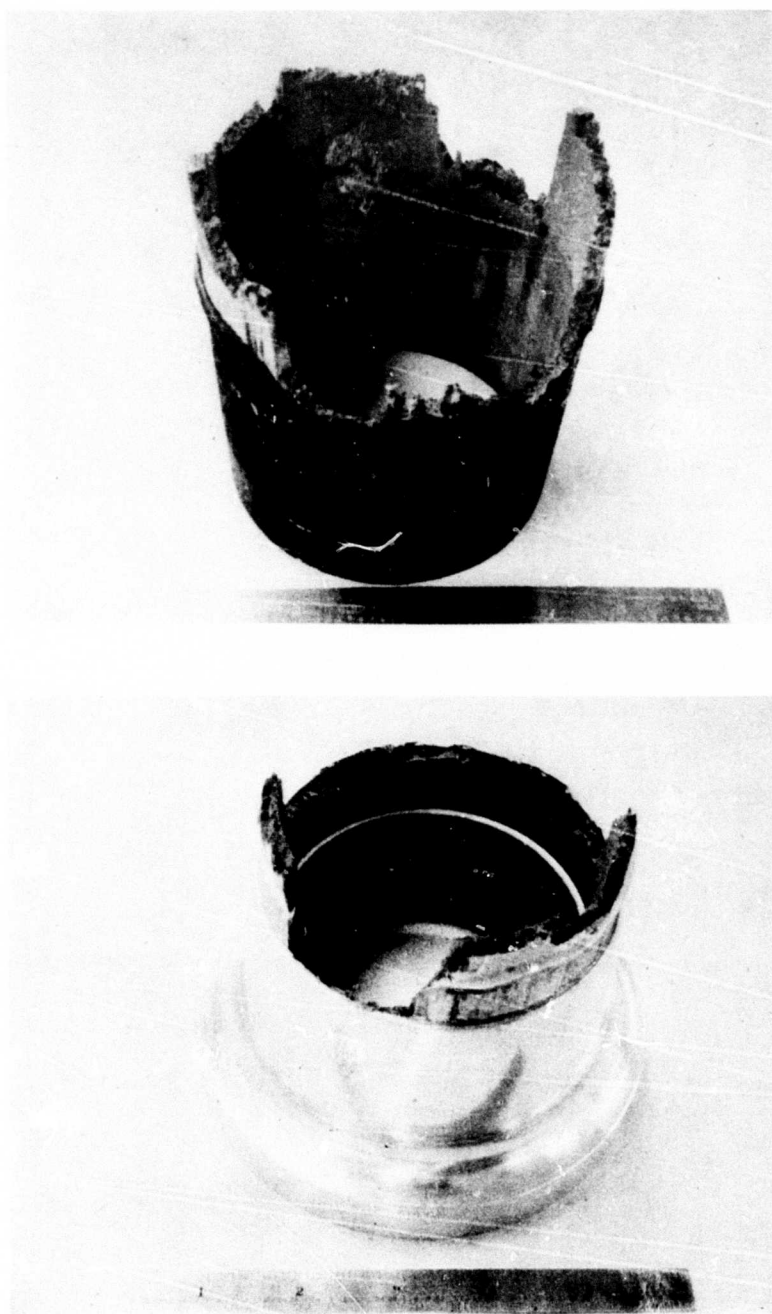
Figure 106. Configuration I Fractured Specimen.
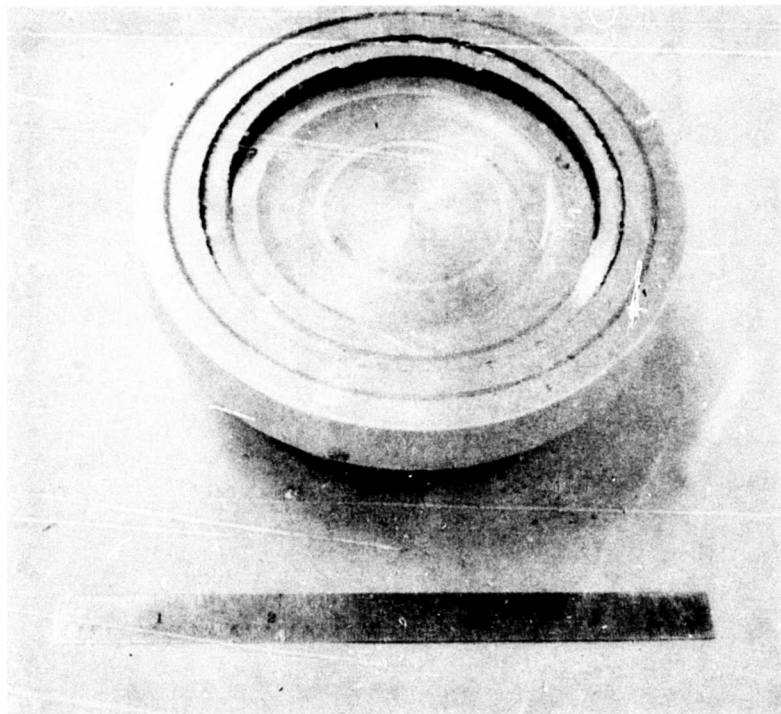
Figure 107. Configuration II Fractured Specimen.

CONCLUSIONS

TITANIUM BARREL

The design study has confirmed that barrel weight can be substantially reduced, as compared to existing V/STOL propeller barrels, by using a titanium barrel reinforced with boron fibers having a more efficient barrel mount structure. A barrel weight of 34 lb can be realized with a new 4-blade barrel design as compared to an 86-lb barrel, which represents today's state-of-the-art technology.

The weights of the 4-blade spherical, shell, and crossed tube barrel designs are essentially equal for this installation. The crossed tube concept did not prove to be a lighter weight configuration in this propeller size. However, larger diameter propellers with higher loadings may be more suited to this concept, in that minimum wall thickness would be eliminated as a criterion.

The weights of the 3-blade spherical, shell, and crossed tube barrel designs are also essentially equal for this installation.

The barrel design study has confirmed that the weights of a 4-blade propeller system and a 3-blade propeller system with the same total solidity are essentially the same. The 4-blade propeller inherently has a static thrust performance advantage, which is important to VTOL applications.

The 4-blade spherical barrel has advantages over the 4-blade crossed tube barrel design in that (1) higher stress allowables are obtained with the improved forgeability and (2) machinability is improved.

MAIN PROPELLER MOUNT BEARING

Bearing calculations have shown that this bearing has sufficient dynamic capacity to ensure the 3000-hr specified design life.

This new type of propeller mounting arrangement will result in approximately 20% less weight when compared to the arrangement used for today's integral gearbox propeller. The bearing weight of 11.9 lb is 1.4 lb lighter than originally estimated during the initial feasibility study.

TITANIUM GEARS

The titanium-nickel intermetallic coating system provides adaquate wear resistance for titanium gearing up to a Hertz stress level of 80,000 psi.

There is little difference in load-carrying capacity between a diffused electroless nickel coating and a diffused duplex nickel coating. Both types of coatings have been found to provide Hertz stress capacity of 85,000 to 90,000 psi with a finite life of approximately 350 million cycles. Infinite-life load capability is estimated to be 80,000-psi Hertz stress. The duplex coating is more difficult to apply.

Weight reduction studies based on projected (1975) increases in the load-carrying capacity of steel gearing show that no weight saving exists for titanium over steel; however, it should be noted that the projected capacity of 1975 steel gearing was established using assumed values of Hertz stress and dynamic bending stress.

The evaluation of ion-sputtered coated gears conducted under this program was limited. Therefore, a full assessment of the potential of ion-sputtered coatings was not attained. The feasibility of coating titanium gears using the ion-sputtering method has been demonstrated. A uniform adherent coating can be applied to the wearing surfaces of titanium gear teeth. Improvements in coating adhesion, coating uniformity, and general coating control would be expected by using a ion-sputtering arrangement that would enable the gear teeth to be coated without rotating the gear.

BORSIC®ALUMINUM BLADE RETENTION

A satisfactory propeller blade retention can be designed and fabricated using Borsic®aluminum advanced composite material. A design in which the fibers are carried to the base of the retention in one group is far superior to a design in which the fibers are separated into three equal groups. Separating the fibers forced them to behave independently rather than produce a more even load distribution as desired.

196

RECOMMENDATIONS

TITANIUM BARREL

It is recommended that a 4-blade titanium barrel with a spherical centerbody structure be manufactured from a pierced titanium forging and subsequently tested. Development testing should include a forging material evaluation program, an experimental stress analysis on a fully machined barrel to verify the theoretical barrel analysis, and a full-scale barrel fatigue test program.

This test is recommended to confirm theoretical stress calculations by means of actual test data and to demonstrate the higher stress allowables that result from improved forging techniques.

MAIN BEARING

It is recommended that a bearing life test be conducted in order to determine what influence the general configuration of the housing might have on this large-diameter small-cross-section bearing.

A static load test is also recommended to ascertain whether the magnitude of non-linear deflections in the bearing will adversely affect the wear pattern of each roller.

TITANIUM GEARS

It is recommended that further test experience with steel gearing be obtained in order to establish a sound technological basis for predicting the maximum load-carrying capacity of 1975 steel gearing.

A full-scale titanium gear development program should be undertaken. Such a program would permit a complete determination of load-carrying capacity. It would include evaluation of the effects of proper material fabrication procedures (forgings versus bar stock), actual gear mounting and lubrication practices, flexible gear configurations (wide rims mounted on thin webs), and general full-scale gearbox operating environment on the performance of coated titanium gearing. Conditions such as these would be expected to have a more favorable effect on gear performance compared to that experienced from operating solid 2.5-in.-pitch-diameter titanium gears in the four-square gear tester. The justification of such a program is based on the successful development of a reproducible coating which has enabled titanium gears to be operated at load levels that indicate weight-saving potential over "today's" steel gearing.

197

As a parallel effort to the full-scale titanium gear development program, it is recommended that the development of ion-sputtered coatings for titanium gearing be continued. Coating hardness, uniformity, thickness, and adhesion would be the primary considerations. It is proposed that ion-sputtered coatings be developed and evaluated as part of the full-scale titanium gear development program with the anticipation that if early test results should prove to be favorable, an ion-sputtering process would be substituted for the diffused nickel process.

BORSIC®ALUMINUM BLADE RETENTION

In view of the encouraging results obtained under this program, a follow-on development program is recommended in which a full-size retention will be designed, fabricated, and fatigue-tested. Since the propeller blade spar is usually sized by the fatigue strength of the retention, this is a very important step toward development of a full-size blade spar. The acquisition of full-scale retention fatigue data along with the continued development of fabrication techniques for a Borsic®aluminum spar by a Hamilton Standard company-sponsored program should lead to the ability to design and fabricate a full-size spar by 1970.

LITERATURE CITED

1. Perry, D. J., AIRCRAFT STRUCTURES, McGraw-Hill Book Co., 1950.

2. Roark, Raymond, FORMULAS FOR STRESS AND STRAIN, McGraw-Hill Book Co., 1954.

3. Singer, F. L., STRENGTH OF MATERIALS, Harper and Row, 1962.

4. Jones, A. B., Consulting Engineer, ROLLING ELEMENT BEARING ANALYSIS PROGRAM, Newington, Connecticut.

5. Palmgren, Arvid, BALL AND ROLLER BEARING ENGINEERING, S. H. Burbank Co., Inc., 1959.

6. Rothbart, Harold A., MECHANICAL DESIGN AND SYSTEMS HANDBOOK, McGraw-Hill Book Co., 1964.

7. Peterson, R. E., STRESS CONCENTRATION DESIGN FACTORS, John Wiley and Sons, Inc., 1966.

8. Adamson, W. M., FEASIBILITY STUDY OF ADVANCED V/STOL PRO-PELLER TECHNOLOGY, Hamilton Standard Div., United Aircraft Corp.; USAAVLABS Technical Report 68-33, U.S. Army Aviation Materiel Laboratories, Fort Eustis, Virginia, June 1968, AD 671029.

9. Neffinger, Norbert, BARREL DESIGN GUIDE, Hamilton Standard Div., United Aircraft Corp., Internal Report, HSER 2572, November 1967.

10. Evans, T. W., Fahy, E. A., and Famiglietti, P. F., TITANIUM PARTS STUDY, Hamilton Standard Div., United Aircraft Corp., Report Number HSER 5382, April 1969. A three-year development program conducted for the Naval Air Systems Command under Contract NOw 66-0063-d.

11. Cohen, S. H., Del Grosso, E. J., Mcgivern, J. F., and Mattavi, J. L., DEVELOPMENT AND TESTING OF INTERMETALLIC COATED TITA-NIUM ALLOY GEARS, Hamilton Standard Div., United Aircraft Corp., Paper presented at 15th National Symposium of the Society of Aero-Space and Material Process Engineers (SAMPE), April 1969.

12. Kalnis, A., ANALYSIS OF SHELLS OF REVOLUTION SUBJECTED TO SYMMETRICAL AND NON-SYMMETRICAL LOADS, Journal of Applied Mechanics, September 1964.

13. SPUR GEAR DESIGN, Hamilton Standard Design Manual, Hamilton Standard Div., United Aircraft Corp.

APPENDIX I
DETERMINATION OF TOOTH LOADS

HERTZ STRESS

$$S_c = 0.564 \left[\frac{W_t}{F_e \cos\phi \, \sin\phi} \left(\frac{1}{R_1} + \frac{1}{R_2} \right) \left(\frac{1}{\frac{1 - \mu_1^2}{E_1} + \frac{1 - \mu_2^2}{E_2}} \right) \right]^{0.5} \tag{80}$$

where

S_c = Hertz stress (psi) at pitch line (PL)

W_t = tangential tooth load (lb) = $\dfrac{\text{torque}}{\text{pitch radius}}$

F_e = minimum effective face width (in.)

ϕ = pressure angle (deg)

R_1 and R_2 = pitch radius (in.)

μ_1 and μ_2 = Poisson's ratio

E_1 and E_2 = modulus of elasticity (psi)

Values of the above functions for the titanium test gearing are given below:

$$F_e = 0.25 \text{ in.}$$
$$\phi = 25° \text{ (8-pitch gear) } 22.5° \text{ (12-pitch gear)}$$
$$R_1 = R_2 = 1.25 \text{ in.}$$
$$\mu_1 = \mu_2 = 0.35$$
$$E_1 = E_2 = 16.5 \times 10^6 \text{ psi}$$
$$W_t = 0.8T \text{ lb}$$

The general Hertz stress equations for the test gearing reduce to

$$S_c = 3950 \sqrt{\frac{T}{\cos\phi \, \sin\phi}} \tag{81}$$

For the 8-pitch gear,

$$S_c = 6380 \sqrt{T} \tag{82}$$

For the 12-pitch gear,

$$S_c = 6650 \sqrt{T} \tag{83}$$

201

DYNAMIC BENDING STRESS[13]

$$S_b = \frac{1.5 \, (W_d) \, (K_t)}{(F) \, (X)} \qquad (84)$$

where

S_b = dynamic bending stress (psi)

K_t = root stress concentration factor

F = face width (in.)

X = tooth form factor

W_d = dynamic load (lb)

$$W_d = \frac{0.05 \, V_p \, (FC_B + W_t)}{0.05 \, V_p + (FC_B + W_t) \cdot 5} + W_t \qquad (85)$$

where

V_p = pitch line velocity (fpm)

F = face width (in.)

C_B = gear material deformation factor

W_t = tangential tooth load (lb)

$W_t = \dfrac{\text{torque}}{\text{pitch radius}}$ = 0.8T (lb) for these test gears only

Values of the above functions for the titanium test gearing are given below:

F = 0.25 in.

C_B = 405

K_t = 1.0 (8-pitch gear), 1.3 (12-pitch gear)

X = 0.076 (8-pitch gear), 0.064 (12-pitch gear)

V_p = 19,635 fpm

W_t = .8T (lb)

Dynamic load reduces to

$$W_d = \frac{980\,(101 + 0.8T)}{980 + (101 + 0.8T)^{0.5}} + 0.8T \tag{86}$$

$$W_d \sim 100 + 1.6T \tag{87}$$

The general dynamic bending stress equation for the titanium test gearing reduces to

$$S_b = (600 + 9.6T)\left(\frac{K_t}{X}\right) \tag{88}$$

For the 8-pitch gear,

$$S_b = 7900 + 126.5T \tag{89}$$

For the 12-pitch gear,

$$S_b = 12,200 + 195T \tag{90}$$

APPENDIX II
TITANIUM GEAR PLAN OF TEST

JOB: TITANIUM GEAR DEVELOPMENT

PLAN PREPARED BY: E. Fahy

PROJECT & ORDER: Contract DAA J02-68-C-0079

APPROVED BY: _____

INSTRUCTION: _____

TEST ENGINEER: _____

TIME PERIOD: 15 November 1968 TO 15 February 1969

1. WHAT IS ITEM BEING TESTED?

2. WHY IS TEST BEING RUN? WHAT WILL RESULTS SHOW OR BE USED FOR?

3. DESCRIBE TEST SET UP INCLUDING INSTRUMENTATION. ATTACH SKETCH OF INSTALLATION.

4. ITEMIZE RUNS TO BE MADE GIVING LENGTH OF EACH AND READINGS TO BE TAKEN.

5. SPECIAL INSTRUCTIONS: SAFETY PRECAUTIONS FOR OPERATORS AND HANDLING EQUIPMENT. OBSERVATIONS BY SIGHT, FEEL, OR HEARING. LIST POINTS OF OBSERVATION WHICH MIGHT CONTRIBUTE TO ANALYSIS OF (A) PERFORMANCE OF UNITS, (B) INCIPIENT TROUBLE BEFORE IT OCCURS, AND (C) CAUSE OF FAILURE.

6. HOW WILL DATA BE USED OR FINALLY PRESENTED? GIVE SAMPLE PLOT, CURVE, OR TABULATION AS IT WILL BE FINALLY PRESENTED.

NUMBER ENTRY AS LISTED ABOVE AND DESCRIBE BELOW

1.0 The items to be tested are 2.5-in.-pitch-dia titanium spur gears (P/N 12X990 and 12X1054)
2.0 The test is being run to evaluate the load-carrying capacity (Hertz stress and dynamic bending stress) of coated titanium gearing. The test results will be used to establish design limits for titanium spur gearing which in turn will be employed in determining the relative weight saving that can be realized by replacing steel gearing with titanium gearing in future propeller gearboxes.
3.0 A four-square test facility will be employed to evaluate the subject hardware. This test facility has been designed such that the loads and speeds (pitch line velocity) of full-scale power gearing can be simulated. The four-square arrangement enables the gears to be operated at high tooth loads with very little driving power. A 0-60,000 rpm air turbine is used to drive the test gearing.

3.1 Torque Stystem

Torque is applied to the test gearing via a split shaft arrangement. The required torque is applied to the split shaft and is locked into the system by bolting together the two flanges located at the split. After loading, the torque required to overcome the frictional forces in the system is recorded prior to and after running the gears. This is used as a reference check on the initial loading. When the gears are in operation, the air pressure required to drive the turbine becomes an indicator for monitoring the load on the test gearing. It should also be noted that the solid shaft has been designed such that its torsional deflection (over the range of torques used for this testing) is great enough to compensate for any loss in the applied torque that might be expected to occur as a result of gear tooth wear; i.e., the coating (approximately .001 in. thick), if completely worn, would result in only a small percentage loss (less than 3%) in the initially applied torque. A 5% loss in torque would result in only a 2.24% loss in Hertz stress.

Instrumentation

Devices have been incorporated into the test setup which will automatically shut down the test rig under the following conditions:

Speed – High-speed and low-speed shutdown is set at ± 1000 rpm of operating speed. Speed is monitored by both digital counter and by galvanometer.

Lubrication – A low oil flow switch ensures sufficient lubrication at the gear meshes.

Coating
Wear – A spark detector consisting of photoelectric cells sensitive to the wavelength of titanium will shut down the test rig upon receiving a signal generated from any sparking occurring at the gear mesh. Sparking will occur as soon as the bare titanium gear teeth are exposed through the coating.

3.2 Lube System

The gearbox incorporates six (6) lube jets for lubricating the test gearing and rig bearings. MIL-L-23699 oil is used as the lubricant and is maintained at an inlet temperature of $250°±10°F$.

205

4.0   Test Procedure

4.1   Preliminary Gear Testing (120 hr of testing)

The gear 12X1054 will be used for this phase of testing.

4.1.1   Installation of Test Gearing

Install gears to be evaluated on test rig. High and low points of mating gears will be matched. When only one set of titanium gears is to be evaluated, the titanium gears will be installed on top and the steel gears on the bottom. Backlash and center distance are to be measured prior to running gears.

4.1.2   Break-in Running

4.1.2.1 Break-in running for a new set of gears will consist of operating the gears at 75,000-psi Hertz stress (126 in.-lb torque) with the speed gradually increased from 0-30,000 rpm over a 15-minute period. Frictional torque is to be recorded before and after running. If the frictional torque drops by more than 5% during the break-in running, the test will be repeated.

4.1.2.2 Repeat 4.1.2.1 at a Hertz stress level of 85,000 psi (162 in.-lb torque).

4.1.3   Initial Test Evaluations

A minimum of six (6) pairs of 12X1054 gears will be subjected to a total of 120 hr of testing at various Hertz stress levels.

4.1.3.1 After satisfactorily completing the initial break-in running (4.1.2), the test gears will then be subjected to successive 10-million-cycle Hertz stress levels until a failure of the coated gear teeth is detected. The initial Hertz stress level for this testing will be at least 85,000 psi. Subsequent load levels will be run at increments of 10,000-psi Hertz stress; i.e., 85,000, 95,000, 105,000, etc. All testing will be accomplished at 30,000 rpm, in order to make a fair comparison in performance of the new gears and gears which were tested previously at this speed. Frictional torque will be recorded before and after each load level.

4.1.3.2 Data To Be Recorded

Data will be recorded per the sample test log data sheet shown in Figure 108.

206

4.1.3.3 Inspection

Test gears will be visually examined after completing each 2 hr of testing at each load level. During these inspections, if the frictional torque is found to be more than 5% lower than that initially recorded at the start of the test, the gears will be retorqued and the test repeated.

4.2 500-Hour Endurance Test

The Hertz stress level to be used in performing the 500-hr endurance run will be based upon the test results obtained from the 120 hr of development testing. If the Hertz stress level selected is greater than 105,000 psi, 8-pitch gears (P/N 12X1054) will be used; if less than 105,000 psi, the 12-pitch gears (P/N 12X990) will be employed. This will limit the maximum dynamic bending stress to 55,000 psi. During the 500 hr of endurance testing, the speed of the gears will be varied from 20,000 rpm to 30,000 rpm in order to evaluate the gears over a representative range of pitch line velocities.

4.2.1 Break-in running will be accomplished as in 4.1.2.

4.2.2 One set of gears will be operated at the selected Hertz stress level for a total of 500 hr. The 500 hr will consist of 100 hr each at the following gear speeds: 20,000, 22,500, 25,000, 27,500, and 30,000 rpm. The gears will be visually inspected and checked for torque every 2 hr for the first 10 hr. (NOTE: Gears will be unloaded and retorqued during these inspections.) If the gears are found to operate satisfactorily during the first 10 hr, inspection periods will then be required every 5 hr for the next 40 hr. The gears will then be operated continuously (inspected and retorqued every 24 hr) until completion of the 100 hr.

4.2.3 Recording of Data – Same as 4.1.3.2

5.0 Special Instructions

Unusual vibration, sharp changes in speed, the reason for any automatic shutdowns, and unusual loss in torque will be noted on the data log sheet. Rig oil filter should be changed every 100 hr; the lubrication oil every 200 hr. Periodic checks of the sparking device should be made to ensure that it is functioning properly.

6.0 Data will be finally presented as part of a final engineering report on USAAVLABS Contract DAAJ02-68-C-0079.

APPENDIX A - INSPECTION REQUIREMENTS

Inspections of Test Gearing Prior to Coating

Each gear to be tested will be inspected to ensure that the desired tooth profile is within the tolerance band of the drawing prior to plating (or coating). Four gear teeth (90° apart) will be randomly selected and examined for profile configurations. Red line charts will be maintained for each gear tooth that is examined; measurement over wires, tooth thickness, pitch runout, and the high and low points on each gear will also be recorded.

Inspection of Gearing Prior to Testing

Prior to testing, profile recordings of the same four teeth of each gear again will be taken and compared to the as-machined tooth profile. After assembling a set of gears to be tested, the backlash and center distance will be recorded prior to running gears. Assembly of the gears will be such as to (where possible) have the high and low points of the respective mating gears matched.

LOG OF TEST
ENGINEERING LABORATORIES

RIG NO. 4 Square Gear Tester Gear History -0.001 in. TiNi Coating H.T. 1300°F 1 Hr.
TYPE OF TEST Evaluation of Ion Sputtered Coated Gears
W.P.I. NO. 191 B00 400A
PLAN OF TEST NO.
SERIAL NO. 214, 215
PART NO. 12X 1054

UNITS → TIME	HR Cum Time	x10⁵ Cycles	IN.-LB Torque	KSI Hertz Stress	KSI Bending Stress	RPM Speed	PSI Air Press.	IN.-OZ FT	PSI Lube Press.	°F Inlet Temp	REMARKS
0800	-	-	126	75.0	25.5	0	30.0	52	20.0	250	
0815	0.25	0.45	126	75.0	25.5	30,000	30.0	51	20.0	249	Break In Running
0830	0.25	0.45	162	85.0	30.3	0	32.0	65	20.0	250	
0845	0.50	0.45	162	85.0	30.3	30,000	31.0	63	20.0	252	
0915	-	-	162	85.0	30.3	30,000	32.0	64	21.0	249	Start
1115	2.0	3.6	162	85.0	30.3	29,500	31.0	58	20.0	247	Stop, Check FT
1130	2.0	3.6	162	85.0	30.3	30,000	31.0	65	20.0	248	Start
1330	4.0	7.2	162	85.0	30.3	30,500	30.0	64	21.0	249	Stop, Check FT
1345	4.0	7.2	162	85.0	30.3	30,000	31.0	64	21.0	250	Start.
1438	5.5	10.0	162	85.0	30.3	30,200	30.0	63	20.0	251	Stop, Check FT
Sample Test Log Data Sheet											
1500	-	-	203	95.0	35.5	30,000	34.0	78	21.0	250	Start.
1700	2.0	3.6	203	95.0	35.5	29,000	34.0	77	20.0	249	Stop.

REMARKS: Backlash Prior to Testing 0.007 in. Center Distance 2.500 in.

Figure 108. Sample Test Log Sheet.

209

APPENDIX III
PROCEDURE FOR DUPLEX ELECTROLESS NICKEL
PLATING OF TITANIUM ALLOYS

1. Degrease and cleanse with scouring powder all part surfaces and bake dry (130°F, 30 min).

2. Mask surfaces not to be plated with Turcoat #4378 (double-dip coat with 30-min air dry and 15- to 20-min 212°F bake after each application). Several carefully applied brush-coats are also satisfactory, with similar baking and drying considerations.

3. Recleanse with scouring powder areas to be plated.

4. Rack part into appropriate plating fixture, providing for stout electrical connection. An in-dwelling nickel anode should be provided in the fixture, or provision should be made for rapid insertion of the same as required in the process. Management of the anode must not consume time in transfer.

5. Etch surfaces to be plated in solution as follows:

   5-10% (vol) HF (48%)
   30-35% (vol) HNO_3 (conc)
   Balance water
   Room temperature, approximately 2 min

After rinsing, examine part areas to be plated for appearance of "water-breaks". The appearance of these after etching is indication of insufficient cleansing in such areas. Cleanse again (locally) with scouring powder and repeat etch cycle. Repeat until no water breaks are observed.

6. Transfer part to HAc-HF anodic etch made and used as follows:

   875 ml of glacial acetic acid
   125 ml of 48% HF
   Temperature - 100° to 120°F
   Surface to be plated made anodic at 20 asf, 2 min
   Solution continuously sparged with dry nitrogen

This solution should be made fresh for each part being processed and should be discarded after use. If a large volume is made for use on a number of small parts, the solution should be kept covered and sparged with nitrogen for at least 2 hr prior to use.

7. Transfer part to electroless nickel-plating solution through a boiling-water (distilled) rinse. Because of drag-in possibilities, this rinse should be fresh for each part to be processed.

8. As part enters the electroless nickel-plating solution, the surface being plated should be made cathodic at 20 asf (electroplated) until the normal, overall gassing characteristic of good electroless plating has been achieved (normally 10 to 15 sec), whereupon the power is stopped and, when convenient, the anode is removed from the working setup.

9. Continue electroless plating until the thickness desired has been developed.

10. Transfer part to electrolytic tank for coating with pure nickel.

Notes:

a. The choice of electroless nickel-plating soulution is not critical. Alkaline, acid chloride, and acid sulfate types have been used, and it has been found that the bath called Lustraloy, which is an acid chloride type, is easy to manage. Therefore, the bulk of our work with titanium alloy parts has employed this solution.

b. Specifications and directions for operation of electroless nickel plating may be found in production method procedures documentation, pursuant to the requirements of Hamilton Standard Specification 201.

c. In order to regulate the time to given plate thickness, a test panel of convenient geometry is used. This panel should be started in electroless plating at the time that the processing on the Ti hardware is begun. As soon as the Ti hardware is in the electroless nickel solution, the panel should be withdrawn, cooled, measured to within 0.0001 in., and replaced in the bath. By checking this same measurement for change after an additional 30 min of running, it is possible to evaluate closely the plating rate (tenths per hr). The out time for the hardware may then be computed. A check on the test panel 10 or 15 min before expected out time will refine the estimate and will allow close control of finished plate thickness.

d. During the plating process, a change in nickel deposition rate in excess of 20% of the starting rate is cause for aborting the run. Since stoppages of the plating on the part are cause for stripping and starting over, the changes mentioned are cause for rerun.

211

e. Stripping of nickel from titanium alloys may be accomplished in dilute (30 to 50%) nitric acid. The condition of maskant materials after a nickel strip operation should be critically reviewed before proceeding on a rerun. In all probability, the masking should be completely replaced.

APPENDIX IV
PROCEDURE FOR DIFFUSION OF DUPLEX NICKEL PLATE INTO TITANIUM GEARS

The following procedure was used to diffuse nickel plate into titanium gears:

1. Plated gears are cleaned with Gibson cleaner and water to remove any possible contamination on the gears.

2. Gears and plated control tab specimen of material similar to the gears are placed in the vacuum furnace, and thermocouples are placed against the gears.

3. Furnace is heated to $1000°F$ at a rate of $20°F$ per min and is held there until the gears are at this temperature for 2 hr.

4. The temperature is then increased to $1550°F \pm 10°F$ at a rate of $13°F$ per min and is held at this temperature for 1 hr.

5. The furnace is then turned off; the gears are allowed to cool in vacuum to room temperature and then are removed from the furnace.

Note: Vacuum in the furnace is maintained between 10^{-4} and 10^{-7} torr.

DOCUMENT CONTROL DATA - R & D

(Security classification of title, body of abstract and indexing annotation must be entered when the overall report is classified)

1. ORIGINATING ACTIVITY *(Corporate author)*	2a. REPORT SECURITY CLASSIFICATION
Hamilton Standard Division of United Aircraft Corporation Windsor Locks, Connecticut	Unclassified
	2b. GROUP

3. REPORT TITLE

DETAILED DESIGN OF A 2000-SHP ADVANCED TECHNOLOGY V/STOL
PROPELLER SYSTEM

4. DESCRIPTIVE NOTES *(Type of report and inclusive dates)*
Final Report

5. AUTHOR(S) *(First name, middle initial, last name)*

D. P. Currie

6. REPORT DATE	7a. TOTAL NO. OF PAGES	7b. NO. OF REFS
September 1969	232	12

8a. CONTRACT OR GRANT NO.	9a. ORIGINATOR'S REPORT NUMBER(S)
DAAJ02-68-C-0079	
b. PROJECT NO.	USAAVLABS Technical Report 69-59
Task 1G162203D14415	
c.	9b. OTHER REPORT NO(S) *(Any other numbers that may be assigned this report)*
d.	

10. DISTRIBUTION STATEMENT

This document is subject to special export controls, and each transmittal to
foreign governments or foreign nationals may be made only with prior approval
of US Army Aviation Materiel Laboratories, Fort Eustis, Virginia 23604.

11. SUPPLEMENTARY NOTES	12. SPONSORING MILITARY ACTIVITY
	U.S. Army Aviation Materiel Laboratories Fort Eustis, Virginia

13. ABSTRACT

The purpose of this program was to establish a sound technical foundation for the inclusion of
lightweight titanium barrels, titanium power gearing, and composite boron-aluminum spar
blades in an advanced (1970-1975) V/STOL propeller system.

Several new titanium barrel concepts were designed and analyzed. This study has led to the
recommendation of a titanium barrel with a spherical hub structure for subsequent fabrication
and development testing.

Endurance testing of titanium gears was performed which indicated that improved wear coatings
would be required in order to demonstrate a significant weight saving potential over 1975 steel
gearing. However, the diffused nickel coating would permit significant weight reductions over
current steel power gearing.

Titanium gears were also coated and evaluated under this program using an ion-sputtering coating
technique. Limited testing of such gears resulted in early scuffing and wear of the coating; how-
ever, the basic coating is sound and processing refinements have been defined that indicate
potential for sputtered-coated titanium gears.

The fabrication and testing of boron-aluminum composite blade retention specimens proved to be
successful and have provided a sound basis for the fabrication and development testing of
full-scale propeller blades.

DD _{FORM} **1473** REPLACES DD FORM 1473, 1 JAN 64, WHICH IS
1 NOV 65 OBSOLETE FOR ARMY USE.

14. KEY WORDS	LINK A		LINK B		LINK C	
	ROLE	WT	ROLE	WT	ROLE	WT
V/STOL Propeller System Titanium Barrels Titanium Gearing Boron-Aluminum Spar Blades Ion-Sputtering Coating Diffused Nickel Coating						